REPORT DOCUMENTATION PAGE

Form Approved OMB NO. 0704-0188

The public reporting burden for this collection of information is estimated to average 1 hour per response, including the time for reviewing instructions, searching existing data sources, gathering and maintaining the data needed, and completing and reviewing the collection of information. Send comments regarding this burden estimate or any other aspect of this collection of information, including suggesstions for reducing this burden, to Washington Headquarters Services, Directorate for Information Operations and Reports, 1215 Jefferson Davis Highway, Suite 1204, Arlington VA, 22202-4302. Respondents should be aware that notwithstanding any other provision of law, no person shall be subject to any oenalty for failing to comply with a collection of information if it does not display a currently valid OMB control number.
PLEASE DO NOT RETURN YOUR FORM TO THE ABOVE ADDRESS.

1. REPORT DATE (DD-MM-YYYY)	2. REPORT TYPE	3. DATES COVERED (From - To)
09-11-2015	Final Report	15-Sep-2012 - 14-Sep-2015

4. TITLE AND SUBTITLE
Final Report: Optical Physics and Imaging Science (12.5): Nonlocal Plasmonic Metamaterials for Ultrafast and Nonlinear Optics

5a. CONTRACT NUMBER
W911NF-12-1-0533

5b. GRANT NUMBER

5c. PROGRAM ELEMENT NUMBER
611102

6. AUTHORS
Viktor A. Podolskiy, Anatoly V. Zayats

5d. PROJECT NUMBER

5e. TASK NUMBER

5f. WORK UNIT NUMBER

7. PERFORMING ORGANIZATION NAMES AND ADDRESSES
University of Massachusetts - Lowell
600 Suffolk Street, Suite 226

Lowell, MA 01854 -3643

8. PERFORMING ORGANIZATION REPORT NUMBER

9. SPONSORING/MONITORING AGENCY NAME(S) AND ADDRESS (ES)
U.S. Army Research Office
P.O. Box 12211
Research Triangle Park, NC 27709-2211

10. SPONSOR/MONITOR'S ACRONYM(S)
ARO

11. SPONSOR/MONITOR'S REPORT NUMBER(S)
61388-PH.20

12. DISTRIBUTION AVAILIBILITY STATEMENT
Approved for Public Release; Distribution Unlimited

13. SUPPLEMENTARY NOTES
The views, opinions and/or findings contained in this report are those of the author(s) and should not contrued as an official Department of the Army position, policy or decision, unless so designated by other documentation.

14. ABSTRACT
The three-year program was focused on analysis of light interaction with complex multiscale plasmonic structures, nanorod metamaterials that offer unique platform to realize low-loss hyperbolic media, uniaxial materials with components of permittivity tensor of different sign, enabling sub-diffraction light manipulation. Over first two years of the program we have shown that the optical properties of nanorod metamaterials are strongly affected by optical nonlocality caused by collective excitation of plasmonic modes supported by individual nanorods, developed analytical description of the underlying physics, and verified it in experiments. Over the third year of the

15. SUBJECT TERMS
metamaterials, light-matter interaction, spatial dispersion

16. SECURITY CLASSIFICATION OF:			17. LIMITATION OF ABSTRACT	15. NUMBER OF PAGES	19a. NAME OF RESPONSIBLE PERSON
a. REPORT	b. ABSTRACT	c. THIS PAGE			Viktor Podolskiy
UU	UU	UU	UU		19b. TELEPHONE NUMBER 978-934-3398

Standard Form 298 (Rev 8/98)
Prescribed by ANSI Std. Z39.18

Report Title

Final Report: Optical Physics and Imaging Science (12.5): Nonlocal Plasmonic Metamaterials for Ultrafast and Nonlinear Optics

ABSTRACT

The three-year program was focused on analysis of light interaction with complex multiscale plasmonic structures, nanorod metamaterials that offer unique platform to realize low-loss hyperbolic media, uniaxial materials with components of permittivity tensor of different sign, enabling sub-diffraction light manipulation. Over first two years of the program we have shown that the optical properties of nanorod metamaterials are strongly affected by optical nonlocality caused by collective excitation of plasmonic modes supported by individual nanorods, developed analytical description of the underlying physics, and verified it in experiments. Over the third year of the program the research was mostly focused on understanding emission in nonlocal nanorod arrays and on nonlinear response of these unique systems. Theoretically, the two groups have developed formalism to interaction of emitted light with complex plasmonic structures, and used the developed formalism to analyze emission inside bulk nanowire media as well as emission inside finite-sized nanorod composites. In terms of nonlinear response of metamaterials, we have numerically analyzed second- and third-order nonlinearities in plasmonic nanorod arrays. Experimentally, emission inside nanorod metamaterial was investigated. Nonlinear processes inside nanorod arrays were experimentally studied. The program resulted in 10 publications (with several more in preparation), one M.S. and one Ph.D. theses, and over 30 conference presentations, including over 20 invited talks.

Enter List of papers submitted or published that acknowledge ARO support from the start of the project to the date of this printing. List the papers, including journal references, in the following categories:

(a) Papers published in peer-reviewed journals (N/A for none)

Received		Paper
08/28/2013	2.00	Vladimir P. Drachev, Viktor A. Podolskiy, Alexander V. Kildishev. Hyperbolic metamaterials: new physics behind a classical problem, Optics Express, (06 2013): 0. doi: 10.1364/OE.21.015048
08/28/2013	3.00	S.M. Prokes, Orest J. Glembocki, J. E. Livenere, T. U. Tumkur, J. K. Kitur, G. Zhu, B. Wells, V. A. Podolskiy, M. A. Noginov. Hyperbolic and plasmonic properties of Silicon/Ag aligned nanowire arrays, Optics Express, (06 2013): 0. doi: 10.1364/OE.21.014962
08/29/2014	6.00	Brian M. Wells, Anatoly V. Zayats, Viktor A. Podolskiy. Nonlocal optics of plasmonic nanowire metamaterials, Physical Review B, (01 2014): 35111. doi: 10.1103/PhysRevB.89.035111
11/09/2015	12.00	Andres D. Neira, Nicolas Olivier, Mazhar E. Nasir, Wayne Dickson, Gregory A. Wurtz, Anatoly V. Zayats. Eliminating material constraints for nonlinearity with plasmonic metamaterials, Nature Communications, (07 2015): 0. doi: 10.1038/ncomms8757
11/09/2015	13.00	G. A. Wurtz, N. Vasilantonakis, V. A. Podolskiy, A. V. Zayats. Refractive index sensing with hyperbolic metamaterials: strategies for biosensing and nonlinearity enhancement, Optics Express, (05 2015): 0. doi: 10.1364/OE.23.014329
11/09/2015	15.00	Gregory A. Wurtz, Jen-You Chu, Tian-You Cheng, Huai-Hsien Wang, Kun-Tong Tsai, Alexey V. Krasavin, Jr-Hau He, Brian M. Wells, Viktor A. Podolskiy, Juen-Kai Wang, Yuh-Lin Wang, Anatoly V. Zayats. Looking into Meta-Atoms of Plasmonic Nanowire Metamaterial, Nano Letters, (09 2014): 0. doi: 10.1021/nl501283c
11/09/2015	14.00	Pavel Ginzburg, Brian Wells, Anatoly V. Zayats, Viktor A. Podolskiy. Light emission in nonlocal plasmonic metamaterials, Faraday Discuss., (01 2015): 0. doi: 10.1039/C4FD00186A
11/09/2015	16.00	Brian M. Wells, Christopher M. Roberts, Viktor A. Podolskiy. Metamaterials-based Salisbury screens with reduced angular sensitivity, Applied Physics Letters, (10 2014): 0. doi: 10.1063/1.4899131

TOTAL: **8**

Number of Papers published in peer-reviewed journals:

(b) Papers published in non-peer-reviewed journals (N/A for none)

Received	Paper

TOTAL:

Number of Papers published in non peer-reviewed journals:

(c) Presentations

1. (invited) OSA incubator on nonlinear metamaterials Towards engineering bulk nonlinear polarizability with nonlocal plasmonic metamaterials (Aug 2015)
2. (invited) SPIE optics and photonics Light emission in nonlocal plasmonic metamaterials (Aug 2015)
3. B. Wells, P. Ginzburg, A. Zayats, V.A. Podolskiy, Light emission in nonlocal plasmonic nanowire metamaterials, CLEO/QELS 2015 paper number FM2C.4
4. (invited) Tri-service review meeting Nonlocal homogenization of metamaterials and metasurfaces (Nov 2014)
5. Faraday Discussions on Plasmonics, Light emission in nonlocal plasmonic metamaterials (Feb 2015)
6. V. Podolskiy (invited) Tri-service review meeting Nonlocal homogenization of metamaterials and metasurfaces (Nov 2014)
7. B. Wells, A. Zayats, V.A. Podolskiy, Analytical approximation of dispersion of longitudinal waves in plasmonic nanowire metamaterials, MRS meeting (2014)
8. A. V. Zayats (invited) URSI General assembly, Beijing, China (Aug. 2014), Anisotropic plasmonic metamaterials for nanophotonic applications
9. A. V. Zayats (invited) 1st European Optical Society meeting on Optics at the nanoscale, Capri, Italy (Sept . 2013), Hyperbolic metamaterials as a platform for quantum and nonlinear plasmonics
10. A. V. Zayats (invited) Hyperbolic metamaterials: a new plasmonic platform, Molecular Materials meeting (Singapore, 2015)
11. A. D. Barbosa Neira1, G. Marini1, S. Peruh1, A. Krasavin1, N. Olivier1, M. Nasir, W. Dickson1, G. A. Wurtz1, A. V. Zayats1, (invited) Nonlinear processes in plasmonic metamaterials, Metamaterials conference (New York City, 2015)
12. M. Nasir, W. Dickson1, G. A. Wurtz1, A. V. Zayats1 (invited) Large area nanorod metamaterials for sensing and magneto-optical applications, Metamaterials conference (New York City, 2015)
13. A. Barbosa Neira, S. Peruh, G. Marini, M. Nasir, A. V. Krasavin, N. Olivier, W. Dickson, G. A. Wurtz, A. V. Zayats (invited), Nonlinearities in hyperbolic plasmonic metamaterials, SPIE Optics and Photonics Conference (San Diego, 2015)
14. A. V. Zayats (invited) Nonlinear optics of plasmonic metamaterials, ICMAT Singapore (2015)
15. W. Dickson, G. A. Wurtz, A. V. Zayats (invited) Hyperbolic plasmonic metamaterials: engineering nonlinearities and spontaneous emission. SPIE Optoelectronics (Prague, Chech republic, 2015)
16. W. Dickson, A. V. Krasavin, A. V. Zayats (invited), Hyberbolic plasmonic metamaterials for nanophotonic applications: active functionalitis, SPIE- Photonics West (San Francisco, CA, 2015)
17. A. V. Zayats (invited) Nonlinear plasmonic metamaterials, Australian Institute of Physics Congress (Canberra, 2014)
18. Wayne Dickson, Gregory A. Wurtz, P. Ginzburg, A. V. Krasavin, Anatoly V. Zayats (invited), Guiding, switching and sensing with nanorod metamaterials, SPIE Optics and Photonics (San Diego, CA, 2014)
19. V. Podolskiy, (invited) King's College London Subwavelength focusing and imaging with multiscale compostes (May 2014)
20. B. Wells, C. Roberts, V.A. Podolskiy, Angle-independent Salisbury screens based on nonlocal nanowire metamaterials, CLEO: QELS 2014 paper: FW1K.3
21. B. Wells, A. Zayats, V.A. Podolskiy, Nonlocal optics of plasmonic nanorod metamaterials, MRS fall meeting 2013, talk SS1.05
22. V. Podolskiy, (invited) University of Buffalo, Subwavelength focusing and imaging with multiscale composites (Nov. 2013)
23. V. Podolskiy, (invited) OSA Incubator Structured Light in Structured Media Optical Nonlocalities and Additional Waves in Uniaxial Metamaterials (Sep. 2013)
24. V. Podolskiy (invited) Correlation optics – 2013, Chernivtsy, Ukraine, Nonlocal optical metamaterials for sensing and nonlinear applications (Sep. 2013)
25. V. Podolskiy (invited) SPIE optics and Photonics, San Diego, CA, Analytical description of optical nonlocalities in nanowire metamaterials (Aug. 2013)
26. W. Dickson, G. A. Wurtz, A. V. Zayats, "Anisotropic plasmonic metamaterials," keynote talk at the 4th International Conference on Metamaterials and Plasmonics (META-13), Sharja (UAE), March 2013.
27. W. Dickson, G. A. Wurtz, A. V. Zayats, "Plasmonic nanorod arrays: 3D metamaterial with hyperbolic dispersion," invited talk at the SPIE Optics and Optoelectronics conference, Prague (Czech republic), April 2013.
28. W. Dickson, G. A. Wurtz, A. V. Zayats, "Plasmonic nanorod metamaterials," invited talk at the SPIE Microelectronics conference, Grenoble (France), April 2013.
29. B. Wells, A. V. Zayats, V. A. Podolskiy, "Nonlocal response of plasmonic metamaterials," talk at the American Physical Society Mach Meeting, Boston (MA, US), 2013.
30. A. V. Zayats, "Integrated nanophotonic devices based on plasmonics," invited talk at the SPIE Photonics West conference. San Francisco (CA, USA), 2012.
31. A. V. Zayats, "Plasmonic nanorod metamaterials for nanophotonics," invited talk at the IEEE Photonics Global conference (Singapore, December 2012)
32. B. M. Wells, A. V. Zayats, V. A. Podolskiy, "Nonlocal response of plasmonic nanowire metamaterials in the ENZ regime," talk at the Materials Research Society Fall Meeting, Boston (MA, US), 2012.
33. V.A. Podolskiy, B.M. Wells, V.A. Podolskiy "Analytical description of optical nonlocalities in nanowire metamaterials", invited talk at SPIE optics and Photonics 2013, San Diego, CA, US, 2013

Number of Presentations: 33.00

Non Peer-Reviewed Conference Proceeding publications (other than abstracts):

Received	Paper

TOTAL:

Number of Non Peer-Reviewed Conference Proceeding publications (other than abstracts):

Peer-Reviewed Conference Proceeding publications (other than abstracts):

Received		Paper
08/28/2013	5.00	Brian Wells, Anatoly Zayats, Viktor Podolskiy. Nonlocal Optics of Plasmonic Nanowire Metamaterials, CLEO/QELS 2013. 11-JUN-13, . : ,
08/29/2014	9.00	Brian Wells , Christopher Roberts, Viktror Podolskiy. Angle-independent Salisbury screens based on nonlocal nanowire metamaterials, CLEO/QELS 2014. 08-JUN-14, . : ,

TOTAL: **2**

Number of Peer-Reviewed Conference Proceeding publications (other than abstracts):

(d) Manuscripts

Received		Paper
08/28/2013	4.00	Brian Wells, Anatoly Zayats, Viktor Podolskiy. Nonlocal optics of plasmonic nanowire metamaterials, (submitted) (08 2013)
08/29/2014	7.00	Kun-Tong Tsai, Gregory A. Wurtz, Jen-You Chu, Tian-You Cheng, Huai-Hsien Wang, Alexey V. Krasavin, Jr-Hau He, Brian M. Wells, Viktor A. Podolskiy, Juen-Kai Wang, Yuh-Lin Wang, Anatoly V. Zayats. Looking into Meta-Atoms of Plasmonic Nanowire Metamaterial, Nano Letters (08 2014)
08/29/2014	10.00	Brian M. Wells, Christopher M. Roberts, Viktor A. Podolskiy. Metamaterials-based Salisbury Screens with Reduced Angular Sensitivity, Applied Physics Letters (under consideration) (08 2014)
11/09/2015	18.00	Giuseppe Marino, Paulina Segovia, Alexey V. Krasavin, Pavel Ginzburg, Nicolas Olivier, Gregory A. Wurtz, Anatoly V. Zayats. Second-harmonic generation from hyperbolic plasmonic nanorod metamaterial slab, arXiv:1508.07586 (08 2015)
11/09/2015	19.00	Alexey P. Slobozhanyuk, , Pavel Ginzburg, David A. Powell, Ivan Iorsh, Alexander S. Shalin, Paulina Segovia, Alexey V. Krasavin, Gregory A. Wurtz, Viktor A. Podolskiy, Pavel A. Belov, Anatoly V. Zayats. Purcell effect in hyperbolic metamaterial resonators, PHYSICAL REVIEW B (Submitted) (04 2015)

TOTAL: **5**

Number of Manuscripts:

Books

Received	Book

TOTAL:

Received Book Chapter

TOTAL:

Patents Submitted

Patents Awarded

Awards

1. V.A. Podolskiy elected to Fellow of The Optical Society of America, effective 2015
2. A.V. Zayats elected Fellow Royals Society of Chemistry (2014)
3. A.V. Zayats, The Royal Society Wolfson Research Merit Award (2014)

Graduate Students

NAME	PERCENT_SUPPORTED	Discipline
Brian Wells	0.94	
Bo Fal	0.14	
FTE Equivalent:	**1.08**	
Total Number:	**2**	

Names of Post Doctorates

NAME	PERCENT_SUPPORTED
Alexey Krasavin	0.33
FTE Equivalent:	**0.33**
Total Number:	**1**

Names of Faculty Supported

NAME	PERCENT_SUPPORTED	National Academy Member
Anatoly Zayats	0.08	
Viktor Podolskiy	0.10	
FTE Equivalent:	**0.18**	
Total Number:	**2**	

Names of Under Graduate students supported

NAME	PERCENT_SUPPORTED
FTE Equivalent:	
Total Number:	

Student Metrics

This section only applies to graduating undergraduates supported by this agreement in this reporting period

The number of undergraduates funded by this agreement who graduated during this period: 0.00

The number of undergraduates funded by this agreement who graduated during this period with a degree in science, mathematics, engineering, or technology fields:..... 0.00

The number of undergraduates funded by your agreement who graduated during this period and will continue to pursue a graduate or Ph.D. degree in science, mathematics, engineering, or technology fields:..... 0.00

Number of graduating undergraduates who achieved a 3.5 GPA to 4.0 (4.0 max scale):..... 0.00

Number of graduating undergraduates funded by a DoD funded Center of Excellence grant for Education, Research and Engineering:..... 0.00

The number of undergraduates funded by your agreement who graduated during this period and intend to work for the Department of Defense 0.00

The number of undergraduates funded by your agreement who graduated during this period and will receive scholarships or fellowships for further studies in science, mathematics, engineering or technology fields:..... 0.00

Names of Personnel receiving masters degrees

NAME
Total Number:

Names of personnel receiving PHDs

NAME	
Brian Wells	
Total Number:	**1**

Names of other research staff

NAME	PERCENT_SUPPORTED
FTE Equivalent:	
Total Number:	

Sub Contractors (DD882)

1 a. Kings College London

1 b. Strand

London WC2R 2LS

Sub Contractor Numbers (c):

Patent Clause Number (d-1):

Patent Date (d-2):

Work Description (e):

Sub Contract Award Date (f-1):

Sub Contract Est Completion Date(f-2):

Inventions (DD882)

Scientific Progress

see attachment

Technology Transfer

Nonlocal plasmonic metamaterials for ultrafastand nonlinear optics

V.A. Podolskiy and A.V. Zayats

Final report: Sep 15 2012 to Sep 14 2015

Scientific Progress and Accomplishments:

Overview of projects goals and objectives

The main motivation of this project is to understand the counterintuitive optical properties of a unique member of metamaterials family, plasmonic nanorod assemblies, that is being rapidly developed into a flexible and extendable platform for a variety of optical applications in imaging, sensing, and nonlinear optics [1-4]. Over the past decade, several important novel optical phenomena, including negative refraction, sensing, and ultrafast optical nonlinearities have been demonstrated in plasmonic nanorod systems [1,4]. Initial studies have shown that optical response of plasmonic nanorods resembles that of strongly anisotropic uniaxial material, a material with (diagonal) components of permittivity tensor having different signs [5]. The materials having such strong anisotropy are often called hyperbolic materials since the components of the wavevector of plane waves propagating in these systems lie on the surface of the hyperboloid (in contrast to the surface of ellipsoid often seen in conventional birefringent materials). The topological transition between (bounded) ellipsoid and (unbounded) hyperboloid virtually eliminates the diffraction limit, and introduces a number of peculiar optical phenomena that stem from dramatic reduction of the lifetime of quantum emitters positioned inside the hyperbolic system[2]. Our previous research [6] has demonstrated that the above topological transition that takes place at epsilon-near-zero (ENZ) frequency is accompanied by a fundamental change in optical response of nanorod composites, accompanied optical nonlocalities and excitation of additional waves. **The goal of this program is to develop an understanding of optics of nonlocal nanorod arrays.**

Nonlocality, also known as spatial dispersion, is a result of collective excitation of materials when electric field at one point in space excites polarization at another (distant) point. Since real and wavevector spaces are inter-related through Fourier transformation, the nonlocal polarization formally yields wavevector-dependent permittivity. In the limit of weak nonlocality, permittivity of the composite can ϵ^{nl} be written as

$$\epsilon_{xx}^{nl} \simeq \epsilon_{xx}(\omega) + \delta_{xx}\frac{k_x^2 c^2}{\omega^2} \quad \text{.....} \quad (1)$$

with $\epsilon_{xx}(\omega)$ being "conventional" (local) permittivity, given by

$$\epsilon_{xx} = p\,\epsilon_m + (1-p)\epsilon_d \quad \text{.....} \quad (2)$$

$$\epsilon_{yz} = \frac{p\,\epsilon_m\,E_m + (1-p)\epsilon_d E_d}{p\,E_m + (1-p)E_d} \quad \text{.....} \quad (3)$$

with $E_m = 2E_d\epsilon_d/(\epsilon_m + \epsilon_d)$, and parameters p, ϵ_m, and ϵ_d corresponding to the (surface) concentration of the metallic nanorods in the dielectric matrix (filling fraction), and the permittivities of metallic nanorods, and of the dielectric matrix, respectively. The remaining parameter $|\delta_{xx}| \ll 1$ describes the nonlocal correction. In such model, dispersion of the plane TM-polarized waves is given by [6,7]

$$2\,\delta_{xx}k_x^2 = \frac{\omega^2}{c^2}\left[\epsilon_{xx} + \delta_{xx}\epsilon_{yz} \pm \sqrt{\left(\epsilon_{xx} - \delta_{xx}\epsilon_{yz}\right)^2 + 4\epsilon_{yz}\delta_{xx}\frac{k_z^2c^2}{\omega^2}}\right] \quad \text{..... (4)}$$

Note that in contrast to local materials that support two modes that differ by their polarization, nonlocal media support propagation of at least three plane waves, at least two of which have identical (TM) polarization. In the limit $\delta_{xx} \to 0$, one of the roots of Eq.(4) converges to the prediction of local effective medium theory,

$$\frac{k_x^2}{\epsilon_{yz}} + \frac{k_y^2+k_z^2}{\epsilon_{xx}} = \frac{\omega^2}{c^2} \quad \text{..... (5)}$$

describing the propagation of what is known as main wave, while another root yields $k_x \to \infty$ [additional wave]. Thus, additional wave is always present in nonlocal metamaterial, but huge index/impedance mismatch may prevent its coupling with free-space plane waves.

Although the general formalism, presented above, has been proven successful in describing transmission and reflection in real nanorod arrays, dependence of nonlocality parameter δ_{xx} on parameters of the system (loss, geometry, wavelength, etc) was not understood. Understanding the behavior of nonlocality parameter is the first goal of this program. The remaining goals of this program aim at understanding of implications of optical nonlocality on active and nonlinear behavior of nanorod composites. Table 1 summarizes the goals and initial projected timeline of the project.

Goal	Yr1	Yr2	Yr3
Goal 1 (linear nonlocal response)	(A) Additional boundary conditions (N) Behavior of parameter δ_{xx} (E) Dispersion of high-index modes	(A) Properties of δ_{xx} (N) Nonlocal mode matching code (E) Applications of nonlocal nanorod arrays (sensing with high-index modes)	(E) Applications of nonlocal nanorod arrays (ENZ systems)
Goal 2 Emission, and ultrafast optics in nonlocal systems	(N) Density of optical states in nonlocal systems (E)Light emission in nonlocal systems	(N) Incorporation of gain and light emission in numerical codes (E) Optical gain	(A) Density of states calculations (N) Nonlinear optics codes (E) nonlinear optics and optical communications
Key:	Completed	In progress	Not Started

Table 1. Projected timeline of the project; (A), (N), and (E) correspond to analytical, numerical, and experimental sub-tasks respectively.

As of now, analytically and numerically, we have been successful in developing analytical properties of passive nonlocal systems, developed transfer matrix codes, and expanded and optimized these codes to incorporate light emission and density of states calculations in nonlocal structures [8,9]. We have analyzed density of states in several practical nanorod structures and compared our theoretical predictions to experimental results[10]. In a separate project, we have experimentally analyzed field

distribution across the unit cell of the system. [11]. We have also explored the applications of nonlocal nanowire arrays in sensing, selective absorption, and spectrum manipulations [12].

In a separate project we have developed numerical codes for analysis of nonlinear optics in nanowire arrays. In this regard, we have analyzed pump-probe spectrum manipulation and second harmonic generation in nanowire media. [13,14] The sample for analysis of second harmonic generation in nanorod arrays, based on the results of our numerical modelling has been fabricated and is being currently analyzed.

We therefore successfully completed the program.

Research progress over the period

Completed research:

1. Analytical description of optical nonlocalities in wire media

As described in our previous report, we have completed the development of analytical description of optics of passive nonlocal nanowire systems. We have finalized the manuscript detailing these findings, which was published in Phys.Rev.B in 2014 [8]. The numerial techniques have been validated to adequately predict the optical response of a layer of nanowire metamaterial sandwiched between local homogeneous dielectrics. (Fig.1)

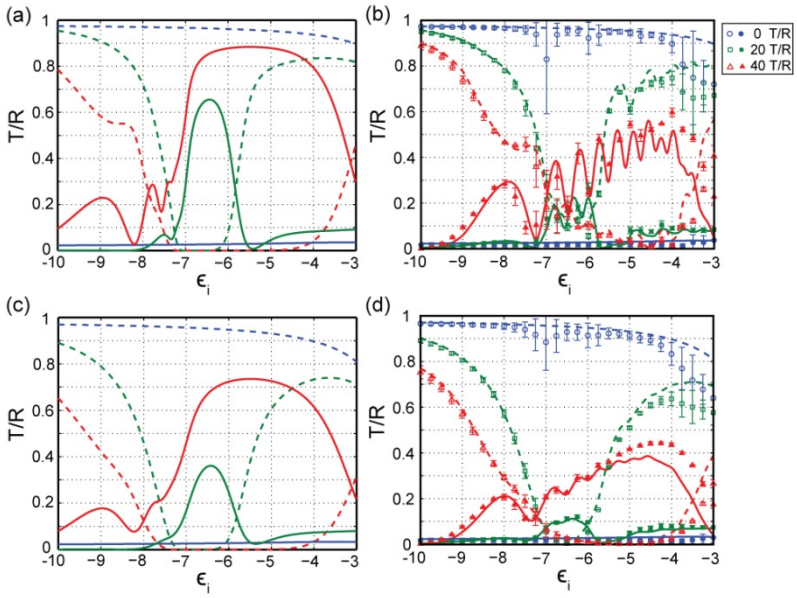

Fig.1 Transmission and reflection of light through a parallel slab of nanowire media, suspended in air with imaginary part of nanowire permittivity $Im\ \epsilon_i = 0.1$ (a,b) and $Im\ \epsilon_i = 0.25$ (c,d). (a,c): local TMM calculations, (b,d): nonlocal EMT developed here (lines) and numerical solutions of Maxwell equations (symbols); Solid lines and filled symbols represent reflection, dashed lines and empty symbols - transmission

We have demonstrated, that in contrast to conventional belief, nonlocality affects optical properties of nanowires across the majority of optical spectrum, not just in vicinity to ENZ frequency. The strongest effect of nonlocality can be seen above the ENZ frequency, where optical response of the composite is affected by the existence of *propagating* additional electromagnetic wave with hyperbolic-like dispersion. Our ongoing research shows that this wave dramatically affects density of optical states in the system.

2. Applications of nanowire composites for reducing sensitivity of Salisbury screens

Salisbury screen is one of the basic designs of perfect absorber structures. Due to their simplicity and versatility, Salisbury screens, and other absorber designs that stem from Salisbury screens are widely used in microwave and THz communities. Unfortunately, the absorption of Salisbury screens strongly depends on incident angle of incoming radiation. We have shown that nanowire metamaterials offer a solution to this problem.

Salisbury screen is essentially a three-layer structure, consisting of perfect electric conductor reflector, covered by a dielectric quarter-wavelength-plate, which in turn covered by a thin impedance matching layer (Fig.2). Perfect absorption results from destructive interference of two beams, the one reflected by the impedance layer, and the one reflected by the PEC ground plane. The angular dependence results from the dependence of optical path of light propagating inside the quarter-wavelength-plate.

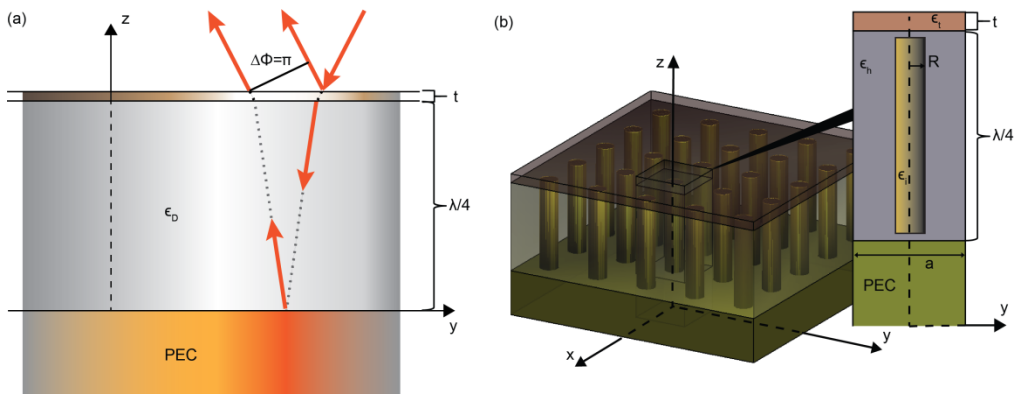

FIG. 2. (a) Schematic of a basic three layered Salisbury screen absorber which consists of a bottom perfectly conducting substrate, a middle quarter-wavelength-thick layer of dielectric and thin impedance-matching coupling top layer. (b) Schematic geometry of Salisbury screen with wire metamaterial replacing the quarter-wavelength-thick layer of dielectric that is found in traditional Salisbury screens

We have demonstrated that introduction of nanowire metamaterials into the dielectric quarter wavelength plate dramatically reduces angular dependence of Salisbury screens on angle of incidence for TM-polarized light. The nonlocal effective medium theory, developed in this project, has been demonstrated to adequately describe the observed behavior (see Fig.3). Our results are summarized in a manuscript that is published in Appl.Phys.Lett[12].

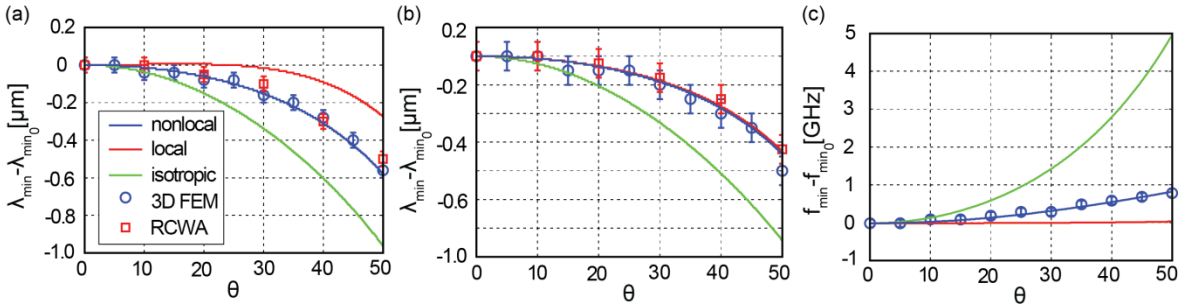

FIG. 3. Reflection minimum shift of Salisbury screens at three different frequency ranges, near-IR [operating wavelength $\lambda_{min_0} = 1\mu m$] (a), mid-IR $\lambda_{min_0} = 10\mu m$ (b) and GHz $f_{min_0} = 10\,GHz$ (c) frequencies. The blue and red solid lines represent the nonlocal and local EMT that takes into account material dispersion of noble-metal wires while the green represents the shift seen for the isotropic dielectric layer. The circle and square symbols represent 3D- FEM and RCWA -based solutions respectively[12].

3. Understanding of light distribution across the "meta-atom" in metamaterial

Light interaction with metamaterials is often explained in terms of effective medium theories where the collective optical response of the composite structure is related to the averaged response of an isolated inclusion in metamaterial, meta-atom. The effective medium theory developed as part of this work is one such approach. However, the validity of effective medium theories is often assessed through comparing their predictions to far-field, whole-metamaterial optical response.

In contrast to the majority of previous studies, we have aimed to analyze the optical properties of metamaterial *at the meta-atom scale*. With this goal in mind, we have fabricated nanowire metamaterial structure and analyzed the field distribution above such structure with phase- and amplitude-resolved near field microscopy. Our results, shown in Fig.4 clearly demonstrate that the component of electric field aligned with nanowire is mainly concentrated in the vicinity of wire-matrix border, forming characteristic crescent-like shapes. Similar field distribution is reproduced in full-wave numerical solutions of Maxwell equations. Finally, the nonlocal effective medium theory, developed in Ref.[8] can be used to relate these field distributions to the interplay between the two TM-polarized waves propagating inside the nanowire system. We therefore, for the first time, demonstrated the validity of effective medium theory at the level of single meta-atom response. Results of this study are detailed in publication in NanoLett [11].

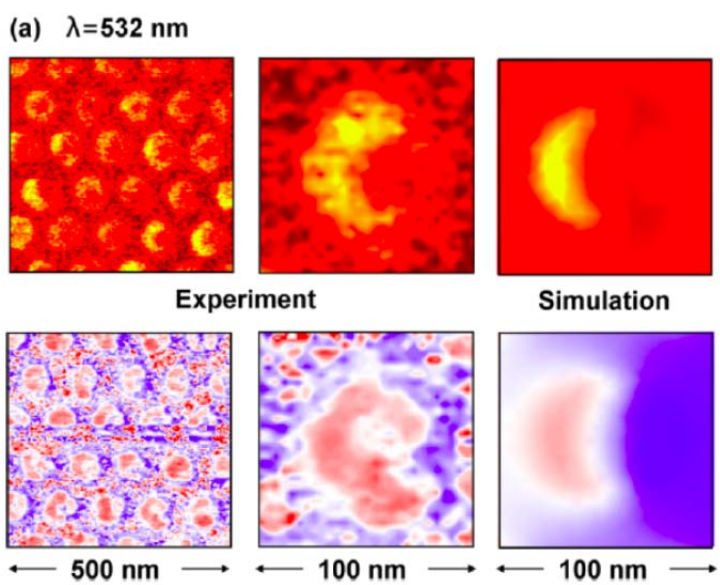

Fig.4. Measured (left an center) and simulated (right) distribution of amplitude (top) and phase (bottom) electric field across the nanowire metamaterial. Crescent-shape field distribution reflects the superposition of longitudinal and transverse waves. The former has circular profile of electric field, maximized around nanowire edge; while the latter has constant amplitude and linearly changing phase across the unit cell [11]

4. Understanding light emission in metamaterials

We have shown, theoretically, that the presence of additional electromagnetic wave, caused by optical nonlocality, dramatically affects lifetime modulation in nanorod arrays. In particular, it has previously suggested that nanorod arrays operating in elliptic regime, would have reasonably small deray rate enhancement; substantial enhancement, limited mostly by composite nature of metamaterial was expected in ENZ and in hyperbolic regimes. In contrast to this behavior, our theoretical calculations suggest that maximal decay rate enhancement in nonlocal nanorod arrays is maximized when metamaterial operates in elliptic regime; (see Fig.5). The manuscript detailing this study is published in Faraday discussions [9].

In a separate study, emission of point dipoles in finite nanorod arrays was analyzed numerically. We have shown that size (thickness) of nanorod arrays plays crucial role in modulation of decay rate. In particular, we have shown that in finite-size arrays emission can be dominated by well-defined Fabri-Perot type resonances. The manuscript detailing this study is accepted to Phys.Rev.B.[9]

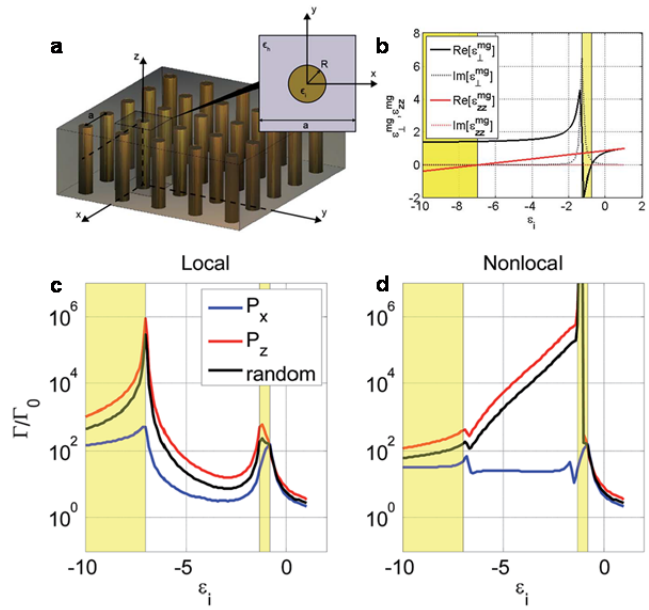

Fig.5 Emission in nonlocal nanowire metamaterials (a) that behave as uniaxial dielectrics with optical axis parallel along z axis; $a = \lambda_0/15$; (b) components of permittivity tensor as a function of permittivity of wire ϵ_i, calculated with local effective medium theory; (c,d) predictions of lifetime decay rate enhancement according to local (c) and nonlocal (d) effective medium theory; the latter takes into account existence of additional electromagnetic mode related to collective excitation of SPPs along nanowires [9]

To test our theoretical predictions, we have prepared nanorod array where the matrix between nanorods was removed. While general fabrication procedures for plasmonic nanorod metamaterials were in place before this project, the requirements of the project on the studies of active emitters incorporated in metamaterials required to design suitable nanostructures in order to prevent molecules to stick to the nanorod surface and thus experience strong nonradiative quenching. In order to achieve this, the following procedure has been developed.

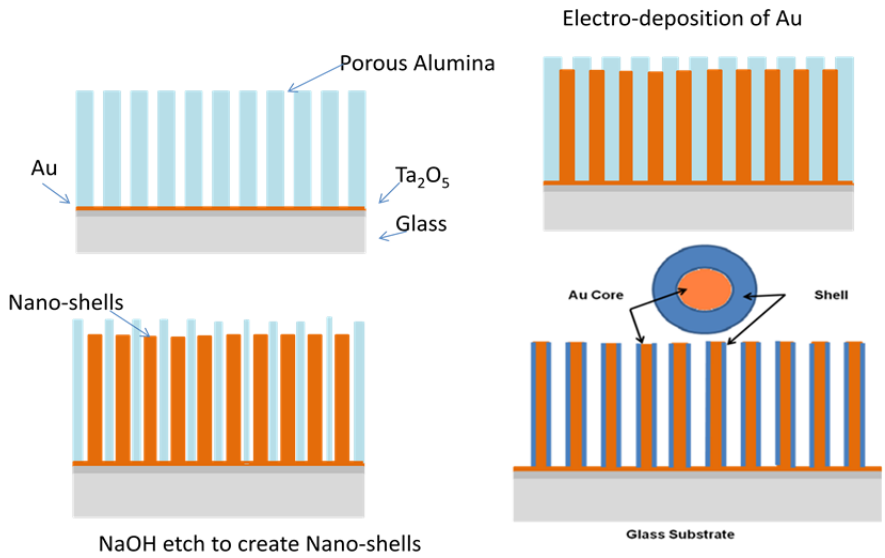

Fig. 6. Fabrication procedure for the metamaterial consisting of Au nanorod covered with dielectric shell to prevent photoluminescence quenching by avoiding direct contact of molecules and Au rods.

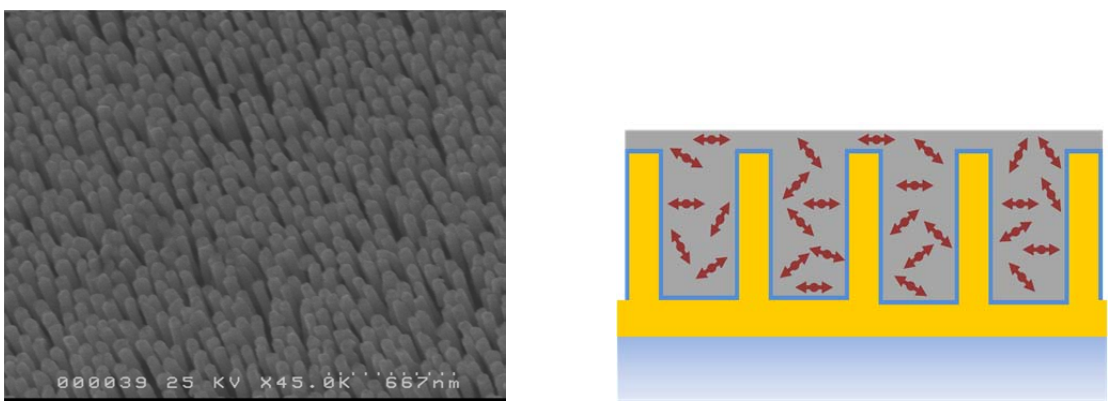

Fig.7. SEM image of the representative metamaterial and schematics of the sample for PL measurements (dye in polymer deposited between the core-shell nanorods).

This study allows us to test modulation of decay rate in the same metamaterial as a function of emission wavelength. In our experimental study we do not see substantial variation of decay rate enhancement when metamaterial transitions from elliptical to ENZ to hyperbolic regime; the behavior which is consistent with our nonlocal effective medium theory, and that fully agrees with results of our 3D numerical solutions of Maxwell equations.

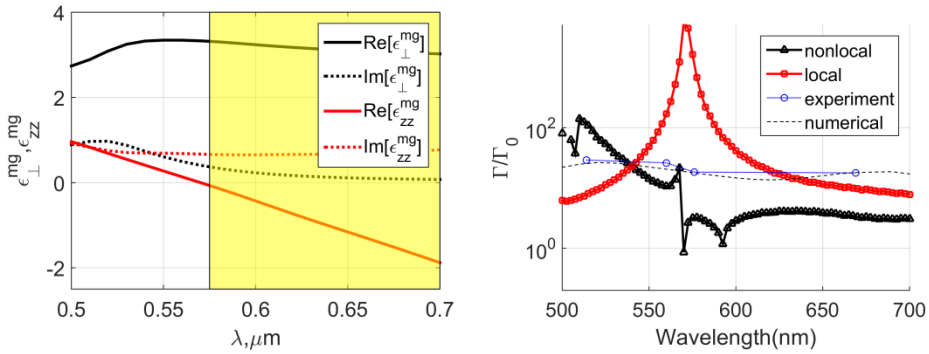

Fig.8 Enhancement of emission decay rate in nonlocal nanorod metamaterials; (left) local effective medium parameters of the composite; (right) enhancement of emission decay rate obtained in experiments (blue circles), calculated using local (red squares) and nonlocal (black triangles) EMTs, and calculated with full 3D numerical solutions of Maxwell equations (dashed black line) [10]

5. Nonlocal guided modes and cubic nonlinearities in nanorod composites

A planar slab of high-index dielectric may support a set of guided modes that can be used for photonics circuitry or as a basis for sensing and nonlinear optics applications where variation in material parameters (due to additives or nonlinear processes) result in variation in dispersion of the modes, that is detected by the optical means. Often, optical sensing and nonlinearities are analyzed by coupling light into guided modes through a high-index prism in attenuated total internal reflection geometry (also commonly known as Kretchman geometry)[15], where a minimum of reflectivity can be related to the excitation of the mode. Spectral dependence of this minimum is primarily governed by the dispersion of the underlying guided waves.

Here, we studied the modes supported by the waveguide formed by gold nanorod arrays. Modes of planar waveguides with uniaxial cores with optical axis perpendicular to the waveguide walls can be characterized by their polarization, TE or TM. When the waveguide core operates in hyperbolic regime, local effective medium theory suggest excitation of negative –index TM polarized modes[1]. Three-dimensional solutions of Maxwell equations confirm these predictions. However, detailed analysis of the modes supported by a planar nanorod layer revealed that negative-refraction modes are also supported when the waveguide operates in elliptic regime. These modes appear to originate from coupling of light to additional electromagnetic wave. Nonlocal effective medium theory, developed in this project, perfectly describes such coupling (Figs.8,9).

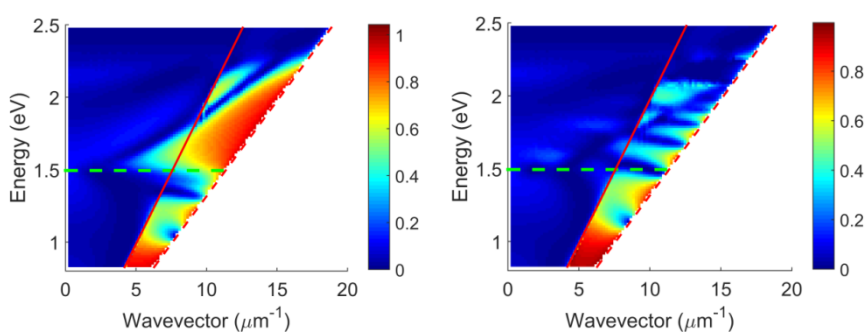

Fig.8 Reflection spectrum of a finite-thickness nanorod array, calculated with local (left) and nonlocal (right) effective medium theories; solid red line represents light line; dashed green line represents ENZ frequency; reflectivity minima to the right of the light line correspond to guided modes; results of full-wave 3D numerical solutions of Maxwell equations are shown in Fig.9

Ultrafast excitations of nanorod materials primarily deposit energy into electronic subsystem of gold nanorods. As result of excitation, permittivity of gold nanorods changes, in turn changing reflectivity profile of the nanorod composite. Mathematically, such modulation of optical properties at the probe frequency ω as result optical excitation at pump frequency Ω is described by cubic nonlinearity of permittivity with energy conservation give by $\omega + \Omega - \Omega \rightarrow \omega$. The predicted nonlocality-enhanced modulation of optical response of the planar nanorod composite is shown in Fig.9. The manuscript detailing this study is currently prepared for submission.

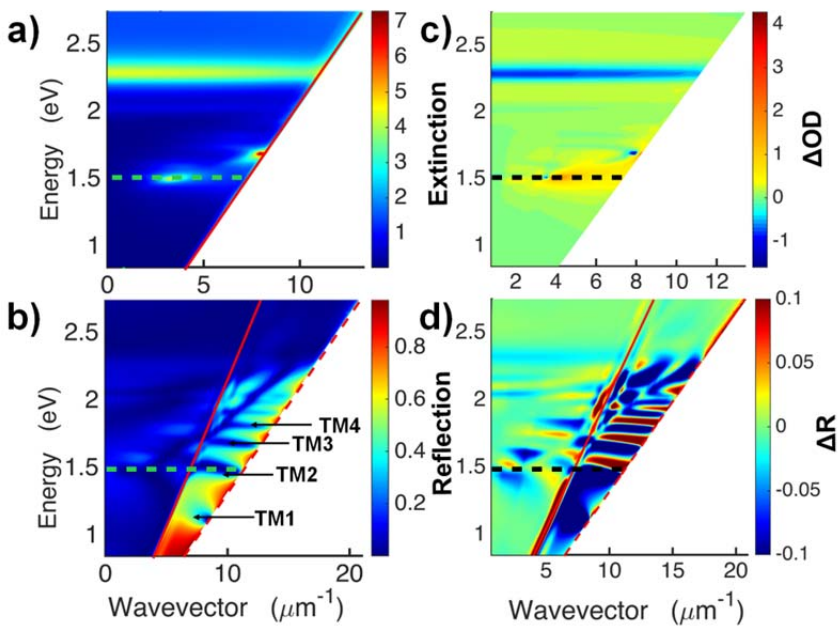

Fig.9 Dispersions of the linear (a) extinction and (b) reflection of the metamaterial slab and the dispersions of the differential (c) extinction and (d) reflection calculated at 200 fs after the excitation with 50 fs pulse centered at a wavelength of 820 nm at the angle of incidence of 20° in a substrate. Control and signal light are p-polarised. The light line in air and the substrate are indicated. The effective plasma frequency is shown with a horizontal solid line. The waveguided modes are identified

6. Second harmonic generation in nonlocal nanorod composites

In a separate study, we analyzed second harmonic generation (SHG) by nanowire metamaterials. Although gold and other nobel metals, due to their cubic symmetry, do not generate SHG signal in dipolar approximation, gold films are known to produce second harmonic light [16]. The origin of this generation is two-fold. First, inhomogeneity of electromagnetic field (and electron distribution) in the bulk of metal produces SHG signal due to quandrupolar term. Second, the surface of finite metal structure breaks the symmetry of the underlying material, producing SGH light. Within hydrodynamic model in non-depleted pump approximation, both processes can be treated within the same three-stage process. First, the field distribution across the system at the pump frequency is calculated. Second, nonlinear polarization is calculated across the system, according to

$$\boldsymbol{P}^{(2\omega)} = -\omega^2 \sum_k \frac{\partial}{\partial r_k}\left(\frac{\boldsymbol{j}^{(1\omega)} j_k^{(1\omega)}}{eN}\right) + \frac{e\omega^2}{m_e}\left[\epsilon_0\left(\boldsymbol{\nabla}\cdot\boldsymbol{E}^{(1\omega)}\right)\boldsymbol{E}^{(1\omega)} + \boldsymbol{j}^{(1\omega)} \times \boldsymbol{B}^{(1\omega)}\right]$$

Finally, nonlinear polarization is used as a source of second harmonic light, resulting in the out-coupled SHG signal.

During the third year of the program, we have implemented the above formalism into commercial finite-element solver, COMOSL Multiphysics, and used the resulting framework to understand the generation of SHG light by nanowire composites and compare SHG light in nanorod metamaterials to SHG from smooth and patterned metal films. The results of these calculations are summarized in Fig.10. It is seen that the SHG in nanowire composites is dramatically enhanced as compared to SHG in the comparable nanolayer structures. More importantly, analysis of the dependence of SHG on wire length suggests that nanowire metamaterial exhibits *bulk* nonlinear susceptibility. We are currently working on development of analytical description of this phenomenon, and are planning to submit the summary of our analysis to peer-review journal in the nearest future[14].

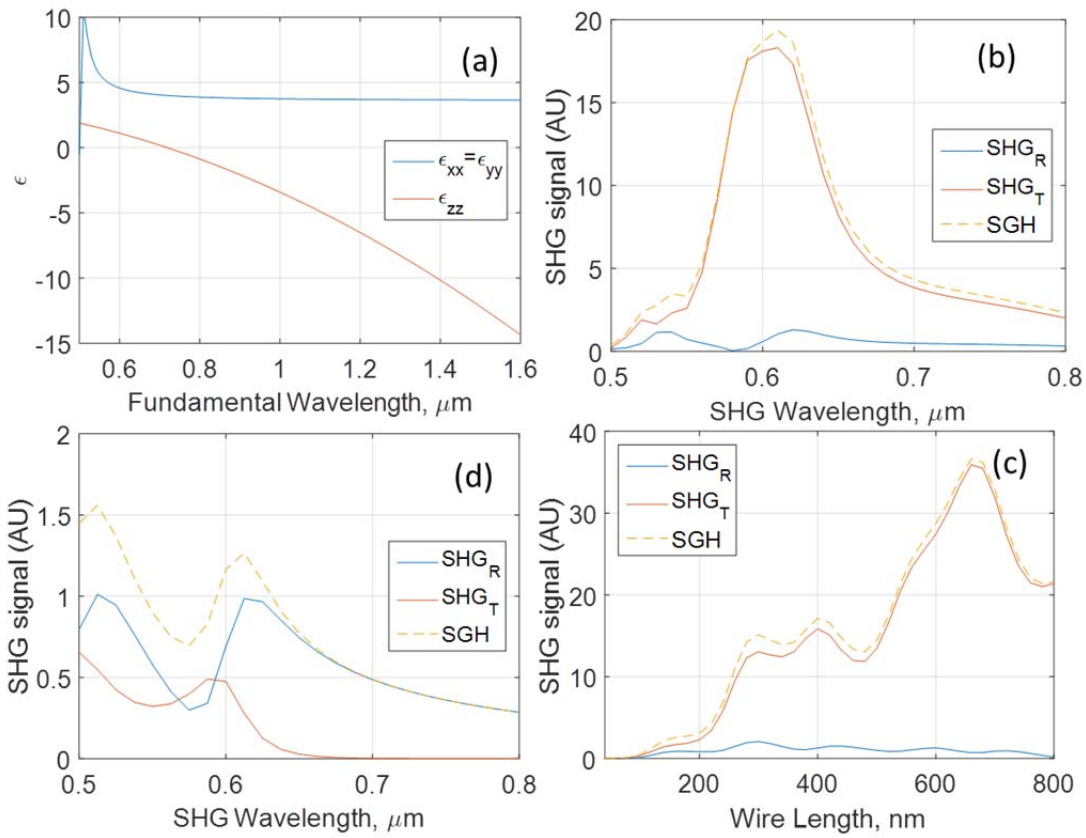

Fig.10 SHG in gold nanorod structures; (a) effective medium response of gold nanorods used in the analysis; (b) SHG from 300-nm-thick gold nanorod metamaterial excited at oblique incidence (20°); note that the spectral range of maximum SHG signal coincides with spectral range when metamaterial operates in nonlocal elliptical regime; (c) dependence of SHG signal (calculated at pump wavelength of 1230 nm) on the wire length; note that oscillation in SHG response, indicating presence of bulk $\chi^{(2)}$ response; (d) SHG signal from multilayer gold-dielectric metamaterial with ENZ frequency of $0.7\mu m$; note that nonlocal nanowire structure provides orders-of magnitude stronger response than its nanolayer counterpart

7. Related research activities

Field enhancement in nonlocal nanowire composites

[collaboration with group of N.Litchinitser, U.Buffalo]

Materials with gradually changing refractive index (also known as transition materials) have been suggested to have applications in sensing and nonlinear optics [17]. One of the most exciting transition

material designs calls for gradual change of permittivity from positive to negative values. Nanowire structures with spatially dependent wire radius offer a realization of such structures. Local effective medium predicts strong, order of magnitude, enhancement of local electric field. We have demonstrated that nonlocal effective medium theory accurately predicts field enhancement in conical arrays of conical wires (Fig.11). We are finalizing manuscript that summarizes these results.

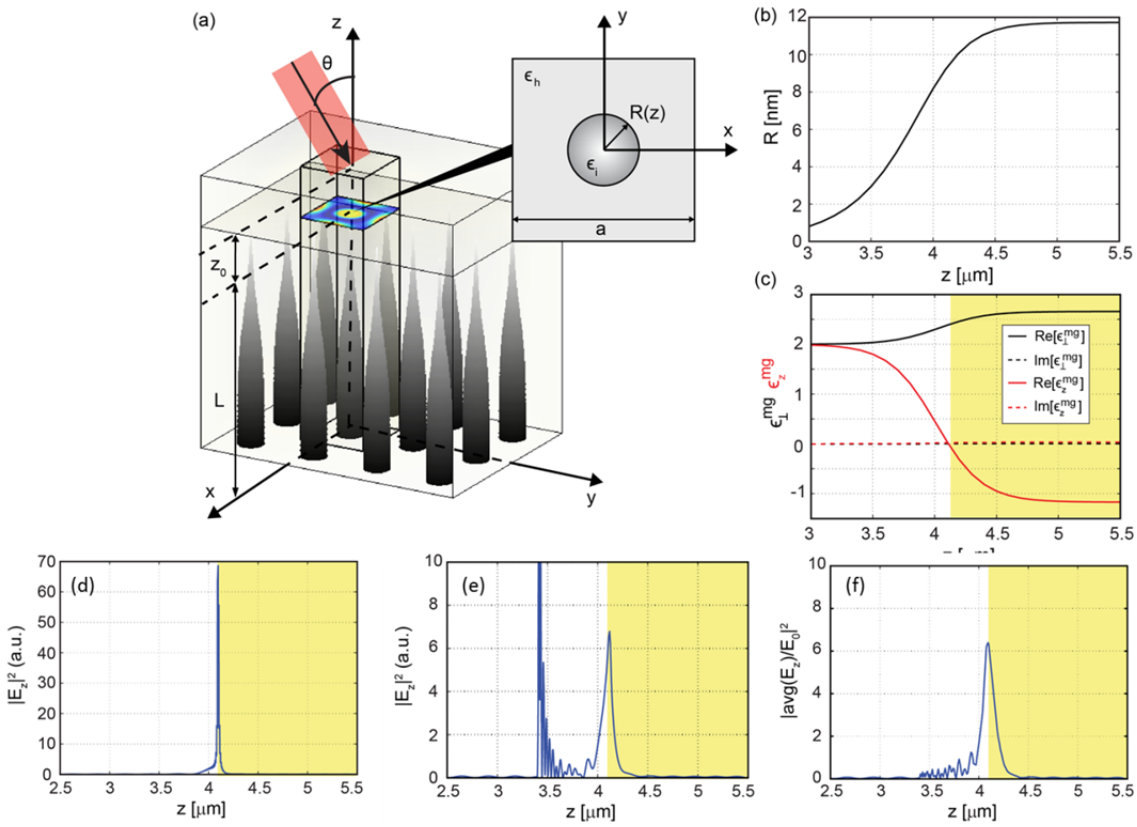

Fig.11 Field enhancement in transitional metamaterials; (a…c) schematic geometry of the composite, and profile of radius and local effective medium parameters along z coordinate; (d…f) field enhancement in metamaterial as predicted by (d) local EMT, (e) nonlocal EMT and (f) full-wave numerical solutions of Maxwell equations; field oscillations predicted by nonlocal EMT at $z \simeq 3.25\ \mu m$ are related to numerical artifacts stemming from discretization of smooth conical wires into array of thin cylindrical segments with sharp conners

Inter-group communication

No productive research is possible without efficient communication. Over the course of the program, the team members have extensively collaborated with each other; the following list summarizes some of these activities

- We regularly communicated via e-mail, and exchanged data via dropbox and OneDrive services
- We held regular (approximately weekly) telecom conferences via Skype and/or phone
- Dr. P. Ginzburg, member of A. Zayats' team visited U Mass Lowell in Sep. 2013
- V. Podolskiy's team visited UK in May 2014 and in Feb 2015
- Prof. A. Zayats will visit UML in December 2015

Student training and education

The presented computational and analytical research forms the basis for M.S.&Ph.D thesis of Brian Wells, a graduate student in V. Podolskiy's group. Brian Wells has defended his M.S. thesis on Dec.12 2013 and defended his Ph.D in summer of 2015. He is currently an Assistant Professor at U Hartford.

References

1. C.Simovski, et.al. Adv.Mat **24** 4229 (2012); J. Yao et al., Science **321**, 930 (2008); P.A. Belov et.al. Phys. Rev. B **77**, 193108 (2008) S. Thongrattanasiri and V.A. Podolskiy, Opt. Lett. **34**, 890 (2009); J. Elser, R. Wangberg, V.A. Podolskiy, E.E. Narimanov Appl.Phys.Lett. **89**, 261102 (2006)
2. Z. Jacob, I.I. Smolyaninov, E.E. Narimanov, Appl.Phys.Lett. **100**, 161103 (2012); A.N. Poddubny, P.A. Belov, and Y.S. Kivshar, Phys. Rev. A **84**, 023807 (2011); O. Kidwai, S.V. Zhukovsky, and J E. Sipe, Opt. Lett. **36**, 2530 (2011); W.Yan, M.Wubs, N.A.Mortensen, Phys.Rev.B, **86,** 205429 (2012)
3. Z. Jacob, L.V. Alekseyev, and E. Narimanov, Opt. Exp, **14**, 8247 (2006); A. Salandrino and N. Engheta, Phys. Rev. B **74**, 075103 (2006); Z. Liu et al., Science, **315**, 1686 (2007).
4. A. Kabashin, et.al., Nat.Mat., **8**, 867 (2009); G. A. Wurtz, et.al. Nat. Nanotech. **6**, 107 (2011)
5. J.C.M. Garnett, Philos. Trans. R. Soc. London, Ser. B **203**, 385 (1904); A.K. Sarychev, R.C. McPhedran, V.M. Shalaev, Phys.Rev.B **62**, 8531 (2000); R. Atkinson et al., Phys. Rev. B **73**, 235402 (2006); J. Elser et al., Appl. Phys. Lett. **89**, 261102 (2006); G.A. Wurtz et.al. Opt.Exp. **16**, 7460 (2008)
6. R.J. Pollard, A. Murphy, W.R. Hendren, P.R. Evans, R. Atkinson, G.A. Wurtz, A.V. Zayats, V.A. Podolskiy Phys.Rev.Lett. **102**, 127405 (2009)
7. S.I. Pekar, Sov.Phys.JETP **6**, 785 (1958)
8. B. Wells, A.V. Zayats, V.A. Podolskiy, *Nonlocal optics of plasmonic nanowire metamaterials*, Phys Rev B **89**, 035111 (2014)
9. V.A. Podolskiy, P. Ginzburg, B. Wells, A.V. Zayats, *Light emission in nonlocal plasmonic metamaterials*, Faraday Discussions **178**, 61 (2015); A.P. Slobozhanyuk, P. Ginzburg, D.A. Powell, I. Iorsh, A.S. Shalin, P. Segovia, A.V. Krasavin, G.A. Wurtz, V. A. Podolskiy, P.A. Belov, A.V. Zayats, *Purcell effect in Hyperbolic Metamaterial Resonators,* accepted; Phys. Rev. B
10. P. Ginzburg, D. Roth, M. Nair, P. Segovia Olvera, A.V. Krasavin, J. Levitt, L. Hiirvonen, B. Wells, K. Huhling, D.R. Richards, V.A. Podolskiy, A.V. Zayats *Spontaneous emission in nonlocal materials*, in preparation
11. K-T. Tsai, G. Wurtz, J-Y. Chu, T-Y. Cheng, H-H. Wang, A. Krasavin, J-H. He, B. Wells, V.A. Podolskiy, J-K. Wang, Y-L. Wang, A. Zayats, *Looking into "meta-atoms" of plasmonic nanowire metamaterial*, Nano Lett. **14** 4971 (2014)
12. B. Wells, C. Roberts, V.A. Podolskiy *Metamaterials-based Salisbury Screens with Reduced Angular Sensitivity*, Appl.Phys.Lett. **105**, 161105 (2014); N. Vasilantonakis, G.A. Wurtz, V.A. Podolskiy, A.V. Zayats, *Refractive index sensing with hyperbolic metamaterials: strategies for biosensing and nonlinearity enhancement*, Opt.Exp. **23**, 14329 (2015)
13. S. Peruch, A. Neira, G.A. Wurtz, B. Wells, V.A. Podolskiy A.V. Zayats, *Ultrafast Kerr nonlinearity in plasmonic metamaterial waveguides: comparative studies of elliptic and hyperbolic dispersion regimes*, in preparation
14. G. Marino, P. Segovia, A.V. Krasavin, P. Ginzburg, N. Olivier, G.A. Wurtz, A.V. Zayats, *Second-harmonic generation from hyperbolic plasmonic nanorod metamaterial slab*, arXiv:1508.07586 (2015); B. Wells, A.V. Zayats, V.A. Podolskiy, *Second harmonic generation in metamaterials: towards engineering bulk nonlinearity in plasmonic composites*, in preparation
15. H.Raethner, *Surface plasmons on smooth and rough surfaces* (Springer, Berlin 1988); L. Novotny and B. Hecht, *Principles of Nano-Optics*, Cambridge U Press (Cambridge, UK 2006)
16. N. Bloembergen, R.K. Chang, S.S. Jha, C.H Lee, *Optical second harmonic generation in reflection from media with inversion symmetry* Phys. Rev **174** 813 (1968); *Y*. Zeng, W. Hoyer, J. Liu, S.W. Koch, J.V. Moloney *Classical theory for second harmonic generation from metallic nanoparticles*, Phys.Rev.B. **79** 235109 (2009)
17. N. Litchinitser, A. Maimistov, I. Gabitov, R. Sagdeev, V.Shalaev, *Metamaterials: electromagnetic enhancement at zero-index transition*, Opt. Lett. **33**, 2350 (2008)

Appendices:

Manuscripts published

1. N. Vasilantonakis, G.A. Wurtz, V.A. Podolskiy, A.V. Zayats, *Refractive index sensing with hyperbolic metamaterials: strategies for biosensing and nonlinearity enhancement*, Opt.Exp. **23**, 14329 (2015) **[selected for Virt.J. for Biomed. Opt v.10(6) 2015]**
2. A.D. Neira, N. Olivier, M. E. Nasir, W. Dickson, G. A. Wurtz, A.V. Zayats, *Eliminating material constraints for nonlinearity with plasmonic metamaterials*, Nat. Comm. **6**, 7757 (2015)
3. V.A. Podolskiy, P. Ginzburg, B. Wells, A.V. Zayats, *Light emission in nonlocal plasmonic metamaterials*, Faraday Discussions **178**, 61 (2015); see also Faraday Discussions **178,** 123 (2015)
4. B. Wells, C. Roberts, V.A. Podolskiy *Metamaterials-based Salisbury Screens with Reduced Angular Sensitivity*, Appl.Phys.Lett. **105**, 161105 (2014)
5. K-T. Tsai, G. Wurtz, J-Y. Chu, T-Y. Cheng, H-H. Wang, A. Krasavin, J-H. He, B. Wells, V.A. Podolskiy, J-K. Wang, Y-L. Wang, A. Zayats, *Looking into "meta-atoms" of plasmonic nanowire metamaterial*, Nano Lett. **14** 4971 (2014)
6. B. Wells, A.V. Zayats, V.A. Podolskiy, *Nonlocal optics of plasmonic nanowire metamaterials*, Phys.Rev.B **89**, 035111 (2014)
7. S.M. Prokes, O. J. Glembocki, J. E. Livenere, T. U.Tumkur, J. K. Kitur, G. Zhu, B. Wells, V. A. Podolskiy, M. A. Noginov, *Hyperbolic and Plasmonic Properties of Silicon/Ag aligned nanowire arrays*, Optics Express, **21**, 14962 (2013)
8. V. Drachev, V.A. Podolskiy, A. Kildishev, *Hyperbolic metamaterials: new physics behind a classical problem*, Optics Express, **21**, 15048 (2013)
   [#10 most downloaded manuscript in Optics Express, Jun 2013]

Theses published:

1. B. Wells, *Nonlocal optical response of plasmonic nanowire metamaterials*, MS Thesis (2013)
2. B. Wells, *Emission Modulation and Other Applications of Nonlocal Plasmonic Nanowire Metamaterials*, Ph.D thesis (2015)

Manuscripts accepted for publication and under review

1. A.P. Slobozhanyuk, P. Ginzburg, D.A. Powell, I. Iorsh, A.S. Shalin, P. Segovia, A.V. Krasavin, G.A. Wurtz, V. A. Podolskiy, P.A. Belov, A.V. Zayats, *Purcell effect in hyperbolic metamaterial resonators,* Accepted, Phys.Rev.B
2. G. Marino, P. Segovia, A.V. Krasavin, P. Ginzburg, N. Olivier, G.A. Wurtz, A.V. Zayats, *Second-harmonic generation from hyperbolic plasmonic nanorod metamaterial slab*, arXiv:1508.07586 (2015)

Refractive index sensing with hyperbolic metamaterials: strategies for biosensing and nonlinearity enhancement

N. Vasilantonakis,[1,*] G. A. Wurtz,[1] V. A. Podolskiy,[2] and A. V. Zayats[1]

[1]*Department of Physics, King's College London, Stand, London, WC2R 2LS, UK*
[2]*Department of Physics and Applied Physics, University of Massachusetts, Lowell, Massachusetts 01854, USA*
[*]*nikolaos.vasilantonakis@kcl.ac.uk*

Abstract: Metamaterials with hyperbolic dispersion based on metallic nanorod arrays provide a flexible platform for the design of bio- and chemical sensors and nonlinear devices, allowing the incorporation of functional materials into and onto the plasmonic metamaterial. Here, we have investigated, both analytically and numerically, the dependence of the optical response of these metamaterials on refractive index variations in commonly used experimental sensing configurations, including transmission, reflection, and total internal reflection. The strategy for maximising refractive index sensitivity for different configurations has been considered, taking into account contributions from the superstrate, embedding matrix, and the metal itself. It is shown that the sensitivity to the refractive index variations of the host medium is at least 2 orders of magnitude higher than to the ones originating from the superstrate. It is also shown that the refractive index sensitivity increases for higher-order unbound and leaky modes of the metamaterial sensor. The impact of the transducer's thickness was also analysed showing significant increase of the sensitivity for the thinner metamaterial layers (down to few 0.01 fraction of wavelength and, thus, requiring less analyte) as long as modes are supported by the structure. In certain configurations, both TE and TM-modes of the metamaterial transducer have comparable sensitivities. The results provide the basis for the design of new ultrasensitive chemical and biosensors outperforming both surface plasmon polaritons and localised surface plasmons based transducers.

© 2015 Optical Society of America

OCIS codes: (240.6680) Surface plasmons; (250.5403) Plasmonics; (280.1415) Biological sensing and sensors; (350.4238) Nanophotonics and photonic crystals.

References and links

1. J. Homola, *Surface Plasmon Resonance Based Sensors* (Springer, 2006).
2. J. N. Anker, W. P. Hall, O. Lyandres, N. C. Shah, J. Zhao, and R. P. Van Duyne, "Biosensing with plasmonic nanosensors," Nat. Mater. **7**(6), 442–453 (2008).
3. M. E. Stewart, C. R. Anderton, L. B. Thompson, J. Maria, S. K. Gray, J. A. Rogers, and R. G. Nuzzo, "Nanostructured plasmonic sensors," Chem. Rev. **108**(2), 494–521 (2008).
4. B. Liedberg, C. Nylander, and I. Lunström, "Surface-plasmon resonance for gas-detection and biosensing," Sens. Actuators B Chem. **4**, 299–304 (1983).
5. M. Kauranen and A. V. Zayats, "Nonlinear plasmonics," Nat. Photonics **6**(11), 737–748 (2012).
6. A. V. Zayats and S. Maier, *Active Plasmonics and Tunable Plasmonic Metamaterials* (Wiley, 2014).
7. S. Lal, S. Link, and N. J. Halas, "Nano-optics from sensing to waveguiding," Nat. Photonics **1**(11), 641–648 (2007).
8. M. Svedendahl, S. Chen, A. Dmitriev, and M. Käll, "Refractometric sensing using propagating versus localized surface plasmons: A direct comparison," Nano Lett. **9**(12), 4428–4433 (2009).
9. A. V. Kabashin and P. I. Nikitin, "Surface plasmon resonance interferometer for bio- and chemical-sensors," Opt. Commun. **150**(1-6), 5–8 (1998).
10. P. N. Prasad, *Introduction to Biophotonics* (Wiley-Interscience, 2003).

#234045 - $15.00 USD Received 25 Mar 2015; revised 6 May 2015; accepted 12 May 2015; published 22 May 2015

11. S. Nie and S. R. Emory, "Probing single molecules and single nanoparticles by surface-enhanced Raman scattering," Science **275**(5303), 1102–1106 (1997).
12. A. J. Haes and R. P. Van Duyne, "A unified view of propagating and localized surface plasmon resonance biosensors," Anal. Bioanal. Chem. **379**(7-8), 920–930 (2004).
13. C. M. Soukoulis and M. Wegener, "Past achievements and future challenges in the development of three-dimensional photonic metamaterials," Nat. Photonics **5**, 523–530 (2011).
14. A. Poddubny, I. Iorsh, P. Belov, and Y. Kivshar, "Hyperbolic metamaterials," Nat. Photonics **7**(12), 948–957 (2013).
15. L. Ferrari, C. Wu, D. Lepage, X. Zhang, and Z. Liu, "Hyperbolic metamaterials and their applications," Prog. Quantum Electron. **40**, 1–40 (2015).
16. J. Yao, Z. Liu, Y. Liu, Y. Wang, C. Sun, G. Bartal, A. M. Stacy, and X. Zhang, "Optical negative refraction in bulk metamaterials of nanowires," Science **321**(5891), 930 (2008).
17. N. Vasilantonakis, M. Nasir, W. Dickson, G. A. Wurtz, and A. V. Zayats, "Bulk plasmon-polaritons in hyperbolic nanorod metamaterial waveguides," Laser Photon. Rev. (2015).
18. G. A. Wurtz, R. Pollard, W. Hendren, G. P. Wiederrecht, D. J. Gosztola, V. A. Podolskiy, and A. V. Zayats, "Designed ultrafast optical nonlinearity in a plasmonic nanorod metamaterial enhanced by nonlocality," Nat. Nanotechnol. **6**(2), 107–111 (2011).
19. M. E. Nasir, W. Dickson, G. A. Wurtz, W. P. Wardley, and A. V. Zayats, "Hydrogen detected by the naked eye: optical hydrogen gas sensors based on core/shell plasmonic nanorod metamaterials," Adv. Mater. **26**(21), 3532–3537 (2014).
20. W. Dickson, G. A. Wurtz, P. Evans, D. O'Connor, R. Atkinson, R. Pollard, and A. V. Zayats, "Dielectric-loaded plasmonic nanoantenna arrays: a metamaterial with tuneable optical properties," Phys. Rev. B **76**(11), 115411 (2007).
21. V. V. Yakovlev, W. Dickson, A. Murphy, J. McPhillips, R. J. Pollard, V. A. Podolskiy, and A. V. Zayats, "Ultrasensitive non-resonant detection of ultrasound with plasmonic metamaterials," Adv. Mater. **25**(16), 2351–2356 (2013).
22. J. Elser, R. Wangberg, V. A. Podolskiy, and E. E. Narimanov, "Nanowire metamaterials with extreme optical anisotropy," Appl. Phys. Lett. **89**(26), 261102 (2006).
23. P. B. Johnson and R. W. Christy, "Optical constants of the noble metals," Phys. Rev. B **6**(12), 4370–4379 (1972).
24. B. M. Wells, A. V. Zayats, and V. A. Podolskiy, "Nonlocal optics of plasmonic nanowire metamaterials," Phys. Rev. B **89**(3), 035111 (2014).
25. K.-T. Tsai, G. A. Wurtz, J.-Y. Chu, T.-Y. Cheng, H.-H. Wang, A. V. Krasavin, Jr-H. Hell, B. M. Wells, V. A. Podolskiy, J.-K. Wang, Y.-L. Wang, and A. V. Zayats, "Looking into meta-atoms of plasmonic nanowire metamaterial," Nano Lett. **14**(9), 4971–4976 (2014).
26. W. N. Hansen, "Electric fields produced by the propagation of plane coherent electromagnetic radiation in a stratified medium," J. Opt. Soc. Am. **58**(3), 380–388 (1968).
27. J. Feng, V. S. Siu, A. Roelke, V. Mehta, S. Y. Rhieu, G. T. R. Palmore, and D. Pacifici, "Nanoscale plasmonic interferometers for multispectral, high-throughput biochemical sensing," Nano Lett. **12**(2), 602–609 (2012).
28. H. Liao, C. L. Nehl, and J. H. Hafner, "Biomedical applications of plasmon resonant metal nanoparticles," Nanomedicine (Lond) **1**(2), 201–208 (2006).
29. G. A. Wurtz, W. Dickson, D. O'Connor, R. Atkinson, W. Hendren, P. Evans, R. Pollard, and A. V. Zayats, "Guided plasmonic modes in nanorod assemblies: strong electromagnetic coupling regime," Opt. Express **16**(10), 7460–7470 (2008).
30. G. A. Wurtz, P. R. Evans, W. Hendren, R. Atkinson, W. Dickson, R. J. Pollard, A. V. Zayats, W. Harrison, and C. Bower, "Molecular plasmonics with tunable exciton-plasmon coupling strength in J-aggregate hybridized Au nanorod assemblies," Nano Lett. **7**(5), 1297–1303 (2007).

1. Introduction

The refractive index sensitivity of plasmonic and waveguided resonances forms the basis of commercial and newly emerging optical sensing techniques for label-free biosensing and chemical identification [1–4] as well as active nanophotonic components [5, 6]. In the former class of applications, the presence of an analyte substance modifies the eingenmodes of the nanostructure, a change that can be detected by a shift of the resonant wavelengths of the structure or by changes of transmitted or reflected light intensity. In the latter, the refractive index changes are induced by external stimuli, such as temperature, acoustic pressure, external static electric or magnetic field, or indeed optical field via nonlinear effects in the surrounding dielectric or metal [6]. The strong modification of the optical response in plasmonic nanostructures arises from the strong confinement of the electromagnetic field near the metal/dielectric interface. Both sensing and active nanophotonic devices can make use of macroscopic thin metal films or nanostructured surfaces where surface electromagnetic waves

#234045 - $15.00 USD Received 25 Mar 2015; revised 6 May 2015; accepted 12 May 2015; published 22 May 2015
© 2015 OSA

called surface plasmon polaritons (SPPs) propagate, or nanoparticles and their assemblies supporting localised surface plasmons (LSPs) [2, 3, 7].

Surface plasmon resonance (SPR) biosensors use SPP waves for the detection of binding events, lifetime measurements or molecule concentration, based on the attenuated total internal reflection (ATR) configuration [1]. Due to a strong field confinement of SPPs, sensing limits are greatly enhanced, exceeding 3,000 nm per refractive index unit (RIU) [8] and can be even further boosted via phase-sensitive interferometry [9]. Nonetheless, SPP-based techniques have restrictions in detecting small molecule analytes, typically smaller than 500 Da, where Da is the atomic mass unit, making it problematic for modern nanoscale chemical and biochemical tasks [10]. An alternative route is to use LSP modes on plasmonic nanoparticles that provide an even stronger field confinement and, thus, are more sensitive to smaller-size molecules [2, 11]. However, the overall sensitivity provided by LSPs is typically orders of magnitude smaller than for SPPs, not exceeding 100-300 nm/RIU [2, 12].

Recently, plasmonic metamaterials have been demonstrated to provide the record refractive index sensitivity for biosensing, ultrasound detection and high effective Kerr-type nonlinearities [13]. In particular, the class of anisotropic metamaterials based on arrays of strongly interacting, aligned plasmonic nanorods, exhibits hyperbolic dispersion [14, 15], with one negative (ε_z) and two positive effective permittivity tensor components ($\varepsilon_{x,y}$), leading to a metamaterial with hyperbola-shaped isofrequency contours expressed as $k_x^2/\varepsilon_z + k_y^2/\varepsilon_z + k_z^2/\varepsilon_{x,y} = (\omega/c_0)^2$, where ω is the angular frequency, c_0 is the speed of light, and $k_{x,y,z}$ are the wavevector components along Cartesian directions. This unique isofrequency surface enables a plethora of applications, from guiding and imaging beyond the diffraction limit [16, 17], to enhanced nonlinearities [5, 18], and chemo- and biosensing [5, 6, 19]. Additionally, selected resonances of plasmonic nanorod metamaterials have been shown to exhibit a strong sensitivity to the thickness change of the dielectric load [20], ultrasensitive detection of ultrasound [21], and ultrafast sub-ps response times due to optical nonlocality [18].

In this work, we present a comprehensive analysis of the dependence of the optical response of an anisotropic nanorod-based metamaterial on refractive index changes of analyte above and between the nanorods, in order to develop strategies for optimising its sensing properties. We consider only the wavelength range of hyperbolic dispersion and study reflection, transmission, and total internal reflection modalities of operation, examining the role of perturbations of both the real and imaginary parts of the refractive index in the superstrate, the host medium where the nanorods are placed, as well as from the metal itself. All components of the permittivity tensor determine the formation of these modes and, thus, their refractive index sensitivities. It is shown that the refractive index variations of the host medium most strongly influence the optical response of the metamaterial, providing highest sensitivity, outperforming both SPP and LSP-based biosensors. The sensitivity is greatly enhanced for higher-order modes of the metamaterial slab due to both the spectral positions of these modes, closer to the resonance of some permittivity tensor components at short wavelengths, and the increase of the field gradients with increasing mode order. This resonant contribution is significant for large nanorod filling factors, leading to comparable refractive index sensitivities of TE and TM-modes of the metamaterial slab. For lower metal filling factors, the sensitivity of TM-modes prevails. The role of the transducer's thickness is also investigated showing an increased sensitivity for thinner metamaterial layers.

2. Numerical model

We have studied the refractive index sensing capabilities of a metamaterial in several configurations where the anisotropic metamaterial slab is illuminated in both conventional and total internal reflection conditions. Changes in the intensity transmitted and/or reflected upon modifications of the refractive index and absorption of the analyte are monitored as a

#234045 - $15.00 USD Received 25 Mar 2015; revised 6 May 2015; accepted 12 May 2015; published 22 May 2015
© 2015 OSA

function of wavelength [Fig. 1(a)]. The metamaterial is considered to be composed of an array of gold nanorods arranged periodically [Fig. 1(a)]. The thickness of the metamaterial slab (height of the nanorods) is *l*, and it is sandwiched between a substrate and superstrate with refractive indices of n_{sub} and n_{sup}, respectively.

The Maxwell-Garnett (MG) approximation was followed to derive the tensor of the effective permittivity of the anisotropic metamaterial [22]. Considering an array of rods in the x-y plane, the effective permittivities for ordinary and extraordinary axes take the form

$$\varepsilon_{\mathrm{x,y}}^{\mathrm{eff}} = \frac{p\varepsilon_{\mathrm{Au}}\varepsilon_{\mathrm{h}} + \varepsilon_{\mathrm{h}}(1-p)\tilde{\varepsilon}}{p\varepsilon_{\mathrm{h}} + (1-p)\tilde{\varepsilon}}, \tag{1}$$

$$\varepsilon_{\mathrm{z}}^{\mathrm{eff}} = p\varepsilon_{\mathrm{Au}} + (1-p)\varepsilon_{\mathrm{h}}, \tag{2}$$

where $p = \pi(r/d)^2$ defines the nanorod filling factor, with *d* being the period of the array and *r* is the nanorod radius, $\varepsilon_{\mathrm{Au}}$ and ε_{h} are the permittivities of gold [23] and host medium, respectively, and $\tilde{\varepsilon} = (\varepsilon_{\mathrm{Au}} + \varepsilon_{\mathrm{h}})/2$. Note that the same period is considered in both *x* and *y* directions, thus, $\varepsilon_{\mathrm{x}}^{\mathrm{eff}} = \varepsilon_{\mathrm{y}}^{\mathrm{eff}}$. The MG approximation breaks down for wavevectors close to the Brillouin zone boundary, however for a typical period of 100 nm considered here, the 1st Brillouin zone boundary is close to $k_{\mathrm{x}} \approx 31$ μm^{-1}, which is far from the investigated regime ($k_{\mathrm{x}} < 17$ μm^{-1}). Additionally, the wavelength range where $\mathrm{Re}(\varepsilon_{\mathrm{z}}^{\mathrm{eff}})$ vanishes (ENZ regime) requires special considerations; the ENZ and elliptic dispersion regime will not be considered in this work [24, 25].

To examine the refractive index sensitivity of the optical properties of the metamaterial, the effective permittivity has been designed to achieve hyperbolic dispersion throughout the visible spectral range. Figure 1(b) shows the real and imaginary parts of the components of the effective permittivity tensor for a typical nanorod array parameters and a water-like permittivity for the host medium. The validity of the EMT approach used here was checked with full vectorial 3D numerical simulations. For this geometry, $\varepsilon_{\mathrm{z}}^{\mathrm{eff}}$, the permittivity component for light polarized along the nanorod axis, is negative for wavelengths longer than approximately 475 nm [Fig. 1(b)], while the transverse permittivity $\varepsilon_{\mathrm{x,y}}^{\mathrm{eff}}$, for light polarized perpendicular to the nanorod axes, is always positive, exhibiting a resonant behaviour near a wavelength of 540 nm, where the imaginary part of the permittivity reaches a maximum. For wavelengths above 540 nm the transverse component of permittivity's imaginary part is small relative to its real counterpart and does not exhibit any resonances.

#234045 - $15.00 USD Received 25 Mar 2015; revised 6 May 2015; accepted 12 May 2015; published 22 May 2015
© 2015 OSA

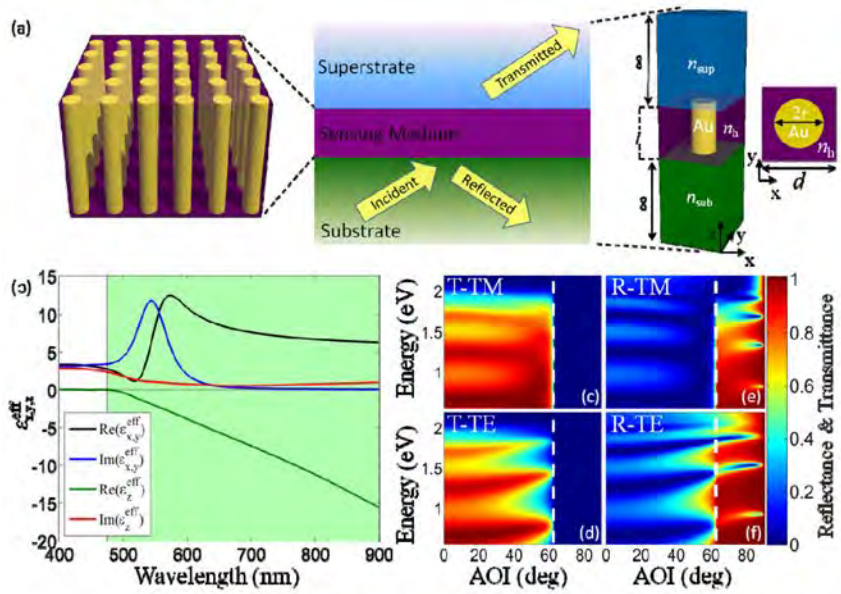

Fig. 1. (a) Left: Schematic of the metamaterial transducer made of an array of Au nanorods embedded in a host environment (analyte); middle: Schematic of the typical experimental realization of refractive index sensing experiments in the reflection or transmission geometry; right: Schematics of the unit cell of the metamaterial. (b) Effective permittivities of the metamaterial in a water-like analyte (n_h = 1.33) with the nanorod period d = 100 nm and radius r = 40 nm. The green area shows the hyperbolic dispersion regime where $\varepsilon_z^{\text{eff}} < 0$. (c-f) Transmittance and reflectance dispersions for (c),(e) TM- and (d),(f) TE-polarized light. Geometry is the same as in (b). The substrate is glass (n_{sub} = 1.5) and superstrate is water (n_{sup} = 1.33). Height of nanorods is l = 400 nm. In all dispersions the TIR occurs at an angle of incidence of 62.46° indicated with dashed line.

The reflectance and transmittance spectra of the metamaterial transducer have been calculated for angles of incidence (AOI) 0° ─ 90° using the transfer matrix method [26] and taking into account a glass substrate (n_{sub} = 1.5), a water superstrate (n_{sup} = 1.33), and Au nanorods of height l = 400 nm. Figures 1(c) and 1(e) along with Figs. 1(d) and 1(f) show the transmittance and reflectance dispersions for both TM and TE-polarizations, respectively. Unbound modes that leak in both substrate and superstrate exist below the critical angle θ_c appear as maxima (minima) in the transmittance (reflectance), while "leaky" modes, homogeneous in the substrate, are only present above θ_c and their effect is only visible in the reflectance of the structure. These modes are quantized solutions of the wavevector (k_z) due to the 1D confinement of the metamaterial slab in the z-direction. For the glass/water (substrate/superstrate) interface, total internal reflection (TIR) occurs at θ_c = 62.46°, above which there is no transmission, and thus transmission-detection sensing is possible only below TIR angles.

In order to compare the sensing capabilities of different transducers and geometries, it is convenient to introduce two figures of merit (FoMs): FoM_λ is to characterize the spectral shift induced by the refractive index changes of an analyte, while FoM_I is to characterize induced intensity variations of the transmitted or reflected light. We define $\text{FoM}_\lambda = (\Delta\lambda/\delta\lambda)/\Delta n$, where $\Delta\lambda$ is the resonance shift of a metamaterial resonance to a refractive index change Δn, and $\delta\lambda$ is the reference full-width at half maximum of the resonance [27]. This definition accounts simultaneously for both the wavelength shift of a given mode per refractive index change, and the sharpness of the resonance. For intensity measurements, $\text{FoM}_I = (\Delta I/I_0)/\Delta n$, where ΔI is the change of the transmitted or reflected intensity corresponding to a refractive index change Δn, and I_0 is the initial intensity [27]. While intensity measurements are simpler to implement

#234045 - $15.00 USD Received 25 Mar 2015; revised 6 May 2015; accepted 12 May 2015; published 22 May 2015
© 2015 OSA

than spectral shift measurements, in some cases the latter may provide better sensitivity [19]. Both FoMs represent the sensitivity to an average analyte refractive index changes rather than to local binding events of sensed molecules to nanorods. We will use these FoMs to evaluate the sensing capabilities of the metamaterial in the numerical results obtained below.

3. Effective permittivity sensitivity to refractive index variations of constituents

We now examine the sensitivity of the effective permittivities $\varepsilon_{\mathrm{x,y}}^{\mathrm{eff}}$ and $\varepsilon_{\mathrm{z}}^{\mathrm{eff}}$, which determine the optical response of the metamaterial, on the refractive index changes of the metamaterial's constituents $n_{\mathrm{h}} = \sqrt{\varepsilon_{\mathrm{h}}' + i\varepsilon_{\mathrm{h}}''}$ and $n_{\mathrm{Au}} = \sqrt{\varepsilon_{\mathrm{Au}}' + i\varepsilon_{\mathrm{Au}}''}$, for the host medium and Au, respectively. The modification of the refractive index of the metal can be achieved for example in nonlinear optical experiments, when the metamaterial is under femtosecond optical excitation due to the Kerr-type third-order nonlinearity of Au, but can also be induced by environmental change in temperature or pressure [19, 25]. The refractive index of the host medium can be changed in sensing experiments when analyte is incorporated between the nanorods or if nonlinear or temperature effects are important in the host dielectric. To evaluate this sensitivity, we study the partial derivative of Eqs. (1) and (2) with regards to the permittivity components of each constituent, obtaining:

$$\frac{\partial \varepsilon_{\mathrm{x,y}}^{\mathrm{eff}}}{\partial \varepsilon_{\mathrm{h}}'} = -i\frac{\partial \varepsilon_{\mathrm{x,y}}^{\mathrm{eff}}}{\partial \varepsilon_{\mathrm{h}}''} = \frac{P\varepsilon_{\mathrm{Au}} + 2\varepsilon_{\mathrm{h}}}{P\varepsilon_{\mathrm{h}} + \varepsilon_{\mathrm{Au}}} - P\varepsilon_{\mathrm{h}}\frac{P\varepsilon_{\mathrm{Au}} + \varepsilon_{\mathrm{h}}}{(P\varepsilon_{\mathrm{h}} + \varepsilon_{\mathrm{Au}})^2}, \quad (3)$$

$$\frac{\partial \varepsilon_{\mathrm{x,y}}^{\mathrm{eff}}}{\partial \varepsilon_{\mathrm{Au}}'} = -i\frac{\partial \varepsilon_{\mathrm{x,y}}^{\mathrm{eff}}}{\partial \varepsilon_{\mathrm{Au}}''} = \varepsilon_{\mathrm{h}}\left[\frac{P}{P\varepsilon_{\mathrm{h}} + \varepsilon_{\mathrm{Au}}} - \frac{P\varepsilon_{\mathrm{Au}} + \varepsilon_{\mathrm{h}}}{(P\varepsilon_{\mathrm{h}} + \varepsilon_{\mathrm{Au}})^2}\right], \quad (4)$$

$$\frac{\partial \varepsilon_{\mathrm{z}}^{\mathrm{eff}}}{\partial \varepsilon_{\mathrm{h}}'} = -i\frac{\partial \varepsilon_{\mathrm{z}}^{\mathrm{eff}}}{\partial \varepsilon_{\mathrm{h}}''} = 1 - p, \quad (5)$$

$$\frac{\partial \varepsilon_{\mathrm{z}}^{\mathrm{eff}}}{\partial \varepsilon_{\mathrm{Au}}'} = -i\frac{\partial \varepsilon_{\mathrm{z}}^{\mathrm{eff}}}{\partial \varepsilon_{\mathrm{Au}}''} = p, \quad (6)$$

where $1 < P = (1+p)/(1-p) \leq 8.32$. The above expressions allow us to selectively track the response of the effective permittivities when either the real or the imaginary part of the constituents' permittivity changes. Figure 2 illustrates this behaviour for the same metamaterial as in Fig. 1(b). The response of $\varepsilon_{\mathrm{z}}^{\mathrm{eff}}$ to the refractive index modifications is extremely broadband and constant across the spectral range considered for both the real and imaginary parts [Figs. 2(a)-2(d)], determined solely by the nanorod filling factor via *p* [Eqs. (5) and (6)]. On the other hand, $\varepsilon_{\mathrm{x,y}}^{\mathrm{eff}}$ exhibits the strongest changes close to its resonance at 540 nm [Fig. 1(b)] and strongly decreases for lower nanorod filling factors. Beyond the resonance at longer wavelengths, inspecting the dependence of $\varepsilon_{\mathrm{x,y}}^{\mathrm{eff}}$ on the host medium refractive index, one notices that it is always exceeds the sensitivity of $\varepsilon_{\mathrm{z}}^{\mathrm{eff}}$ [Figs. 2(a) and 2(b)], while both are similar at low nanorod filling factors. The $\varepsilon_{\mathrm{z}}^{\mathrm{eff}}$ sensitivity to the refractive index of the plasmonic material dominates at long wavelengths, while the resonant behaviour of $\varepsilon_{\mathrm{x,y}}^{\mathrm{eff}}$ proves in general more strongly sensitive to the host medium refractive index. To examine the impact of filling factor *p* more extensively, the dispersion diagrams of the derivative of $\varepsilon_{\mathrm{x,y}}^{\mathrm{eff}}$ with respect to $\varepsilon_{\mathrm{h}}'$ are presented in Figs. 2(e) and 2(f); the derivative of $\varepsilon_{\mathrm{x,y}}^{\mathrm{eff}}$ with respect to $\varepsilon_{\mathrm{h}}''$ can then be trivially extracted from Eq. (3). All refractive index

#234045 - $15.00 USD Received 25 Mar 2015; revised 6 May 2015; accepted 12 May 2015; published 22 May 2015
© 2015 OSA

sensitivity dispersions are dominated by a dispersive-shape resonance, which red-shifts and increases in magnitude with increasing nanorod filling factor. Both the dispersive behaviour and spectral shift observed in Figs. 2(e) and 2(f) can be linked to the spectral sensitivity of the resonance in $\varepsilon_{x,y}^{eff}$ shown in Fig. 1(b), which red-shifts with both an increase in ε_h and nanorod filling factor. The same calculations were repeated for ε'_{Au} showing a trend similar to Figs. 2(e) and 2(f), but with the resonant sensitivity approximately one order of magnitude smaller (data not shown).

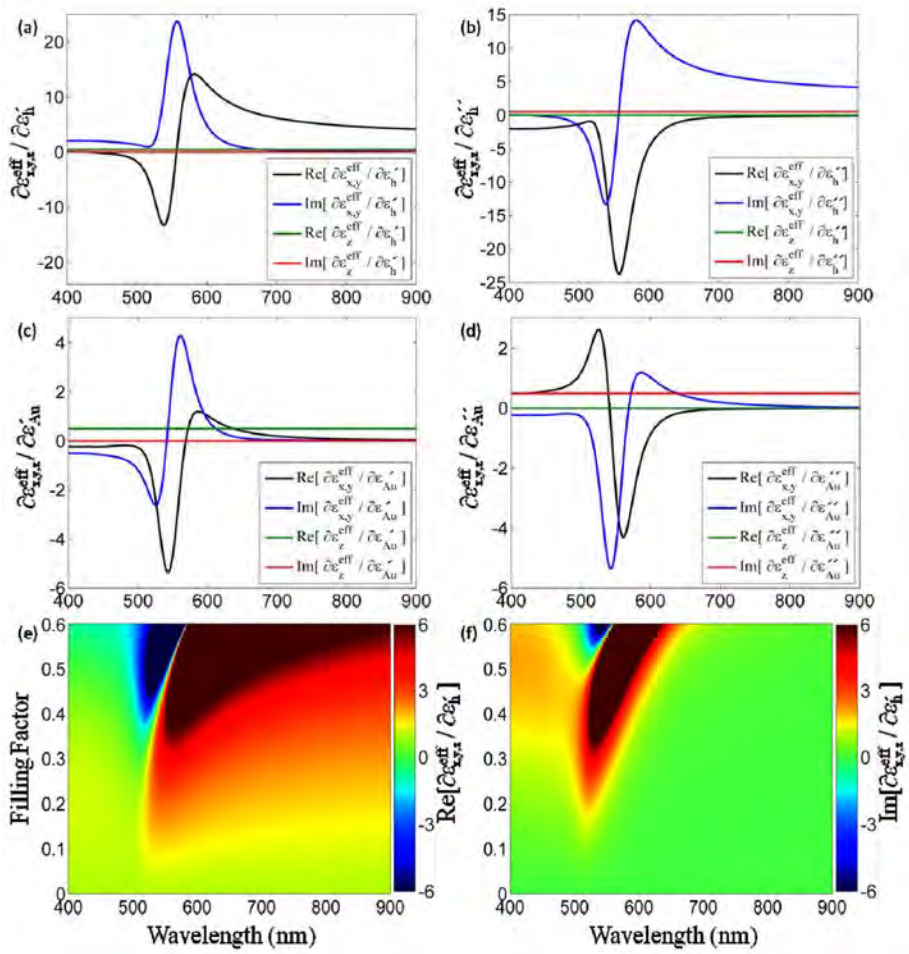

Fig. 2. The spectral dependence of the effective permittivity variations with respect to (a) ε'_h, (b) ε''_h, (c) ε'_{Au} and (d) ε''_{Au} modifications for a filling factor of p = 0.5. The dependence of (e) real and (f) imaginary parts of the effective permittivity on ε'_h variations. Only filling factors below 0.6 are shown since the effective medium approximation ceases to be accurate at high filling factors.

4. Mode frequency dependence on the refractive index of analyte

All the components of the effective permittivity tensor are important for defining the behaviour of TM-modes of the metamaterial and, thus, their sensing capabilities. At the same time, only $\varepsilon_{x,y}^{eff}$ components define TE modes. To get better insight into the sensing capabilities of the unbounded, leaky, and waveguided modes of the metamaterial transducer,

#234045 - $15.00 USD Received 25 Mar 2015; revised 6 May 2015; accepted 12 May 2015; published 22 May 2015
© 2015 OSA

let us consider an approximate analytic model for extraordinary modes in the case of the anisotropic metamaterial layer [17]. We restrict ourselves primarily to TM-modes, while TE-polarization can be treated similarly. Neglecting phase shifts at the metamaterial's boundaries, we obtain a simple analytical approximation for the wavevector component k_x of TM-modes supported by the metamaterial slab as [17]

$$k_{\mathrm{x}}^2 = \varepsilon_{\mathrm{z}}^{\mathrm{eff}} k_0^2 - \left(\frac{q\pi}{l}\right)^2 \left(\frac{\varepsilon_{\mathrm{z}}^{\mathrm{eff}}}{\varepsilon_{\mathrm{x,y}}^{\mathrm{eff}}}\right), \tag{7}$$

where $k_0 = \omega / c_0$, and quantization $q\pi/l$ emerges from the transversal confinement of the wavevector component perpendicular to the metamaterial's interfaces with the integer $q > 0$ referring to the mode number. Unbounded, leaky, and waveguided modes then satisfy the condition $k_{\mathrm{x}} < n_{\mathrm{sub}} k_0$, $n_{\mathrm{sub}} k_0 \le k_{\mathrm{x}} < n_{\mathrm{sup}} k_0$, and $k_{\mathrm{x}} \ge n_{\mathrm{sup}} k_0$, respectively, with the mode frequency

$$\omega_{\mathrm{q}} = c_0 \sqrt{\frac{k_{\mathrm{x}}^2}{\varepsilon_{\mathrm{z}}^{\mathrm{eff}}} + \left(\frac{q\pi}{l}\right)^2 \frac{1}{\varepsilon_{\mathrm{x,y}}^{\mathrm{eff}}}}, \tag{8}$$

where the number of supported modes being determined by the sign of the permittivity components. For higher-order modes, it may be necessary to take into account deviations from the EMT due to spatial dispersion effects [24]. The sensitivity of the mode frequency ω_{q} to variations in both ε_{h} and $\varepsilon_{\mathrm{Au}}$, for a given q and k_x, immediately follows as:

$$\begin{aligned} \frac{\partial \omega_{\mathrm{q}}}{\partial \varepsilon_{\mathrm{h}}'} = -i \frac{\partial \omega_{\mathrm{q}}}{\partial \varepsilon_{\mathrm{h}}''} &= -\frac{c_0^2}{2\omega_{\mathrm{q}}} \left[\left(\frac{k_{\mathrm{x}}}{\varepsilon_{\mathrm{z}}^{\mathrm{eff}}}\right)^2 \frac{\partial \varepsilon_{\mathrm{z}}^{\mathrm{eff}}}{\partial \varepsilon_{\mathrm{h}}'} + \left(\frac{q\pi}{l\varepsilon_{\mathrm{x,y}}^{\mathrm{eff}}}\right)^2 \frac{\partial \varepsilon_{\mathrm{x,y}}^{\mathrm{eff}}}{\partial \varepsilon_{\mathrm{h}}'} \right] = \\ &= i \frac{c_0^2}{2\omega_{\mathrm{q}}} \left[\left(\frac{k_{\mathrm{x}}}{\varepsilon_{\mathrm{z}}^{\mathrm{eff}}}\right)^2 \frac{\partial \varepsilon_{\mathrm{z}}^{\mathrm{eff}}}{\partial \varepsilon_{\mathrm{h}}''} + \left(\frac{q\pi}{l\varepsilon_{\mathrm{x,y}}^{\mathrm{eff}}}\right)^2 \frac{\partial \varepsilon_{\mathrm{x,y}}^{\mathrm{eff}}}{\partial \varepsilon_{\mathrm{h}}''} \right], \end{aligned} \tag{9}$$

$$\begin{aligned} \frac{\partial \omega_{\mathrm{q}}}{\partial \varepsilon_{\mathrm{Au}}'} = -i \frac{\partial \omega_{\mathrm{q}}}{\partial \varepsilon_{\mathrm{Au}}''} &= -\frac{c_0^2}{2\omega_{\mathrm{q}}} \left[\left(\frac{k_{\mathrm{x}}}{\varepsilon_{\mathrm{z}}^{\mathrm{eff}}}\right)^2 \frac{\partial \varepsilon_{\mathrm{z}}^{\mathrm{eff}}}{\partial \varepsilon_{\mathrm{Au}}'} + \left(\frac{q\pi}{l\varepsilon_{\mathrm{x,y}}^{\mathrm{eff}}}\right)^2 \frac{\partial \varepsilon_{\mathrm{x,y}}^{\mathrm{eff}}}{\partial \varepsilon_{\mathrm{Au}}'} \right] = \\ &= i \frac{c_0^2}{2\omega_{\mathrm{q}}} \left[\left(\frac{k_{\mathrm{x}}}{\varepsilon_{\mathrm{z}}^{\mathrm{eff}}}\right)^2 \frac{\partial \varepsilon_{\mathrm{z}}^{\mathrm{eff}}}{\partial \varepsilon_{\mathrm{Au}}''} + \left(\frac{q\pi}{l\varepsilon_{\mathrm{x,y}}^{\mathrm{eff}}}\right)^2 \frac{\partial \varepsilon_{\mathrm{x,y}}^{\mathrm{eff}}}{\partial \varepsilon_{\mathrm{Au}}''} \right], \end{aligned} \tag{10}$$

Note the connection of the mode frequency with respect to the real and imaginary parts of permittivity; this is a direct consequence of Eqs. (3)-(6). Equations (9) and (10), along with Eqs. (1) and (2) indicate the important interplay between the absolute values and variations in $\varepsilon_{\mathrm{x,y}}^{\mathrm{eff}}$ and $\varepsilon_{\mathrm{z}}^{\mathrm{eff}}$ for determining shifts in mode frequencies. Their relative contributions also depend on the nanorod filling factor and resonant wavelength. Following the same steps described above, one can find the sensitivity of the mode frequency for TE-modes: $\partial \omega_{\mathrm{q}} |_{\mathrm{TE}} / \partial \varepsilon_{\mathrm{h}}' = -(\omega_{\mathrm{q}} |_{\mathrm{TE}} / 2\varepsilon_{\mathrm{x,y}}^{\mathrm{eff}})(\partial \varepsilon_{\mathrm{x,y}}^{\mathrm{eff}} / \partial \varepsilon_{\mathrm{h}}')$ with $\omega_{\mathrm{q}} |_{\mathrm{TE}} = (c_0 / \sqrt{\varepsilon_{\mathrm{x,y}}^{\mathrm{eff}}})(\sqrt{k_{\mathrm{x}}^2 |_{\mathrm{TE}} + (q\pi / l)^2})$, where $k_{\mathrm{x}}^2 |_{\mathrm{TE}} = \varepsilon_{\mathrm{x,y}}^{\mathrm{eff}} k_0^2 - (q\pi / l)^2$, and similarly for sensitivity of to the plasmonic metal permittivity. The changes in the refractive medium of the analyte between the nanorods results in the effective permittivity changes, affecting both TM and TE-modes.

#234045 - $15.00 USD Received 25 Mar 2015; revised 6 May 2015; accepted 12 May 2015; published 22 May 2015
© 2015 OSA

The mode position dependence with respect to the real part of the constituents' permittivities is plotted in Fig. 3 within the 1st Brillouin zone to ensure EMT validity. As the mode number increases from q = 1 to q = 5 there is an order of magnitude increase in the sensitivity of the mode frequency to the host medium refractive index variations [Fig. 3(a)] and a two orders of magnitude increase to that of Au [Fig. 3(c)]. The superior refractive index sensitivity of high-order modes is a consequence of their spectral position close to the resonance in $\varepsilon_{x,y}^{\mathrm{eff}}$ [Fig. 2] and the increased field gradients inside the metamaterial for higher-order modes. These gradients are determined by the mode's spatial frequency $q\pi/l$, increasing with increasing q value or decreased sensor thickness l. Interestingly, this leads to an increase in the mode sensitivity as the mode shifts to shorter wavelengths, a trend opposite to that observed with conventional SPR or LSPR transducers. In particular, shifting the resonance frequency of the fundamental mode (q = 1) from 0.5 eV to 1.5 eV, by decreasing the metamaterial layer thickness from 500 nm to 130 nm, results in a ~500% increase in sensitivity as monitored in both transmittance and reflectance at normal incidence. An increase in the nanorod filling factor p, all other parameters being kept constant, leads to a decrease in the sensitivity of the mode position. Again, this is reminiscent of the increased mode delocalization within the metamaterial with decreasing frequency. Comparing Figs. 3(a) and 3(c) we can also observe that, for a given mode q, the rate of change of the resonance position is stronger with respect to changes in the real part of the host permittivity compared to changes in the real part of Au permittivity, $\partial\omega_{\mathrm{q}} / \partial\varepsilon'_{\mathrm{h}} \gg \partial\omega_{\mathrm{q}} / \partial\varepsilon'_{\mathrm{Au}}$. This is the result of the modal field distribution being mainly present in the host medium.

The mode frequency sensitivity with respect to $\varepsilon''_{\mathrm{h}}$ and $\varepsilon''_{\mathrm{Au}}$ is not shown here but was also examined, giving a similar trend to Figs. 3(a) and 3(c), but with a one-to-two orders of magnitude smaller sensitivity to the variations in either or $\varepsilon'_{\mathrm{Au}}$. This indicates that the real parts of both the host medium and Au will affect sensing more than the imaginary counterparts. Monitoring the analyte's refractive index changes at normal incidence provides the lowest sensitivity with regards to the modes' spectral shift [Fig. 3].

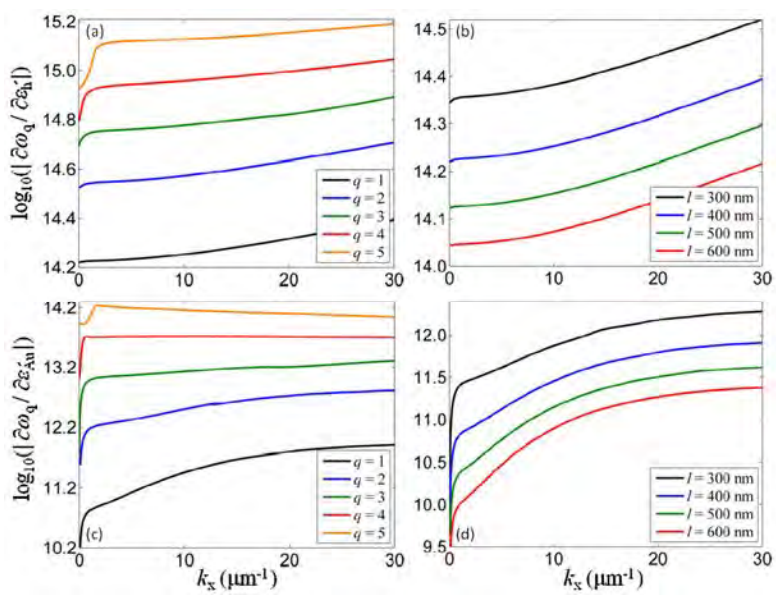

Fig. 3. The mode frequency shift with (a),(b) $\varepsilon'_{\mathrm{h}}$ and (c),(d) $\varepsilon'_{\mathrm{Au}}$ variations: (a),(c) the first five modes (q = 1-5) for l = 400 nm and (b),(d) the fundamental mode (q = 1) for various transducer thicknesses. Geometry is the same as in Fig. 1(b).

#234045 - $15.00 USD Received 25 Mar 2015; revised 6 May 2015; accepted 12 May 2015; published 22 May 2015
© 2015 OSA

Next, the impact of the thickness of the metamaterial transducer, l, was examined. Figures 3(b) and 3(d) show the q = 1 mode frequency sensitivity with respect to $\varepsilon'_{\mathrm{h}}$ and $\varepsilon'_{\mathrm{Au}}$ as l varies from 300 nm to 600 nm. In both cases, as the waveguide thickness increases, the sensitivity drops, in agreement with the mode position shift to lower frequencies. A similar behaviour is observed for higher-order modes. This behaviour can be clarified more explicitly by examining the normal incidence behaviour of the mode resonance frequency, simplifying Eq. (9) to $\partial\omega_{\mathrm{q}} / \partial(\varepsilon'_{\mathrm{h}}, \varepsilon'_{\mathrm{Au}}) = -[c_0\pi(\varepsilon^{\mathrm{eff}}_{\mathrm{x,y}})^{-3/2} / 2l]\partial\varepsilon^{\mathrm{eff}}_{\mathrm{x,y}} / \partial(\varepsilon'_{\mathrm{h}}, \varepsilon'_{\mathrm{Au}})$, clearly showing the inverse proportionality of the mode resonance sensitivity to the metamaterial thickness l for unbound modes. Thus, for a given mode number, a thinner transducer will be more sensitive. This result has been verified using numerical simulations as long as the mode considered had a frequency not exceeding that corresponding to a free-space wavelength of 650 nm, or beyond the range of high losses due to $\mathrm{Im}(\varepsilon^{\mathrm{eff}}_{\mathrm{x,y}})$ [Fig. 1(b)].

5. Numerical simulations

In order to show the complete pattern of the metamaterial behaviour with the refractive index modifications of its constituents, which are used to describe the sensing capabilities of the metamaterial and its active nanophotonic properties, we have also numerically studied the modification of the metamaterial resonances with changes of the complex refractive index of the superstrate, n_{sup}, and embedding medium, n_{h}. For all numerical calculations the refractive indices were the same before introduction of the analyte. These changes may originate from an unknown analyte or a material with nonlinear or electro-optical properties used for switching/modulation purposes. It may also be represented by Au itself as a source of nonlinearity for all-optical control or as temperature sensor. We examine how the latter two parameters translate into the sensitivity of the metamaterial transducer for the detection of the bulk refractive index changes of an analyte. We first consider a non-absorptive analyte (Section 5.1) for which only the real part of the refractive index changes. Then, the effect of changes in the absorption of analyte is studied (Section 5.2). Finally, the impact modifications of the refractive index of Au have on the optical properties of the metamaterial is discussed in Section 5.3. For all simulations, the sensing geometry was kept the same as in Fig. 1(b) with a nanorod height fixed at 400 nm.

5.1 Sensing refractive index variations

We start with the nonabsorptive case, corresponding to the situation of an analyte consisting of nonresonant molecules. In this situation, changes in the refractive index may be induced through Kerr nonlinearities of the host medium or superstrate, electro-optical, thermo-optical or pressure effects. Figures 4(a)-4(c) show the reflectance sensitivity ($\mathrm{FoM_I}$) for different wavelengths and angles of incidence for TM-polarization, when changes of the refractive index originate from either the superstrate (Δn_{sup}), host medium (Δn_{h}), or both simultaneously (Δn_{b}). The $\mathrm{FoM_I}$ has a dispersive behaviour, changing sign in the vicinity of the mode resonances [Figs. 4(b) and 4(c)]. This behaviour is observed as a result of a simultaneous change in both the intensity (ΔI) and wavelength ($\Delta\lambda$) of the metamaterial modes. However, when ΔI has a dominating role, the $\mathrm{FoM_I}$ retains its sign (for example, Fig. 4(a) for the angular range between 0° and 50°). From Fig. 4(a), it is clear that the strongest variations of the optical response are observed in the vicinity of the modes of the metamaterial transducer, but with a sensitivity maximised near the critical angle θ_{c}. The reason is that when the refractive index of the superstrate is changed by Δn_{sup}, the critical angle itself will be affected leading to a strong sensitivity along the superstrate light line, the so-called near cut-off regime.

A different behaviour is observed for the variations of the refractive index of the host medium Δn_{h} [Fig. 4(b)]. In this case, the sensitivity of leaky modes is higher than that of unbound modes. When both the refractive index of the host medium and the superstrate

#234045 - $15.00 USD Received 25 Mar 2015; revised 6 May 2015; accepted 12 May 2015; published 22 May 2015
© 2015 OSA

change, a combination of the above individual cases is observed, although not just a simple addition of individual sensitivities since modes from the metamaterial layer are penetrating the superstrate medium [Fig. 4(c)]. Not surprisingly, the results show that a small change in the refractive index of the superstrate affects the sensitivity only at angles very close to θ_c, while for any other incidence angle the host medium has a dominating role. Both TM [Figs. 4(a)-4(c)] and TE [Figs. 4(d)-4(f)] modes of the metamaterial transducer have comparable sensitivities if the analyte is incorporated between the rods. This is not surprising giving the nature of the anisotropic waveguided modes determined by all components of the effective permittivity tensor. For low filling factors, the role of TM-modes increases, when the $\varepsilon_{x,y}^{eff}$ sensitivity becomes smaller. The changes in the refractive medium of the analyte between the nanorods results in the effective permittivity changes, affecting both TM and TE-modes.

Figures 4(g)-4(i) show the sensitivity for selected wavelengths and angles of incidence. The spectral dependence of FoM_I at normal incidence [Fig. 4(g)] reveals that the mode with the highest sensitivity (q = 3) reaches FoM_I exceeding 400, with the host medium being mainly responsible for this enhanced sensitivity. As mode number increases from q = 1 to q = 3, the FoM_I also increases in agreement with the analytical examination [Fig. 3(a)]. However, the q = 4 mode, located close to 2 eV, shows a decreased sensing capability contrary to the analytical scenario. This is due to the increased absorption of $\varepsilon_{x,y}^{eff}$ [Fig. 1(b)] at wavelengths below 650 nm (> 1.9 eV), which are not tracked with the analytical model discussed in Section 4. Figure 4(h) examines the angular dependence of the sensitivity for the modes with the highest sensitivities: (q = 3) at 1.7 eV for TM-polarization and q = 2 at 1.4 eV for TE-polarization. These plots show a typical dispersive behaviour of the mode position, with high sensitivities observed on both sides of the resonance. As expected, the highest FoM_I is observed above θ_c for leaky modes. This behaviour is better observed in Fig. 4(i) which depicts the global maximum FoM_I for TM-polarization, for the q = 4 mode located at a wavelength of about 645 nm and for an angle of incidence of about 79°, above the critical angle. Similarly for the TE-case, the highest FoM_I is observed for the q = 2 mode for a wavelength close to 870 nm and at 84°. Only variations in the superstrate refractive index lead to high sensitivity lies just below θ_c, at 58.8° for reasons already explained above. In the following sections, we will concentrate only on the sensing with TM-modes, pointing out that in the case of absorption variation sensing, discussed below, TE-modes also have comparable but slightly lower FoM_I.

The q = 1 mode exhibits the highest resonant shift reaching almost 4000 nm/RIU, while the highest $FoM_\lambda \approx 167$ is observed for the mode q = 3, outperforming both SPR and LSPR sensors which have typical FoM_λ around 23 [2] and 8 [2, 28], respectively. The origin of such high FoM_λ is in the influence of the analyte not only directly on the electomagnetic mode properties, as usual for conventional sensors, but also on the effective permittivity of the metamaterial which is connected to the host medium refractive index [Fig. 2], on the microscopic level, this is the result of plasmon-plasmon interactions within the nanorod array [20, 29, 30]. The intensity figure of merit (FoM_I) is proportional to $(\Delta R/\Delta n)/R_0$ and can be directly observed in Fig. 4. Depending on the wavelength and AOI, FoM_I can be as high as 25,000, significantly higher that any LSP- and SPP-based [27] sensors [Fig. 4(i)]. It should be noted that given the standard definition of the FoM_I commonly used in the literature, which includes a normalization to the initial reflected or transmitted intensity I_0, the highest values of FoM_I occur in spectral regions closed to the metamaterial's resonances where I_0 is small, the absolute variations of the intensity, however, have the same angular and spectral dependences as FoM_I. Both FoM_I and FoM_λ can be further tailored and enhanced with geometrical parameters of the transducer, with FoM_λ reaching up to 300 has been experimentally demonstrated [18].

#234045 - $15.00 USD Received 25 Mar 2015; revised 6 May 2015; accepted 12 May 2015; published 22 May 2015
© 2015 OSA

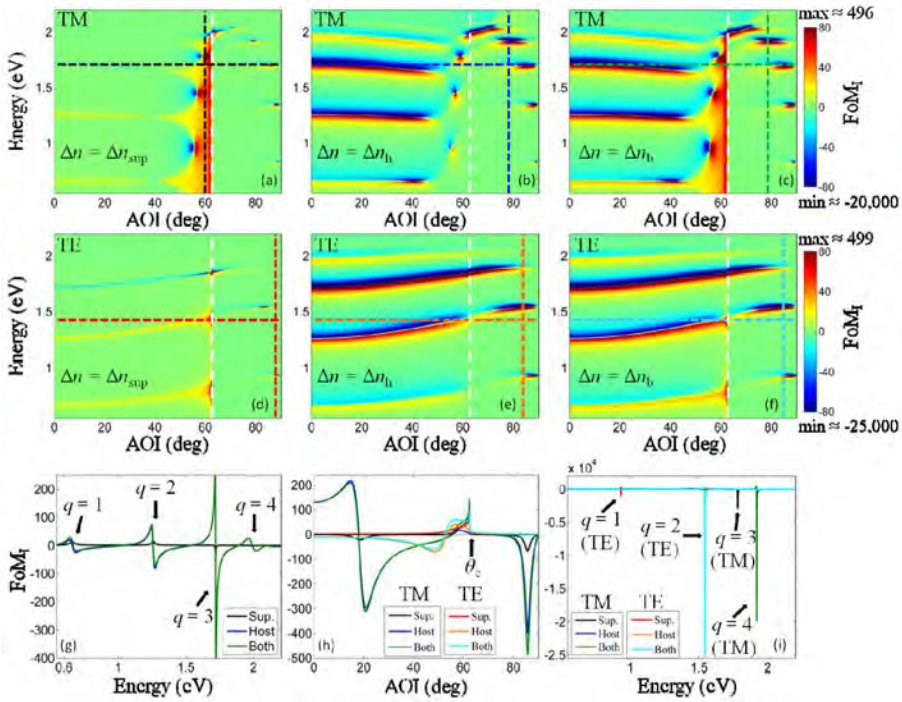

Fig. 4. Spectral and angular dependencies of the intensity figure of merit (FoM_I) for the changes of the refractive index of superstrate (a,d), host medium (b,e) and both (c,f) for (a-c) TM-polarization and (d-f) TE-polarization. Superstrate light line is also shown (white dashed line). Colour scale is the same for enable comparison. (g) Cross-sections of (a)-(f) at normal incidence. (h) Cross-sections of (a)-(f) tracking the q = 3 mode (horizontal dashed lines) at 1.7 eV for TM-polarization and q = 2 mode at 1.4 eV for TE-polarization. (i) Cross-sections of (a)-(f) at angles where highest sensitivity is observed (vertical dashed lines).

5.2 Sensing absorption variations

Turning to the impact of the absorption variations on the metamaterial transducer response, Figs. 5(a)-5(c) show the reflectance variations for different wavelengths and angles of incidence for TM-polarized incident light with changes in the imaginary part of the refractive index of either the superstrate (Δn_{sup}), the host medium (Δn_h), or both simultaneously (Δn_b). Similar to changes in the refractive index [Figs. 4(a)-4(c)], the sensitivity of the transducer originates from the modal dispersion of the metamaterial slab. Interestingly, an increase in the absorption leads to an increased reflection for some angles, while others behave oppositely. Again, an increased sensitivity is observed for higher mode order moving from q = 1 to 3, with the decreased sensitivity for the q = 4 mode due to losses [Fig. 5(d)].

Similarly to the nonabsorbing case, the mode with the highest FoM_I (q = 3) depicted in Fig. 5(d), showed a resonant shift of more than 700 nm/RIU, while the q = 1 mode exhibits the highest resonant shift reaching values close to 4,000 nm/RIU. Tracking the q = 3 mode at various AOI [Fig. 5(e)], its sensitivity is enhanced around both 20° and 85°, where the mode is leaky. The FoM_λ of the q = 3 mode in Fig. 5(d) is close to 167, similar to the nonabsorbing analytes discussed in Section 5.1. However, its FoM_I reaches a value of almost 1,000, or at least twice higher than the corresponding one in Fig. 4(g) for the same mode (q = 3) since the influence of the imaginary part of the permittivity is on reflection is stronger than the real one. The highest FoM_I in Fig. 5(f) exceeds 24,000, which is a significant 25% higher than the TM-FoM_I for sensing nonabsorbing analytes [Fig. 4(i)].

#234045 - $15.00 USD Received 25 Mar 2015; revised 6 May 2015; accepted 12 May 2015; published 22 May 2015
© 2015 OSA

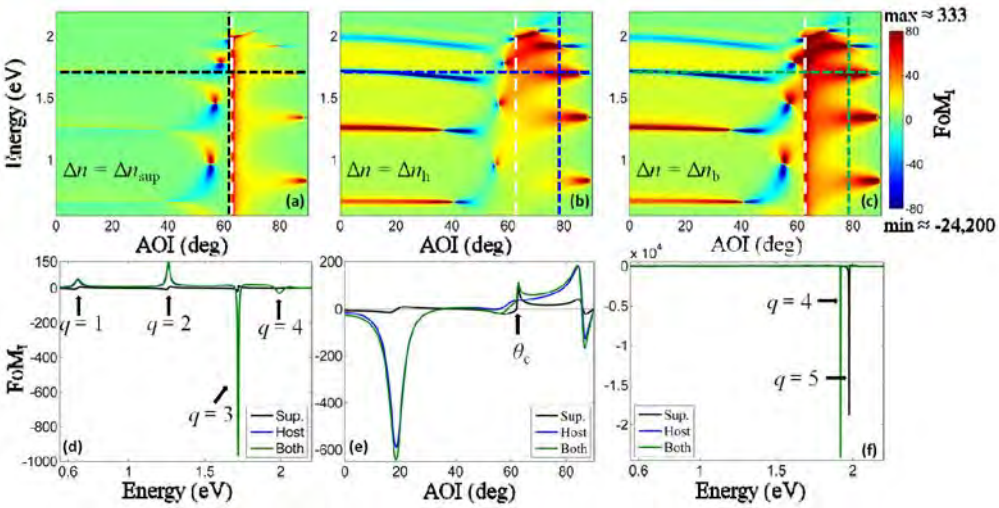

Fig. 5. Spectral and angular dependencies of the intensity figure of merit (FoM_I) with the changes of the absorption of superstrate (a), host medium (b) and both (c) for TM-polarization. Superstrate light line is also shown (white dashed line). Colour scale is the same for enable comparison. (d) Cross-sections of (a)-(c) at normal incidence (vertical dashed lines). (e) Cross-sections of (a)-(c) tracking the q = 3 mode (horizontal dashed lines) at 1.7 eV. (f) Cross-sections of (a)-(c) at angles where highest sensitivity is observed (vertical dashed lines).

5.3 The effects of refractive index variations in Au

Lastly, the dispersive sensitivity of the metamaterial for refractive index variations of the gold nanorods (Δn_{Au}) was investigated. These can be induced either optically, via the Kerr-type nonlinearity of the metal, or via thermo-optical effects. Figures 6(a) and 6(b) depict the reflectance variations when either the real or the imaginary part of the refractive index of Au varies. Note that the variations were set to be wavelength independent, which would correspond to different electronic/lattice temperatures at different wavelengths, to allow for comparison with the previous section but without altering the generality of the results. The sensitivity is smallest below the superstrate light line. More specifically, low-q modes exhibit lower sensitivities compared to high-q modes, located close to 2 eV. Again, material losses at higher frequency eventually limit the sensitivity of these modes as well. Interestingly, the sensitivity observed here is smaller than those resulting from changes in either host medium or superstrate discussed above. Examining again the mode with the highest sensitivity (q = 3) at normal incidence as shown in Figs. 6(c) and 6(d), one can clearly see that FoM_I is approximately one order of magnitude less than for the scenarios in Figs. 4(g) and 5(d). The FoM_λ of the aforementioned mode to Au permittivity variations is 168, very close to FoM_λ observed for sensing of the analytes above. At the same time, the intensity figure of merit for Au permittivity modification is much smaller than for the sensing of analytes giving a maximum value of only 1,200 [Fig. 6(e)]. It should be mentioned that the resonant shift per RIU is only a few nm regardless of the mode chosen; a result that applies for variations in both the real and imaginary part of the refractive index of Au.

#234045 - $15.00 USD Received 25 Mar 2015; revised 6 May 2015; accepted 12 May 2015; published 22 May 2015
© 2015 OSA

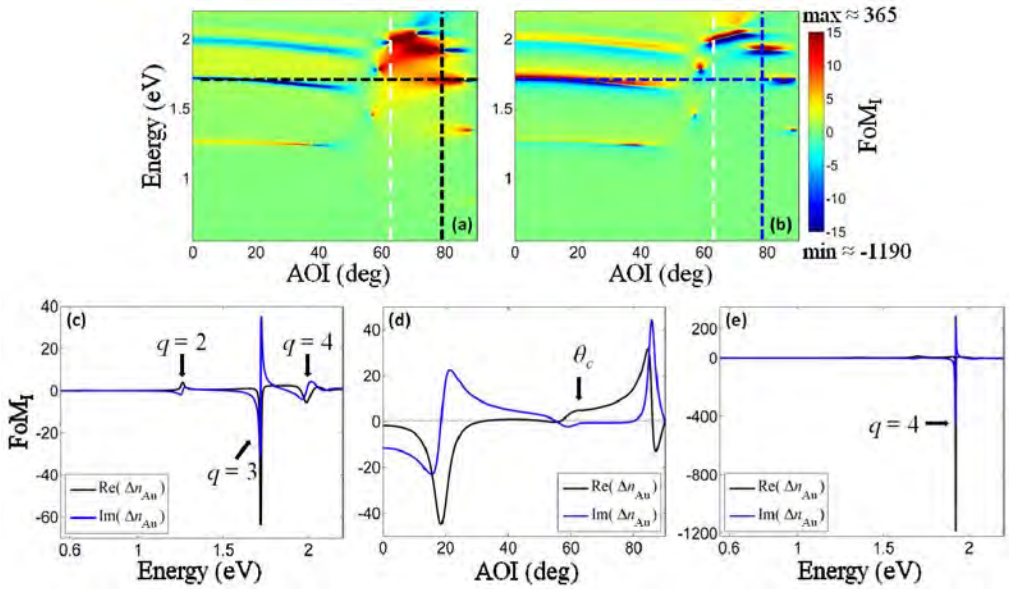

Fig. 6. Spectral and angular dependencies of the intensity figure of merit (FoM_I) with the changes of (a) refractive index and (b) absorption of Au for TM-polarization. Superstrate light line is also shown (white dashed line). Colour scale is the same for enable comparison. (c) Cross-sections of (a)-(b) at normal incidence (vertical dashed lines). (d) Cross-sections of (a)-(b) tracking the q = 3 mode (horizontal dashed lines) at 1.7 eV. (f) Cross-sections of (a)-(b) at angles where highest sensitivity is observed (vertical dashed lines).

6. Conclusion

We have analyzed, both analytically and numerically, the performance of a metamaterial transducer in sensing applications varying different geometrical and optical parameters such as the refractive indices of host medium, superstrate, and Au as well as the filling factor and height of nanorods. The analytical model shows the increased refractive index sensitivities for higher-order modes (q) and decreasing thickness (l) of the transducer. The numerical model captured the same trend as long as the excited modes are away from the resonant absorption associated with ordinary modes of the metamaterial. The sensitivity to changes in the refractive index of a host medium is much stronger than that of the superstrate refractive index, confirming the important role of the interaction between plasmonic resonances of the nanorod assembly in the sensing performance of the metamaterial. Furthermore, the sensitivity is increased when sensing the analyte's absorption variations.

The variations of reflection and transmission of the metamaterial to changes in the refractive index of Au, which can be induced either via Kerr-nonlinearity of metal or thermal effects, have been shown to be more modest. In the studied purely hyperbolic regime, the metamaterial's response was found to be smaller to Au permittivity modifications (the mode resonance shifts of a few nm/RIU) than that resulting from the similar changes of the refractive index of either the superstrate or the host medium (reaching many hundreds of nm/RIU). Furthermore, the reflection variations were an order of magnitude higher with refractive index changes of a dielectric (reaching several tens of percent) than for the same variations of Au refractive index.

Interestingly, in certain configurations, both TE and TM-modes of the metamaterial transducer have comparable sensitivities, opening up opportunities for polarization multiplexing in sensing experiments. The metamaterial transducer is shown to provide enhanced sensing performance compared to both SPP and LSP-based geometries presented in the literature to date, both in terms of $FoM_{\lambda,I}$ and nm/RIU characteristics achievable. The

#234045 - $15.00 USD Received 25 Mar 2015; revised 6 May 2015; accepted 12 May 2015; published 22 May 2015
© 2015 OSA

above conclusions are valid in the hyperbolic dispersion regime and may be modified if the operating wavelength overlaps the ENZ regime of the metamaterial dispersion. The results can be used as a design strategy to enhance flexibility of ultrasensitive transducers for bio- or chemical sensors or nonlinear photonic devices based on plasmonic hyperbolic metamaterials.

Acknowledgments

This work was supported, in part, by EPSRC (U.K.), the ERC iPLASMM project (321268), and NSF Materials World Network program (grant # DMR-1209761). A.Z. acknowledges support from the Royal Society and the Wolfson Foundation. G.W. acknowledges support from the EC FP7 project 304179 (Marie Curie Actions).

#234045 - $15.00 USD Received 25 Mar 2015; revised 6 May 2015; accepted 12 May 2015; published 22 May 2015
© 2015 OSA

nature COMMUNICATIONS

ARTICLE

Received 16 Feb 2015 | Accepted 5 Jun 2015 | Published 21 jul 2015

DOI: 10.1038/ncomms8757 OPEN

Eliminating material constraints for nonlinearity with plasmonic metamaterials

Andres D. Neira[1], Nicolas Olivier[1], Mazhar E. Nasir[1], Wayne Dickson[1], Gregory A. Wurtz[1] & Anatoly V. Zayats[1]

Nonlinear optical materials comprise the foundation of modern photonics, offering functionalities ranging from ultrafast lasers to optical switching, harmonic and soliton generation. Optical nonlinearities are typically strong near the electronic resonances of a material and thus provide limited tuneability for practical use. Here we show that in plasmonic nanorod metamaterials, the Kerr-type nonlinearity is not limited by the nonlinear properties of the constituents. Compared with gold's nonlinearity, the measured nonlinear absorption and refraction demonstrate more than two orders of magnitude enhancement over a broad spectral range that can be engineered via geometrical parameters. Depending on the metamaterial's effective plasma frequency, either a focusing or defocusing nonlinearity is observed. The ability to obtain strong and fast optical nonlinearities in a given spectral range makes these metamaterials a flexible platform for the development of low-intensity nonlinear applications.

[1] Department of Physics, King's College London, Strand, London WC2R 2LS, UK. Correspondence and requests for materials should be addressed to A.D.N. (email: andres_david.barbosa@kcl.ac.uk).

© 2015 Macmillan Publishers Limited. All rights reserved.

Plasmonic materials, capable of supporting surface plasmon excitations due to the coupling of light to free electrons, provide some of the highest and fastest nonlinearities compared with semiconducting or transparent dielectric materials[1–5]. The strong absorption of optical energy, characteristic of metals, allows an efficient excitation of free electrons leading to a high third-order (Kerr type) optical nonlinearity, which arises from a modification of the electron temperature due to non-equilibrium electron population created by the absorbed light in the conduction band[3–8]. This Kerr-type nonlinearity is expressed as changes in the real and imaginary parts of the refractive index and manifests itself as nonlinear refraction and absorption, respectively. The latter corresponds to the intensity-dependent variation of the material's absorption and the former to the intensity-dependent variation of the phase of the wave as it propagates through the material, leading to focusing (positive nonlinearity) or divergence (negative nonlinearity) of the optical field[1].

For plasmonic materials, both nonlinear absorption and refraction are usually stronger than those of the typical reference nonlinear medium, CS_2, and typical semiconductors such as Si or GaAs[4,9–11]. The strong Kerr nonlinearity of metals is significantly restricted to the spectral range of the interband electronic transitions where efficient electron excitation in the conduction band takes place, leading to the strongest nonlinear response. This nonlinearity becomes weaker at frequencies away from the interband absorption, limiting its usefulness to the (near) ultraviolet spectral range of control light wavelength. On the other hand, the strong absorption near the interband resonance, in many cases, prohibits useful applications when the signal light, which may be controlled by this nonlinearity, overlaps this spectral range.

Plasmonic metamaterials allow engineered light–matter interactions mediated by the plasmonic resonances of their subwavelength constituent elements ('meta-atoms')[12–14]. Different metamaterial realizations have been proposed to design the refractive index and optical properties throughout visible and telecom wavelength range including negative refraction[15] and hyperbolic dispersion[16,17]. These properties have led to the development of numerous applications in sensing[18–21], Purcell factor engineering[22] and all-optical modulation[23–26]. A large nonlinear optical response has been predicted and observed for controlling metamaterials' transmission, reflection and polarization properties with light[27–30]. In most of these approaches, the nonlinear response of the plasmonic metal induced by the interband absorption of a control light was used, and a change of refractive index, strongly diminished away from these transitions, was detected using the metamaterial's ability to act as a sensitive refractive index sensor.

In this work, we go beyond the nonlinearity related to interband transitions in plasmonic metals and show that the plasmonic nanorod metamaterial geometry provides strong nonlinearity, larger than the interband nonlinearity of the plasmonic metal itself, at any *a priori* designed wavelength. We directly measure the third-order nonlinearity of the metamaterial using a femtosecond z-scan technique and show that a positive (focusing) or negative (defocusing) nonlinearity can be achieved by engineering the metamaterial nanostructure in the desired spectral range. The observed enhancement is almost two orders of magnitude larger compared with unstructured Au under interband excitation over a broad spectral range. This opens up opportunities for the on-demand engineering of strong, ultrafast free-electron-based nonlinearities in macroscopic metamaterials.

Results

Linear optical properties. The Au nanorod metamaterial (see Methods for the details of fabrication) displays the typical polarization-dependent transmission resonances (Fig. 1). This behaviour can be reproduced by simulations using an anisotropic permittivity tensor (see Methods for the details on theoretical description and modelling) having diagonal components describing the response to the field polarized perpendicular ($\varepsilon_x = \varepsilon_y$) and along ($\varepsilon_z$) the nanorod axis (Fig. 1b). The extinction spectra exhibits two main features: a resonance at a wavelength of ~550 nm, which has a spectral position invariant with the angle and polarization of the incident light, originates from the interaction of the plasmonic resonances of the nanorods excited perpendicular to their axes, and a resonance at around 600 nm, which can only be excited by light having an electric field component parallel to the nanorod axis and is therefore dependent on the angle of incidence and polarization. The latter arises near the effective plasma frequency of the metamaterial, at which the crossover from elliptic to hyperbolic dispersion regime takes place

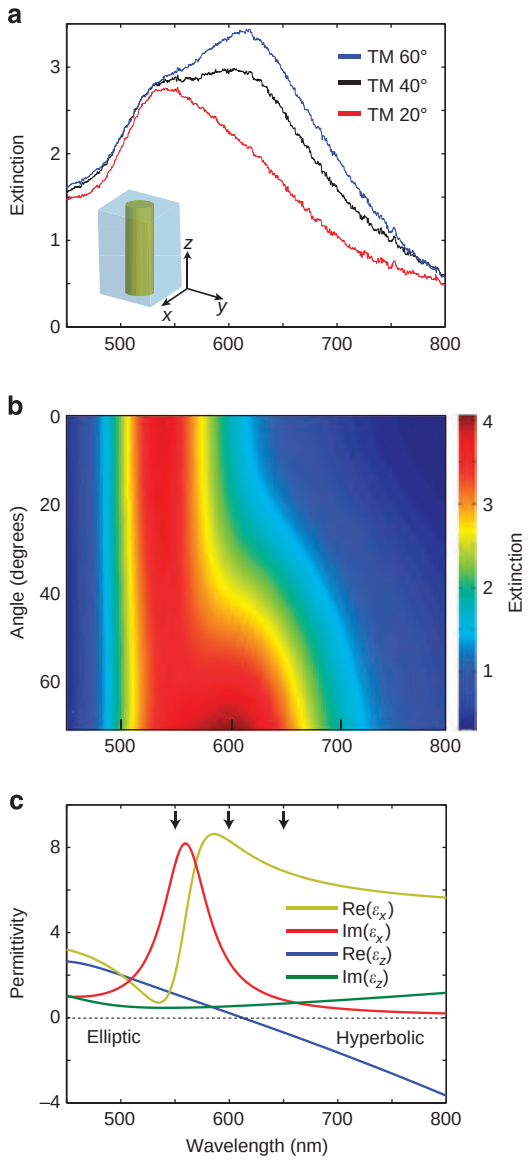

Figure 1 | Plasmonic nanorod metamaterial properties. (**a**) Extinction spectra of the nanorod metamaterial measured at different angles of incidence. (**b**) Simulated extinction dispersion of the metamaterial. (**c**) Effective permittivities of the metamaterial deduced from the effective medium model. Arrows indicate the wavelengths where the nonlinear coefficients were measured.

© 2015 Macmillan Publishers Limited. All rights reserved.

as $\mathrm{Re}(\varepsilon_z)$ transitions from positive to negative values. This frequency can be designed by changing either the geometrical parameters or the plasmonic and dielectric constituents of the metamaterial (see Methods).

Nonlinear optical properties. The third-order nonlinearity of the metamaterial was studied at different angles of incidence and different wavelengths using a femtosecond z-scan technique. Both open and closed aperture measurements (Fig. 2a–d) were performed in a broad spectral range (550–650 nm), covering both the elliptic and hyperbolic regimes of the metamaterial's dispersion, and at different angles of incidence. Similar z-scan measurements were performed in the same conditions for a smooth 50-nm-thick Au film for comparison.

The z-scan allows direct determination of the nonlinear refraction, γ, and absorption, β, coefficients related to the intensity-dependent, complex effective refractive index of the metamaterial $\tilde{n} = n + i\alpha/(2k_0)$, k_0 being the light wave vector and $n(I) = n_0 + \gamma I$ and $\alpha(I) = \alpha_0 + \beta I$, where n_0 and α_0 are the linear refractive index and absorption, respectively, and I is the intensity of the incident light (see Methods for details). As a consequence of the metamaterial's anisotropy, the effective refractive index is angular dependent since $(\tilde{n}(\theta))^2 = \varepsilon_{\mathrm{eff}}(\theta) = (\varepsilon_x\varepsilon_z/(\varepsilon_x \sin^2\theta + \varepsilon_z \cos^2\theta))^{1/2}$, where θ is the angle of propagation within the metamaterial with respect to the nanorod axis. Thus, the retrieved $\gamma(\theta)$ and $\beta(\theta)$ are the effective nonlinear refraction and absorption coefficients corresponding to the variation of the metamaterial's effective linear refractive index for a specific angle of incidence that can be related to the components of the effective third-order nonlinearity tensor of the anisotropic metamaterial (see Methods).

The nonlinear coefficients are very different for a smooth Au film and the Au-based metamaterial both in the value and sign of the nonlinearity (Fig. 2e,f). As expected from their definition, the nonlinear coefficients of the metamaterial are strongly angular dependent, which is especially pronounced near a wavelength of 600 nm, corresponding to the effective plasma frequency. For wavelengths in the elliptic dispersion range ($\lambda < 600$ nm), nonlinear absorption is almost constant, whereas nonlinear refraction that is defocusing for smaller angles, decreases with the incidence angle and changes sign becoming focusing one. In the so-called epsilon near-zero (ENZ) regime with $\mathrm{Re}(\varepsilon_z) \sim 0$ at around 600 nm, both β and γ markedly increase with the incident angle. The largest nonlinearity was experimentally measured in these conditions at an angle of incidence of 60° and at a wavelength close to the effective plasma frequency of the metamaterial: $\gamma \approx -2.4 \times 10^{-11}\,\mathrm{cm^2\,W^{-1}}$ and $\beta \approx -9967\,\mathrm{cm\,GW^{-1}}$. In comparison, the measured nonlinear coefficients for a smooth 50-nm-thick Au film sharply decrease with increasing wavelength

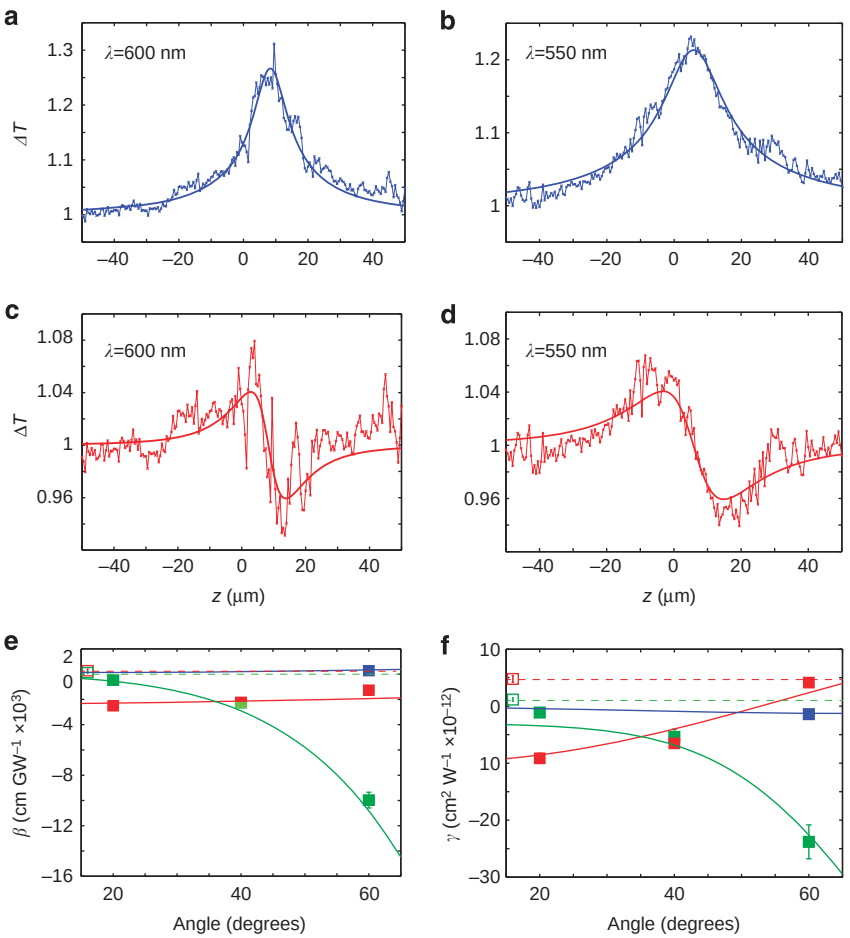

Figure 2 | Nonlinear measurements. (**a**,**b**) Open and (**c**,**d**) closed aperture z-scan measurements (thin lines) and fit (thick lines) at wavelengths near (**a**,**c**) the effective plasma frequency and (**b**,**d**) the Au interband transitions. (**e**) Nonlinear absorption and (**f**) nonlinear refractive index dependence on the angle of incidence for different wavelengths: (squares) experiment, (lines) simulations. Red, 550 nm; green, 600 nm; and blue, 650 nm. Empty squares and dashed lines are for a smooth Au film. All measurements and simulations are for TM-polarized incident light. The errors bars in **e** and **f** are smaller than the size of the square unless indicated.

© 2015 Macmillan Publishers Limited. All rights reserved.

away from the interband transitions with the experimentally measured values $\gamma \approx 4.8 \times 10^{-12}\,\mathrm{cm^2\,W^{-1}}$ and $\beta \approx 272\,\mathrm{cm\,GW^{-1}}$ at 550 nm wavelength and $\gamma \approx 1.2 \times 10^{-12}\,\mathrm{cm^2\,W^{-1}}$ and $\beta \approx 122\,\mathrm{cm\,GW^{-1}}$ at 600 nm wavelength. These values for a smooth Au film are in agreement with those obtained in a previous study using femtosecond pulse excitation[4]. At the same wavelengths, γ and β of the nanorod metamaterial are approximately 20 and 100 times larger than those measured for a smooth Au film. Surprisingly, the maximum value obtained for γ and β for the metamaterial away from Au interband transitions is approximately 5 and 40 times larger than the maximum values measured for a smooth gold film close to the interband transition where they are highest. While in the studied range of frequencies, the nonlinearity of smooth Au is always positive (induced absorption and focusing), the Au nanorod metamaterial can provide either induced absorption, transparency, focusing or defocusing nonlinearity, depending on the combination of light wavelength and angle of incidence. Thus, not only the strength but also the sign of the nonlinearity can be designed.

Discussion

On the basis of the above experimental observations, the dominating contributions of the effective third-order susceptibility components can be identified (see Methods):

$$\varepsilon_{\mathrm{eff}}(\theta_{\mathrm{i}}) \approx \varepsilon^{0}_{\mathrm{eff}}(\theta_{\mathrm{i}}) + 3\varepsilon_{\mathrm{m}}\sin^2(\theta_{\mathrm{i}})E_0^2\left(\frac{\chi^{(3)}_{xxzz}}{\varepsilon_{xx}} + \frac{\chi^{(3)}_{zzzz}}{\varepsilon_{zz}}\right), \qquad (1)$$

where $\chi^{(3)}_{xxzz}$ and $\chi^{(3)}_{zzzz}$ are the components of the third-order nonlinear susceptibility tensor of the metamaterial, dominant for the incident transverse magnetic (TM) light, ε_{m} is the permittivity of the medium adjacent to the metamaterial where the incident wave is coming from, θ_{i} is the angle of incidence, and E_0 is the incident electric field amplitude. As seen from equation (1), the linear anisotropy of the metamaterial can strongly enhance the nonlinear response, particularly when the linear permittivity tensor components become small, as in the case of the ENZ regime.

To understand the nonlinear response of the metamaterial, full-vectorial numerical simulations of the nonlinear optical processes were performed taking into account the internal structure of the metamaterial and the change in the Au permittivity on absorption of the energy from the optical excitation pulse (as described in Methods). We consider that the excitation pulse is absorbed by the metallic nanorods comprising the metamaterial due to the interband or intraband transitions, depending on the excitation wavelength (the anodic alumina oxide (AAO) matrix is considered as non-absorbing). This induces an imbalance between the electron and lattice temperature in the metal nanorods. The excited electrons then relax back to the ground state as a consequence of energy exchange via electron–electron and electron–phonon scattering. Taking into account these processes, the electron temperature variations under the excitation pulse can be calculated depending on its energy and duration, and, thus, the intensity-dependent effective refractive index of the metamaterial can be evaluated, in turn allowing the effective nonlinear coefficients γ and β to be deduced under different excitation wavelengths and incident angles. To validate the model, the nonlinearity of a smooth 50-nm-thick Au film was also simulated and provided excellent agreement with the experimental data (Fig. 3a,b), showing a high nonlinearity at wavelengths shorter than 560 nm near the interband transition of gold. These values are also in a good agreement with the known values of third-order nonlinearity of Au films for similar pulse durations[4].

The simulations for both the smooth film and the metamaterial provide excellent agreement with the measured data in terms of both the observed trends and absolute values of the nonlinear coefficients. Near the metamaterial's absorption resonance ($\sim$550 nm), β is constant and negative for all angles of incidence (Fig. 3c), whereas γ decreases, changing its sign from negative to positive at a given angle (Fig. 3d). On the other hand, near the effective plasma frequency, both β and γ are negative and increase with increasing angle of incidence. It should be noted that the simulations using the nonlinear transfer matrix method and effective medium description of the metamaterial, which

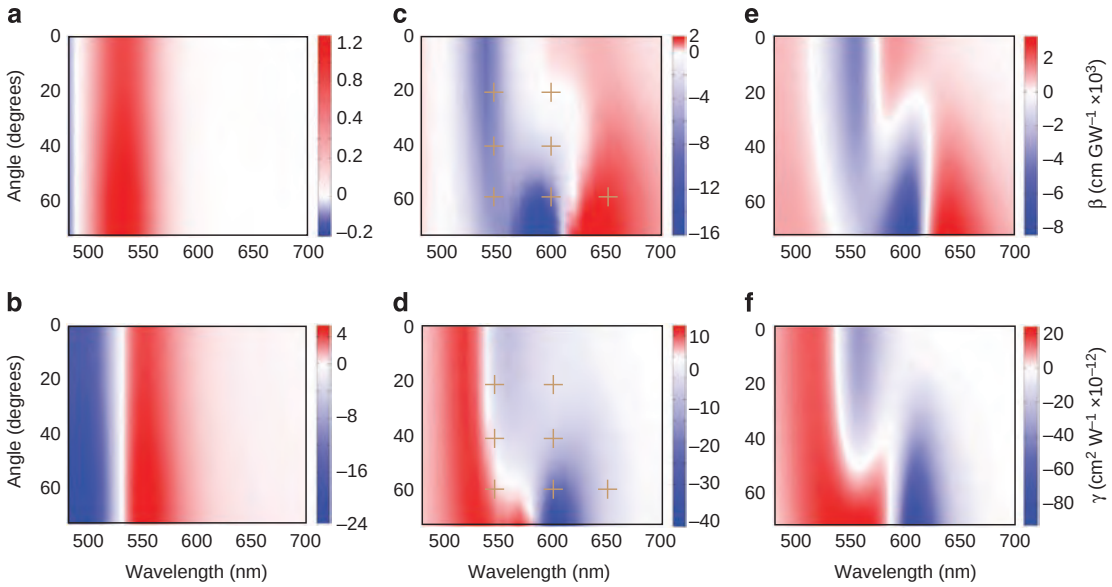

Figure 3 | Nonlinear response model. Nonlinear absorption and refraction coefficients for a smooth gold film and the nanorod array metamaterial calculated using finite element method (**a**–**d**) and the effective medium theory (**e**,**f**): (**a**,**c**,**e**) nonlinear absorption and (**b**,**d**,**f**) nonlinear refractive index simulated for (**a**,**b**) the smooth 50-nm-thick gold film and (**c**–**f**) the nanorod metamaterial. The crosses indicate the points where the experimental data are presented in Fig. 2.

© 2015 Macmillan Publishers Limited. All rights reserved.

does not take into account nonlocal effects[31] or the inhomogeneous distribution of the electron temperature in the nanorods, describe similar spectral and angular behaviour but with underestimated values of the nonlinear coefficients (Fig. 3).

The highest third-order nonlinear response has been observed near the ENZ conditions, corresponding to the effective plasma frequency of the metamaterial[32]. This frequency can be tuned as desired by engineering the metamaterial's geometrical structure with the same constituent materials, and therefore a strong nonlinear response can be achieved at the wavelengths where the constituent materials have negligible nonlinearity. As an example, a nonlinear metamaterial has been designed for the telecommunication spectral range 1–1.6 μm in which Au has negligible nonlinear response (Fig. 4). This has been accomplished by adjusting only the nanorod diameter to achieve an effective plasma frequency at a wavelength of approximately 1.35 μm. Interestingly, despite significantly lower absorption, the observed nonlinear refraction and absorption are only three and five times smaller, respectively, than those of the metamaterial designed for the visible spectral range where the nonlinearity of Au is much stronger. The spectral and angular dependencies of the nonlinear response are similar to those for the visible spectral range, determined by the effective plasma frequency (cf. Figs 3 and 4).

In the ENZ and hyperbolic regimes, the dependence on the angle of incidence is significant since the ε_z component plays a dominating role (Figs 3 and 4). In contrast, in the elliptic regime, the nonlinearity is mainly governed by the value of $\mathrm{Re}(\varepsilon_x)$ and, therefore, the respective nonlinear absorption and refraction are almost invariant with the incident angle. A strong nonlinearity, either focusing ($\gamma > 0$) or defocusing ($\gamma < 0$) can be designed using the metamaterial irrespective of the type of nonlinearity of the constituent materials and the operating wavelength (Figs 3 and 4). As can be observed, the sign of the nonlinear refraction coefficient changes while crossing the effective plasma frequency, providing positive nonlinearity at shorter wavelength (elliptic regime) and negative nonlinearity at longer wavelength (hyperbolic regime). At the same time, the nonlinear refraction (γ) of Au is positive below the interband transition ($\lambda > 550$ nm), while in the case of the metamaterial this coefficient is now negative and becomes positive only at large angles of incidence for wavelengths shorter than that of the effective plasma frequency (Figs 3c,d and 4c,d) reaching an experimentally measured maximum negative value of $\gamma \approx -2.38 \times 10^{-11}$ $\mathrm{cm^2\,W^{-1}}$ and a maximum positive value of $\gamma \approx 4.1 \times 10^{-12}$ $\mathrm{cm^2\,W^{-1}}$. In the case of nonlinear absorption, which is always positive in the spectral range below the interband transitions for a smooth Au film, a strong induced nonlinear transparency ($\beta < 0$) is observed in the elliptic dispersion range, yet strong induced absorption ($\beta > 0$) is present in the hyperbolic regime.

Looking beyond nonlinearities of plasmonic metals, nonlinear transparent dielectrics, such as beta barium borate, lithium triborate or lithium niobate exhibit a weak and broadband third-order nonlinear susceptibility throughout visible and telecom spectral range, which is typically smaller than the nonlinearity of Si at telecom wavelengths[33]. These nonlinearities are typically more than three orders of magnitude smaller than the one observed for Au nanorod-based metamaterials. Semiconductor materials, such as GaAs, exhibit higher nonlinearity which near interband transitions, is only one order of magnitude lower than these metamaterials in a similar spectral range[11]. An interesting example is graphene, which provides a nonlinear response similar to the plasmonic metamaterial in the infrared and the visible[34]. Indeed, graphene and transparent dielectrics provide a broadband nonlinear response throughout the visible and infrared spectral range, with semiconducting materials exhibiting a more narrowband nonlinearity limited to the interband transition wavelength range. The nonlinear response of the nanorod metamaterial (Figs 3 and 4) has also a broader spectral range than typical for semiconductors and metamaterials based on split-ring resonators.

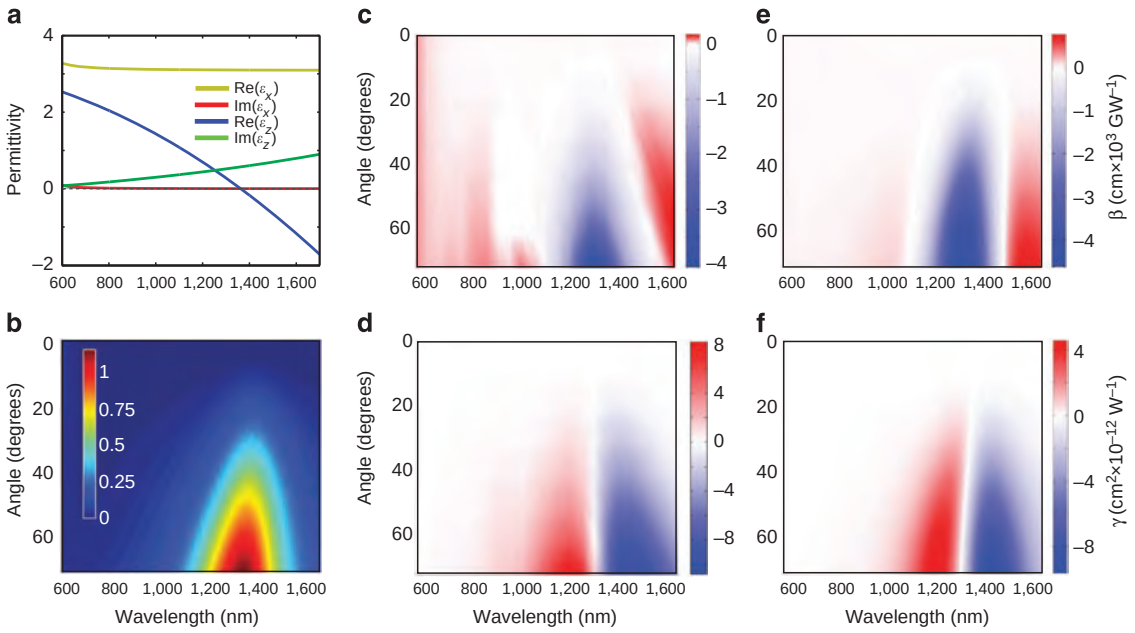

Figure 4 | Tuning the third-order nonlinearity of the metamaterial. (**a**) Effective permittivity spectra of a nanorod metamaterial designed with the effective plasma frequency at around $\lambda = 1.35$ μm (ENZ regime at the telecommunication spectral range). (**b**) Linear extinction dispersion of the metamaterial in **a**. Nonlinear absorption (**c**,**e**) and refraction (**d**,**f**) coefficients calculated using finite element method (**c**,**d**) and EMT (**e**,**f**) of the metamaterial with the parameters as in **a**. Metamaterial consists of Au nanorods of 150-nm height and 17-nm diameter arranged in a square array of 95-nm period embedded in AAO matrix.

© 2015 Macmillan Publishers Limited. All rights reserved.

The enhanced nonlinearity of nanorod metamaterials arises from the specific dispersion of plasmonic metamaterials that results in vanishingly small permittivity components (equation (1)). Such hyperbolic metamaterials can in principle also be designed using highly doped semiconductors in certain frequency ranges and, thus, the nonlinearity of semiconductors can be harnessed via a similar mechanism as in the metamaterials described here. ENZ-enhanced nonlinearities have been recently measured via third-harmonic generation spectroscopy (which is related to third-order susceptibility components) in natural (unstructured) ENZ material indium tin oxide[35]. Similarly, an enhancement of the third-harmonic generation efficiency has been observed in Si nanodisks due to magnetic dipole resonance excitation in individual disks[36]. While the underpinning mechanisms are different than in the discussed nanorod metamaterials, these nonlinearities can be used for designing nonlinear metamaterials to further enhance their nonlinear response and achieve further spectral tuneability.

In conclusion, we have shown that the enhanced focusing ($\gamma > 0$) or defocusing ($\gamma < 0$) nonlinearity and associated induced absorption ($\beta > 0$) or transparency ($\beta < 0$) of Au nanorod-based metamaterials can be designed irrespective of the type of nonlinearity of the constituent materials and their resonant nonlinear response. Thus, strong nonlinearity can be achieved in metamaterials at wavelengths where negligible nonlinearity of the constituent materials exists. Since the temporal response of plasmonic nonlinearities are on the order of few hundreds femtoseconds depending on wavelength and absorbed power, they allow the possibility to modulate light at ultrafast rates exceeding 1 THz[2,5,23,25]. Furthermore, this nonlinearity can be tuned in a broad range of wavelengths through the design of the metamaterial's dimensions. Therefore, the metamaterial can be suitable for spectrally demanding applications, including those at telecom wavelengths, removing the conventional reliance on the electronic transition resonances of conventional nonlinear materials, and providing the freedom to design strongly nonlinear materials at any frequency of interest and choose the sign of the nonlinearity to achieve either focusing or defocusing of light. While optical absorption of plasmonic metamaterials is higher than for dielectric or semiconductor nonlinear materials due to presence of metal, the observed ultrafast nonlinearities that are stronger by three to four orders of magnitude are advantageous for nano- and microscale nonlinear components, which can be integrated into Si photonic circuitry or optical fibres providing designer nonlinear functionalities.

Methods

Sample preparation. Plasmonic nanorod metamaterials were fabricated via Au electrodeposition into nanoporous AAO templates on a glass substrate. An Al film of 800 nm thickness was deposited on a substrate by magnetron sputtering. The substrate comprises a glass cover slip with a 10-nm-thick adhesive layer of tantalum pentoxide and a 7-nm-thick Au film acting as a weakly conducting layer. Highly ordered, nanoporous AAO was synthesized by a two-step anodization in 0.3 M oxalic acid at 40 V. After an initial anodization process, the porous layer formed was removed by etching in a solution of H_3PO_4 (3.5%) and CrO_3 (20 gl^{-1}) at 70 °C. An ordered, patterned surface was obtained after removal of the porous layer formed during first step of anodization. Then, the samples were anodized again under the same conditions as in the first step. The anodized AAO was subsequently etched in 30 mM NaOH to achieve pore widening and remove the barrier layer. Gold electrodeposition was performed with a three-electrode system using a non-cyanide solution. The length of nanorods was controlled by the electrodeposition time. The topography variations of the top surface of the samples are below 10 nm, similar to other samples fabricated with the same approach[32]. The nanorod array parameters used in this work are about 150-nm height, 50-nm diameter and 95-nm period. For comparison, Au films of 50 nm thickness deposited using magnetron sputtering on similar substrates were measured.

Z-scan measurements. An amplified Ti:sapphire femtosecond laser was used to pump an optical parametric amplifier to achieve light pulses in a wavelength range between 500 and 750 nm. These pulses are sent first to a prism-based pulse compression system, which induces negative dispersion to compensate for the dispersion in both the optical parametric amplifier and the experimental setup. A 0.28 numerical aperture objective lens focuses the 50-fs pulse to a spot having a radius of $\sim 1.5\,\mu$m on the sample. The peak power at the focus was $\sim 80\,\mathrm{GW\,cm^{-2}}$. The metamaterial is then scanned across the focus of the beam over a 100-μm range (Supplementary Fig. 1). The fluencies used are within the range used in the other studies of similar nanorod metamaterials[17] and the measured signals were repeatable and reversible in all instances, thus the damage threshold has not been reached in the experiments. The transmission through the sample is then determined from the measurement of the intensities incident on two InGaAs photodiodes having a bandwidth range from 500 to 1,700 nm, for every position of the sample. The z-scan measurements were performed in the so-called closed and open aperture regimes by opening or closing the aperture after the sample[9]. The measurements were performed using either s- or p-polarized light chosen by rotating a half-wave plate. The measurements were taken in pairs at low and high light intensities, and the normalization between these two measurements was performed to average out possible variations of linear transmission (for example, due to roughness or defects) when a sample is z-scanned[9].

Nonlinear coefficients retrieval from z-scan measurements. The intensity-dependent refractive index $n(I)$ and absorption $\alpha(I)$ are defined as

$$n(I) = n_0 + \gamma I, \tag{2}$$

$$\alpha(I) = \alpha_0 + \beta I, \tag{3}$$

where n_0 and α_0 are the linear refractive index and absorption, respectively, β and γ are the nonlinear refraction and absorption coefficients, and I is the intensity of incident light. The coefficients γ and β are related to the real and imaginary part of the third-order nonlinear susceptibility $\chi^{(3)}$ through

$$\frac{\tilde{n}_0 n_0}{283}\left(\gamma + i\frac{\beta}{2k_0}\right) = \chi^{(3)}\left(\mathrm{m^2\,V^{-2}}\right), \tag{4}$$

where $\tilde{n}_0 = n_0 + i\alpha_0/(2k_0)$ is the complex refractive index and $k_0 = 2\pi/\lambda_0$ is the wave vector related to the wavelength in vacuum (λ_0). As a consequence of the metamaterial's anisotropy, the retrieved γ and β are the effective nonlinear refraction and absorption corresponding to the variation of the metamaterial's effective linear refractive index for a specific angle of incidence.

In the open aperture regime (Fig. 2a,b), all the transmitted intensity through the metamaterial is measured. Thus, variations in the transmission only correspond to the nonlinear absorption of the metamaterial, being strongest at the focus and smallest away from it. A positive peak-shaped dependence corresponds to a negative value of β (nonlinear transparency).

In the close aperture regime (Fig. 2c,d), only part of the intensity transmitted through the metamaterial is measured in a specific direction. Thus, variations in the transmission correspond to both nonlinear absorption and self-focusing or defocusing caused by the nonlinear refraction. Therefore, in the closed aperture regime, the transmission variations depend on both β and γ. A dependence solely determined by γ can be obtained by normalizing the close aperture curve with the open aperture curve obtained before. The curves in Fig. 2c,d correspond to a self-divergence of the transmitted beam related to a negative value of γ (defocusing nonlinearity).

Assuming a beam with a Gaussian spatial profile transverse to the scanning direction, the transmission in the case of open aperture is:

$$T_{\mathrm{oa}}(z) = 1 - \frac{\Delta\psi}{1+x^2}, \tag{5}$$

where $x = z/z_0$ and $z_0 = kw^2$ with $k = 2\pi/\lambda$, and $\Delta\psi = 1/2\sqrt{2}(\beta I_0 L)$ with I_0 being the peak intensity at the metamaterial's surface and L is the sample thickness. In the case of close aperture, the transmission after the aperture is

$$T_{\mathrm{ca}}(z) = 1 + \frac{4x\Delta\phi}{(x^2+9)(x^2+1)} - \frac{2(x^2+3)\Delta\psi}{(x^2+9)(x^2+1)}, \tag{6}$$

where $\Delta\phi = (1-S)^{0.25}k\gamma I_0 L$ with S representing the transmission through the aperture. For very small apertures $S \to 0$, this expression can be simplified as $\Delta\phi = k\gamma I_0 L$. Therefore, by fitting the experimentally obtained open and close aperture z-scan transmission profiles with equations (5) and (6), the nonlinear parameters γ and β can be found[1].

The complex effective third-order nonlinear susceptibility obtained from the measured values of β and γ is $\chi^{(3)} \approx (0.18\text{–}1.48i) \times 10^{-17}\,\mathrm{m^2\,V^{-2}}$ at a wavelength of 550 nm and an angle of incidence of 20°, and $\chi^{(3)} \approx (0.28\text{–}1.48i) \times 10^{-16}\,\mathrm{m^2\,V^{-2}}$ at a wavelength of 600 nm and an angle of incidence of 60°, compared with a smooth 50-nm-thick Au film, which is $\chi^{(3)} \approx (-0.09 + 1.19i) \times 10^{-19}\,\mathrm{m^2\,V^{-2}}$ and $\chi^{(3)} \approx (-0.5 + 1.08i) \times 10^{-19}\,\mathrm{m^2\,V^{-2}}$ at wavelength of 550 and 600 nm, respectively, in agreement with known values for smooth gold measured in this range of pulse duration[4]. The metamaterial's nonlinear susceptibility is up to three orders of magnitude larger than that for gold films, with a maximum theoretical value $\chi^{(3)} \approx (0.57\text{–}3.2i) \times 10^{-16}\,\mathrm{m^2\,V^{-2}}$ at a wavelength of 600 nm obtained for the metamaterial at an angle of incidence of 70°.

© 2015 Macmillan Publishers Limited. All rights reserved.

Modelling the optical response of the metamaterial. Anisotropic metamaterials based on nanorod arrays can be described through the effective medium theory with a diagonal anisotropic permittivity tensor

$$\hat{\varepsilon} = \begin{pmatrix} \varepsilon_x & 0 & 0 \\ 0 & \varepsilon_x & 0 \\ 0 & 0 & \varepsilon_z \end{pmatrix}, \tag{7}$$

where the subscripts x and z indicate the components perpendicular and parallel to the nanorod axis, respectively. The components of this tensor are the function of the nanorod dimensions and can be evaluated through the effective medium theory[37]. These are plotted in Fig. 1c for the metamaterial studied.

For a plane wave propagating within the metamaterial at an angle θ to the nanorod axes ($\mathbf{z}$ direction) and polarized perpendicular to them (TE polarization), the effective permittivity of the nanorod array is represented by ε_x. However, if the light has an electric field component along the nanorod axis (TM polarization), the electric field of the wave propagating within the metamaterial is $\mathbf{E} = E_x\mathbf{i} + E_z\mathbf{k} = E_0 \cos\theta\mathbf{i} + E_0 \sin\theta\mathbf{k}$, where E_0 is the amplitude of the electric field. Therefore, the effective permittivity depends on θ and is determined through[38]

$$\varepsilon_{\text{eff}} = \frac{\varepsilon_x \varepsilon_z}{\varepsilon_x \sin^2\theta + \varepsilon_z \cos^2\theta}. \tag{8}$$

The effective permittivity components can derived from the Maxwell Garnet effective medium approximation for a given set of metamaterial's geometrical parameters as[37]

$$\begin{aligned} \varepsilon_x &= \varepsilon_{\text{out}} \frac{(1+N)\varepsilon_{\text{in}} + (1-N)\varepsilon_{\text{out}}}{(1+N)\varepsilon_{\text{out}} + (1-N)\varepsilon_{\text{in}}}, \\ \varepsilon_z &= N\varepsilon_{\text{in}} + (1-N)\varepsilon_{\text{out}}, \end{aligned} \tag{9}$$

where ε_{out} and ε_{in} are the permittivities of the matrix (in this case an AAO matrix having permittivity of 2.89) and of the nanorods (the intensity-dependent permittivity of Au), respectively, and $N = \pi r^2/p^2$ is the concentration of nanorods defined via their radius r and period p of the array. The transfer matrix method[39] was used to model the transmission spectra and plot the extinction dispersion (Fig. 1b). The modelled dispersion is in a good agreement with the experimental measurements as well as the dispersion numerically simulated using finite element modelling taking into account microscopic structure of the metamaterial.

Modelling the intensity-dependent permittivity of Au. The gold permittivity is modelled within the random phase approximation that includes the dependence of the electron scattering on both electron (T_e) and lattice (T_L) temperatures[8]. Within this approximation, the intensity-dependent permittivity of Au can be described as the sum of the intraband permittivity and interband permittivity $\varepsilon = \varepsilon_{\text{inter}} + \varepsilon_{\text{intra}}$, which are dependent on the electron's intraband (transitions within the conduction band) and interband (transitions from the d-band to the conduction sp-band) transitions, respectively. The latter term can be reduced to a Drude-like model as

$$\varepsilon_{\text{intra}} = \varepsilon_\infty - \frac{\omega_p^2}{\omega(\omega + i\gamma_{\text{intra}}(\omega, T_L, T_e)}, \tag{10}$$

where $\omega_p = 2.168 \times 10^{15}\,\text{rad}\,\text{s}^{-1}$, $\varepsilon_\infty \sim 1$ is the high-frequency limit of the permittivity, and $\gamma_{\text{intra}}(\omega,T_L,T_e)$ is due to both electron–electron and electron–phonon scattering. The interband contribution can be expressed as[6,40]

$$\varepsilon_{\text{inter}} = K \int_0^\infty \frac{\sqrt{\hbar x - E_g}}{x}(1 - f(x, T_e)) \frac{(\gamma_{\text{inter}}(\omega, T_L, T_e)^2 - \omega^2 + x^2) + 2i\omega\gamma_{\text{inter}}(\omega, T_L, T_e)}{(\gamma_{\text{inter}}(\omega, T_L, T_e)^2 - \omega^2 + x^2)^2 + 4\gamma_{\text{inter}}(\omega, T_L, T_e)^2\omega^2} dx, \tag{11}$$

where $K = 1.2695 \times 10^{32}$ is the wave vector independent constant reflecting the strength of the transition dipole moment for interband transitions, $E_g = 1.98$ eV is the transition energy between the d- and the sp-bands, $f(x,T_e)$ is the Fermi–Dirac distribution for the electrons at an equilibrium temperature T_e and depends on the Fermi level $E_f = 2.43$ eV and the quasiparticle (electron-hole) scattering for interband transitions $\gamma_{\text{inter}}(\omega,T_L,T_e)$, which also depends on electron and lattice temperatures. In addition, as a consequence of the nanorods fabrication procedure, the mean free path of electrons is reduced from the bulk value L to a restricted value R using the following correction term[38]

$$\varepsilon_r = \varepsilon_{\text{Au}} + \frac{i\omega_p^2\tau(L-R)}{\omega(\omega\tau + i)(\omega\tau R + iL)}, \tag{12}$$

where ε_{Au} is the permittivity of bulk gold obtained from the sum of equations (10) and (11), $L = 35.7$ nm and $R = 15$ nm is derived to fit the measured extinction shown in Fig. 1b. For the simulations of the nonlinear response of a sputtered thin Au film, $R = L$ was used to recover the bulk Au permittivity.

The steady-state electron temperature reached in the nanorods as a result of optical absorption of the transmitted beam is calculated from the energy stored by the electrons $E_s(t)$, under the optical pulse excitation with an input intensity $I_i(t)$. Therefore, the variation in the stored energy is proportional to the energy absorbed by the nanorods in a given interval dt:

$$\frac{dE_s(t)}{dt} = A(E_s(t))I_i(t), \tag{13}$$

where $A(E_s(t))$ is the sample absorption and depends on the energy stored since this one is related to the electron temperature through

$$E_s(t) = \frac{1}{2}C_e T_e(t)^2 V_{\text{rods}}, \tag{14}$$

where C_e is the heat capacity of the electron gas and V_{rods} is the total volume of the rods under excitation and depends on the beam diameter. Equation (14) assumes a homogeneous electron temperature in the nanorod and a short exciting pulse such that the electron temperature is not reduced via electron–phonon scattering processes while the pulse propagates through the nanorods. Since these processes are significant at a timescale of few picoseconds, under femtosecond pulse excitation this assumption holds[8]. Equation (13) is solved numerically in the time domain calculating the term $A(E_s(t))$ with the transfer matrix method using equations (8–11) to calculate the intensity-dependent effective refractive index of the nanorod array. From these results, both the nonlinear refraction and absorption can be obtained (Figs 3e,f and 4e,f).

Numerical modelling of the nonlinear optical response of metamaterial. The optical properties of the plasmonic metamaterial were simulated using the finite element method (FEM, Comsol Multiphysics 4.3a), which accounts for the composite structure of the metamaterial. Furthermore, to also account for the non-homogeneous distribution of the electron temperature in the rods under optical excitation, the two-temperature model[8] is also solved through FEM together with Maxwell's equations. This model relates the phonon temperature (T_L) and the electron temperature (T_e) through:

$$\begin{aligned} C_e T_e \frac{\partial T_e}{\partial t} &= \nabla \cdot (K_e \nabla T_e) - g(T_e - T_L) + \omega_0 \text{Im}(\varepsilon_{Au})\langle \mathbf{E}(r,t) \cdot \mathbf{E}(r,t)\rangle \\ C_L \frac{\partial T_L}{\partial t} &= g(T_e - T_L), \end{aligned} \tag{15}$$

where $C_e = 67.96\,\text{J}\,\text{m}^{-3}\,\text{K}^{-2}$ is the heat capacity of electrons, $g = 2 \times 10^{16}\,\text{W}\,\text{m}^{-3}\,\text{K}^{-1}$ is a constant related to the coupling between electrons and phonons, $\langle \mathbf{E}(r,t) \cdot \mathbf{E}(r,t)\rangle$ is the average over time of electric field, the $K_e = K_{e0} T_e T_e / T_L$ is the electron heat diffusion with $K_{e0} = 318\,\text{W}\,\text{m}^{-1}\,\text{K}^{-1}$ and C_L is the heat capacity for a lattice[41]. The results obtained using FEM for the nonlinear absorption and refraction are shown in (Figs 3c,d and 4c,d).

Analysis of the effective $\chi^{(3)}$ susceptibility tensor of the metamaterial. Due to the anisotropic nature of the metamaterial, which acts as an uniaxial crystal with the extraordinary axis along the nanorods, the effective permittivity and thus nonlinear susceptibility are tensors. Therefore, the measured effective angular-dependent nonlinear refractive index and absorption can be expressed via the angular-independent components of the nonlinear susceptibility tensors in the similar manner as the angular-dependent permittivity is presented by equation (8). The intensity-dependent complex refractive index of the nanorod metamaterial can be analysed by the effective $\chi^{(3)}$ susceptibility. The displacement field is then[1]

$$D_i = \varepsilon_0 \sum_{jkl} \left(\varepsilon_{ij}^0 + 3\chi_{ijkl}^{(3)} |E_k E_l|\right) E_j, \tag{16}$$

where ε_0 is the vacuum permittivity, $E_{j,k,l}$ is the component of the electric field amplitude in j, k or l directions and is the complex linear permittivity. Equation (16) can be rewritten as $D_i = \varepsilon_0 \sum_j \varepsilon_{ij} E_j$, where

$$\varepsilon_{ij} = \varepsilon_{ij}^0 + 3\sum_{kl} \chi_{ijkl}^{(3)} |E_k E_l|. \tag{17}$$

In our case, the linear anisotropic components are $\varepsilon_{xx} = \varepsilon_{yy} = \varepsilon_x \neq \varepsilon_{zz} = \varepsilon_z$, and the incident wave is TM polarized. Therefore, equation (17) becomes

$$\varepsilon_{ii} = \varepsilon_{ii}^0 + 3E_0^2 \left(\chi_{iizz}^{(3)} \sin^2(\theta) + \chi_{iixx}^{(3)} \cos^2(\theta) + \chi_{iixz}^{(3)} \sin(\theta)\cos(\theta)\right). \tag{18}$$

In the case of the elliptic dispersion of the metamaterial for which there is a weak angular dependence for both γ and on the angle of incidence observed in the experiment and numerical modelling, we can conclude that both the contributions from both $\chi_{iixx}^{(3)}$ and $\chi_{iizz}^{(3)}$ are present, since the sum of these contributions has a vanishing angular dependence. However, in the ENZ and hyperbolic regimes, the nonlinear coefficients strongly depend on the angle, and the main contribution comes from component $\chi_{iizz}^{(3)}$. The contribution of components $\chi_{iixz}^{(3)}$ is negligible, since the angular dependences of γ and β do not follow $\sin(2\theta)$ dependence. Thus, the dominating effective nonlinear anisotropic tensor components correspond to

$$\begin{aligned} \varepsilon_{xx} &= \varepsilon_{xx}^0 + 3\chi_{xxzz}^{(3)} \sin^2(\theta) E_0^2 \\ \varepsilon_{zz} &= \varepsilon_{zz}^0 + 3\chi_{zzzz}^{(3)} \sin^2(\theta) E_0^2. \end{aligned} \tag{19}$$

Replacing in equation (8) each nonlinear anisotropic component with

© 2015 Macmillan Publishers Limited. All rights reserved.

equation (19), we obtain the effective nonlinear permittivity

$$\varepsilon_{\mathrm{eff}}(\theta) \approx \frac{\left(\varepsilon_{xx}^{0}+3\chi_{xxzz}^{(3)}\sin^2\theta E_0^2\right)\left(\varepsilon_{zz}^{0}+3\chi_{xxzz}^{(3)}\sin^2\theta E_0^2\right)}{\left(\varepsilon_{xx}^{0}+3\chi_{xxzz}^{(3)}\sin^2\theta E_0^2\right)\sin^2\theta+\left(\varepsilon_{zz}^{0}+3\chi_{xxzz}^{(3)}\sin^2\theta E_0^2\right)\cos^2\theta}. \quad (20)$$

To a first approximation, we can assume that the nonlinear terms in the denominator of equation (20) can be negligible in comparison with the sum of the linear terms and neglect the terms in order of $(E_0)^4$:

$$\varepsilon_{\mathrm{eff}}(\theta) \approx \varepsilon_{\mathrm{eff}}^{0}(\theta)\left(1+3\sin^2\theta\right)E_0^2\left(\frac{\chi_{xxzz}^{(3)}}{\varepsilon_{xx}}+\frac{\chi_{zzzz}^{(3)}}{\varepsilon_{zz}}\right)+\ \ldots \quad (21)$$

We can make an additional approximation assuming again that the nonlinear terms are small compared with the linear term and, thus, Snell's law can be written linearly as $\varepsilon_{\mathrm{eff}}(\theta)\sin^2\theta=\varepsilon_{\mathrm{eff}}^{0}(\theta)\sin^2\theta=\varepsilon_{\mathrm{m}}\sin^2\theta_{\mathrm{i}}$, where ε_{m} is the permittivity of the medium where the incident wave is coming from and θ_{i} is the angle of incidence. Therefore, we can rewrite equation (21) as

$$\varepsilon_{\mathrm{eff}}(\theta_{\mathrm{i}}) \approx \varepsilon_{\mathrm{eff}}^{0}(\theta_{\mathrm{i}})+3\varepsilon_{\mathrm{m}}\sin^2\theta_{\mathrm{i}}E_0^2\left(\frac{\chi_{xxzz}^{(3)}}{\varepsilon_{xx}}+\frac{\chi_{zzzz}^{(3)}}{\varepsilon_{zz}}\right). \quad (22)$$

One can observe that the peculiarity of the linear anisotropy can strongly enhance the effective nonlinearity, particularly if a linear permittivity component approaches zero. Equation (22) provides an understanding of the strong enhancement of the metamaterial's optical nonlinearity near the ENZ wavelength (Figs 3 and 4).

References

1. Boyd, R. W. *Nonlinear Optics.* 3rd edn (Academic Press, 2008).
2. Kauranen, M. & Zayats, A. V. Nonlinear plasmonics. *Nat. Photonics* **6,** 737–748 (2012).
3. Rotenberg, N., Betz, M. & van Driel, H. M. Ultrafast all-optical coupling of light to surface plasmon polaritons on plain metal surfaces. *Phys. Rev. Lett.* **105,** 017402 (2010).
4. Boyd, R. W., Shi, Z. & De Leon, I. The third-order nonlinear optical susceptibility of gold. *Opt. Commun.* **326,** 74–79 (2014).
5. MacDonald, K. F., Samson, Z. L., Stockman, M. I. & Zheludev, N. I. Ultrafast active plasmonics. *Nat. Photonics* **3,** 55–58 (2009).
6. Bigot, J. Y., Merle, J. Y., Cregut, O. & Daunois, A. Electron dynamics in copper metallic nanoparticles probed with femtosecond optical pulses. *Phys. Rev. Lett.* **75,** 4702–4705 (1995).
7. Kohlgraf-Owens, D. C. & Kik, P. G. Numerical study of surface plasmon enhanced nonlinear absorption and refraction. *Opt. Express* **16,** 10823–10834 (2008).
8. Jiang, L. & Tsai, H.-L. Improved two-temperature model and its application in ultrashort laser heating of metal films. *J. Heat Transfer* **127,** 1167–1173 (2005).
9. Sheik-Bahae, M., Said, A. A., Wei, T. H., Hagan, D. J. & Van Stryland, E. W. Sensitive measurement of optical nonlinearities using a single beam. *IEEE J. Quantum Electron.* **26,** 760–769 (1990).
10. Dinu, M., Quochi, F. & Garcia, H. Third-order nonlinearities in silicon at telecom wavelengths. *Appl. Phys. Lett.* **82,** 2954–2956 (2003).
11. Villeneuve, A. *et al.* Nonlinear absorption in a GaAs waveguide just above half the band gap. *IEEE J. Quantum Electron.* **30,** 1172–1175 (1994).
12. Soukoulis, C. M. & Wegener, M. Past achievements and future challenges in the development of three-dimensional photonic metamaterials. *Nat. Photonics* **5,** 523–530 (2011).
13. Husu, H. *et al.* Metamaterials with tailored nonlinear optical response. *Nano Lett.* **12,** 673–677 (2012).
14. Tsai, K.-T. *et al.* Looking into meta-atoms of plasmonic nanowire metamaterial. *Nano Lett.* **14,** 4971–4976 (2014).
15. Pendry, J. B. Negative refraction makes a perfect lens. *Phys. Rev. Lett.* **85,** 3966–3969 (2000).
16. Poddubny, A., Iorsh, I., Belov, P. & Kivshar, Y. Hyperbolic metamaterials. *Nat. Photonic* **7,** 948–957 (2013).
17. Drachev, V. P., Podolskiy, V. A. & Kildishev, A. V. Hyperbolic metamaterials: new physics behind a classical problem. *Opt. Express* **21,** 15048–15064 (2013).
18. Kabashin, A. V. *et al.* Plasmonic nanorod metamaterials for biosensing. *Nat. Mater.* **8,** 867–871 (2009).
19. Yakovlev, V. V. *et al.* Ultrasensitive non-resonant detection of ultrasound with plasmonic metamaterials. *Adv. Mater.* **25,** 2351–2356 (2013).
20. Nasir, M. E., Dickson, W., Wurtz, G. A., Wardley, W. P. & Zayats, A. V. Hydrogen detected by the naked eye: optical hydrogen gas sensors based on core/shell plasmonic nanorod metamaterials. *Adv. Mater.* **26,** 3532–3537 (2014).
21. Liu, N., Mesch, M., Weiss, T., Hentschel, M. & Giessen, H. Infrared perfect absorber and its application as plasmonic sensor. *Nano Lett.* **10,** 2342–2348 (2010).
22. Krishnamoorthy, H. N. S., Jacob, Z., Narimanov, E., Kretzschmar, I. & Menon, V. M. Topological transitions in metamaterials. *Science* **336,** 205–209 (2012).
23. Ren, M. *et al.* Nanostructured plasmonic medium for terahertz bandwidth all-optical switching. *Adv. Mater.* **23,** 5540–5544 (2011).
24. Neira, A. D., Wurtz, G. A., Ginzburg, P. & Zayats, A. V. Ultrafast all-optical modulation with hyperbolic metamaterial integrated in Si photonic circuitry. *Opt. Express* **22,** 10987–10994 (2014).
25. Wurtz, G. A. *et al.* Designed ultrafast optical nonlinearity in a plasmonic nanorod metamaterial enhanced by nonlocality. *Nat. Nanotechnol.* **6,** 107–111 (2011).
26. Nikolaenko, A. E. *et al.* Carbon nanotubes in a photonic metamaterial. *Phys. Rev. Lett.* **104,** 153902 (2010).
27. Xiao, S. *et al.* Loss-free and active optical negative-index metamaterials. *Nature* **466,** 735–738 (2010).
28. Moitra, P. *et al.* Realization of an all-dielectric zero-index optical metamaterial. *Nat. Photonics* **7,** 791–795 (2013).
29. Ginzburg, P. *et al.* Manipulating polarization of light with ultrathin epsilon-near-zero metamaterials. *Opt. Express* **21,** 14907–14917 (2013).
30. Ren, M., Plum, E., Xu, J. & Zheludev, N. I. Giant nonlinear optical activity in a plasmonic metamaterial. *Nat. Commun.* **3,** 833 (2012).
31. Wells, B. M., Zayats, A. V. & Podolskiy, V. A. Nonlocal optics of plasmonic nanowire metamaterials. *Phys. Rev. B* **89,** 035111 (2014).
32. Vasilantonakis, N., Nasir, M. E., Dickson, W., Wurtz, G. A. & Zayats, A. V. Bulk plasmon-polaritons in hyperbolic nanorod metamaterial waveguides. *Laser Photonics Rev.* **9,** 345–353 (2015).
33. Dmitriev, V. G., Gurzadyan, G. G. & Nikogosyan, D. N. *Handbook of Nonlinear Optical Crystals* (Springer, 1991).
34. Yang, H. *et al.* Giant two-photon absorption in bilayer graphene. *Nano Lett.* **11,** 2622–2627 (2011).
35. Capretti, A., Wang, Y., Engheta, N. & Dal Negro, L. Enhanced third-harmonic generation in Si-compatible epsilon-near-zero indium tin oxide nanolayers. *Opt. Lett.* **40,** 1500–1503 (2015).
36. Shcherbakov, M. R. *et al.* Enhanced third-harmonic generation in silicon nanoparticles driven by magnetic response. *Nano Lett.* **14,** 6488–6492 (2014).
37. Elser, J., Wangberg, R., Podolskiy, V. A. & Narimanov, E. E. Nanowire metamaterials with extreme optical anisotropy. *Appl. Phys. Lett.* **89** (2006).
38. Atkinson, R. *et al.* Anisotropic optical properties of arrays of gold nanorods embedded in alumina. *Phys. Rev. B* **73,** 235402 (2006).
39. Ekgasit, S., Thammacharoen, C. & Knoll, W. Surface plasmon resonance spectroscopy based on evanescent field treatment. *Anal. Chem.* **76,** 561–568 (2003).
40. Pines, D. *Elementary Excitations in Solids: Lectures on Protons, Electrons, and Plasmons* (Perseus Books, 1999).
41. Hohlfeld, J. *et al.* Electron and lattice dynamics following optical excitation of metals. *Chem. Phys.* **251,** 237–258 (2000).

Acknowledgements

This work was supported, in part, by EPSRC (UK), the ERC iPLASMM project (321268), and US Army Research Office (W911NF-12-1-0533). A.Z. acknowledges support from the Royal Society and the Wolfson Foundation. G.W. acknowledges support from the EC FP7 project 304179 (Marie Curie Actions).

Author contributions

A.D.N. and A.V.Z. developed the idea; M.E.N. and W.D. fabricated the samples; A.D.N. and N.O. performed the measurements; and A.D.N and G.A.W. performed the modelling. All authors analysed the data and prepared the manuscript.

Additional information

Supplementary Information accompanies this paper at http://www.nature.com/naturecommunications

Competing financial interests: The authors declare no competing financial interests.

Reprints and permission information is available online at http://npg.nature.com/reprintsandpermissions/

How to cite this article: Neira, A.D. *et al.* Eliminating material constraints for nonlinearity with plasmonic metamaterials. *Nat. Commun.* 6:7757 doi: 10.1038/ncomms8757 (2015).

This work is licensed under a Creative Commons Attribution 4.0 International License. The images or other third party material in this article are included in the article's Creative Commons license, unless indicated otherwise in the credit line; if the material is not included under the Creative Commons license, users will need to obtain permission from the license holder to reproduce the material. To view a copy of this license, visit http://creativecommons.org/licenses/by/4.0/

© 2015 Macmillan Publishers Limited. All rights reserved.

Published on 16 October 2014. Downloaded by University of Massachusetts - Lowell on 26/05/2015 21:17:43.

Faraday Discussions

Cite this: *Faraday Discuss.*, 2015, **178**, 61

PAPER

View Article Online
View Journal | View Issue

Light emission in nonlocal plasmonic metamaterials

Viktor A. Podolskiy,*[a] Pavel Ginzburg,[bc] Brian Wells[a] and Anatoly V. Zayats[b]

Received 30th September 2014, Accepted 16th October 2014
DOI: 10.1039/c4fd00186a

We present analytical and computational studies of light emission in nonlocal metamaterials formed by arrays of aligned plasmonic nanowires. We demonstrate that the emission lifetime in these composites is a complex function of geometrical and material parameters of the system that cannot be reduced to the "trivial" hyperbolic or elliptical dispersion topology of a homogenised metamaterial. In particular, our studies suggest that the Purcell factor can often be maximized when the composite operates in the elliptic regime, with strong radiation coupling to an additional TM-polarized mode supported by the nonlocal composite, in contrast to the accepted "hyperbolicity related" enhancement.

1. Introduction

Metamaterials, composites designed from dissimilar components of sub-wavelength size, offer new avenues for controlling light generation, propagation, and absorption.[1,2] Recently, plasmonic nanowire arrays have emerged as flexible platforms for confinement and manipulation of optical pulses at deep sub-wavelength scale, along with applications in negative refraction, sensing, and non-linear optics.[3] It has been demonstrated, experimentally and numerically, that the optical response of these composites is strongly affected by the spatial dispersion of the effective permittivity – the dependence of components of the permittivity tensor on a wavevector.[4] Analytical description of optical nonlocality in nanowire arrays has recently been developed.[5] In particular, it was shown that optical nonlocality yields an additional wave, an extra TM-polarized optical mode, that has hyperbolic-like properties at frequency ranges where the main TM wave has elliptic dispersion. In this work, we use the nonlocal effective medium theory to analyse the emission of point dipoles in nanowire media and show that non-locality significantly affects light emission in metamaterials, enhancing the

[a]*Department of Physics and Applied Physics, University of Massachusetts Lowell, One University Ave., Lowell, MA, 01854, USA. E-mail: viktor_podolskiy@uml.edu*
[b]*Department of Physics, Kings College London, Strand, London WC2R 2LS, UK*
[c]*ITMO University, St. Petersburg 197101, Russia*

Published on 16 October 2014. Downloaded by University of Massachusetts - Lowell on 26/05/2015 21:17:43.

photonic density of states in the elliptic regime, in contrast with previous theoretical proposals[6] that predict that Purcell enhancement is maximized in the hyperbolic regime. We relate the apparent contradiction to the excitation of plasmonic modes in metamaterial constituents, missed in the local effective medium theory, and argue that the nonlocal effective medium theory provides a more adequate description of the underlying physics.

The manuscript is organized as follows – we first describe the modal structure of the nanowire metamaterial and provide the relationship between the geometrical parameters of the metamaterial, its spatially dispersive permittivity, and dispersion of the optical modes in the composite. The developed nonlocal effective medium theory (EMT) allows solving the boundary condition problem for plane wave incidence. We then employ the plane wave decomposition of a dipolar emitter for the calculation of spontaneous emission rates *via* classical-quantum correspondence and the formalism of the radiation reaction force.

2. Nonlocal optical response of nanowire media

2.1. Optical modes supported by nanowire metamaterials

Plasmonic nanowire arrays represent collections of aligned metallic wires (with permittivity ε_i and average radius r) embedded into a dielectric host (permittivity ε_h) with mean centre-to-centre separation a. Nanowire metamaterials typically operate in the effective medium regime where $r < a \ll \lambda_0$, with $\lambda_0 = 2\pi c/\omega$ being the free-space wavelength, ω being the angular frequency of optical radiation, and c being the speed of light in vacuum. In this regime, the optical properties of the composite may be well described by averaged geometric parameters (concentration $p = \pi r^2/a^2$; [here $p \ll 1$] and, in the case of nonlocal effective medium theory, the shape of the unit cell) and are weakly affected by the details of wire distribution (variations of the wire radius or unit cell size across the composite). In this work, we follow the approach introduced in ref. 5 and consider nanowire metamaterials having square unit cells (see Fig. 1).

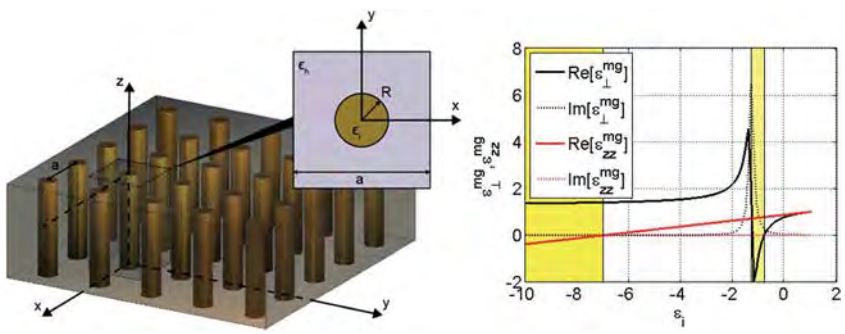

Fig. 1 Geometry of the nanowire composite (left) and the local effective medium parameters (right); $\mathrm{Im}(\varepsilon_i) = 0.1$; shaded areas represent the spectral range where the metamaterial operates in the hyperbolic regime; when $\varepsilon_i \gtrsim -1$, the metamaterial is local; an additional wave exists for $\varepsilon_i \lesssim -1$; this wave propagates inside the metamaterial for $-7 \lesssim \varepsilon_i \lesssim -1$ (the main wave has elliptical dispersion); when $\varepsilon_i \lesssim -7$, the longitudinal wave exponentially decays along the wires, while the main wave has hyperbolic dispersion.

 This journal is © The Royal Society of Chemistry 2015

Published on 16 October 2014. Downloaded by University of Massachusetts - Lowell on 26/05/2015 21:17:43.

As follows from symmetry considerations, nanowire metamaterials have an uniaxial anisotropic response with an optical axis parallel to the wires ($\hat{z}$ axis in this work). In the Cartesian coordinates used in this work, the effective permittivity tensor is diagonal, with components $\varepsilon_{xx} = \varepsilon_{yy} = \varepsilon_{\perp}$, $\varepsilon_{zz} \neq \varepsilon_{\perp}$. In the quasistatic limit, the Maxwell Garnett effective medium theory predicts the following relation between the effective permittivity $\varepsilon^{\mathrm{mg}}$, the permittivities of the components of the composite, and the geometrical parameters of the metamaterial:

$$\varepsilon_{\perp}^{\mathrm{mg}} = \varepsilon_{\mathrm{h}} \frac{(1+p)\varepsilon_{\mathrm{i}} + (1-p)\varepsilon_{\mathrm{h}}}{(1+p)\varepsilon_{\mathrm{h}} + (1-p)\varepsilon_{\mathrm{i}}}; \quad \varepsilon_{zz}^{\mathrm{mg}} = p\varepsilon_{\mathrm{i}} + (1-p)\varepsilon_{\mathrm{h}} \tag{1}$$

As any uniaxial material, the modes supported by the infinite nanowire metamaterial can be characterized according to their polarization. The modes of the first kind, often referred to as ordinary waves or transverse-electric (TE)-polarized waves, have their electric field in the xy plane. Propagation of these waves is not affected by the metamaterial anisotropy and is completely determined by the $\varepsilon_{\perp}$ component of the permittivity tensor.

In contrast to this behaviour, propagation of the waves that have a non-vanishing component of the electric field in the $\hat{z}$ direction is (strongly) affected by the material anisotropy. Depending on the relationship between ε_{i}, ε_{h}, and p, these extraordinary (TM polarized) modes have elliptic (when $\varepsilon_{\perp}^{\mathrm{mg}} \times \varepsilon_{zz}^{\mathrm{mg}} > 0$) or hyperbolic (when $\varepsilon_{\perp}^{\mathrm{mg}}\, \varepsilon_{zz}^{\mathrm{mg}} < 0$) dispersion (see Fig. 1).

In addition to these transverse electromagnetic waves, a plasmonic nanowire metamaterial may support propagation of longitudinal electromagnetic waves that represent coupled cylindrical surface plasmon (CSP) waves propagating along the wires. As shown in ref. 5, dispersion of these waves can be related to the solution of the eigenvalue problem with eigenvalues and eigenvectors representing propagation constants (k_z^{l}) and sets of amplitudes, respectively, describing contributions of individual cylindrical waves propagating in the nanowires of the composite to the coupled CSP modes. These CSP modes do not exist when wires are dielectric ($\varepsilon_{\mathrm{i}} > 0$), they propagate in the plasmonic elliptic regime ($\varepsilon_{zz}^{\mathrm{mg}} > 0$, $\varepsilon_{\mathrm{i}} < -\varepsilon_{\mathrm{h}}$); and exponentially decay along the wires in the hyperbolic regime ($\varepsilon_{zz}^{\mathrm{mg}} < 0$). In the limit of PEC wires ($\varepsilon_{\mathrm{i}} \to -\infty$), the propagation constant of the longitudinal wave approaches the limit $k_z^{\mathrm{l}} \to n_{\infty}^{\mathrm{l}}\omega/c$.

From the effective medium standpoint, the same dispersion relation can be written as $\varepsilon_{zz}(k_z, \omega/c) = 0$ with

$$\varepsilon_{zz}(k_z) = \xi\left(k_z{}^2 - k_z^{\mathrm{l}^2}\right)\frac{c^2}{\omega^2}; \quad \xi = p\frac{\varepsilon_{\mathrm{i}} + \varepsilon_{\mathrm{h}}}{\varepsilon_{\mathrm{h}} - \left(n_{\infty}^{\mathrm{l}}\right)^2}\ . \tag{2}$$

Note that the spatial dispersion, the explicit dependence of the permittivity on the wavevector, is a necessary condition for the existence of the longitudinal electromagnetic wave.

Although transverse electromagnetic waves that enter the nanowire material at normal incidence cannot couple to a longitudinal mode, light that obliquely enters the metamaterial can couple to both longitudinal and transverse modes. In a strict effective medium approach, light propagating inside the metamaterial should be represented as a linear combination of three modes. The first of these

Published on 16 October 2014. Downloaded by University of Massachusetts - Lowell on 26/05/2015 21:17:43.

modes is an ordinary TE wave, described above, whilst the other two represent a mix of the "local" transverse TM and "nonlocal" longitudinal waves. Dispersion of these two waves and the relative contributions of "local" and "nonlocal" components are given by the coupled-oscillator-like expression,

$$\left(k_z{}^2 - k_z^{l^2}\right)\left(k_z{}^2 - \varepsilon_\perp^{\mathrm{mg}}\frac{\omega^2}{c^2}\right) = -\frac{\varepsilon_\perp^{\mathrm{mg}}}{\xi}\frac{\omega^2}{c^2}\,k_x{}^2. \tag{3}$$

To better illustrate our results, in this work we have fixed the operating wavelength and geometric parameters of the metamaterial, the permittivity of the dielectric host medium, and varied the permittivity of the wire inclusions. For the set of parameters used in this work ($r = 20$ nm, $a = 100$ nm, $\varepsilon_\mathrm{h} = 1$, $\lambda_0 = 1.5$ μm), the epsilon near-zero (ENZ) transition occurs at $\varepsilon_\mathrm{i} \simeq -7$ with the elliptic regime realized for $\varepsilon_\mathrm{i} > -7$, and the hyperbolic regime realized for $\varepsilon_\mathrm{i} < -7$ (see Fig. 1 for predictions of local EMT). Dispersions of the three modes propagating inside the nanowire material are shown in Fig. 2. Note that in the regime when the main TM mode is elliptic, the additional wave has hyperbolic-like dispersion.

2.2. Transmission and reflection of light into nonlocal nanowire metamaterials

To understand the transmission and reflection of optical waves by nanowire metamaterials with finite thickness, the solutions to Maxwell's equations in each of the bulk layers are represented as linear combinations of (plane) waves that differ by their polarization and direction (towards the interface or away from the interface; see Fig. 3). The amplitudes of the waves in the neighbouring regions are then related to each other *via* boundary conditions. This relationship is then used to calculate the amplitudes of the waves propagating away from the interface as a function of the amplitude of the waves propagating towards the interface. Such linear relationship between the amplitudes can be conveniently represented in terms of the scattering (S-) matrix.

In conventional local materials, it suffices to enforce the continuity of tangential components of electric and magnetic fields to calculate the S-matrix of the interface. In nonlocal metamaterials, the existence of an additional (TM-

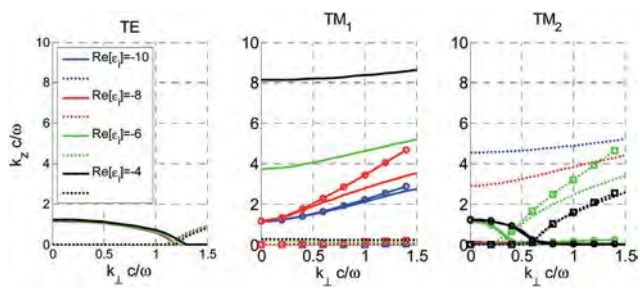

Fig. 2 Dispersion of the three waves supported by the metamaterial for different permittivities of the nanowires: (solid line) Re[$k_z c/\omega$], (dashed line) Im[$k_z c/\omega$], (symbols) dispersion of the "main" TM-polarized mode according to local EMT. All other parameters as in Fig. 1.

 This journal is © The Royal Society of Chemistry 2015

Published on 16 October 2014. Downloaded by University of Massachusetts - Lowell on 26/05/2015 21:17:43.

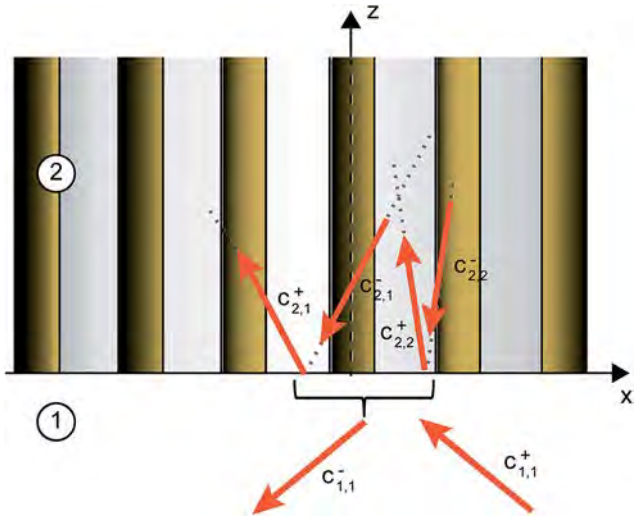

Fig. 3 Schematic of light reflection and transmission at the interface between local and nonlocal media.

polarized) mode requires the introduction of additional boundary conditions (ABCs). Here, we used the methodology of ref. 5 and used the continuity of the tangential electric field, the continuity of the normal electric displacement, and the continuity of the first moment of normal electric displacement (the product of $D(x)\exp 2\pi ix/a$, averaged over the unit cell) to calculate the S-matrix of each interface in the system.

3. Light emission in nanowire metamaterials

In this work, we have followed the well-developed technique that relates the enhancement in the decay rate of the dipole to the regular part of the field generated by this dipole at the origin. Explicitly,

$$\frac{\Gamma}{\Gamma_0} \simeq \frac{3}{2} \frac{\mathrm{Im}(\vec{E}\cdot\vec{P})}{\omega^3|P|^2} \tag{4}$$

where $\vec{E}$ represents the field generated by the point dipole $\vec{P}$. The main objective of this work is to analyse the enhancement of the decay rate in plasmonic nanowire composites and to relate this enhancement to spectral properties of the composites. It is worth noting that placing a dipole directly inside ideal hyperbolic or realistic (lossy) materials leads to unphysical singularities.[7,8] Various real or virtual cavity approaches have been suggested to address the impact of the surrounding media on a host emitter.[9] To address these key issues, in this work we have removed the singularity inside the hyperbolic metamaterial by limiting the wavevector spectrum used in the calculations of the field $\vec{E}$ in eqn (4) and by employing the following three-step strategy that allows us to address the issue of material absorption.

Published on 16 October 2014. Downloaded by University of Massachusetts - Lowell on 26/05/2015 21:17:43.

First, we calculated the emission of the point dipole inside hypothetical, lossless, metamaterial. Predictions of both local and nonlocal effective medium theories were analysed, with two TM-polarized modes in nonlocal metamaterials taken as two competing decay channels.

Second, the emission of the point 3D dipole positioned in the small (vacuum-filled) slit surrounded by two infinite slabs of hypothetical lossless metamaterial was analysed. Combined with the first step, these calculations allow us to estimate geometry-dependent local-field-correction effects.[10] Local field correction is the frequently employed technique to account for the arrangement of the emitter and the host matrix. It is worth noting that the geometry of the artificially created cavity could affect the spontaneous emission rate; here we have used the slit geometry, approaching its physical dimensions to zero thickness.

Finally, we calculated the emission of the point dipole positioned in the small vacuum slit surrounded by lossy metamaterial and used the local field correction, estimated above, to calculate the modulation of the dipole lifetime due to the metamaterial.

3.1. Plane wave expansion of Green's function in an homogeneous material

To calculate the modification of a dipole lifetime, we represented Green's function for the anisotropic metamaterial as a set of plane waves, and used eqn (4) to calculate the modification of the dipole lifetime. Since we are considering the emission inside the anisotropic material, the field generated by the dipole needs to be separated into TE and TM-polarized components.

It can be explicitly shown[10] that the field of the $\hat{z}$ polarized dipole is TM-polarized, with the regular part of $E_z^{\mathrm{TM}} = \mathrm{i}P\varepsilon_\perp \int_0^{k^{\max}} k^3 \mathrm{d}k/(k_z \varepsilon_{zz}{}^2)$, where the integration parameter k represents the in-plane component of the wavevector. In this work, we have taken into account the fact that any effective medium theory fails in the limit when $k \simeq \pi/a$. We therefore constrained the integral above to the range of wavevectors inside the first Brillouin zone of our metamaterial, $k < k^{\max} = \pi/a$.

On the other hand, the $\hat{x}$ polarized dipole emits both TE- and TM-polarized waves, with amplitudes yielding the plane-wave expansion of the field: $E_x^{\mathrm{TM}} = \mathrm{i}P \int_0^{k^{\max}} k_z k \, \mathrm{d}k/(2\varepsilon_\perp)$, and $E_x^{\mathrm{TE}} = \mathrm{i}P \int_0^{k^{\max}} \omega^2 k \, \mathrm{d}k/(2c^2 k_z)$. Due to the uniaxial symmetry of the problem, the y-component of the electric field generated by a y-polarized dipole is identical to the E_x generated by a $\hat{x}$-polarized dipole.

3.2. Emission in lossless metamaterials and local field correction analysis

We began by analysing the emission of a point dipole positioned inside an infinite material described by the local effective medium parameters given by eqn (1), keeping in mind the high-wavevector cut-off due to the finite unit cell size. The results of these calculations are shown in Fig. 4. It is seen that, in agreement with previous studies,[6] the local effective medium theory suggests that the enhancement of the photonic density of states can be linked to (i) plasmon resonance in the wires (corresponding to $\varepsilon_{\mathrm{i}} \simeq -1$) and (ii) the broadband spectral range starting from ENZ ($\varepsilon_{\mathrm{i}} \simeq -7$) and continuing through

 This journal is © The Royal Society of Chemistry 2015

Published on 16 October 2014. Downloaded by University of Massachusetts - Lowell on 26/05/2015 21:17:43.

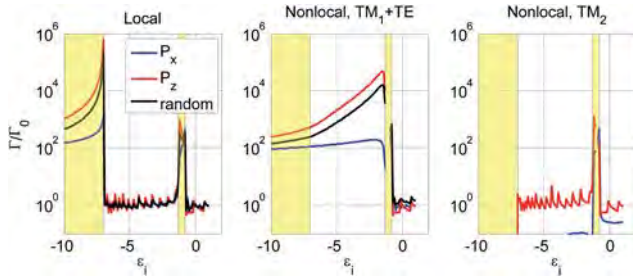

Fig. 4 Enhancement of the decay rate in infinite lossless metamaterials (lines of different colours represent different orientations of the dipole).

the hyperbolic regime of the metamaterial dispersion ($\varepsilon_i < -7$). Interestingly, the ENZ regime seems to provide the maximum reduction of the lifetime.

Calculations of the lifetime modifications were repeated for a situation when a point dipole is positioned inside the homogeneous material described by the nonlocal EMT model [eqn (2) and (3)]. In this case, we assumed that the dipole can independently emit into two TM-polarized channels. As seen in Fig. 4, predictions of the nonlocal EMT drastically differ from predictions of its local counterpart. The main difference, the dramatic enhancement of the decay rate in the elliptic regime can be traced to the existence of an additional electromagnetic mode, originating from the collective excitation of CSPs in the nanowire composite. Note that the hyperbolic-like CSP-rich mode (mode TM_1 in Fig. 2) dominates the emission across both elliptic and hyperbolic regimes. Also note that the nonlocality removes the singularity associated with ENZ regime (at $\varepsilon_i \simeq -7$).

To analyse the emission of the dipole in realistic, lossy, metamaterials, it becomes necessary to place the dipole inside a substantially small cavity carved in the homogeneous material. In this work, we have assumed that the cavity takes the shape of a small planar slit, oriented perpendicular to the wires. The emission of the point dipole was calculated according to the plane-wave expansion, described above, incorporated into the transfer-matrix formalism, as suggested in ref. 11.

For substantially small slit sizes (below ~10 nm), the enhancement of decay rate becomes independent of the slit size due to the high-wavevector k_{max} cut-off described earlier. Furthermore, for a local metamaterial, it becomes possible to eliminate local field correction effects by renormalizing the emission of $\hat{z}$-polarized dipole by $1/(\varepsilon_{zz}^{mg})^2$ (Fig. 5). Similarly, renormalization of the emission of the $\hat{z}$-polarized dipole by $1/\varepsilon_{zz}(k)^2$ positioned inside the slit carved in the nonlocal metamaterial also yields results that qualitatively agree with the total decay rate calculated for a dipole positioned inside the nonlocal medium (the exact nature of the resonance predicted by the nonlocal EMT in the ENZ region will be addressed in our future work). Therefore, we have used the above normalization to take into account local field correction effects.

3.3. Effect of finite material absorption

Finally, we calculated the decay rate of the dipole positioned in the slit between two slabs of lossy nanowire metamaterial with $\mathrm{Im}(\varepsilon_i) = 0.1$ (Fig. 6). As expected,

Published on 16 October 2014. Downloaded by University of Massachusetts - Lowell on 26/05/2015 21:17:43.

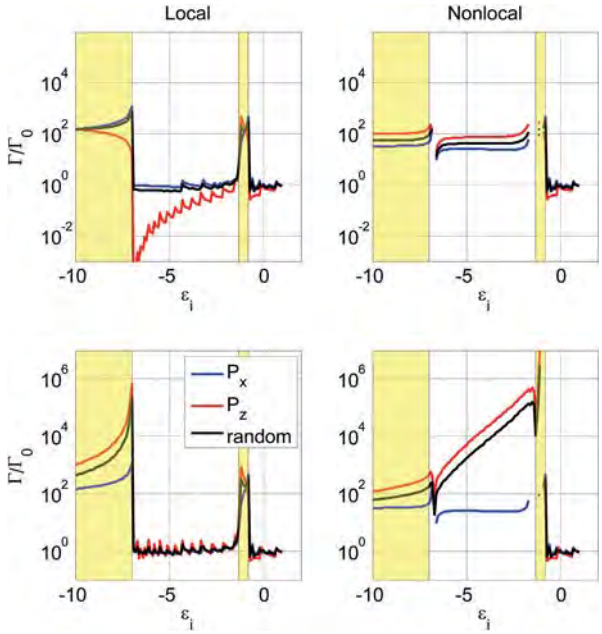

Fig. 5 Emission of the point dipole positioned in the vacuum slit inside the lossless nanowire metamaterial; top and bottom rows correspond, respectively, to results of calculations that are not and are accounted for local field corrections.

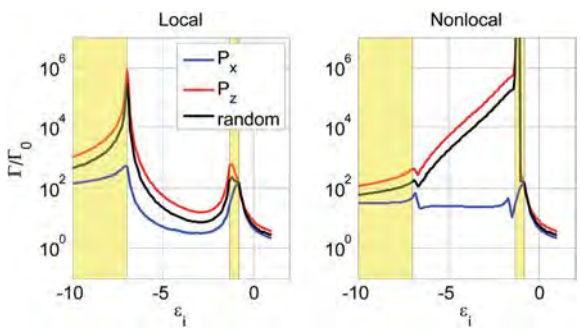

Fig. 6 Enhancement of decay rate in metamaterials with finite losses; the plots take into account local field corrections; $\mathrm{Im}(\varepsilon_i) = 0.1$; see Fig. 1 for effective medium parameters.

the presence of material absorption does not fundamentally alter the dynamics of the emission. In general, an increase in $\mathrm{Im}(\varepsilon_i)$ leads to further enhancement of the decay rate throughout the "plasmonic" spectral range ($\varepsilon_i < -\varepsilon_h$).

4. Discussion

It is clear that predictions by local and nonlocal effective medium theories regarding the enhancement of the decay rate for a dipole emitting inside nanowire metamaterials disagree with each other. It is therefore reasonable to ask which (if any) theory accurately predicts the response of the dipole in real

 This journal is © The Royal Society of Chemistry 2015

Published on 16 October 2014. Downloaded by University of Massachusetts - Lowell on 26/05/2015 21:17:43.

metamaterials. The fundamental reason for the disagreement between the predictions of the two effective medium theories lies in the existence of an additional wave in nonlocal EMT. The existence of this additional wave has been validated in both full-wave numerical solutions of Maxwell's equations in nanowire composites and in experimental studies.[4,5] It is therefore reasonable to assume that nonlocal EMT adequately describes the emission inside the composite. Our main results can be interpreted in the following intuitive manner: the fundamental change in the density of optical states in a nanowire medium is associated not with the onset of hyperbolicity, but rather with the onset of the plasmonic response in the nanowires.

A similar effect is expected in layered materials with low fill-fraction where the layer's transition to plasmonic response is spectrally separated from the composite's transition to hyperbolicity. It should also be mentioned that, in realistic nanowire composites, the enhancement of the decay rate will be affected by standing wave Fabry–Perot type resonances.

5. Conclusions

We have analysed the enhancement of the decay rate of the dipole emitting inside a plasmonic nanowire composite. Predictions of the nonlocal effective medium response, previously demonstrated to adequately describe refraction in nanowire composites,[5] suggest a significant enhancement of the decay rate across the spectral range where nanowires are plasmonic and, in particular, across the spectral range where the composite as a whole exhibits elliptic response.

Acknowledgements

This research was supported by US Army Research Office (Grant #W911NF-12-1-0533), EPSRC (UK), and the ERC iPLASMM project (321268). A. Z. acknowledges support from the Royal Society and the Wolfson Foundation.

References

1 *Tutorials in Metamaterials*, ed. M. Noginov and V. A. Podolskiy, CRC press, 2012.

2 Z. Jacob, L. V. Alekeyev and E. Narimanov, *Opt. Express*, 2006, **14**, 8247; A. Salandrino and N. Engheta, *Phys. Rev. B: Condens. Matter Mater. Phys.*, 2006, **74**, 075103; J. B. Pendry, D. Schurig and D. Smith, *Science*, 2006, **312**, 1780; W. Cai, U. K. Chettiar, A. V. Kildishev and V. M. Shalaev, *Nat. Photonics*, 2007, **1**, 224; R. W. Ziolkowski, *Phys. Rev. E: Stat., Nonlinear, Soft Matter Phys.*, 2004, **70**, 046608; N. Engheta, *Science*, 2013, **340**, 286.

3 A. Kabashin, P. Evans, S. Pastkovsky, W. Hendren, G. A. Wurtz, R. Atkinson, R. Pollard, V. A. Podolskiy and A. V. Zayats, *Nat. Mater.*, 2009, **8**, 867; G. A. Wurtz, R. Pollard, W. Hendren, G. P. Wiederrecht, D. J. Gosztola, V. A. Podolskiy and A. V. Zayats, *Nat. Nanotechnol.*, 2011, **6**, 107.

4 P. A. Belov, R. Marques, S. I. Maslovski, I. S. Nefedov, M. Silverinha, C. R. Simovski and S. A. Tretyakov, *Phys. Rev. B: Condens. Matter Mater. Phys.*, 2003, **67**, 113103; A. L. Pokrovsky and A. L. Efros, *Phys. Rev. B: Condens. Matter Mater. Phys.*, 2002, **65**, 045110; M. Silverinha, *Phys. Rev. E:*

Published on 16 October 2014. Downloaded by University of Massachusetts - Lowell on 26/05/2015 21:17:43.

Stat., Nonlinear, Soft Matter Phys., 2006, **73**, 046612; R. J. Pollard, A. Murphy, W. R. Hendren, P. R. Evans, R. Atkinson, G. A. Wurtz, A. V. Zayats and V. A. Podolskiy, *Phys. Rev. Lett.*, 2009, **102**, 127405; K.-T. Tsai, G. Wurtz, J.-Y. Chu, T.-Y. Cheng, H.-H. Wang, A. Krasavin, J.-H. He, B. Wells, V. A. Podolskiy, J.-K. Wang, Y.-L. Wang and A. Zayats, *Nano Lett.*, 2014, **14**, 4971.

5 B. Wells, A. Zayats and V. A. Podolskiy, *Phys. Rev. B: Condens. Matter Mater. Phys.*, 2014, **89**, 035111.

6 Z. Jacob, I. Smolyaninov and E. Narimanov, *Proc. Front. in Opt*, 2009, PDPB6; H. N. S. Krishnamoorthy, Z. Jacob, E. Narimanov, I. Kretzschman and V. M. Menon, *Science*, 2012, **336**, 205; O. Kidwai, S. Zhukovsky and J. E. Sipe, *Opt. Lett.*, 2011, **36**, 2530; C. I. Cortes, W. Newman, S. Molesky and Z. Jacob, *J. Opt.*, 2012, **14**, 063001; A. N. Poddubny, P. A. Belov, P. Ginzburg, A. V. Zayats and Y. S. Kivshar, *Phys. Rev. B: Condens. Matter Mater. Phys.*, 2012, **86**, 035148.

7 W. Vogel and D.-G. Welsch, *Quantum Optics*, Wiley, 3rd, Revised and Extended edn, 2006.

8 S. M. Barnett, B. Huttner and R. Loudon, *Phys. Rev. Lett.*, 1992, **68**, 3698.

9 H. T. Dung, S. Y. Buhmann and D. G. Welsch, *Phys. Rev. A*, 2006, **74**, 023803; S. Scheel, L. Knoll and D. G. Welsch, *Phys. Rev. A: At., Mol., Opt. Phys.*, 1999, **60**, 4094; S. Scheel, L. Knoll and D. G. Welsch, *Phys. Rev. A: At., Mol., Opt. Phys.*, 2000, **61**, 069901.

10 L. Novotny and B. Hecht, *Principles of Nano-optics*, Cambridge U. Press, 2012.

11 S. R. J. Brueck, *IEEE J. Sel. Top. Quantum Electron.*, 2000, **6**, 899.

 This journal is © The Royal Society of Chemistry 2015

Metamaterials-based Salisbury screens with reduced angular sensitivity

Brian M. Wells,[a] Christopher M. Roberts, and Viktor A. Podolskiy
Department of Physics and Applied Physics, University of Massachusetts Lowell, One University Avenue, Lowell, Massachusetts 01854, USA

(Received 1 August 2014; accepted 11 October 2014; published online 21 October 2014)

We demonstrate that the incorporation of nonlocal nanowire metamaterials into Salisbury screens allows for a substantial reduction of the dependence of incident angle on the absorption maximum. Realizations of angle-independent Salisbury screens for the near-IR, mid-IR, and GHz frequencies are proposed and their performances are analyzed analytically and numerically. It is shown that nonlocal effective medium theory adequately describes the angular dependence of nanowire-based Salisbury screens. © *2014 AIP Publishing LLC*. [http://dx.doi.org/10.1063/1.4899131]

Since their introduction, Salisbury screens[1] have become one of the most basic perfectly absorbing structures due to the simplicity of their design and their scalability across different frequency ranges. Over the years, the concept of Salisbury screens has been extended to construct multi-frequency or broadband absorbers.[2] However, all perfect absorber schemes inspired by Salisbury screens suffer from a common limitation, their operational frequency strongly depends on the incident angle, θ. In this manuscript, we demonstrate that nonlocal nanowire arrays, uniaxial metamaterials previously proposed for sensing and subwavelength imaging applications,[3–10] can be instrumental in constructing angle-independent Salisbury screen-like absorbers. We propose realizations of perfect absorbers for the near-IR, mid-IR, and GHz frequencies and analyze their angular performances with analytical and numerical solutions of Maxwell's equations.

A Salisbury screen comprises a three-layer structure: a perfectly conducting substrate, a quarter-wavelength-thick transparent dielectric layer, and a thin impedance-matching coupling sheet [Fig. 1(a)]. Perfect absorption results from the destructive interference of light reflected, respectively, by the top (air-coupling layer) and bottom [dielectric-perfect electric conductor (PEC)] interfaces of the system. The operating frequency of the Salisbury screen can be adjusted by modulating the thickness or the permittivity of the dielectric layer. The permittivity (conductivity) of the thin coupling layer is chosen to match the impedance of the structure: at GHz frequencies, graphite-based mixtures, "artificial dielectrics,"[11] are used to achieve the required conductivity; at higher frequencies, metamaterials can be used to achieve the required impedance.

The typical performance of a Salisbury screen is illustrated in Fig. 2(a). The particular configuration ($\epsilon_D = 2.75 + 2 \cdot 10^{-4} i$, $t = 0.15\ \mu$m, $\epsilon_t = -3.41 + 5.99i$) results in the perfect absorption of normally incident light at the free-space wavelength $\lambda = 1\ \mu$m.[12] Note however, that for higher incident angles, the perfect absorption maximum experiences a blue shift that originates from an increased optical path for the portion of the beam propagating inside the dielectric. Mathematically, the optical path for the one-way trip inside the dielectric is equal to $k_z \frac{c}{\omega} t$, where k_z represents the z component of the wavevector, t is the layer thickness, ω is the angular frequency of incident radiation, and c is the speed of light in vacuum. In an isotropic material with permittivity ϵ, $k_z = \frac{\omega}{c}\sqrt{\epsilon - \sin^2\theta}$, which explains the angular dependence of the absorption maximum. However, in anisotropic materials, this dependence can be eliminated. Explicitly, in uniaxial materials with the optical axis oriented along the z direction, permittivity can be described by a diagonal tensor $\hat{\epsilon}$, with non-zero elements $\epsilon_{xx} = \epsilon_{yy} = \epsilon_\perp$, $\epsilon_{zz} \neq \epsilon_\perp$, while magnetic permeability is described by the tensor μ, with non-zero components $\mu_{xx} = \mu_{yy} = \mu_\perp$, $\mu_{zz} \neq \mu_\perp$. In the limit $\epsilon_{zz} = \mu_{zz} \to \infty$ (so-called near-pole materials), $k_z^2 = \frac{\omega^2}{c^2}\epsilon_\perp \mu_\perp$, eliminating the angular dependence of optical path, and thus eliminating the angular dependence of the absorption maximum found in Salisbury screens. In non-magnetic anisotropic materials (materials with $\mu \equiv 1$), the optical path of extraordinary (TM-polarized) waves will be affected by anisotropy via $k_z = \frac{\omega}{c}\sqrt{\epsilon_\perp\left(1 - \frac{\sin^2\theta}{\epsilon_{zz}}\right)}$. Therefore, by employing materials with $|\epsilon_{zz}| \gg |\epsilon_\perp|$, the angular sensitivity of Salisbury screens to TM-polarized radiation can be dramatically reduced. Although only few natural materials possess the required strong anisotropy,[13–16] mainly at UV and far IR frequency ranges, it is possible to design a composite system (metamaterial) which would realize epsilon-near-pole behavior at other frequencies across the optical spectrum.

Metamaterials, composite structures with engineered dispersion, have recently been proposed to solve several fundamental problems in optics.[17–19] Here, we consider a metamaterial composed from an array of parallel plasmonic wires with radius R, embedded into a dielectric slab, with mean inter-wire separation a ($R < a \ll \lambda$). From the effective medium standpoint, the wire metamaterial represents a uniaxial medium with its optical axis parallel to the wires. The optical spectra of wire metamaterials are typically dominated by two extinction resonances, associated with the resonant excitation of transverse and longitudinal plasmons. The spectral locations of these resonances correspond to the conditions $\epsilon_h + \epsilon_m \simeq 0$ and $\epsilon_{zz} \simeq 0$, respectively. For a typical nanowire system, these extinction resonances occur at visible frequencies.[7,8,21] At longer wavelengths, the permittivity of noble metals $|\epsilon_m| \gg 1$; therefore, it is expected that a wire medium with permittivities $\epsilon_\perp \sim \epsilon_h$ and $\epsilon_{zz} \sim \epsilon_m \frac{\pi R^2}{a^2}$ (Ref. 20) will serve as ideal realization of an epsilon-near-pole material. Fabrication of optically thick nanowire structures with $R < a \ll \lambda$ has been demonstrated from visible[8,21] to GHz (Ref. 4) frequencies. The main

[a]E-mail: brian_wells@student.uml.edu

 © 2014 AIP Publishing LLC

This article is copyrighted as indicated in the article. Reuse of AIP content is subject to the terms at: http://scitation.aip.org/termsconditions. Downloaded to IP: 129.63.141.221 On: Tue, 21 Oct 2014 19:19:56

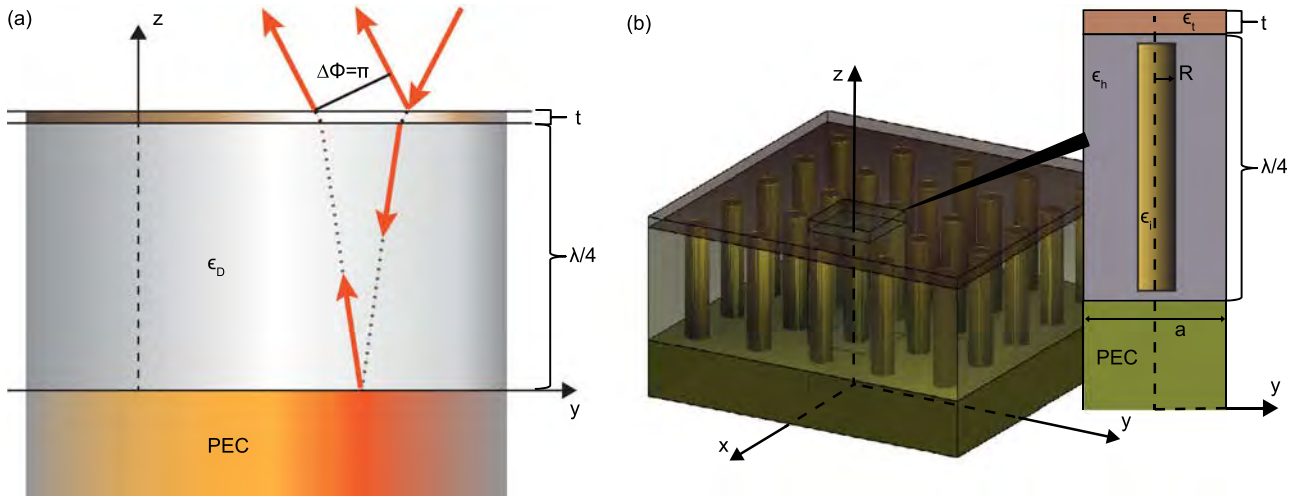

FIG. 1. (a) Schematic of a three layered Salisbury screen absorber that consists of (from bottom to top) a perfectly conducting substrate, a quarter-wavelength-thick layer of dielectric and thin impedance-matching coupling sheet. (b) Schematic geometry of Salisbury screen with wire metamaterial replacing the quarter-wavelength-thick layer of dielectric that is found in traditional Salisbury screens.

objective of this work is to explore the perspectives of this metamaterial platform for Salisbury screen-type perfect absorbers with substantially reduced angular sensitivity. A schematic of such nanowire metamaterial-based Salisbury screen is presented in Fig. 1(b).

The optical response of nanowire metamaterials has been a topic of active research for the past decade. It has been shown that, although the properties of nanowire composites are, in general, described by uniaxial Maxwell-Garnett-type effective medium theory (EMT),[6,7,22–24] important deviations from the predictions of this theory are expected at both high-frequency (visible) and low-frequency (GHz) ends of optical spectrum. In particular, it has been demonstrated that the properties of wire media are substantially affected by optical nonlocality, dependence of material permittivity on wavevector.[10,25,26] A comprehensive nonlocal effective medium theory of wire media has been presented in Ref. 20.

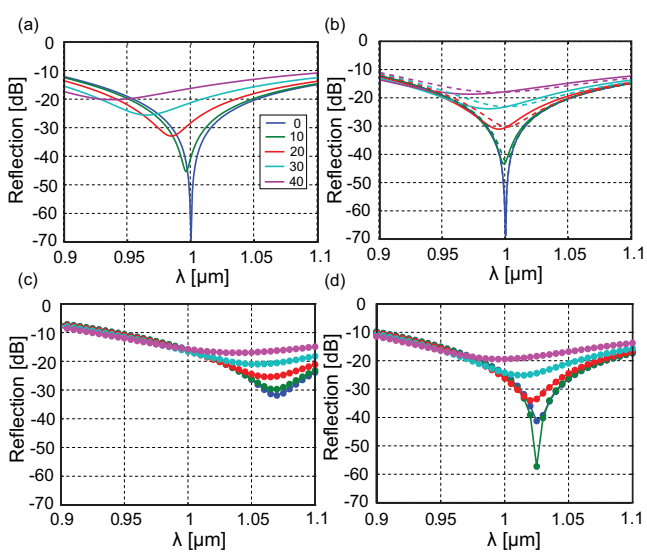

FIG. 2. Reflection of Salisbury screens in near-IR frequency regime with isotropic non-dispersive dielectric (a), and nanowire metamaterial (b)–(d) core layer; (b) represents predictions of local (dashed lines) and nonlocal (solid lines) effective medium theories, while (c) and (d) represent FEM and RCWA-based solutions of Maxwell equations, respectively.

To illustrate the benefits of a nanowire media for Salisbury screen design, we analyze the performance of Salisbury screens with metamaterial cores in three different frequency ranges, near-IR, mid-IR, and GHz frequencies. In this analysis, we assume that the properties of both the nanowires and of high-conductivity substrate are described by the Drude model,[27] $\epsilon_m = \epsilon_\infty - \frac{\omega_p^2}{\omega^2 + i\Gamma\omega}$ with $\epsilon_\infty = 9.5$, $\omega_p = 1.36 \times 10^{16}$Hz, and $\Gamma = 1.05 \times 10^{14}$ Hz corresponding to optical response of Au. For near- and mid-IR frequencies, we assume that the wires, with radius $R = 12.5$nm, are arranged into a square lattice with lattice size $a = 60$ nm, and are submerged into dielectric matrix with permittivity $\epsilon_h = 2.7$, representing practical nanowire composites fabricated with electrochemical deposition in anodized alumina substrates.[21] The particular configuration results in effective permittivities $\epsilon_{zz} = -3.42 + 0.39i, \epsilon_\perp = 3.73 + 0.01i$ for $\lambda_0 = 1\,\mu$m and $\epsilon_{zz} = -538 + 301i$, $\epsilon_\perp = 3.59 + 6 \cdot 10^{-4}i$ for $\lambda_0 = 10\,\mu$m. For GHz frequencies, we assume that wires, with radius 250 μm, are arranged into lattice size 0.25 cm, resulting in $\epsilon_{zz} = 1.0 + 3.33 \cdot 10^6 i, \epsilon_\perp = 1.06$ for $f_0 = 10$ GHz. To prevent artifacts related to coupling of nanowires through high-conductivity substrate,[8] we introduce a small, 5nm gap between nanowire in the core of Salisbury screen and the substrate (see inset in Fig. 1(b)). In general, wire-based Salisbury screens can be designed for virtually any frequency provided that quarter-wavelength-thick wire composite can be fabricated and material to realize thin impedance-matching sheet is available.[28]

In this work, several techniques are used to calculate the optical response of Salisbury screens. First, the reflectivity spectrum is calculated analytically, using both local and nonlocal effective medium theories, described in detail in Ref. 20. Second, Maxwell equations are solved numerically, with the finite-element microscopy (FEM) technique.[29] To improve the convergence of the FEM solver, the end-points of nanowire are assumed to be not perfectly flat but slightly ellipsoidal. Finally, to further validate our results, optical response of the near-IR and mid-IR systems are analyzed with Rigorous Coupled-Wave analysis (RCWA)[30] utilizing

This article is copyrighted as indicated in the article. Reuse of AIP content is subject to the terms at: http://scitation.aip.org/termsconditions. Downloaded to IP: 129.63.141.221 On: Tue, 21 Oct 2014 19:19:56

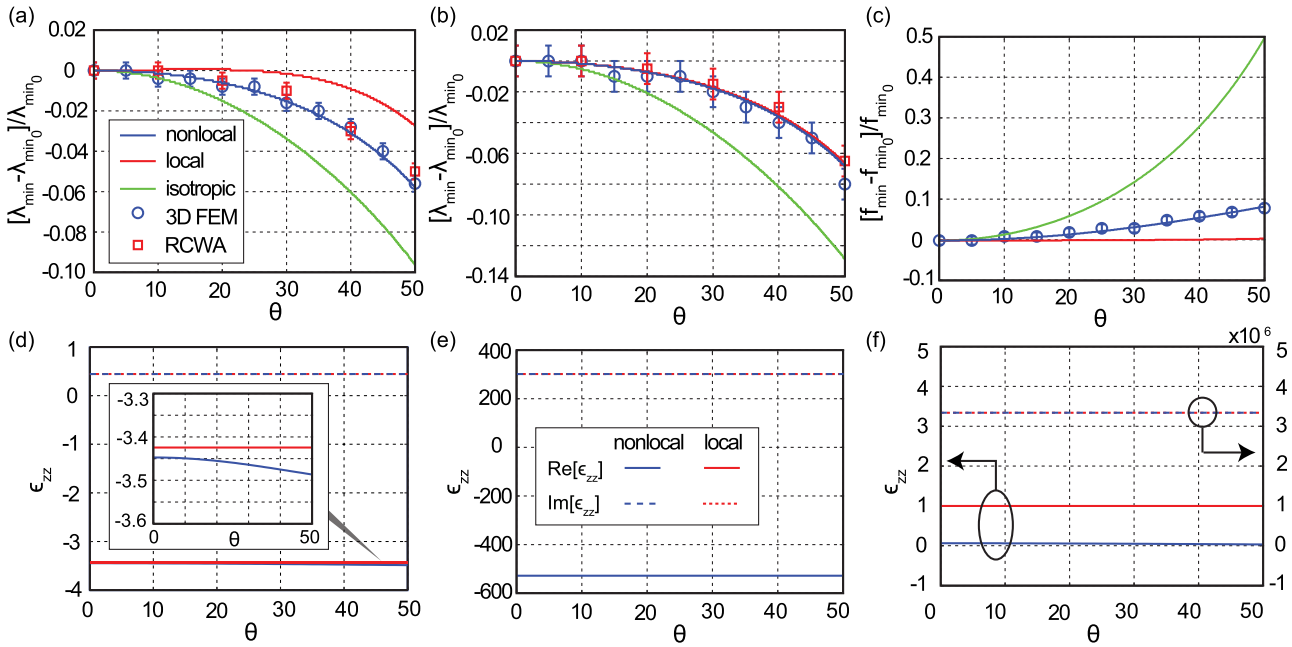

FIG. 3. Dependence of spectral position of reflection minimum of Salisbury screens at three different frequency ranges, near-IR [$\lambda_{min_0} = 1\mu$m] (a), mid-IR [$\lambda_{min_0} = 10\,\mu$m] (b), and GHz [$f_{min_0} = 10$ GHz] (c) frequencies; blue and red solid lines represent the nonlocal and local EMT that accounts for material dispersion of noble-metal wires; green lines represent results for isotropic non-dispersive dielectric core layers; circles and squares represent 3D-FEM and RCWA-based solutions, respectively. (d)–(f) illustrate effective permittivity of wire metamaterials, calculated with local (red) and nonlocal (blue) effective medium models; geometry and spectral properties of composites in panels (d)–(f) are identical to those in panels (a)–(c), respectively; solid and dashed lines represent real and imaginary parts of permittivity, respectively. The nonlocal nature of nanowire response is clearly seen in the inset in (d); in panel (e), predictions of local and nonlocal EMTs are indistinguishable.

the normal vector method.[31] The results of these calculations are shown in Fig. 2. It is clearly seen that nanowire medium substantially reduces angular dependence of the position of absorption maximum of Salisbury screen for TM-polarized light. At the same time, it is seen that the position of the reflectivity minimum depends on the technique used to solve Maxwell equations. This minor shift in reflectivity minimum is likely due to fundamental limits of floating-point calculations, related to extremely small reflectivity values, encountered in our calculations. The angular dependence of the minimum (the blue shift of the minimum with respect to its spectral position for normal incidence), however, remains consistent between RCWA and FEM solutions. Therefore, this parameter is used to describe the performance of the metamaterial-based Salisbury screen.

The angular dependence of reflectivity minimum for the systems operating in all three spectral ranges is summarized in Fig. 3. It is clearly seen that nanowire-based Salisbury screens are much less sensitive to incident angle of the beam than their isotropic counterparts. It is also seen that nonlocal effective medium theory adequately describes this angular dependence. Local effective medium theory, on the other hand, tends to under-estimate the angular dependence of the absorption maximum and its predictions converge to the predictions of nonlocal EMT only in the limit $\frac{a}{\lambda} \to 0$ [Fig. 3(b)]. It is interesting to note that even though local EMT predicts effective permittivity of the composite with reasonable accuracy [see Figs. 3(d)–3(f)], it fails to adequately predict coupling of electromagnetic waves into the composite, in turn, affecting the calculations of overall optical response of the nanowire slab.

To summarize, we have demonstrated that introduction of a nanowire medium into the dielectric slab of Salisbury screen substantially reduces the angular dependence of the absorption maximum of Salisbury screens for TM-polarized light. The nonlocal effective medium theory adequately describes this spectral behavior. The introduction of anisotropic magnetic metamaterials may result in polarization- and angle-independent Salisbury screens.

This research was supported by ARO (Grant No. W911NF-12-1-0533) and NSF MWN Program (Grant No. 1209761).

[1]W. Salisbury and W. Winfield, U.S. patent 2,599,944 (10 June 1952).
[2]R. L. Fante and M. T. McCormack, IEEE Trans. Antennas Propag. **36**, 1443 (1988).
[3]M. Silveirinha and N. Engheta, Phys. Rev. Lett. **97**, 157403 (2006).
[4]J. B. Pendry, D. Schurig, and D. Smith, Science **312**, 1780 (2006).
[5]W. Cai, U. K. Chettiar, A. V. Kildishev, and V. M. Shalaev, Nat. Photonics **1**, 224 (2007).
[6]J. Elser, R. Wangberg, V. A. Podolskiy, and E. E. Narimanov, Appl. Phys. Lett. **89**, 261102 (2006).
[7]R. Atkinson, W. R. Hendren, G. A. Wurtz, W. Dickson, A. V. Zayats, P. Evans, and R. J. Pollard, Phys. Rev. B **73**, 235402 (2006).
[8]J. Yao, Z. Liu, Y. Liu, Y. Wang, C. Sun, G. Bartal, A. M. Stacy, and X. Zhang, Science **321**, 930 (2008).
[9]B. D. F. Casse, W. T. Lu, Y. J. Huang, E. Gultepe, L. Menon, and S. Sridhar, Appl. Phys. Lett. **96**, 023114 (2010).
[10]P. A. Belov, R. Marques, S. I. Maslovski, I. S. Nefedov, M. Silveirinha, C. R. Simovski, and S. A. Tretyakov, Phys. Rev. B **67**, 113103 (2003).
[11]K. Gaylor, *The Measurement of Surface Reflectivity at Millimetre Wavelengths* (DSTO Materials Research Laboratory, 1989).
[12]These parameters are chosen to provide adequate comparison with performance of nanowire-metamaterials based Salisbury screens, described later in the text. In particular, $\epsilon_D = \epsilon_\perp$ and all geometrical parameters of this isotropic Salisbury screen are identical to those of nanowire-based structure. The angular response of Salisbury screens with different isotropic dielectric cores is similar to the one shown in Fig. 2(a).
[13]J. Sun, J. Zhou, B. Li, and F. Kang, Appl. Phys. Lett. **98**, 101901 (2011).

This article is copyrighted as indicated in the article. Reuse of AIP content is subject to the terms at: http://scitation.aip.org/termsconditions. Downloaded to IP: 129.63.141.221 On: Tue, 21 Oct 2014 19:19:56

[14]X. Gerbaux, M. Tazawa, and A. Hadni, Ferroelectrics **215**(1), 47 (1998).
[15]M. Schubert, T. E. Tiwald, and C. M. Herzinger, Phys. Rev. B **61**, 8187 (2000).
[16]W. S. Boyle, A. D. Brailsford, and J. K. Galt, Phys. Rev. **109**, 1396 (1958).
[17]J. B. Pendry, A. Aubry, D. R. Smith, and S. A. Maier, Science **337**, 549 (2012).
[18]V. G. Veselago, Sov. Phys.-Usp. **10**(4), 509 (1968).
[19]*Tutorials in Metamaterials*, edited by M. A. Noginov and V. A. Podolskiy (CRC Press, Boca Raton, FL, 2012).
[20]B. Wells, A. Zayats, and V. Podolskiy, Phys. Rev. B **89**, 035111 (2014).
[21]A. V. Kabashin, P. Evans, S. Pastkovsky, W. Hendren, G. A. Wurtz, R. Atkinson, R. Pollard, V. A. Podolskiy, and A. V. Zayats, Nat. Mater. **8**, 867 (2009).
[22]A. K. Sarychev, R. C. McPhedran, and V. M. Shalaev, Phys. Rev. B **62**, 8531 (2000).
[23]G. A. Wurtz, W. Dickson, D. O'Connor, R. Atkinson, W. Hendren, P. Evans, R. Pollard, and A. V. Zayats, Opt. Express **16**, 7460 (2008).
[24]J. C. M. Garnett, Philos. Trans. R. Soc. London, Ser. B **203**, 385 (1904).
[25]M. G. Silveirinha, Phys. Rev. E **73**, 046612 (2006).
[26]M. G. Silveirinha, P. A. Belov, and C. R. Simovski, Phys. Rev. B **75**, 035108 (2007).
[27]J. D. Jackson, *Classical Electrodynamics*, 3rd ed. (John Wiley and Sons, New York, 1999).
[28]Optical properties of impedance-matching layer depend, in part, on absorption in wire composite.
[29]COMSOL Multiphysics 4.3b, COMSOL AB, 2013.
[30]M. G. Moharam, D. A. Pommet, E. B. Grann, and T. K. Gaylord, J. Opt. Soc. Am. A **12**, 1077 (1995).
[31]T. Schuster, J. Ruoff, N. Kerwien, S. Rafler, and W. Osten, J. Opt. Soc. Am. A **24**, 2880 (2007).

This article is copyrighted as indicated in the article. Reuse of AIP content is subject to the terms at: http://scitation.aip.org/termsconditions. Downloaded to IP: 129.63.141.221 On: Tue, 21 Oct 2014 19:19:56

NANO LETTERS

Letter

pubs.acs.org/NanoLett

Looking into Meta-Atoms of Plasmonic Nanowire Metamaterial

Kun-Tong Tsai,[†,‡,§] Gregory A. Wurtz,[§] Jen-You Chu,[∥] Tian-You Cheng,[⊥] Huai-Hsien Wang,[‡] Alexey V. Krasavin,[§] Jr-Hau He,[*,†,¶] Brian M. Wells,[#] Viktor A. Podolskiy,[#] Juen-Kai Wang,[*,‡,⊥] Yuh-Lin Wang,[*,‡,∇] and Anatoly V. Zayats[*,§]

[†]Graduate Institute of Photonics and Optoelectronics and Department of Electrical Engineering, National Taiwan University, Taipei 10617, Taiwan

[‡]Institute of Atomic and Molecular Sciences, Academia Sinica, Taipei 10617, Taiwan

[§]Department of Physics, King's College London, Strand, London WC2R 2LS, U.K.

[∥]Material and Chemical Research Laboratories, Industrial Technology Research Institute, Hsin-Chu 31040, Taiwan

[⊥]Center for Condensed Matter Sciences, National Taiwan University, Taipei 10617, Taiwan

[#]Department of Physics and Applied Physics, University of Massachusetts Lowell, Lowell, Massachusetts 01854, United States

[∇]Department of Physics, National Taiwan University, Taipei 10617, Taiwan

[¶]Computer, Electrical and Mathematical Sciences and Engineering Division, King Abdullah University of Science & Technology, Thuwal 23955-6900, Saudi Arabia

Supporting Information

ABSTRACT: Nanowire-based plasmonic metamaterials exhibit many intriguing properties related to the hyperbolic dispersion, negative refraction, epsilon-near-zero behavior, strong Purcell effect, and nonlinearities. We have experimentally and numerically studied the electromagnetic modes of individual nanowires (meta-atoms) forming the metamaterial. High-resolution, scattering-type near-field optical microscopy has been used to visualize the intensity and phase of the modes. Numerical and analytical modeling of the mode structure is in agreement with the experimental observations and indicates the presence of the nonlocal response associated with cylindrical surface plasmons of nanowires.

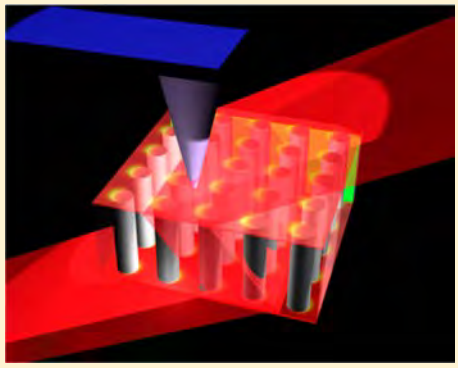

KEYWORDS: *Metamaterials, plasmonics, nanowires, SNOM, nonlocality, epsilon-near-zero*

Metamaterials enable unprecedented control over light propagation[1,2] and enhanced light−matter interactions at the nanoscale,[3−6] opening new avenues for the applications beyond the scope covered by natural materials. One of the practical metamaterial designs is based on the constituent meta-atoms in the form of aligned metal wires placed in the embedding dielectric with both wire diameter and interwire separation much smaller than the wavelength of light at the operating frequency. Such wire metamaterials[7] are of special interest due to their unusual anisotropic optical properties manifested in hyperbolic dispersion,[8,9] optical nonlocality effects,[10,11] and extreme field confinement[12] important for numerous applications in imaging,[2,13−16] active nanophotonics,[11,17,18] and bio/chemo-sensing.[19] Since the metamaterial structure is relatively simple, the barrier associated with the fabrication difficulties is greatly reduced compared to top-down fabricated metamaterials based on, e.g., split-ring resonators or fishnets,[20,21] and scaling down to optical operational frequencies is relatively easy.[7] Therefore, these metamaterials enable operating frequencies spanning a very broad range from infrared to visible and, possibly, to the ultraviolet wavelength range.

For wire metamaterials operating at optical frequencies, namely, near-infrared and visible, constituent elements are usually plasmonic nanowires of relatively short length (also called nanorods) to achieve resonances in the desired wavelength range. The behavior of these optically dense arrays of nanowires embedded in dielectric matrices can be conceptually described using an effective medium approximation, introducing the anisotropic effective permittivity tensor of the metal−dielectric composite. In such metamaterials, the components of the permittivity tensor along and perpendicular to the nanowire axis may have opposite signs resulting in the hyperbolic isofrequency surfaces of the dispersion.[8] The hyperbolic dispersion enables the broadband negative refraction[2,13] and controllable spontaneous emission[4] in the

Received: April 7, 2014
Revised: July 29, 2014
Published: August 12, 2014

 © 2014 American Chemical Society dx.doi.org/10.1021/nl501283c | *Nano Lett.* 2014, 14, 4971−4976

nanowire metamaterials. Other applications, such as subwavelength color imaging,[12] sensing,[22] and designed ultrafast optical nonlinearity,[11] are also of significant interest.

Although the optical properties of plasmonic nanorod and nanowire metamaterials have been extensively studied, the observations are generally limited to far-field measurements reflecting the effective medium behavior of the metamaterial. At the same time, microscopic phenomena related to the internal structure of the composite, accessible in the near-field region of the metamaterial where its structure is important, have been inferred only numerically via simulations of microscopic field distributions. The direct observation of the local field distribution down to the meta-atom scale in the nanowire metamaterial at optical frequency has not been characterized experimentally, inhibiting fundamental understanding of electromagnetic phenomena within the metamaterial, including Purcell and nonlocal effects, for which the internal metamaterial structure is of great importance.[23]

The experimental demonstration of the optical signatures of individual nanowires within the array structure remains a major challenge due to the limited spatial resolution of optical microscopy. Recently, the development of scattering-type (also called apertureless) scanning near-field optical microscopy (s-SNOM)[24−26] allows one to reveal the optical details at the deep subwavelength scales and has already provided insight into electromagnetic (EM) waves interaction with composite metamaterials.[27−32] Complementary far-field and near-field optical studies are required to gain a rational understanding of the character of the underlying mechanisms of light interaction with metamaterials on the nanoscale, providing the opportunity for a controlled improvement of new metamaterial designs.

In this letter, we report on the first experimental observation of near-field behavior of nanowire metamaterials on the meta-atom scale at visible frequencies. The optical mode within the unit cell less than 100 nm is visualized utilizing s-SNOM. The results are consistent with numerical simulations confirming the near-field signature of individual meta-atoms in the nanowire metamaterials. We show that the near-field behavior of meta-atoms in metamaterial is similar to the behavior of an isolated nanorod, determined by the excitation of cylindrical surface plasmons, while the far-field response is dominated by coupling between the meta-atoms.

The nanowire metamaterial studied in this work (Figure 1) is made of vertically aligned silver nanowires (AgNWs) embedded in an anodic aluminum oxide (AAO) matrix (Figure 1a). The fabrication of the nanowire metamaterial has been described in detail elsewhere[14] (also see Supporting Information). In brief, the nanowire metamaterial is fabricated by performing an electrochemical deposition of silver into the empty pores of the AAO templates. AAO templates are made with the arrays of highly ordered nanochannels, and a mechanical chemical polish process is carried out to ensure its flatness, which allows the geometries in the experiment to be compared to simulations. The diameter and length of the nanowires are of about 50 nm and 5 μm, respectively. They are arranged in an array with a hexagonal close-packed (hcp) lattice of about 100 nm period. The atomic force microscope (AFM) topography image (Figure 1b) shows the sample's flatness with a root-mean-square roughness as small as 3.5 nm.

The effective permittivity of the metamaterial (Figure 1c) deduced using the Maxwell−Garnet effective medium approximation[33] shows that the hyperbolic regime occurs for the

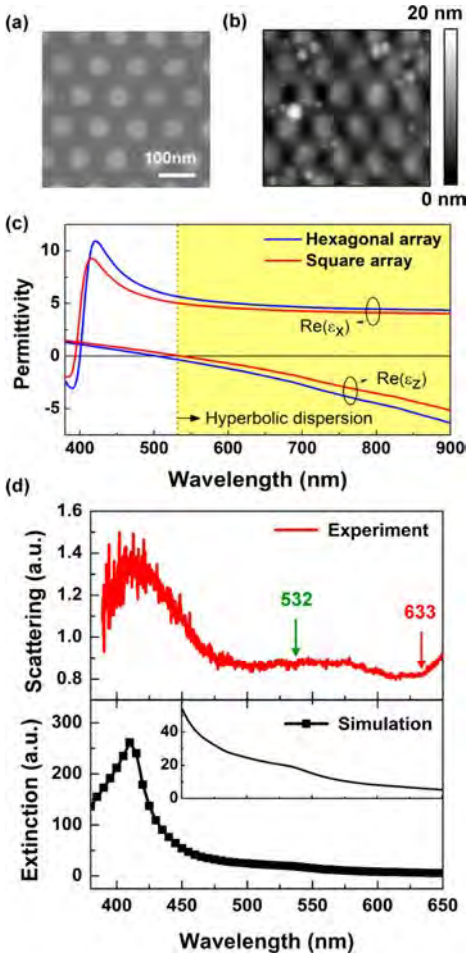

Figure 1. (a) Scanning electron microscope and (b) atomic force microscope topography images, and (c) effective permittivities (real parts) of the nanowire metamaterials. (d) Measured dark-field scattering spectrum and the simulated extinction spectrum for the nanowire metamaterial. The arrows indicate the laser lines used in the s-SNOM measurements. The simulated extinction spectrum is obtained at the incident angle of 60°, which corresponds to the illumination condition in the s-SNOM experiment.

wavelengths longer than around 530 nm. The measured scattering spectrum and the extinction spectrum calculated using the finite-element simulations (see Methods in Supporting Information for details) are shown in Figure 1d. The scattering spectrum has a dominant peak at the wavelength of about 415 nm, which is the transverse mode of the AgNWs, related to the resonant electron oscillations perpendicular to the nanowire axes.[34] At this resonant peak, strong scattering and high absorption occur. We focus on the optical properties away from this resonance where the absorption is relatively low. The wavelengths of 532 and 633 nm, used in the near-field measurements, are away from high absorption and close to the epsilon-near-zero (ENZ) condition and in the hyperbolic dispersion range, respectively.

To map the near-field distribution over the nanowire metamaterials, an amplitude- and phase-resolved scattering-type scanning near-field optical microscope (s-SNOM) has been used (Figure S3, Supporting Information).[24] An objective lens focuses a TM-polarized laser beam onto the AFM tip at an incident angle of 60°. A Pt−Ir-coated Si cantilever was used in the experiments since its plasmonic resonance is away from the

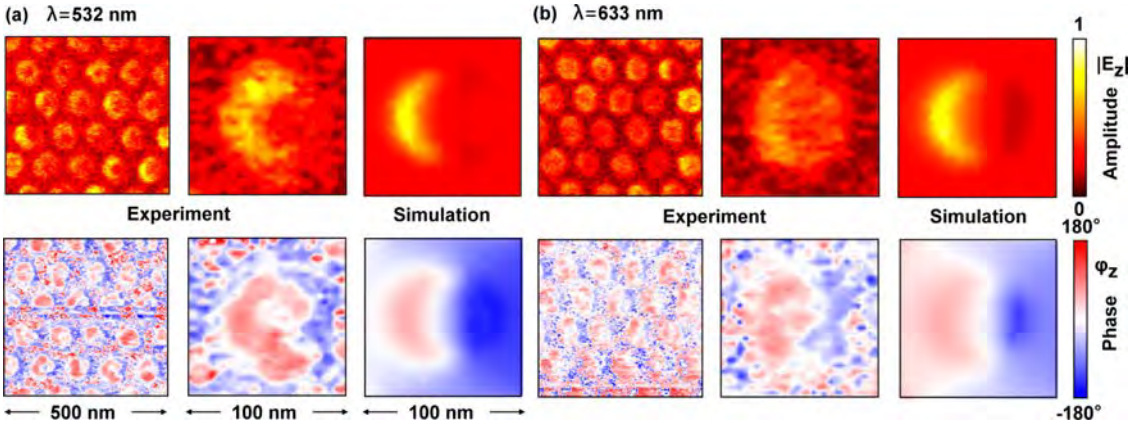

Figure 2. Measured and simulated near-field distributions of the electric-field (z-component) and phase above the nanowire metamaterials at the wavelengths of (a) 532 and (b) 633 nm. The simulated distributions are presented at the height of 5 nm above the nanowire metamaterial's surface. The illumination of the metamaterial is from the right at 60° angle of incidence.

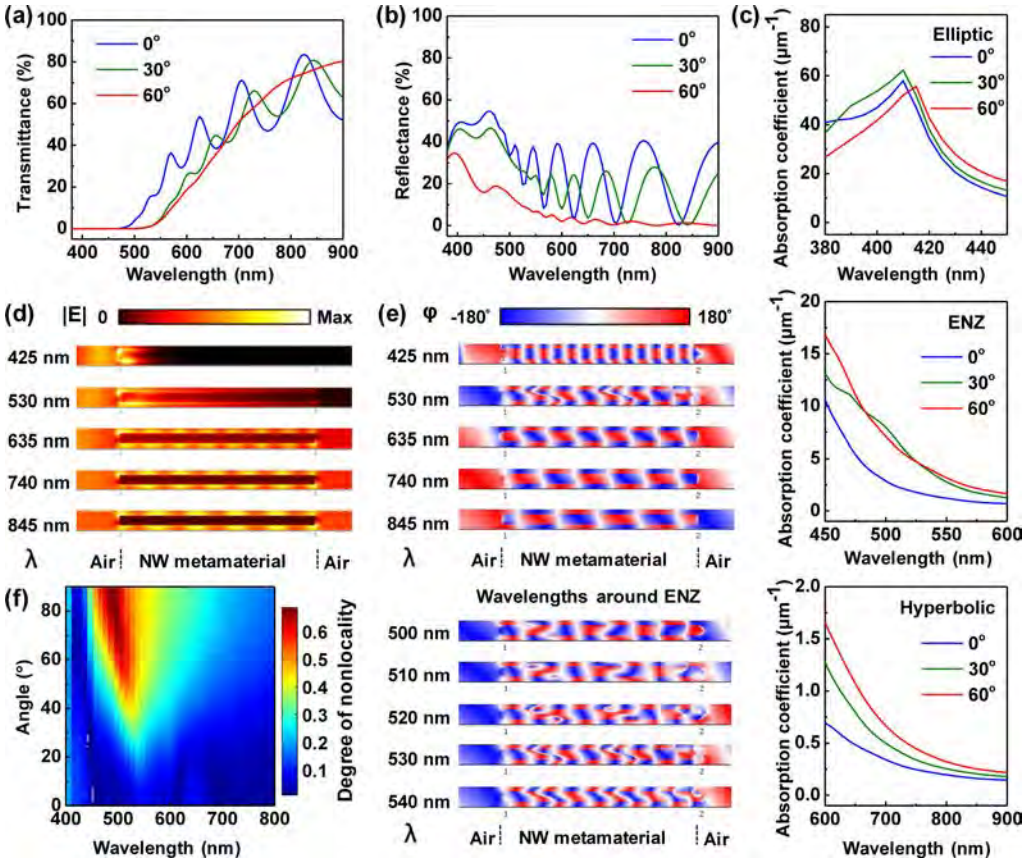

Figure 3. Simulated (a) transmittance, (b) reflectance, and (c) absorption coefficient spectra of the nanowire metamaterial at the incident angles of 0°, 30°, and 60°. (d) The electric field distributions (|*E*|) and (e) phase distributions (φ) for different wavelengths at the incident angle of 30°. (f) The amplitude contribution of the additional TM wave, calculated using a nonlocal EMT theory[36] for different wavelengths and angles of incidence. The metamaterial consists of 1 μm long silver nanowires, all other parameters as in Figure 2.

laser wavelengths used in this study and relatively wavelength insensitive, therefore preventing the introduction of unwanted near-field electromagnetic interactions from the tip apex. A heterodyne interferometric setup has been employed to extract the amplitude and phase of the electromagnetic field near the metamaterial surface. In order to remove the background of the far-field scattered light, the optical signal modulated at the fourth harmonic of the tip vibration was monitored.[25] The resolution of the s-SNOM setup was typically sub-10 nm and therefore adequate to detect the details of near-field information on the nanowire metamaterials with the metamaterial unit cell less than 100 nm.

The measured and calculated near-field intensity and phase distributions in the arrays of nanowires are shown in Figure 2a,b for the illumination with the TM polarized light at the wavelengths of 532 and 633 nm, respectively (see Figure S4, Supporting Information, for the images with saturated contrast). The periodic pattern of the near-field intensity

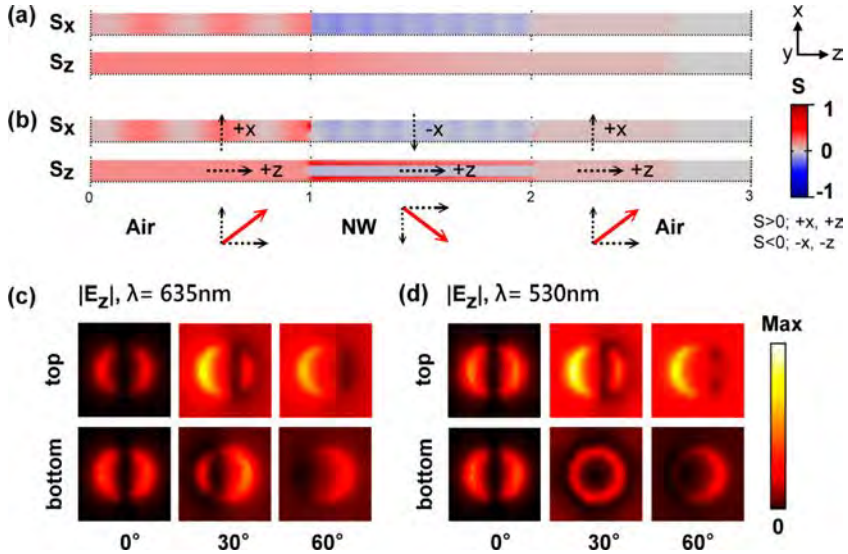

Figure 4. Simulated distribution of the x- and z-components of the time-averaged energy flow for (a) a layer of a homogeneous effective medium and (b) AgNWs/AAO composite (with square lattice) at the wavelength of 635 nm and an incident angle of 30°. The arrows indicate the direction of the energy flow. (c,d) The simulated amplitude distributions of the electric field (z-component) at the wavelengths of 635 and 530 nm, respectively, for different angles of incidence. The field is measured at the height of 5 nm above (below) the top (bottom) metamaterial's surface. The amplitude of $|E_z|$ at the bottom surface in panel d at the incident angles of 30° and 60° is magnified 2.5 and 1.4 times, respectively. The nanowire parameters are the same as those in Figure 3.

reflects the microscopic structure of the metamaterial. The close-up of the near-field distribution around individual meta-atoms forming the metamaterial reveals crescent-shaped distributions around the nanorods for both the intensity and the phase. The symmetry breaking is due to the oblique illumination of the metamaterial from the right at the 60° angle of incidence. The experimental near-field distributions are well reproduced by the map of the z-component of the field only (Figures 2 and S5, Supporting Information); it agrees with the fact that s-SNOM is more sensitive to the field component, which is perpendicular to the sample surface (i.e., $|E_z|$, in our configuration).[24,35] For comparison, the simulation results of the field distribution on the top surface of the metamaterial at the incident angle of 0° is shown in Figure S5b, Supporting Information. The symmetry of the field distribution indicates that the field is built by electron oscillations perpendicular to the nanowire axes. The phase difference at the two ends of the field patterns is around 180°. These properties correspond to the excitation of cylindrical surface plasmons on the nanowires. These charge oscillations are also responsible for nonlocal effects in this system.[36] Over a wide range of wavelengths, the field distributions exhibit similar behavior with the angle of incidence (Figure S5b,c, Supporting Information). It is important to note that the observed field distributions around the nanowires forming metamaterial are similar to those for individual nanowires with a crescent shape for oblique incidence but with different amplitudes in the lobes, indicative of the interaction between the meta-atoms in the metamaterial (Figure S6, Supporting Information). While the near-field behavior of meta-atoms in metamaterial is similar to the behavior of an isolated nanorod, the far-field response is dominated by coupling between the meta-atoms.

The optical properties of the nanowire metamaterials are presented in Figure 3. The absorption is significant over the broad visible spectral range, with the dominating transmission at longer wavelengths (Figure 3a) and reflection at short wavelengths (Figure 3b). The oscillations observed in the spectra are related to the Fabry–Pérot-type resonances due to the reflections of the cylindrical surface plasmons on the metamaterial interfaces. At short-wavelengths (below 450 nm), the absorption due to the transverse resonances of the metamaterial (electron oscillations perpendicular to wire axis) dominates, leading to short penetration depth of light in the metamaterial (Figure 3c). For longer than the ENZ wavelengths, corresponding to the hyberbolic dispersion regime, characteristic field oscillations of the cylindrical surface plasmon interference pattern are observed. The EM waves are mainly confined and propagates along the surface of the Ag NWs. It is interesting to note that, at around the ENZ wavelength (500–540 nm; the ENZ occurs at 537 or 507 nm for the metamaterial with square or hcp lattice, respectively), the intrinsic absorption coefficient of the metamaterial has a peculiarity with increased absorption despite that the local effective parameters behave monotonously. In optically thick materials, nonlocality gives rise to a longitudinal wave that fundamentally changes the optical properties of the system. The two main phenomena associated with the longitudinal wave are illustrated in Figure 3d–f. Coupling of the incident plane wave to the longitudinal wave results in the spectral dependencies of the reflection from and transmission through the metamaterial, which substantially deviate from the predictions of the local effective medium theory for short wavelengths (elliptical dispersion regime) (Figure S7, Supporting Information). Signatures of the interference between the two waves, including vanishing transmission and length-dependent absorption coefficient, are expected in the spectral range where the amplitudes of both waves are comparable to each other (Figure 3f). In both amplitude and especially phase distributions, peculiarities related to interference of two p-polarized waves supported by nonlocal nanowire material are observed around the wavelength of 530 nm (Figure 3d,e).

In order to confirm the negative refraction in the nanowire metamaterial in the hyperbolic regime and to understand the interplay between macroscopic and microscopic behavior, we

investigated the spatial distribution of the time-averaged energy flow through the metamaterial (Figure 4). Figure 4a,b show the simulated x- and z-components of time-averaged energy flow distributions (i.e., S_x and S_z) for the nanowire metamaterial as a layer of effective medium and the AgNW/AAO composite, respectively. For similar metamaterials, the negative refraction has been experimentally demonstrated.[13] Both effective medium and discrete composite model give the same far-field properties of the metamaterial. In the effective medium scenario (Figure 4a), the sign of S_x flips at the air/metamaterial interface, which indicates an energy flow backward in the lateral direction. At the same time, the S_z homogeneously flows away from the interface. While a similar behavior is observed in the discrete system of nanowires forming the metamaterial, there is a subtle difference between them. In the AgNW/AAO composite, both S_x and S_z show the characteristic near-field signatures of the nanowire geometry (Figure 4b). Further from the nanowire interface, S_x is comparable to the one obtained in the effective medium layer in terms of the power flow distribution.

Figure 4c,d show the simulated angle-dependent amplitude of electric field (z-component as measured with a-SNOM) at the wavelength of 635 and 530 nm, corresponding to the hyperbolic dispersion and the ENZ regime, respectively, in the case of square lattice nanowire array. These distributions are practically independent of the type of the lattice, which is expected within validity of the effective medium approximation. At the wavelength of 635 nm, the field distributions at the top and bottom interfaces change with the incident angle, in agreement with the experimental observations. For the wavelength close to the ENZ conditions, a different behavior is observed at 30° angle of incidence, which is related to the nonlocal effects: $|E_z|$ distributed circularly at the bottom surface; at this wavelength−angle combination (Figure 3f), the contribution of the additional wave is significant.

In conclusion, we have experimentally studied the near-field and phase distributions in the composite NW metamaterials using s-SNOM, revealing the response of individual meta-atoms, and numerically simulated their behavior in different regimes of hyperbolic and ENZ dispersions. The near-field measurements reveal collective electronic oscillations (CSPs) of each nanowire, which determine the far-field optical response of the NW metamaterial and are responsible for the nonlocal behavior of the composite.

■ ASSOCIATED CONTENT

Supporting Information

Materials and methods (fabrication of metamaterials, dark-field spectroscopy, finite-element simulations, and scanning near-field optical microscopy). Supplementary Figures. This material is available free of charge via the Internet at http://pubs.acs.org.

■ AUTHOR INFORMATION

Corresponding Authors

*(J.-H.H.) E-mail: jhhe@cc.ee.ntu.edu.tw.
*(J.-K.W.) E-mail: jkwang@ntu.edu.tw.
*(Y.-L.W.) E-mail: ylwang@pub.iams.sinica.edu.tw.
*(A.V.Z.) E-mail: a.zayats@kcl.ac.uk.

Notes

The authors declare no competing financial interest.

■ ACKNOWLEDGMENTS

This work was supported, in part, by the Ministry of Science and Technology of Taiwan (MOST 102-2628-M-001-008 and MOST 102-2112-M-002-011-MY3), US Army Research Office (W911NF-12-1-0533), EPSRC (U.K.), and the ERC iPLASMM project (321268). K.T.T. acknowledges the support from National Science Council of Taiwan via the Graduate Student Study Abroad Program of Taiwan and NanoCore facilities at Academia Sinica. A.Z. acknowledges support from the Royal Society and the Wolfson Foundation. G.W. acknowledges support from the EC FP7 project 304179 (Marie Curie Actions). The authors are grateful to D. O'Connor for help with the numerical model.

■ REFERENCES

(1) Lemoult, F.; Kaina, N.; Fink, M.; Lerosey, G. *Nat. Phys.* **2013**, *9*, 55−60.
(2) Yao, J.; Liu, Z.; Liu, Y.; Wang, Y.; Sun, C.; Bartal, G.; Stacy, A. M.; Zhang, X. *Science* **2008**, *321*, 930−930.
(3) Krishnamoorthy, H. N. S.; Jacob, Z.; Narimanov, E.; Kretzschmar, I.; Menon, V. M. *Science* **2012**, *336*, 205−209.
(4) Noginov, M. A.; Li, H.; Barnakov, Y. A.; Dryden, D.; Nataraj, G.; Zhu, G.; Bonner, C. E.; Mayy, M.; Jacob, Z.; Narimanov, E. E. *Opt. Lett.* **2010**, *35*, 1863−1865.
(5) Jacob, Z.; Kim, J. Y.; Naik, G. V.; Boltasseva, A.; Narimanov, E. E.; Shalaev, V. M. *Appl. Phys. B: Laser Opt.* **2010**, *100*, 215−218.
(6) Kauranen, M.; Zayats, A. V. *Nat. Photonics* **2012**, *6*, 737−748.
(7) Poddubny, A.; Irosh, I.; Belov, P.; Kivshar, Y. *Nat. Photonics* **2013**, *7*, 958−967.
(8) Noginov, M. A.; Barnakov, Y. A.; Zhu, G.; Tumkur, T.; Li, H.; Narimanov, E. E. *Appl. Phys. Lett.* **2009**, *94*, 151105.
(9) Custodio, L. M.; Sousa, C. T.; Ventura, J.; Teixeira, J. M.; Marques, P. V. S.; Araujo, J. P. *Phys. Rev. B* **2012**, *85*, 165408.
(10) Pollard, R. J.; Murphy, A.; Hendren, W. R.; Evans, P. R.; Atkinson, R.; Wurtz, G. A.; Zayats, A. V.; Podolskiy, V. A. *Phys. Rev. Lett.* **2009**, *102*, 127405.
(11) Wurtz, G. A.; Pollard, R.; Hendren, W.; Wiederrecht, G. P.; Gosztola, D. J.; Podolskiy, V. A.; Zayats, A. V. *Nat. Nanotechnol.* **2011**, *6*, 106−110.
(12) Kawata, S.; Ono, A.; Verma, P. *Nat. Photonics* **2008**, *2*, 438−442.
(13) Yao, J.; Wang, Y.; Tsai, K.-T.; Liu, Z.; Yin, X.; Bartal, G.; Stacy, A. M.; Wang, Y.-L.; Zhang, X. *Philos. Trans. R. Soc., A* **2011**, *369*, 3434−3446.
(14) Yao, J.; Tsai, K.-T.; Wang, Y.; Liu, Z.; Bartal, G.; Wang, Y.-L.; Zhang, X. *Opt. Express* **2009**, *17*, 22380−22385.
(15) Casse, B. D. F.; Lu, W. T.; Huang, Y. J.; Gultepe, E.; Menon, L.; Sridhar, S. *Appl. Phys. Lett.* **2010**, *96*, 023114.
(16) Belov, P. A.; Palikaras, G. K.; Zhao, Y.; Rahman, A.; Simovski, C. R.; Hao, Y.; Parini, C. *Appl. Phys. Lett.* **2010**, *97*, 191905.
(17) Ginzburg, P.; Rodriguez Fortuno, F. J.; Wurtz, G. A.; Dickson, W.; Murphy, A.; Morgan, F.; Pollard, R. J.; Iorsh, I.; Atrashchenko, A.; Belov, P. A.; Kivshar, Y. S.; Nevet, A.; Ankonina, G.; Orenstein, M.; Zayats, A. V. *Opt. Express* **2013**, *21*, 14907−14917.
(18) Narimanov, E. E.; Li, H.; Barnakov, Y. A.; Tumkur, T. U.; Noginov, M. A. *Opt. Express* **2013**, *21*, 14956−14961.
(19) Kabashin, A. V.; Evans, P.; Pastkovsky, S.; Hendren, W.; Wurtz, G. A.; Atkinson, R.; Pollard, R.; Podolskiy, V. A.; Zayats, A. V. *Nat. Mater.* **2009**, *8*, 867−871.
(20) Soukoulis, C. M.; Linden, S.; Wegener, M. *Science* **2007**, *315*, 47−49.
(21) Soukoulis, C. M.; Wegener, M. *Nat. Photonics* **2011**, *5*, 523−530.
(22) Yakovlev, V. V.; Dickson, W.; Murphy, A.; McPhillips, J.; Pollard, R. J.; Podolskiy, V. A.; Zayats, A. V. *Adv. Mater.* **2013**, *25*, 2351−2356.
(23) Ginzburg, P.; Krasavin, A. V.; Poddubny, A. N.; Belov, P. A.; Kivshar, Y. S.; Zayats, A. V. *Phys. Rev. Lett.* **2013**, *111*, 036804.

(24) Chu, J.-Y.; Wang, T.-J.; Chang, Y.-C.; Lin, M.-W.; Yeh, J.-T.; Wang, J.-K. *Ultramicroscopy* **2008**, *108*, 314−319.
(25) Keilmann, F.; Hillenbrand, R. *Philos. Trans. R. Soc., A* **2004**, *362*, 787−805.
(26) Bek, A.; Vogelgesang, R.; Kern, K. *Rev. Sci. Instrum.* **2006**, *77*, 043703.
(27) Alonso-Gonzalez, P.; Albella, P.; Schnell, M.; Chen, J.; Huth, F.; Garcia-Etxarri, A.; Casanova, F.; Golmar, F.; Arzubiaga, L.; Hueso, L. E.; Aizpurua, J.; Hillenbrand, R. *Nat. Commun.* **2012**, *3*, 684.
(28) Chen, J.; Badioli, M.; Alonso-Gonzalez, P.; Thongrattanasiri, S.; Huth, F.; Osmond, J.; Spasenovic, M.; Centeno, A.; Pesquera, A.; Godignon, P.; Zurutuza Elorza, A.; Camara, N.; Javier Garcia de Abajo, F.; Hillenbrand, R.; Koppens, F. H. L. *Nature* **2012**, *487*, 77−81.
(29) Cheng, T.-Y.; Wang, H.-H.; Chang, S. H.; Chu, J.-Y.; Lee, J.-H.; Wang, Y.-L.; Wang, J.-K. *Phys. Chem. Chem. Phys.* **2013**, *15*, 4275−4282.
(30) Zentgraf, T.; Dorfmueller, J.; Rockstuhl, C.; Etrich, C.; Vogelgesang, R.; Kern, K.; Pertsch, T.; Lederer, F.; Giessen, H. *Opt. Lett.* **2008**, *33*, 848−850.
(31) Alonso-Gonzalez, P.; Schnell, M.; Sarriugarte, P.; Sobhani, H.; Wu, C.; Arju, N.; Khanikaev, A.; Golmar, F.; Albella, P.; Arzubiaga, L.; Casanova, F.; Hueso, L. E.; Nordlander, P.; Shvets, G.; Hillenbrand, R. *Nano Lett.* **2011**, *11*, 3922−3926.
(32) Dorfmueller, J.; Dregely, D.; Esslinger, M.; Khunsin, W.; Vogelgesang, R.; Kern, K.; Giessen, H. *Nano Lett.* **2011**, *11*, 2819−2824.
(33) Elser, J.; Wangberg, R.; Podolskiy, V. A.; Narimanov, E. E. *Appl. Phys. Lett.* **2006**, *89*, 261102.
(34) Evans, P. R.; Kullock, R.; Hendren, W. R.; Atkinson, R.; Pollard, R. J.; Eng, L. M. *Adv. Funct. Mater.* **2008**, *18*, 1075−1079.
(35) Schnell, M.; Garcia-Etxarri, A.; Huber, A. J.; Crozier, K. B.; Borisov, A.; Aizpurua, J.; Hillenbrand, R. *J. Phys. Chem. C* **2010**, *114*, 7341−7345.
(36) Wells, B. M.; Zayats, A. V.; Podolskiy, V. A. *Phys. Rev. B* **2014**, *89*, 035111.

Nonlocal optics of plasmonic nanowire metamaterials

Brian M. Wells,[1] Anatoly V. Zayats,[2] and Viktor A. Podolskiy[1]
[1]*Department of Physics and Applied Physics, University of Massachusetts Lowell, Lowell, Massachusetts 01854, USA*
[2]*Department of Physics, King's College London, Strand, London WC2R 2LS, United Kingdom*
(Received 15 August 2013; revised manuscript received 16 December 2013; published 9 January 2014)

We present an analytical description of the nonlocal optical response of plasmonic nanowire metamaterials that enable negative refraction, subwavelength light manipulation, and emission lifetime engineering. We show that dispersion of optical waves propagating in nanowire media results from coupling of transverse and longitudinal electromagnetic modes supported by the nanowires and derive the nonlocal effective medium approximation for this dispersion. We derive the profiles of electric field across the unit cell, and use these expressions to solve the long-standing problem of additional boundary conditions in calculations of transmission and reflection of waves by nonlocal nanowire media. We verify our analytical results with numerical solutions of Maxwell's equations and discuss generalization of the developed formalism to other uniaxial metamaterials.

DOI: 10.1103/PhysRevB.89.035111 PACS number(s): 78.20.Ci, 42.70.−a, 78.20.Bh

I. INTRODUCTION

Nanowire-based composites have recently attracted significant attention due to their unusual and counterintuitive optical properties that include negative refraction, subwavelength confinement of optical radiation, and modulation of photonic density of states [1–6]. Due to relatively low loss and ease of fabrication, nanowire composites found numerous applications in subwavelength imaging, biosensing, acousto-optics, and ultrafast all-optical processing, spanning visible to THz frequencies [7–19]. Wire materials are a subclass of uniaxial metamaterials that have homogeneous internal structure along one preselected direction. In all, this class of composites represents a flexible platform for engineering of optical landscape from all-dielectric birefringent media, to epsilon-near-zero, to hyperbolic, and epsilon-near-infinity regimes, each of which has its own class of benefits and applications [20–23].

In this work we present an analytical technique that provides adequate description of electromagnetism in wire-based metamaterials taking into account nonlocal optical response originating from the homogenization procedure. The approach can be straightforwardly extended to describe optics of coaxial-cable-like media [24–26] and numerous other uniaxial composites. The developed formalism reconciles the local and nonlocal effective-medium theories often used to describe the optics of nanowire composites in different limits [27–35]. More importantly, the formalism relates the origin of optical nonlocality to collective (averaged over many nanowires) plasmonic excitation of wire composite, and provides the recipe to implement additional boundary conditions in composite structures.

We illustrate the developed technique on the example of plasmonic nanowire metamaterials, formed by an array of aligned plasmonic nanowires embedded in a dielectric host. For simplicity, we fix the frequency of electromagnetic excitations and the unit cell parameters of the system, and vary only the permittivity of the wire inclusions. (The developed formalism can be readily applied for systems where both permittivity and frequency are changed at the same time.) We assume that the system operates in the effective-medium regime (its unit cell $a \ll \lambda_0$ with λ_0 being the free-space wavelength) and that the surface concentration of plasmonic wires is small $p = \pi R^2/a^2 \ll 1$. The parameters used in this work are $R = 20$ nm, $a = 100$ nm, $\epsilon_h = 1$ or $\epsilon_h = 2.25$, $L = 1$ μm, $\lambda_0 = 1.5$ μm (see Fig. 1), which are typical for composites fabricated with anodized alumina templates [2,13]. Supplementary information (SI) [36] presents the analysis of full-wave solutions of Maxwell equations in wire media.

II. ELECTROMAGNETIC WAVES SUPPORTED BY BULK NANOWIRE COMPOSITES

As previously mentioned, the optical response of nanowire materials resembles that of uniaxial media with optical axis parallel to the direction of the nanowires (z). Therefore, dielectric permittivity tensor describing properties of waves propagating in the wire media is diagonal with components $\epsilon_x = \epsilon_y = \epsilon_{x,y}$ and ϵ_z.

It has been shown that at optical and near-IR frequencies, the behavior of these components is largely described by Maxwell-Garnett type effective medium theory (EMT) [27–30,37]. In this approach, the microscopic distribution of the field is given by solutions of the Maxwell equations in quasistatic limit

$$E_z^{mg} = \mathfrak{e}_z^{mg},$$
$$E_x^{mg} = \mathfrak{e}_x^{mg} \times \begin{cases} 2\frac{\epsilon_h}{\epsilon_h+\epsilon_i}, & r \leqslant R, \\ 1 + R^2 \frac{\epsilon_h-\epsilon_i}{\epsilon_h+\epsilon_i} \frac{y^2-x^2}{(x^2+y^2)^2}, & r > R, \end{cases} \quad (1)$$

with ϵ_i and ϵ_h being the permittivities of wire inclusions and of host material, respectively, and parameters $\mathfrak{e}_x^{mg}$ and $\mathfrak{e}_z^{mg}$ are the field amplitudes. Straightforward averaging of the jth component ($j = x,y,z$) of the fields over the unit cell yields the effective permittivity $\epsilon_j^{mg} = \langle \epsilon(x,y) E_j^{mg}(x,y)\rangle / \langle E_j^{mg}(x,y)\rangle$:

$$\epsilon_{x,y}^{mg} = \epsilon_h \frac{(1+p)\epsilon_i + (1-p)\epsilon_h}{(1+p)\epsilon_h + (1-p)\epsilon_i},$$
$$\epsilon_z^{mg} = p\epsilon_i + (1-p)\epsilon_h. \quad (2)$$

By adjusting composition of the metamaterial and operating wavelength, the optical response of the composite can be controlled between all-dielectric elliptic ($\epsilon_{x,y}^{mg} > 0, \epsilon_z^{mg} > 0$),

 ©2014 American Physical Society

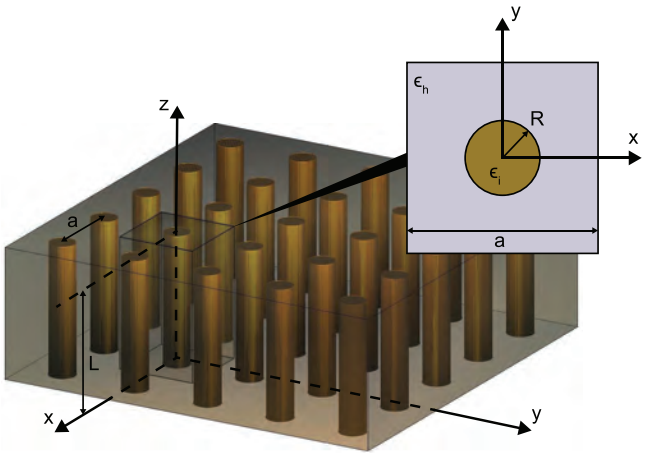

FIG. 1. (Color online) Schematic geometry and a unit cell of a nanowire composite.

epsilon-near-zero (ENZ, $\epsilon_z^{mg} \simeq 0$) and hyperbolic ($\epsilon_{x,y}^{mg} > 0, \epsilon_z^{mg} < 0$) regimes. In the two latter regimes, metamaterial supports optical waves with either small or large effective modal index motivating a number of potential applications in molding of light [20–22], cloaking [14–16], and subwavelength light manipulation [1,9–12].

At the same time, it has been shown that at lower frequencies where $-\epsilon_i \gg 1$, ϵ_z of wire composites becomes strongly nonlocal (exhibits strong dependence on k_z) [31–34]. Similar dependence has been recently shown to take place at visible frequencies in the ENZ regime [35]. Nonlocality, especially in the ENZ regime, has been shown to fundamentally alter the optical response of wire composite, leading to excitation of new types of optical waves, and requiring additional boundary conditions for analytical description of their excitation [32–35,38]. Despite extensive previous research, existing first-principal theoretical models describing optics of wire composites [32–34] cannot be used at visible and (near)-IR frequencies (see Appendix C), with remaining models requiring fitting [35] or numerical solutions of Maxwell equations. Here we present a formalism free of the above shortcomings.

The dispersion of plane waves propagating inside homogeneous (nonlocal) uniaxial materials can be derived from the well-known relation

$$\det\left|\vec{k}\cdot\vec{k}\,\delta_{ij} - k_i k_j - \epsilon_{ij}\frac{\omega^2}{c^2}\right| = 0, \tag{3}$$

with $\vec{k}$ and ω being the wave vector and the angular frequency of the plane wave, respectively, c being the speed of light in vacuum, ϵ being the generally nonlocal dielectric permittivity tensor of the metamaterial, and subscripts ij corresponding to Cartesian components [39]. In the local regime permittivity tensor is diagonal with $\epsilon_{ii} = \epsilon_i^{mg}$.

We now focus on the development of the model for the nonlocal effective permittivity of a nanowire composite. For propagation along the optical axis ($k_x = k_y = 0$), Eq. (3) allows two types of solutions. One is the well-known solution $k_z^{mg} = \sqrt{\epsilon_{x,y}}\omega/c$. In nanowire composites, this solution corresponds to the local permittivity $\epsilon_{xx} = \epsilon_{yy} = \epsilon_{x,y}^{mg}$ which is related to plasmonic oscillations perpendicular to the wire axes [27–30] and is thus influenced by the plasmonic resonance of the composite, slightly shifted from the position of the localized surface plasmon resonances in isolated wires due to interwire interaction.

The second solution of Eq. (3) corresponds to $\epsilon_z(k_z) = 0$. It describes a longitudinal wave propagating in the z direction, with $\vec{E}\|\vec{k}\|\hat{z}$. This solution is also known as the additional (TM-polarized) wave.

As we show below, in nanowire systems this mode results from the interaction between cylindrical surface plasmon (CSP) modes [40] of the individual wires that comprise the collective (related to many wires) longitudinal electromagnetic mode. The components of the fields of the this mode can be related to its z components that in turn can be written as a linear combination of cylindrical waves. For the square unit cell geometry, considered in this work, the latter combination will only contain cylindrical modes with $m = 0,4,8,\ldots$. Explicitly,

$$\begin{aligned} E_z^l &= e^{-ik_z^l z}\sum_m \cos(m\phi) \\ &\quad\times \begin{cases} a_m J_m(\kappa_i r), & r \leqslant R, \\ [\alpha_m^+ H_m^+(\kappa_h r) + \alpha_m^- H_m^-(\kappa_h r)], & r > R, \end{cases} \\ H_z^l &= e^{-ik_z^l z}\sum_m \begin{Bmatrix} 1, & m = 0 \\ \sin(m\phi), & m \geqslant 1 \end{Bmatrix} \\ &\quad\times \begin{cases} b_m J_m(\kappa_i r), & r \leqslant R, \\ [\beta_m^+ H_m^+(\kappa_h r) + \beta_m^- H_m^-(\kappa_h r)], & r > R, \end{cases} \end{aligned} \tag{4}$$

with $\kappa_{\{i,h\}}^2 + k_z^{l\,2} = \epsilon_{\{i,h\}}\omega^2/c^2$. Note that continuity of E_z, H_z, E_ϕ, and H_ϕ at $r = R$ uniquely define the parameters $\alpha_m^+, \beta_m^+, a_m$, and b_m as a function of α_m^-, and β_m^-. The details of these derivations are provided in Appendix A.

The field of the mode has to satisfy the periodicity condition $E,H|_{x=-a/2} = E,H|_{x=+a/2}$. An analysis of the fields produced by a series in Eq. (4) suggests that such a solution can be realized when $\beta_m^- = 0$, and k_z and α_m^- are obtained from the eigenvalue-type problem

$$\sum_m \widehat{\mathcal{H}}_{y\,jm}(k_z^l)\alpha_m^- = 0, \tag{5}$$

with jm elements of matrix $\widehat{\mathcal{H}}_y$ corresponding to the y component of the magnetic field produced by the m_{th} Hankel function at the location $\{x,y\} = \{\frac{a}{2}, j\frac{a}{2N_m}\}$, with N_m being the number of m terms in Eq. (4) (see Appendix B for details). Our analysis suggests that as number of terms in Eq. (4) increases, the dispersion produced by this analytical technique quickly converges to the dispersion obtained by direct numerical solution of Maxwell's equations (here we use finite element method and rigorous-coupled-wave analysis [36]). Figure 2 demonstrates the excellent agreement between the numerical and analytical solutions corresponding to two- and three-term series $m = \{0,4\}$, $m = \{0,4,8\}$, and clearly demonstrates the longitudinal character of this mode. This wave is strongly dispersive in the regime $\epsilon_i \to -\epsilon_h$, corresponding to the surface plasmon oscillations on the metal-dielectric interface. On the other hand, when $-\epsilon_i \gg \epsilon_h$ (realized at mid-IR and lower frequencies for noble metals), the wave vector of the

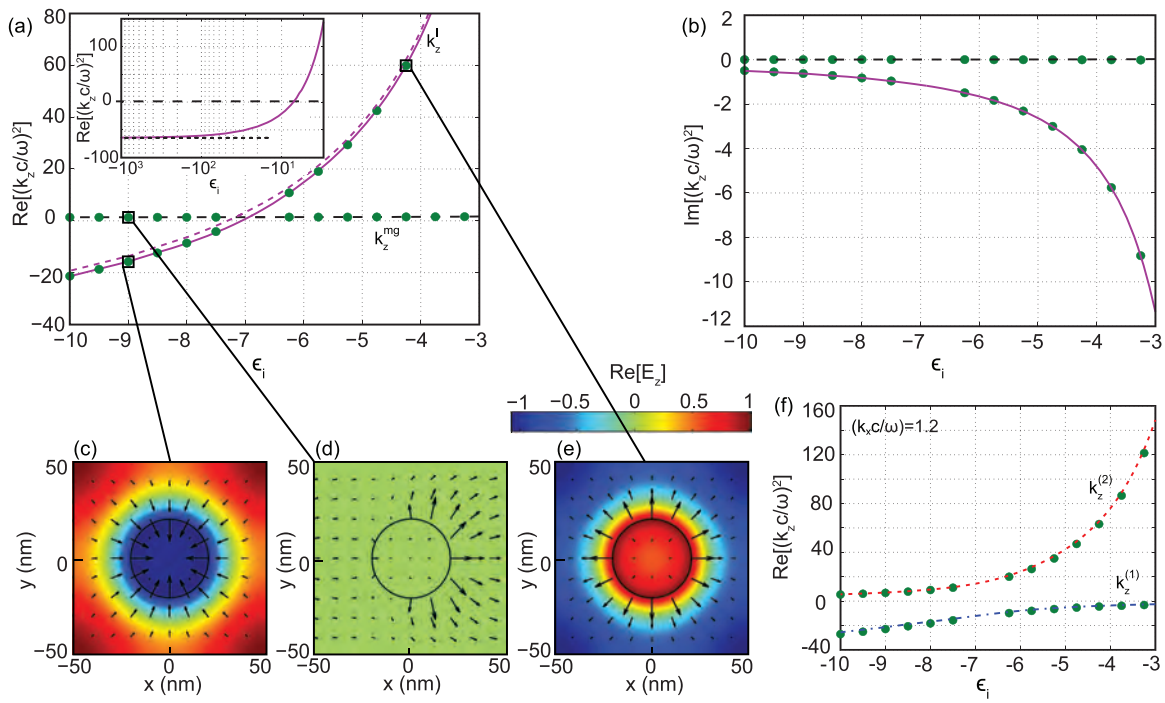

FIG. 2. (Color online) (a) and (b) Dispersion in nanowire composite ($\epsilon_h = 1$) as a function of wire permittivity. Dashed and solid lines represent transverse and longitudinal waves [k_z^{mg} and k_z^l, Eq. (5), $m = \{0,4,8\}$], respectively; dotted line represents results of Eq. (5) for $m = \{0,4\}$; symbols represent numerical solutions of the Maxwell's equations; for $-\epsilon_i \gg \epsilon_h$, $k_z^l \to n_\infty^l \omega/c$ [dotted line in inset in (a)]. (c)–(e) electric field in the unit cell; surface plots and arrows represent E_z and $\vec{E}_{x,y}$ components, respectively. (f) Modal dispersion for off-axis propagation [Eq. (7)].

longitudinal mode approaches $n_\infty^l \omega/c$, and its transverse counterpart approaches light line (see Refs. [32–34] and Fig. 2).

Comparing the dispersion relation corresponding to microscopic [Eq. (5)] and effective medium approximation $\epsilon_z(k_z) = 0$, a complete description of the nonlocal effective permittivity can be obtained. The functional dependence of nonlocal permittivity can be approximated as

$$\epsilon_z(k_z) = \xi\left(k_z^2 - k_z^{l\,2}\right)\frac{c^2}{\omega^2}, \tag{6}$$

where k_z is the wave vector of the mode in the nonlocal effective medium approximation, k_z^l is the wave vector of the mode of the composite in the microscopic theory, and ξ is the factor which will be determined below.

The above considerations can be extended to the case of propagation of waves at an angle to the optical axis. For simplicity we consider the case $k_y = 0, k_x \neq 0$. It is relatively straightforward to transform Eq. (3) into a set of two uncoupled dispersion relations. For nanowire composites, the first of these, $k_x^2 + k_z^2 = \epsilon_{x,y}^{mg}\omega^2/c^2$ describes the propagation of transverse-electric (TE)-polarized waves. The second one, $\epsilon_z(k_z)(k_z^2 - \epsilon_{x,y}^{mg}\frac{\omega^2}{c^2}) = -\epsilon_{x,y}^{mg}k_x^2$, describes the propagation of the transverse-magnetic (TM)-polarized waves. Taking into account Eq. (6), the latter relation can be rewritten as

$$\left(k_z^2 - k_z^{l\,2}\right)\left(k_z^2 - \epsilon_{x,y}^{mg}\frac{\omega^2}{c^2}\right) = -\frac{\epsilon_{x,y}^{mg}}{\xi}\frac{\omega^2}{c^2}k_x^2 \tag{7}$$

that reflects the fact that similar to other nonlocal materials [38], nanowire composites support two TM-polarized waves propagating with different indices.

Equation (7) clearly shows that off-angle ($k_x \neq 0$) propagation of the two TM-polarized waves in anisotropic wire media can be mapped to a microscopic model of optical properties of a nanowire array. In this description, the two TM modes are determined by the components of the effective permittivities arising from (i) transverse (electron oscillations perpendicular to the nanowire axes) and (ii) longitudinal (electron oscillations and the wave vector parallel to the nanowire axes) parts of the cylindrical plasmons of the wires. The off-angle wave vector plays the role of the coupling constant. This nonlocality is present only in the effective medium model due to the homogenization procedure; in the microscopic model of the nanowire array, all the quantities are local.

The remaining free parameter of the model, multiplicative factor ξ, can be determined by requiring that in the limit of small k_x the properties of one of the two TM-polarized waves follow elliptic or hyperbolic dispersion and has $k_z(k_x) =$ const dependence, observed in the wire media when $\epsilon_z^{mg} > 0$, $\epsilon_z^{mg} < 0$, and $\epsilon_z^{mg} \ll -1$, respectively [27–30,32–34]. The relationship

$$\xi = p\frac{\epsilon_i + \epsilon_h}{\epsilon_h - (n_\infty^l)^2} \tag{8}$$

adequately describes optics of wire media in these three limits. The excellent agreement between the predictions of Eq. (7) and the full-wave numerical solutions of Maxwell equations

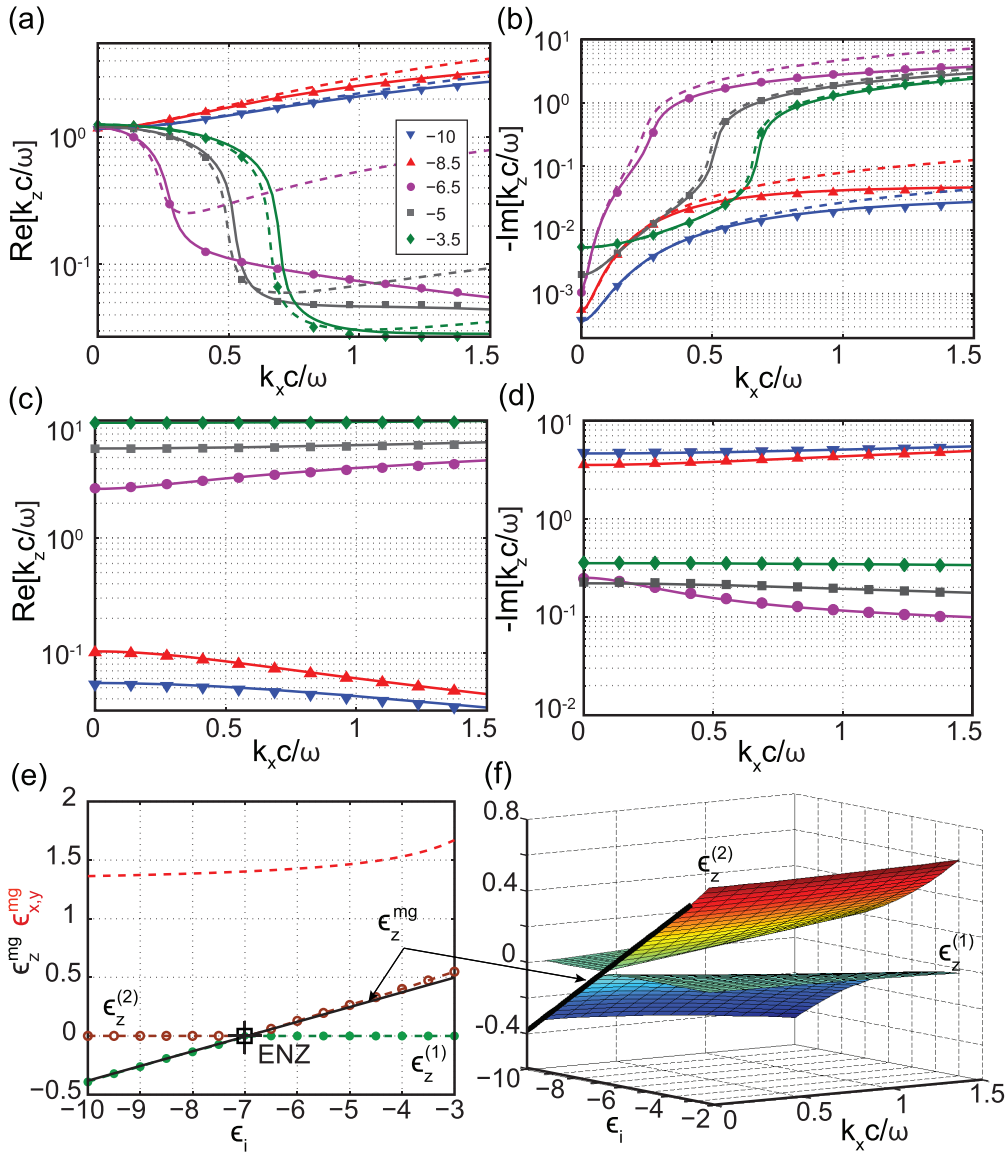

FIG. 3. (Color online) (a)–(d) Isofrequency contours of TM-polarized modes in nanowire composites with $\epsilon_h = 1$. Solid lines and symbols correspond to Eq. (7) and numerical solutions of Maxwell equations, respectively; dashed lines represent local EMT; (a) and (b) represent properties of main TM-polarized mode; (c) and (d) correspond to additional wave. (e) and (f) The effective medium permittivity of nonlocal nanowire composite for $k_x = 0$ (c) and for $k_x \neq 0$ (d); $\epsilon_z^{(1)}, \epsilon_z^{(2)}$ represent two solutions of Eq. (6); cross mark indicates ENZ condition ($\epsilon_z^{mg} \simeq 0$).

is shown in Figs. 2–4. As expected, the isofrequency of the "main" TM-polarized wave resembles ellipse or hyperbola that for small values of k_x is well described by $\hat{\epsilon}^{mg}$. At the same time, the dependence $k_z(k_x)$ in "additional" wave is opposite to that of its main counterpart. The z component of permittivity is described by Eq. (2) only for on-axis ($k_x = 0$) propagation, and exhibits strong spatial dispersion for oblique propagation of light.

The presented formalism provides a mechanism to calculate the deviation of the dispersion of the waves in nanowire materials from the prediction of local effective medium technique. In particular, this deviation places fundamental limits on subwavelengh light manipulation and on increase of local density of photonics states [3–6]. It is also likely to affect the cloaking performance of nanowire-based structures [14–16].

Now that the origin and dispersion of the modes propagating in nanowire systems is understood, we focus on the analysis of the optical properties of finite-size wire arrays. Since in the EMT approximation the fields of TE- and TM-polarized modes are orthogonal to each other, and since propagation of TE-polarized light through the wire-based system is only affected by x, y components of permittivity, this propagation can be successfully described by Eq. (2) [27–30]. Here we focus on the analysis of propagation of TM-polarized light. This analysis must answer two important questions: (i) What is the structure of electromagnetic waves propagating in the system, and (ii) what are the additional boundary conditions needed to determine the amplitudes of the two TM-polarized modes inside the wire system?

Consistent effective medium description requires that the unit-cell averaged fields satisfy both constituent relations $\epsilon_j =$

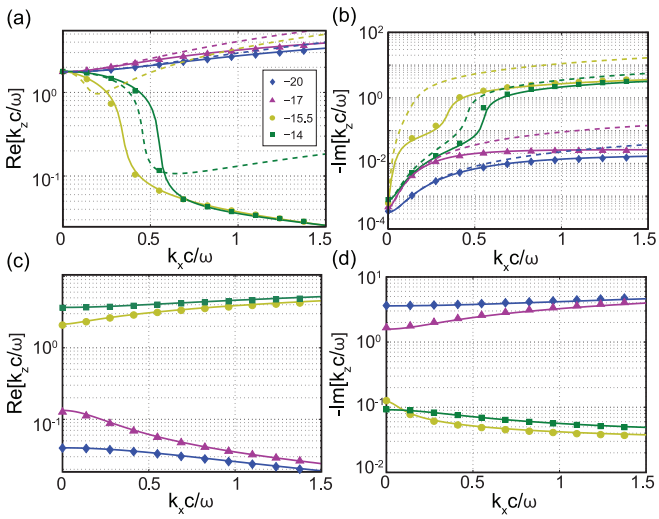

FIG. 4. (Color online) Same as Figs. 3(a)–3(d) for $\epsilon_h = 2.25$.

$\langle \epsilon E_j \rangle / \langle E_j \rangle$ and relations between the field components of the plane wave $\langle \epsilon E_z \rangle = -k_x/k_z \langle \epsilon E_x \rangle$. With these constraints, we start from Eqs. (1) and (4), determine the parameters α_0^-, $\mathfrak{e}_z^{mg}$, and $\mathfrak{e}_x^{mg}$ by normalizing $\langle E_z^l \rangle = \langle E_x^{mg} \rangle = \langle E_z^{mg} \rangle = 1$, and construct the fields of the two waves propagating in the wire media as $\vec{E}(x,y)e^{i\omega t - ik_x x - ik_z z}$ with

$$\begin{aligned} E_x(x,y) &= E_x^{mg}, \\ E_z(x,y) &= \gamma^{mg} E_z^{mg} + \gamma^l E_z^l|_{z=0}, \end{aligned} \tag{9}$$

and

$$\begin{aligned} \gamma^{mg} &= -\frac{\epsilon_{x,y}^{mg} k_x}{\epsilon_z k_z} \frac{\epsilon_z - \epsilon^l}{\epsilon_z^{mg} - \epsilon^l}, \\ \gamma^l &= -\frac{\epsilon_{x,y}^{mg} k_x}{\epsilon_z k_z} \frac{\epsilon_z - \epsilon_z^{mg}}{\epsilon^l - \epsilon_z^{mg}}. \end{aligned} \tag{10}$$

In the expressions above $\epsilon_z \equiv \epsilon_z(k_z)$ is given by Eq. (6), $k_z(k_x)$ by Eq. (7), and $\epsilon^l = \langle \epsilon(x,y) E_z^l(x,y) \rangle / \langle E_z^l(x,y) \rangle$.

Equation (9) represents a transition between full-wave solutions of Maxwell equations in the nanowire array where the fields oscillate on the scale of the individual wires, and effective-medium solutions where plane waves propagate in the homogenized material. Since our model for $\vec{E}^{mg}$ assumes quasistatic limit [Eq. (1)], Eq. (9) is technically valid in the limit $a \ll 2\pi/k_x$, $a \ll \lambda_0$. Any effective medium technique is expected to fail in the limit $k_x \gtrsim 2\pi/a$.

III. TRANSMISSION AND REFLECTION PROPERTIES OF NONLOCAL METAMATERIAL SLABS

Finally, we consider the problem of reflection/refraction of light at the interface of nonlocal (meta-) materials, extending the well-developed transfer-matrix formalism [41,42] to nonlocal composites. The typical geometry of light propagation through a finite-thickness slab of nanowire material is shown in Fig. 5.The problem of calculating reflection/transmission of light through the slab of nanowire material can be reduced to the problem of finding the amplitudes of reflected and transmitted waves throughout the system in terms of the

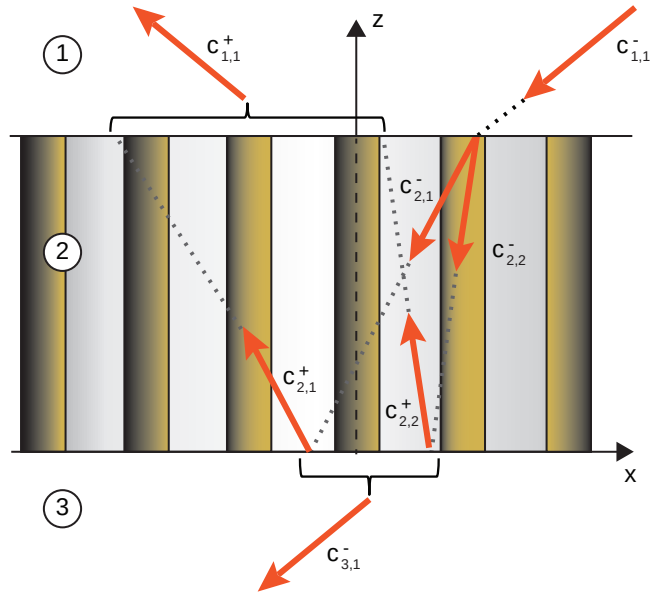

FIG. 5. (Color online) Schematic of TMM for a nanowire composite. Each mode is labeled to clarify notation as well as interface numbers.

amplitude of the single wave incident on the material ($c_{1,1}^-$). This problem, in turn, can be reduced to the problem of finding the amplitudes of waves scattered by each individual interface in terms of the amplitudes of the (multiple) waves incident at this interface.

Maxwell equations require continuity of (microscopic) E_x and D_z, and the effective-medium boundary conditions can be obtained by averaging these relationships across the unit cell. Multiple, linearly independent boundary conditions can be obtained by requiring the continuity of $\mathbb{E}^n = \langle e^{2\pi i n \frac{x}{a}} E_x \rangle$ and $\mathbb{D}^n = \langle e^{2\pi i n \frac{x}{a}} D_z \rangle$ with different integer n.

In particular, for the interface between two conventional materials, continuity of $\mathbb{E}^0, \mathbb{D}^0$ yield conventional TMM results. If one of the media is nonlocal metamaterial, we suggest to complement the above boundary conditions by the additional boundary condition (ABC) of continuity of $\mathbb{D}^1$ (if both materials are nonlocal, addition of second ABC of continuity of $\mathbb{E}^1$ is required). Explicitly, assuming that the top interface is located at $z = z_0$, the boundary conditions for this interface are implemented as

$$\begin{aligned} & c_{1,1}^+ \mathbb{E}_{1,1}^0 e^{ik_{z_{1,1}} z_0} + c_{1,1}^- \mathbb{E}_{1,1}^0 e^{-ik_{z_{1,1}} z_0} \\ &\quad = \sum_{l=1,2} c_{2,l}^+ \mathbb{E}_{2,l}^0 e^{ik_{z_{2,l}} z_0} + c_{2,l}^- \mathbb{E}_{2,l}^0 e^{-ik_{z_{2,l}} z_0}, \\ & c_{1,1}^+ \mathbb{D}_{1,1}^0 e^{ik_{z_{1,1}} z_0} - c_{1,1}^- \mathbb{D}_{1,1}^0 e^{-ik_{z_{1,1}} z_0} \\ &\quad = \sum_{l=1,2} c_{2,l}^+ \mathbb{D}_{2,l}^0 e^{ik_{z_{2,l}} z_0} - c_{2,l}^- \mathbb{D}_{2,l}^0 e^{-ik_{z_{2,l}} z_0}, \\ & c_{1,1}^+ \mathbb{D}_{1,1}^1 e^{ik_{z_{1,1}} z_0} - c_{1,1}^- \mathbb{D}_{1,1}^1 e^{-ik_{z_{1,1}} z_0} \\ &\quad = \sum_{l=1,2} c_{2,l}^+ \mathbb{D}_{2,l}^1 e^{ik_{z_{2,l}} z_0} - c_{2,l}^- \mathbb{D}_{2,l}^1 e^{-ik_{z_{2,l}} z_0}. \end{aligned} \tag{11}$$

In the expressions above the double subscript represents the layer number in the system and the mode number within

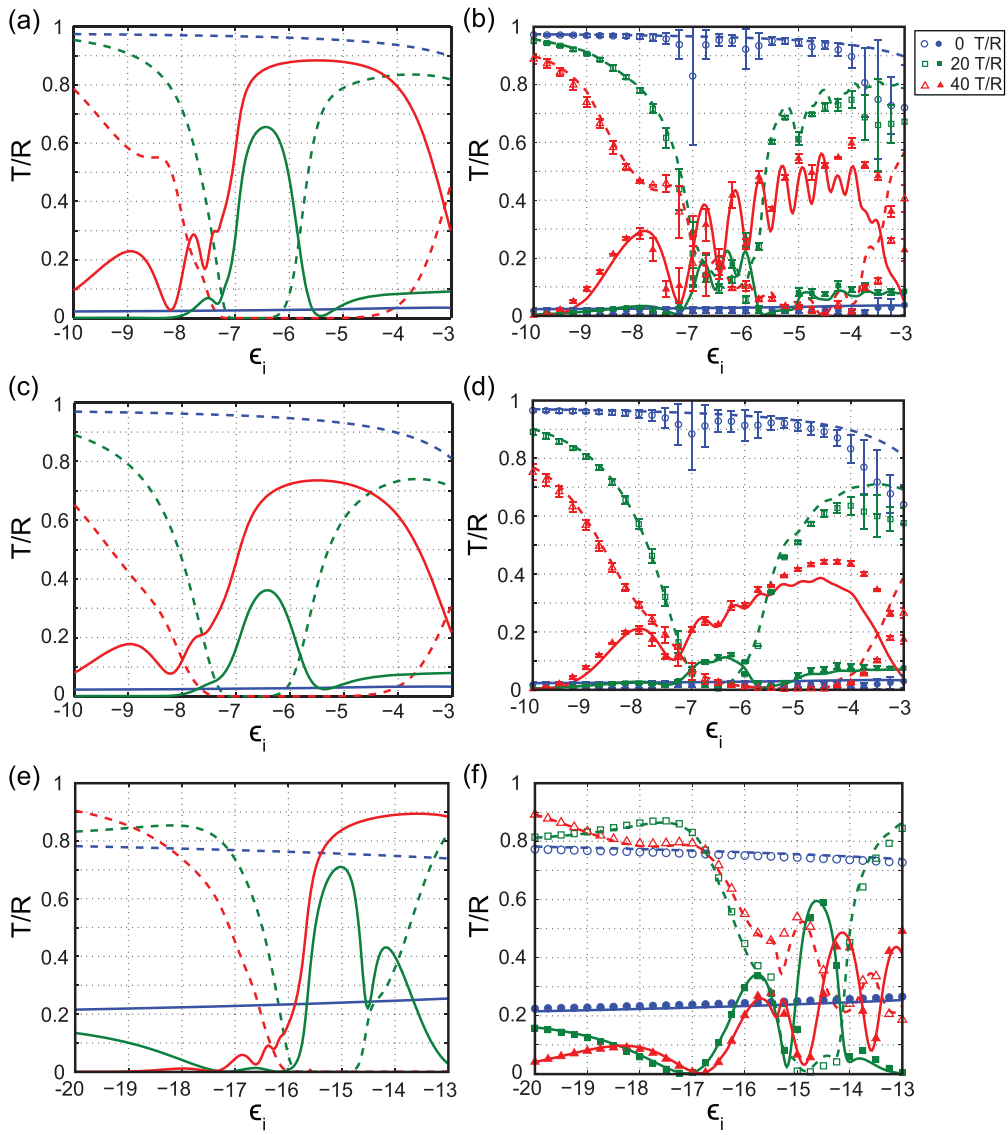

FIG. 6. (Color online) Transmission and reflection of light through a parallel slab of nanowire media, suspended in air for (a)–(d) and in polymer with $\epsilon_h = 2.25$ (e) and (f) with $\mathrm{Im}(\epsilon_i) = -0.1$ (a), (b), (e), and (f), and $\mathrm{Im}(\epsilon_i) = -0.25$ (c) and (d). (a), (c), and (e): Local TMM calculations. (b), (d), and (f): TMM simulations with the nonlocal EMT developed here (lines) and numerical solutions of Maxwell equations (symbols). Solid lines and filled symbols represent reflection. Dashed lines and empty symbols represent transmission; different colors/shapes correspond to different angles for incident angles, blue circles: 0°, green squares: 20°, red triangles: 40°.

the layer, while the "±" superscript represent the direction of the wave propagation (see Fig. 5). The amplitudes of the wave propagating in the system represent the amplitude of $\mathbb{E}^0$; therefore, the amplitudes of E_x are symmetric with respect to change of propagation direction $k_z \to -k_z$, while the amplitudes of E_z, D_z are antisymmetric

Note that since polarization along the optical axis P_z is dominated by the field of longitudinal wave, this ABC is close to the heuristic condition $P_\perp^{\mathrm{nonlocal}} = 0$, proposed for homogeneous [38] and composite [35] materials, and to condition of continuity of $\epsilon_h \mathbb{E}^0$, suggested for ultrathin high-conductivity wires [32–34] (in general the above ABCs are not identical to each other). When both media across the interface are nonlocal, continuity of $\mathbb{E}^1$ plays the role of the second additional boundary condition. Note that due to presence of longitudinal modes on both sides of the interface, $P_\perp^{\mathrm{nonlocal}}$ may not vanish in this configuration. As an additional crosscheck, the proposed combination of ABCs ensures full transmission of light through "virtual" interface between two identical nanowire metamaterials.

Transmission and reflection of metamaterial are compared to the full-vectorial numerical solutions of Maxwell's equations, predictions of conventional (local) effective medium theory, and predictions of the nonlocal EMT developed in this work in Fig. 6. It is seen the smaller the loss and the larger the angle of incidence the more important it becomes to take into account the nonlocal optics of nanowire composites. Interestingly, nonlocal response strongly affects optical response of the wire metamaterials across the broad range of the effective permittivities. This effect is most clearly seen in reflection, but is also visible in transmission, especially in the ENZ regime.

IV. CONCLUSIONS

We presented an approach to describe optics of nonlocal wire metamaterials across the whole optical spectrum. The formalism demonstrates excellent agreement with the results of numerical solutions of Maxwell's equations and is essential in development of an adequate description of optics in wire arrays, from understanding the true density of photonic states to the limits of resolution in these systems. Although not presented here, in our studies we also varied radius and lattice size in the composite (within $p \lesssim 0.3$ limit of applicability of Maxwell-Garnett formalism [29]), and obtained good agreement between analytical and numerical solutions of Maxwell equations. The developed formalism can be straightforwardly extended to describe the optics of other wirelike composites including coated wire structures, and coax-cable-based systems [24–26].

ACKNOWLEDGMENTS

This research is supported by US Army Research Office (Grant No. W911NF-12-1-0533), EPSRC (UK), and the ERC iPLASMM project (321268).

APPENDIX A: DISTRIBUTION OF ELECTROMAGNETIC FIELDS ACROSS THE UNIT CELL

Since the geometry of the system (see Fig. 1) is homogeneous along the z direction, the field in the unit cell can be represented as a linear combination of cylindrical waves having a well-defined value of the wave vector component k_z, given by Eq. (4).

The symmetry of the unit cell chosen in our work dictates the choice of $m = 0,4,8,\ldots$. The approach can be generalized to different unit cells by choosing an appropriate combination of m values. The technique can be further generalized by replacing $\{\sin m\phi, \cos m\phi\} \to \exp im\phi$ and expanding the summation over positive and negative values of m. In-plane components of the microscopic fields can be expressed as follows:

$$\begin{aligned} E_r^l &= \frac{i}{\kappa^2}\left(k_z^l \frac{\partial E_z^l}{\partial r} + \frac{\omega}{rc}\frac{\partial H_z^l}{\partial \phi}\right), \\ E_\phi^l &= \frac{i}{\kappa^2}\left(\frac{k_z^l}{r}\frac{\partial E_z^l}{\partial \phi} - \frac{\omega}{c}\frac{\partial H_z^l}{\partial r}\right), \\ H_r^l &= \frac{i}{\kappa^2}\left(-\frac{\epsilon\omega}{rc}\frac{\partial E_z^l}{\partial \phi} + k_z^l \frac{\partial H_z^l}{\partial r}\right), \\ H_\phi^l &= \frac{i}{\kappa^2}\left(\frac{\epsilon\omega}{c}\frac{\partial E_z^l}{\partial r} + \frac{k_z^l}{r}\frac{\partial H_z^l}{\partial \phi}\right). \end{aligned} \tag{A1}$$

Equation (A1) is valid both inside ($r \leqslant R$) and in-between ($r > R$) the nanowires; the value of r determines the choice of

$$\epsilon,\kappa = \begin{cases} \epsilon_i,\kappa_i, & r \leqslant R, \\ \epsilon_h,\kappa_h, & r > R. \end{cases}$$

For brevity, from this point on, we omit the arguments of Bessel functions; unless otherwise specified, it is assumed that $J_m = J_m(\kappa_i r)$; $H_m^\pm = H_m^\pm(\kappa_h r)$.

Note that only one of the three sets of coefficients $\{a_m,b_m\},\{\alpha_m^+,\beta_m^+\}$, and $\{\alpha_m^-,\beta_m^-\}$ is independent. We begin by using the continuity of the tangential components of the electric and magnetic fields at $r = R$ to obtain an expression for $\{a_m,b_m\},\{\alpha_m^+,\beta_m^+\}$ in terms of $\{\alpha_m^-,\beta_m^-\}$. Explicitly, the linear relationship

$$\begin{pmatrix} \alpha_m^+ \\ \vdots \\ \beta_m^+ \end{pmatrix} = \hat{S}\begin{pmatrix} \alpha_m^- \\ \vdots \\ \beta_m^- \end{pmatrix} \tag{A2}$$

can be derived from

$$\begin{aligned} &\begin{bmatrix} \frac{k_z^l m H_m^+}{R}\left(\frac{1}{\kappa_i^2} - \frac{1}{\kappa_h^2}\right) & \frac{\omega}{c}\left(\frac{J_m' H_m^+}{\kappa_i J_m} - \frac{H_m'^+}{\kappa_h}\right) \\ \frac{\omega}{c}\left(\frac{\epsilon_i J_m' H_m^+}{\kappa_i J_m} - \frac{\epsilon_h H_m'^+}{\kappa_h}\right) & \frac{k_z^l m H_m^+}{R}\left(\frac{1}{\kappa_i^2} - \frac{1}{\kappa_h^2}\right) \end{bmatrix}\begin{pmatrix} \alpha_m^+ \\ \beta_m^+ \end{pmatrix} \\ &= \begin{bmatrix} \frac{k_z^l m H_m^-}{R}\left(\frac{1}{\kappa_i^2} - \frac{1}{\kappa_h^2}\right) & \frac{\omega}{c}\left(\frac{J_m' H_m^-}{\kappa_i J_m} - \frac{H_m'^-}{\kappa_h}\right) \\ \frac{\omega}{c}\left(\frac{\epsilon_i J_m' H_m^-}{\kappa_i J_m} - \frac{\epsilon_h H_m'^-}{\kappa_h}\right) & \frac{k_z^l m}{R}\left(\frac{1}{\kappa_i^2} - \frac{1}{\kappa_h^2}\right) H_m^- \end{bmatrix}\begin{pmatrix} \alpha_m^- \\ \beta_m^- \end{pmatrix}, \end{aligned} \tag{A3}$$

where each of the four submatrices is a diagonal matrix with its elements corresponding to the Bessel function combinations evaluated at $r = R$. In this cylindrically symmetric case, the S matrix can be formally divided into four (diagonal) submatrices

$$\hat{S} = \begin{bmatrix} S_{11} & S_{12} \\ S_{21} & S_{22} \end{bmatrix}. \tag{A4}$$

The components S_{11} and S_{22} represent polarization-preserving TE, TM reflection, while the components S_{12},S_{21} represent polarization-mixing coupling of TM to TE waves. Note that in the cylindrical geometry, polarization-preserving reflection is only possible when either $m = 0$ or $k_z = 0$, which yields $\det S_{12} = \det S_{21} = 0$.

The relationships

$$\begin{aligned} a_m J_m &= \alpha_m^+ H_m^+ + \alpha_m^- H_m^-, \\ b_m J_m &= \beta_m^+ H_m^+ + \beta_m^- H_m^- \end{aligned} \tag{A5}$$

allow one to calculate the amplitudes $\{a,b\}$ based on the amplitudes of $\{\alpha^-,\beta^-\}$.

Combined, Eqs. (1), (A1), (A2), (A3), and (A5) provide complete information about the field distribution inside the unit cell once the parameters k_z^l and $\{\alpha^-,\beta^-\}$ are known. The formalism presented here can be straightforwardly expanded to calculate the field inside the structures with more complicated unit cells, that include multishelled wires, coax-cable-like systems, etc. (see, e.g., Refs. [24–26]). The formalism can be further extended to calculate fields inside the systems with noncircular cross section of the wires, in which case the S matrix ceases to be block diagonal [43–45].

APPENDIX B: DISPERSION OF THE LONGITUDINAL MODE

We now focus on the problem of calculating the dispersion of the mode, which reduces to the problem of calculating the relationship between internal structure of the unit cell and the set of parameters k_z and $\{\alpha^-,\beta^-\}$. The field of the eigenmode propagating in the periodic array of wires should

satisfy the Bloch-periodicity condition

$$\begin{matrix} E \\ H \end{matrix}\Bigg|_{x=-\frac{a}{2},y} = \begin{matrix} E \\ H \end{matrix}\Bigg|_{x=+\frac{a}{2},y} \tag{B1}$$

(here we enforce periodicity of y components of electric and magnetic fields). Although this condition should ideally be satisfied for all values of the y coordinate from the interval $y \in [-a/2, a/2]$, in practice it suffices to enforce the Bloch-periodicity condition for a number of fixed points $\{x_j, y_j\}$ equal to the number of m values in Eq. (4). In our calculations we assume $y_j = \frac{a}{2N_m} j$, with N_m being the number of m terms in expansion in Eq. (4). Our analysis suggests that the choice of the exact location of the points does not significantly alter the dispersion of the mode, derived with the technique described in this work.

Noting that $\sin(\phi) = \sin(\pi - \phi)$, $\cos(\phi) = -\cos(\pi - \phi)$, $\sin(m\phi) = -\sin[m(\pi - \phi)]$, and $\cos(m\phi) = \cos[m(\pi - \phi)]$, it can be shown that components of electric and magnetic field possess the following symmetry:

$$E_y(x,y) = E_y(-x,y),$$
$$H_y(x,y) = -H_y(-x,y).$$

Therefore, Eq. (B1) becomes equivalent to

$$\begin{pmatrix} \hat{0} & \hat{0} \\ \widehat{\widetilde{H^+}} & \widehat{H^+} \end{pmatrix} \begin{pmatrix} \alpha_m^+ \\ \beta_m^+ \end{pmatrix} + \begin{pmatrix} \hat{0} & \hat{0} \\ \widehat{\widetilde{H^-}} & \widehat{H^-} \end{pmatrix} \begin{pmatrix} \alpha_m^- \\ \beta_m^- \end{pmatrix} = \begin{pmatrix} 0 \\ 0 \end{pmatrix}, \tag{B2}$$

where the elements of the submatrices $H^{\pm}$ are evaluated based on Eqs. (1), (A1), and (A2) according to the following rules: The submatrices $\tilde{H}$ and H represent the magnetic field of TM- and TE-polarized waves, respectively; the superscript of the expression $\pm$ corresponds to the superscript of the Hankel function; and the jm_{th} element of each submatrix represent the y component of the magnetic field due to m_{th} Hankel function, evaluated at the point $\{x_j, y_j\} = \{a/2, y_j\}$.

With the help of the S matrix, Eq. (B2) can be further simplified as

$$\begin{pmatrix} \hat{0} & \hat{0} \\ \widehat{\widetilde{H^+}}\widehat{S_{11}} + \widehat{H^+}\widehat{S_{21}} + \widehat{\widetilde{H^-}} & \widehat{\widetilde{H^+}}\widehat{S_{12}} + \widehat{H^+}\widehat{S_{22}} + \widehat{H^-} \end{pmatrix} \begin{pmatrix} \alpha_m^- \\ \beta_m^- \end{pmatrix} = \begin{pmatrix} 0 \\ 0 \end{pmatrix}. \tag{B3}$$

Finally, we represent the amplitudes of the field of longitudinal TM-polarized wave as $\binom{\alpha_m^-}{0}$ with values of the coefficients

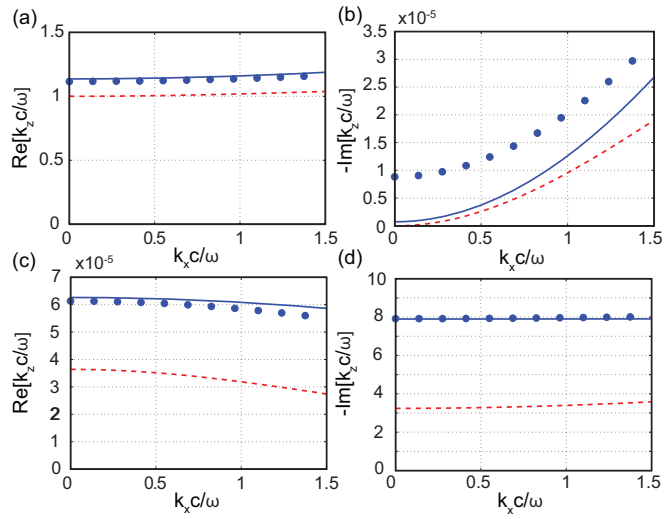

FIG. 8. (Color online) Same as Fig. 7 but for highly conductive wires $\epsilon_i = -200 - 0.1i$; note that $|\text{Im}[k_z c/\omega]| \ll |\text{Re}[k_z c/\omega]|$ in (a) and (b) and that $|\text{Im}[k_z c/\omega]| \gg |\text{Re}[k_z c/\omega]|$ in (c) and (d).

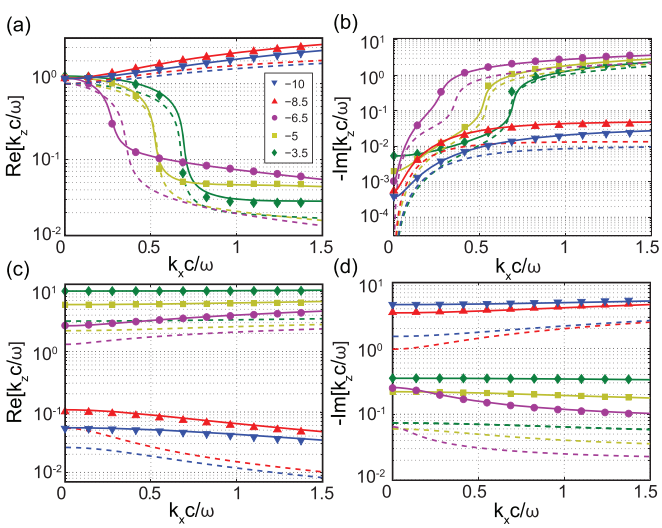

FIG. 7. (Color online) Dispersion of the modes guided by the nanowire metamaterial, calculated with full-wave solutions of Maxwell equations (symbols), the analytical technique presented in this work (solid lines), and with earlier approach, designed for highly conducting wires [33,34] (dashed lines); inset in (a) shows $\text{Re}[\epsilon_i]$; $\text{Im}[\epsilon_i] = -0.1$; $\epsilon_h = 1$.

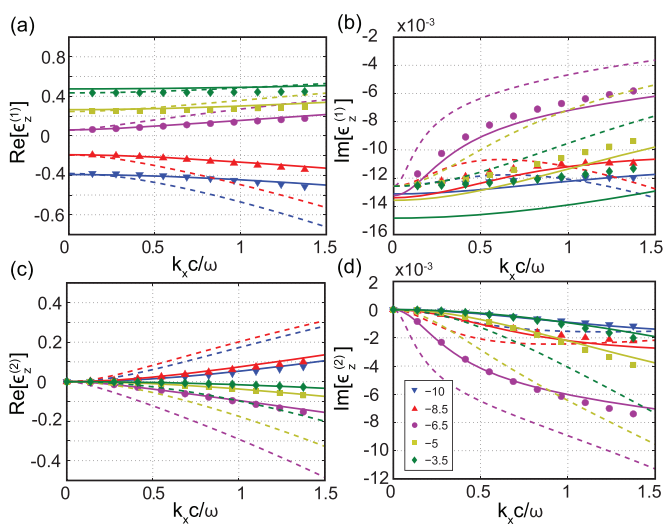

FIG. 9. (Color online) Effective permittivity [defined as $\epsilon_z = \langle \epsilon(x,y) E_z(x,y) \rangle / \langle E_z(x,y) \rangle$, see text] calculated with full-wave solutions of Maxwell equations (symbols), the analytical technique presented in this work (solid lines), and with earlier approach, designed for highly conducting wires [33,34] (dashed lines); note the difference in vertical scale between (a) and (c) and (b) and (d).

given by nontrivial solutions of the linear relationship

$$\widehat{\mathcal{H}}_y\alpha^- = (\widehat{\widetilde{H^+}}\widehat{S_{11}} + \widehat{H^+}\widehat{S_{21}} + \widehat{H^-})\alpha^- = 0, \tag{B4}$$

resulting in Eq. (5).

APPENDIX C: COMPARISON WITH EARLIER NONLOCAL HOMOGENIZATION ATTEMPTS

As described in the paper, the problem of light interaction with nonlocal wire media has been considered before [24–35]. The majority of the studies that focus on high-frequency response of wire composites [24–31] predict a single extraordinary and a single ordinary wave at every frequency. The majority of studies that do predict existence of additional electromagnetic waves [32–35] have focused on optics for highly conductive (PEC-like) wires. References [33] and [34] present an attempt to generalize the developed formalism to the case of plasmonic media. Figures 7, 8, and 9 present a comparison of the formalism from Refs. [33] and [34], the approach described in this work, and full wave numerical solutions of Maxwell equations.

Figures 7 and 8 clearly demonstrate that, in contrast to the formalism presented in this work, the approach developed in Refs. [32–34] severely underestimates effective modal index of the waves propagating in plasmonic wire media (similar phenomenon can also be seen in Fig. 3 of Ref. [33]). This underestimation yields significant errors in calculations of optical properties of wire composites, seen in Fig. 5 of Ref. [34] that can be only be eliminated by using heuristic correction factor.

Finally, we note that our formalism not only adequately describes the effective modal index of light propagating in plasmonic wire media, but it also correctly predicts effective nonlocal permittivity of these modes. The latter fact is clearly seen in Fig. 9 (note that due to difference in vertical scale agreement for $\mathrm{Im}[\epsilon_z]$ looks worse than the agreement for $\mathrm{Re}[\epsilon_z]$).

[1] C. R. Simovski, P. A. Belov, A. V. Atrashchenko, and Y. S. Kivshar, Adv. Mater. **24**, 4229 (2012).
[2] J. Yao, Z. Liu, Y. Liu, Y. Wang, C. Sun, G. Bartal, A. M. Stacy, and X. Zhang, Science **321**, 930 (2008).
[3] Z. Jacob, I. I. Smolyaninov, and E. E. Narimanov, Appl. Phys. Lett. **100**, 161103 (2012).
[4] A. N. Poddubny, P. A. Belov, and Y. S. Kivshar, Phys. Rev. A **84**, 023807 (2011).
[5] O. Kidwai, S. V. Zhukovsky, and J. E. Sipe, Opt. Lett. **36**, 2530 (2011).
[6] W. Yan, M. Wubs, and N. A. Mortensen, Phys. Rev. B **86**, 205429 (2012).
[7] P. A. Belov, Y. Zhao, S. Tse, P. Ikonen, M. G. Silveirinha, C. R. Simovski, S. Tretyakov, Y. Hao, and C. Parini, Phys. Rev. B **77**, 193108 (2008).
[8] P. A. Belov, Y. Zhao, S. Sudhakaran, A. Alomainy, and Y. Hao, Appl. Phys. Lett. **89**, 262109 (2006).
[9] S. Thongrattanasiri and V. A. Podolskiy, Opt. Lett. **34**, 890 (2009).
[10] Z. Jacob, L. V. Alekseyev, and E. Narimanov, Opt. Express **14**, 8247 (2006).
[11] A. Salandrino and N. Engheta, Phys. Rev. B **74**, 075103 (2006).
[12] Z. Liu, H. Lee, Y. Xiong, C. Sun, and X. Zhang, Science **315**, 1686 (2007).
[13] A. V. Kabashin, P. Evans, S. Pastkovsky, W. Hendren, G. A. Wurtz, R. Atkinson, R. Pollard, V. A. Podolskiy, and A. V. Zayats, Nat. Mater. **8**, 867 (2009).
[14] L. S. Dolin, Izv. Vyssh. Uchebn. Zaved. Radiofiz. **4**, 964 (1961).
[15] J. B. Pendry, D. Schurig, and D. Smith, Science **312**, 1780 (2006).
[16] W. Cai, U. K. Chettiar, A. V. Kildishev, and V. M. Shalaev, Nat. Photon. **1**, 224 (2007).
[17] E. Narimanov, H. Li, Yu. A. Barnakov, T. U. Tumkur, and M. A. Noginov, arXiv:1109.5469.
[18] V. V. Yakovlev, W. Dickson, A. Murphy, J. McPhillips, R. M. Pollard, V. A. Podolskiy, and A. V. Zayats, Adv. Mater. **25**, 2351 (2013).
[19] G. A. Wurtz, R. Pollard, W. Hendren, G. P. Wiederrecht, D. J. Gosztola, V. A. Podolskiy, and A. V. Zayats, Nat. Nanotech. **6**, 107 (2011).
[20] R. W. Ziolkowski, Phys. Rev. E **70**, 046608 (2004).
[21] M. Silveirinha and N. Engheta, Phys. Rev. Lett. **97**, 157403 (2006).
[22] N. Engheta, Science **340**, 286 (2013).
[23] M. A. Noginov and V. A. Podolskiy, Eds., *Tutorials in Metamaterials* (CRC, Boca Raton, FL, 2012).
[24] S. P. Burgos, R. Waele, A. Polmam, and H. A. Atwater, Nat. Mater. **9**, 407 (2010).
[25] S. M. Prokes, Orest J. Glembocki, J. E. Livenere, T. U. Tumkur, J. K. Kitur, G. Zhu, B. Wells, V. A. Podolskiy, and M. A. Noginov, Opt. Express **21**, 14962 (2013).
[26] A. Murphy, Y. Sonnefraud, A. V. Krasavin, P. Ginzburg, F. Morgan, J. McPhillips, G. Wurtz, S. A. Maier, A. V. Zayats, and R. Pollard, Appl. Phys. Lett. **102**, 103103 (2013).
[27] A. K. Sarychev, R. C. McPhedran, and V. M. Shalaev, Phys. Rev. B **62**, 8531 (2000).
[28] R. Atkinson, W. R. Hendren, G. A. Wurtz, W. Dickson, A. V. Zayats, P. Evans, and R. J. Pollard, Phys. Rev. B **73**, 235402 (2006).
[29] J. Elser, R. Wangberg, V. A. Podolskiy, and E. E. Narimanov, Appl. Phys. Lett. **89**, 261102 (2006).
[30] G. A. Wurtz, W. Dickson, D. O'Connor, R. Atkinson, W. Hendren, P. Evans, R. Pollard, and A. V. Zayats, Opt. Express **16**, 7460 (2008).
[31] A. L. Pokrovsky and A. L. Efros, Phys. Rev. B **65**, 045110 (2002).
[32] P. A. Belov, R. Marques, S. I. Maslovski, I. S. Nefedov, M. Silveirinha, C. R. Simovski, and S. A. Tretyakov, Phys. Rev. B **67**, 113103 (2003).

[33] M. G. Silveirinha, Phys. Rev. E **73**, 046612 (2006).
[34] M. G. Silveirinhna, P. A. Belov, and C. R. Simovski, Phys. Rev. B **75**, 035108 (2007).
[35] R. J. Pollard, A. Murphy, W. R. Hendren, P. R. Evans, R. Atkinson, G. A. Wurtz, A. V. Zayats, and V. A. Podolskiy, Phys. Rev. Lett. **102**, 127405 (2009).
[36] See Supplemental Material at http://link.aps.org/supplemental/10.1103/PhysRevB.89.035111 for details of numerical solutions of Maxwell equations and supplemental numerical codes.
[37] J. C. M. Garnett, Philos. Trans. R. Soc. London B **203**, 385 (1904).
[38] S. I. Pekar, Sov. Phys. JETP **6**, 785 (1958).
[39] J. D. Jackson, *Classical Electrodynamics*, 3rd ed. (John Wiley and Sons, New York, 1999).
[40] A. Boardman, *Electromagnetic Surface Modes* (John Wiley and Sons, Sydney, 1982).
[41] S. M. Rytov, Sov. Phys. JETP, **2**, 466 (1956).
[42] P. Yeh, A. Yariv, and C.-S. Hong, J. Opt. Soc. Am. **67**, 423 (1977).
[43] E. Doron and U. Smilansky, Phys. Rev. Lett. **68**, 1255 (1992).
[44] O. A. Starykh, P. R. J. Jacquod, E. E. Narimanov, and A. D. Stone, Phys. Rev. E **62**, 2078 (2000).
[45] H. E. Tureci, H. G. L. Schwefel, P. Jacquod, and A. D. Stone, Progr. Optics, **47**, 75 (2005).

Hyperbolic and plasmonic properties of Silicon/Ag aligned nanowire arrays

S.M. Prokes,[1]* Orest J. Glembocki,[1] J. E. Livenere,[2] T. U.Tumkur,[2] J. K. Kitur,[2] G. Zhu,[2] B. Wells,[3] V. A. Podolskiy,[3] and M. A. Noginov[2]

[1]*Electronic Science and Technology Division, Naval Research Lab, Washington DC, 20375, USA*
[2]*Center for Materials Research, Norfolk State University, Norfolk, VA 23504, USA*
[3] *Department of Physics and Applied Physics, University of Massachusetts at Lowell, Lowell, MA, 01854, USA*
Prokes@nrl.navy.mil

Abstract: The hyperbolic and plasmonic properties of silicon nanowire/Ag arrays have been investigated. The aligned nanowire arrays were formed and coated by atomic layer deposition of Ag, which itself is a metamaterial due to its unique mosaic film structure. The theoretical and numerical studies suggest that the fabricated arrays have hyperbolic dispersion in the visible and IR ranges of the spectrum. The theoretical predictions have been indirectly confirmed by polarized reflection spectra, showing reduction of the reflection in p polarization in comparison to that in s polarization. Studies of dye emission on top of Si/Ag nanowire arrays show strong emission quenching and shortening of dye emission kinetics. This behavior is also consistent with the predictions for hyperbolic media. The measured SERS signals were enhanced by almost an order of magnitude for closely packed and aligned nanowires, compared to random nanowire composites. These results agree with electric field simulations of these array structures.

© 2013 Optical Society of America

OCIS Codes: (160.4236) Nanomaterials; (160.3918) Metamaterials; (160.1245) Artificially engineered materials; (160.4670) Optical properties.

References and Links

1. N. Engheta and R. W. Ziolkowski, *Electromagnetic Metamaterials: Physics and Engineering Explorations* (John Wiley & Sons, 2006).
2. M. A. Noginov and V. A. Podolskiy, eds., *Tutorials in Metamaterials*, Series in Nano-optics and Nanophotonics (CRC Press, 2011), p. 293.
3. D. R. Smith, W. J. Padilla, D. C. Vier, S. C. Nemat-Nasser, and S. Schultz, "Composite medium with simultaneously negative permeability and permittivity," Phys. Rev. Lett. **84**(18), 4184–4187 (2000).
4. R. A. Shelby, D. R. Smith, and S. Schultz, "Experimental verification of a negative index of refraction," Science **292**(5514), 77–79 (2001).
5. A. A. Houck, J. B. Brock, and I. L. Chuang, "Experimental observations of a left-handed material that obeys Snell's law," Phys. Rev. Lett. **90**(13), 137401 (2003).
6. C. G. Parazzoli, R. B. Greegor, K. Li, B. E. C. Koltenbah, and M. Tanielian, "Experimental verification and simulation of negative index of refraction using Snell's law," Phys. Rev. Lett. **90**(10), 107401 (2003).
7. V. M. Shalaev, W. Cai, U. K. Chettiar, H.-K. Yuan, A. K. Sarychev, V. P. Drachev, and A. V. Kildishev, "Negative index of refraction in optical metamaterials," Opt. Lett. **30**(24), 3356–3358 (2005).
8. J. B. Pendry, "Negative refraction makes a perfect lens," Phys. Rev. Lett. **85**(18), 3966–3969 (2000).
9. A. Grbic and G. V. Eleftheriades, "Overcoming the diffraction limit with a planar left-handed transmission-line lens," Phys. Rev. Lett. **92**(11), 117403 (2004).
10. Z. Jacob, L. V. Alekseyev, and E. Narimanov, "Optical hyperlens: Far-field imaging beyond the diffraction limit," Opt. Express **14**(18), 8247–8256 (2006).
11. A. Salandrino and N. Engheta, "Far-field subdiffraction optical microscopy using metamaterial crystals: Theory and simulations," Phys. Rev. B **74**(7), 075103 (2006).
12. A. V. Kildishev and E. E. Narimanov, "Impedance-matched hyperlens," Opt. Lett. **32**(23), 3432–3434 (2007).
13. I. I. Smolyaninov, Y. J. Hung, and C. C. Davis, "Magnifying superlens in the visible frequency range," Science **315**(5819), 1699–1701 (2007).

#187087 - $15.00 USD Received 15 Mar 2013; revised 15 May 2013; accepted 16 May 2013; published 17 Jun 2013

14. Z. W. Liu, H. Lee, Y. Xiong, C. Sun, and X. Zhang, "Far-field optical hyperlens magnifying sub-diffraction-limited objects," Science **315**(5819), 1686 (2007).
15. J. B. Pendry, D. Schurig, and D. R. Smith, "Controlling electromagnetic fields," Science **312**(5781), 1780–1782 (2006).
16. W. S. Cai, U. K. Chettiar, A. V. Kildishev, and V. M. Shalaev, "Optical cloaking with metamaterials," Nat. Photonics **1**(4), 224–227 (2007).
17. D. J. Bergman and M. I. Stockman, "Surface plasmon amplification by stimulated emission of radiation: Quantum generation of coherent surface plasmons in nanosystems," Phys. Rev. Lett. **90**(2), 027402 (2003).
18. M. T. Hill, Y.-S. Oei, B. Smalbrugge, Y. Zhu, T. De Vries, P. J. Van Veldhoven, F. W. M. Van Otten, T. J. Eijkeman, J. P. Turkiewicz, H. De Waardt, E. J. Geluk, S.-H. Kwon, Y.-H. Lee, R. N. Tzel, and M. K. Smit, "Lasing in metallic-coated nanocavities," Nat. Photonics **1**(10), 589–594 (2007).
19. M. A. Noginov, G. Zhu, A. M. Belgrave, R. Bakker, V. M. Shalaev, E. E. Narimanov, S. Stout, E. Herz, T. Suteewong, and U. Wiesner, "Demonstration of a spaser-based nanolaser," Nature **460**(7259), 1110–1112 (2009).
20. R. F. Oulton, V. J. Sorger, T. Zentgraf, R.-M. Ma, C. Gladden, L. Dai, G. Bartal, and X. Zhang, "Plasmon lasers at deep subwavelength scale," Nature **461**(7264), 629–632 (2009).
21. M. Khajavikhan, A. Simic, M. Katz, J. H. Lee, B. Slutsky, A. Mizrahi, V. Lomakin, and Y. Fainman, "Thresholdless nanoscale coaxial lasers," Nature **482**(7384), 204–207 (2012).
22. D. R. Smith and D. Schurig, "Electromagnetic wave propagation in media with indefinite permittivity and permeability tensors," Phys. Rev. Lett. **90**(7), 077405 (2003).
23. P. A. Belov, R. Marqués, S. I. Maslovski, I. S. Nefedov, M. Silveirinha, C. R. Simovski, and S. A. Tretyakov, "Strong spatial dispersion in wire media in the very large wavelength limit," Phys. Rev. B **67**(11), 113103 (2003).
24. Z. Jacob, L. V. Alekseyev, and E. Narimanov, "Optical Hyperlens: Far-field imaging beyond the diffraction limit," Opt. Express **14**(18), 8247–8256 (2006).
25. A. Salandrino and N. Engheta, "Far-field subdiffraction optical microscopy using metamaterial crystals: Theory and simulations," Phys. Rev. B **74**(7), 075103 (2006) (5 pages).
26. Z. Jacob, I. I. Smolyaninov, and E. E. Narimanov, "Broadband Purcell effect: Radiative decay engineering with metamaterials," Appl. Phys. Lett. **100**(18), 181105 (2012).
27. M. A. Noginov, H. Li, Y. A. Barnakov, D. Dryden, G. Nataraj, G. Zhu, C. E. Bonner, M. Mayy, Z. Jacob, and E. E. Narimanov, "Controlling spontaneous emission with metamaterials," Opt. Lett. **35**(11), 1863–1865 (2010).
28. H. N. S. Krishnamoorthy, Z. Jacob, E. Narimanov, I. Kretzschmar, and V. M. Menon, "Metamaterial based broadband engineering of quantum dot spontaneous emission," arXiv:0912.2454.
29. Z. Jacob, J.-Y. Kim, G. V. Naik, A. Boltasseva, E. E. Narimanov, and V. M. Shalaev, "Engineering photonic density of states using metamaterials," Appl. Phys. B **100**(1), 215–218 (2010).
30. T. Tumkur, G. Zhu, P. Black, Yu. A. Barnakov, C. E. Bonner, and M. A. Noginov, "Control of spontaneous emission in a volume of functionalized hyperbolic metamaterial," Appl. Phys. Lett. **99**(15), 151115 (2011).
31. J. Kim, V. P. Drachev, Z. Jacob, G. V. Naik, A. Boltasseva, E. E. Narimanov, and V. M. Shalaev, "Improving the radiative decay rate for dye molecules with hyperbolic metamaterials," Opt. Express **20**(7), 8100–8116 (2012).
32. H. N. S. Krishnamoorthy, Z. Jacob, E. Narimanov, I. Kretzschmar, and V. M. Menon, "Topological transitions in metamaterials," Science **336**(6078), 205–209 (2012).
33. A. N. Poddubny, P. A. Belov, and Y. S. Kivshar, "Spontaneous radiation of a finite-size dipole emitter in hyperbolic media," Phys. Rev. A **84**(2), 023807 (2011).
34. E. M. Purcell, "Spontaneous emission probabilities at radio frequencies," Phys. Rev. **69**, 681 (1946).
35. T. U. Tumkur, J. K. Kitur, B. Chu, L. Gu, V. A. Podolskiy, E. E. Narimanov, and M. A. Noginov, "Control of reflectance and transmittance in scattering and curvilinear hyperbolic metamaterials," Appl. Phys. Lett. **101**(9), 091105 (2012).
36. E. E. Narimanov, H. Li, Yu. A. Barnakov, T. U. Tumkur, and M. A. Noginov, "Reduced reflection from roughened hyperbolic metamaterial," submitted to Optics Express.
37. A. Boltasseva, "Fabrication of optical metamaterials," in *Tutorials in Metamaterials*, (Series in Nano-optics and Nanophotonics) A. M. A. Noginov and V. A. Podolskiy, Eds. (CRC Press, 2011).
38. P. R. Evans, G. A. Wurtz, R. Atkinson, W. Hendren, D. O'Connor, W. Dickson, R. J. Pollard, and A. V. Zayats, "Plasmonic core/shell nanorod arrays: subattoliter controlled geometry and tunable optical properties," J. Phys. Chem. C **111**(34), 12522–12527 (2007).
39. W. Dickson, G. A. Wurtz, P. Evans, D. O'Connor, R. Atkinson, R. Pollard, and A. V. Zayats, "Dielectric-loaded plasmonic nanoantenna arrays: A metamaterial with tuneable optical properties," Phys. Review B **76** 115411 (2007).
40. A. V. Kabashin, P. Evans, S. Pastkovsky, W. Hendren, G. A. Wurtz, R. Atkinson, R. Pollard, V. A. Podolskiy, and A. V. Zayats, "Plasmonic nanorod metamaterials for biosensing," Nat. Mater. **8**(11), 867–871 (2009).
41. J. Yao, Z. Liu, Y. Liu, Y. Wang, C. Sun, G. Bartal, A. M. Stacy, and X. Zhang, "Optical negative refraction in bulk metamaterials of nanowires," Science **321**(5891), 930 (2008).
42. M. A. Noginov, Yu. A. Barnakov, G. Zhu, T. Tumkur, H. Li, and E. E. Narimanov, "Bulk photonic metamaterial with hyperbolic dispersion," Appl. Phys. Lett. **94**(15), 151105 (2009).
43. D. A. Pawlak, "Eutectic fibers with self-organized structures," Adv. Mater. Res. **8**, 129–139 (2007).

#187087 - $15.00 USD Received 15 Mar 2013; revised 15 May 2013; accepted 16 May 2013; published 17 Jun 2013
(C) 2013 OSA

44. A. J. Hoffman, L. Alekseyev, S. S. Howard, K. J. Franz, D. Wasserman, V. A. Podolskiy, E. E. Narimanov, D. L. Sivco, and C. Gmachl, "Negative refraction in semiconductor metamaterials," Nat. Mater. **6**(12), 946–950 (2007).
45. S. M. Prokes, O. J. Glembocki, E. Cleveland, J. D. Caldwell, E. Foos, J. Niinistö, and M. Ritala, "Spoof-like plasmonic behavior of plasma enhanced atomic layer deposition grown Ag thin films," Appl. Phys. Lett. **100**(5), 053106 (2012).
46. Y. Wu, Y. Cui, L. Huynh, C. J. Barrelet, D. C. Bell, and C. M. Lieber, "Controlled growth and structures of molecular-scale silicon nanowires," Nano Lett. **4**(3), 433–436 (2004).
47. H. Pan, S. Lim, C. Poh, H. Sun, X. Wu, Y. Feng, and J. Lin, "Growth of Si nanowires by thermal evaporation," Nanotechnology **16**(4), 417–421 (2005).
48. J. Westwater, D. Gosain, S. Tomiya, and S. Usui, "Growth of silicon nanowires via gold/silane vapor-liquid-solid reaction," J. Vac. Sci. Technol. B **15**(3), 554 (1997).
49. K. Peng, Y. J. Yan, S. P. Gao, and J. Zhu, "Synthesis of large-area silicon nanowire arrays via self-assembling nanoelectrochemistry," Adv. Mater. **14**(16), 1164 (2002).
50. M. L. Zhang, K. Peng, X. Fan, J. S. Jie, R. Q. Zhang, S. T. Lee, and N. B. Wong, "Preparation of large/area uniform silicon nanowires arrays through metal-assisted chemical etching," J. Phys. Chem. C **112**(12), 4444–4450 (2008).
51. M. Kariniemi, J. Niinisto, T. Hatanpaa, M. Kemell, T. Sajavaara, M. Ritala, and M. Leskela, "Plasma-enhanced atomic layer deposition of silver thin films," Chem. Mater. **23**(11), 2901–2907 (2011).
52. O. J. Glembocki, S. M. Prokes, E. Cleveland, R. W. Rendell, and E. Foos, "Metamaterial properties of silver films deposited by ALD," Proceeding of ALD 2012, **129** (2012).
53. www.comsol.com
54. *Handbook of Optical Constants of Solids*, E. D. Palik, ed. (Academic, 1998)
55. R. J. Pollard, A. Murphy, W. R. Hendren, P. R. Evans, R. Atkinson, G. A. Wurtz, A. V. Zayats, and V. A. Podolskiy, "Optical nonlocalities and additional waves in epsilon-near-zero metamaterials," Phys. Rev. Lett. **102**(12), 127405 (2009).
56. N. Felidj, J. Aubard, G. Levi, J. R. Krenn, A. Hohenau, G. Schider, A. Leitner, and F. R. Assenegg, "Optimized surface-enhanced Raman scattering on gold nanoparticle arrays," Appl. Phys. Lett. **82**(18), 3095 (2003).
57. S. M. Prokes, O. J. Glembocki, R. W. Rendell, and M. G. Ancona, "Enhanced plasmon coupling in crossed dielectric/metal nanowire composite geometries and applications to surface-enhanced Raman spectroscopy," Appl. Phys. Lett. **90**(9), 093105 (2007).
58. S. M. Prokes, D. A. Alexson, O. J. Glembocki, H. D. Park, and R. W. Rendell, "Effect of crossing geometry on the plasmonic behavior of dielectric core/metal sheath nanowires," Appl. Phys. Lett. **94**(9), 093105 (2009).
59. R. Aroca and A. Thedchanamoorthy, "Vibrational studies of molecular organization in evaporated phthalocyanine thin solid films," Chem. Mater. **7**(1), 69–74 (1995).
60. M. Lütt, M. R. Fitzsimmons, and D. Li, "X-ray reflectivity study of self-assembled thin films of macrocycles and macromolecules," J. Phys. Chem. B **102**(2), 400–405 (1998).
61. J. P. Kottmann and O. J. F. Martin, "Plasmon resonant coupling in metallic nanowires," Opt. Express **8**(12), 655–663 (2001).

1. Introduction

Metamaterials are engineered composite materials containing subwavelength inclusions with rationally designed shapes, sizes, mutual arrangements and orientations, which often exhibit unparalleled properties not available in nature or traditional synthetic materials [1,2]. The field of metamaterials has brought about novel designs, since researchers have been able to overcome the constraints associated with conventional materials and explore entirely new concepts with a much larger range of material parameters available through structured media. Materials with negative indices of refraction [3–7], "perfect" lenses [8,9] and hyperlenses [10–14] that focus and image with resolution beyond the diffraction limit, invisibility cloaks [15,16], and nanoscopic lasers [17–21] are just some of the novel concepts that have been put forward.

A new class of uniaxial (meta)materials has been reported [22–25], which have highly unusual iso-frequency surfaces defined by allowed wavevectors at constant frequency. When all principal components of the dielectric permittivity tensor are positive, the iso-frequency surface is "closed" and forms a spheroid or ellipsoid in the wavevector space (k-space). In such media, the magnitude of the wavenumber is limited, constraining the resolution of optical imaging, and the density of photonic states. In contrast, a highly anisotropic metamaterial, whose dielectric permittivity in orthogonal directions has different signs, exhibits a hyperbolic iso-frequency surface, and thus is referred to as hyperbolic. Such materials have an almost unlimited magnitude of a wave vector k and near infinite local

#187087 - $15.00 USD Received 15 Mar 2013; revised 15 May 2013; accepted 16 May 2013; published 17 Jun 2013
(C) 2013 OSA

density of photonic states [26]. Recent theoretical predictions [26] and experimental results in hyperbolic metamaterial structures [27–33] have shown that, in line with the seminal work by Purcell [34], the high density of photonic states can control spontaneous emission of luminescent centers and reflectance of roughened metamaterials' surfaces [35,36].

The most common approach to fabricate a metamaterial is by patterning periodic arrays of individual elements, which can be metal, dielectric, plastics, etc., depending on application. The properties of metamaterials can then be tailored by controlling the individual element shape, size and geometry, as well as the array periodicity and/or arrangement [1,2]. However, most of traditional cleanroom fabrication techniques are prohibitively expensive and hardly scalable [37]. Much more appealing are bottom-up techniques capable of producing centimeter size samples, which include electroplating growth of metallic nanowires in porous alumina membranes [38-42], eutectic crystal growth of split ring resonator structures [43], and deposition of lamellar semiconductor or metal-dielectric film structures [28–32,44]. In addition, a metamaterial can also be formed by Atomic Layer Deposition (ALD) growth-induced patterning, as has recently been reported for Ag [45].

The density of photonic states in hyperbolic metamaterials (which can control a variety of quantum and classical phenomena) is significantly larger *inside* the structure than on its surface [29]. Therefore, many applications require impregnation of hyperbolic metamaterials with nonlinear and luminescent chromophores and other active components. One realization of hyperbolic metamaterials, allowing their easy functionalization, is arrays of parallel metal-coated nanowires that are separated by air gaps, which is studied in this work theoretically and experimentally.

In this work, we fabricate and examine the optical properties of closely spaced long Si/Ag nanowire composite arrays. We predict, theoretically and numerically, that these structures have hyperbolic dispersion in the visible and infrared ranges of the spectrum. The results of reflection and dye emission experiments are consistent with the model predictions. We also report an enhancement of surface enhanced Raman scattering (SERS), which is, most likely, due to plasmonic coupling of closely spaced nanowires and enhanced density of photonic states in hyperbolic metamaterials.

2. Formation of closely spaced Si nanowire arrays

There are a number of approaches in forming silicon nanowires (NWs), such as chemical vapor deposition [46] and thermal evaporation [47], but in general, these processes require very specific growth chambers which are expensive and which can require rather dangerous gases, such as silane. Furthermore, most of these systems produce randomly grown Si nanowires. In order to form aligned and ordered Si nanowire arrays with small diameters, the vapor liquid solid (VLS) growth mechanism is used [48], and small diameter nanowires can be formed by control of the metal catalyst size, which may require further lithographic steps. Instead, we have chosen a metal assisted chemical etching process [49], which allows a simple and inexpensive way of forming silicon nanowire arrays, with very few equipment requirements.

Preparation of silicon nanowires through chemical etching has been found to work well when silver is used to enhance the etching [50]. The etching process can be described as follows: Ag nanoparticles are deposited onto the silicon substrate. Some of the Ag is oxidized and dissolved in solution, forming Ag + ions, which react with Si at the Si/Ag nanoparticle interface, so that enhanced silicon etching occurs, and it is localized to the regions covered by the Ag nanoparticles. As this enhanced Si etching continues, channels are formed into the silicon substrate, leaving silicon walls in regions with no Ag nanoparticles, thus creating a Si NW array.

A number of Silicon substrates were investigated, including Si(100), Si(111), lightly doped p and n-type wafers, heavily doped p and n-type wafers, as well as p-doped 50 micron thick Si wafers. The silicon wafers were cut into 1x1 cm^2 pieces, washed with acetone,

#187087 - $15.00 USD Received 15 Mar 2013; revised 15 May 2013; accepted 16 May 2013; published 17 Jun 2013
(C) 2013 OSA

ethanol, and DI water, followed by a piranha etch (sulfuric acid and hydrogen peroxide in a 3:1 v/v ratio). The samples were then dipped in 5% HF/water solution for 3 minutes, placed in a 4.8 M HF and 0.005M $AgNO_3$ solution to form the Ag catalyst [49]. The resultant samples were rinsed in deionized (DI) water and the remaining Ag catalyst was removed using a nitric acid/DI solution. The nanowires were characterized via scanning electron microscopy (SEM).

2.1 Effect of Si substrate doping on array formation

A number of silicon substrates were investigated, using the optimal electroless Ag catalyst deposition and optimal HF etching conditions. Figure 1 shows the SEM images of some of the resulting nanowires etched under the same conditions as a function of substrate doping. Figure 1(a) shows an SEM micrograph of a lightly boron doped p-type silicon wafer with a resistivity of 1-30 ohm-cm, Fig. 1(b) shows an image for a lightly phosphorus doped n-type silicon with a resistivity of 1-20 ohm-cm, Fig. 1(c) shows a heavily boron doped p-type silicon wafers with resistivity of 0.01-0.02 ohm-cm, Fig. 1(d) shows a heavily arsenic doped n-type silicon with a resistivity of 0.0015-0.007 ohm-cm and Fig. 1(e) shows Si arrays that can be formed on both sides of a Si wafer, assuming the etching conditions are properly optimized.

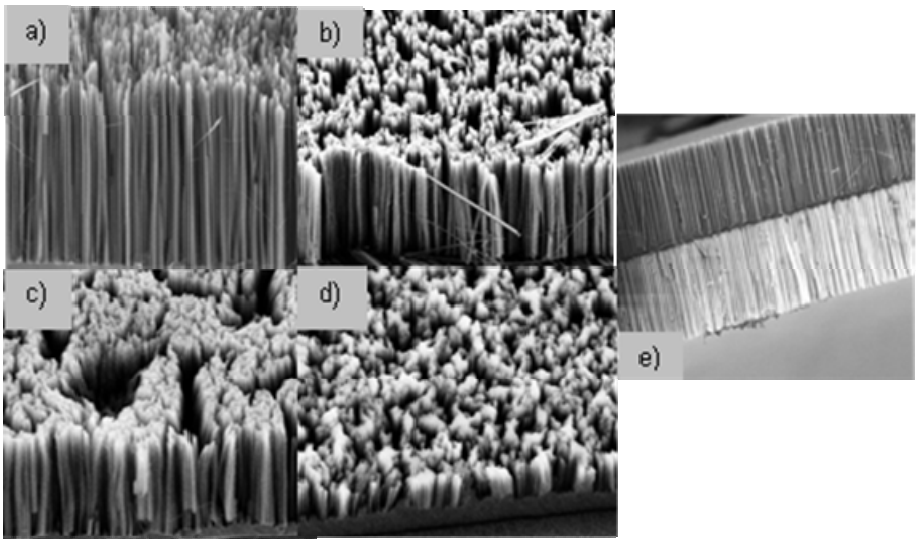

Fig. 1. Si NWs produced using a) p-type silicon, 1-30 ohm-cm, b) n-type silicon, 1-20 ohm-cm, c) p-type silicon, 0.01-0.02 ohm-cm, d) n-type silicon, 0.0015-0.007 ohm-cm and e) p-type Si (100) 50 micron thick wafer, etched from both sides.

As is evident from Fig. 1, the metal assisted chemical etching process worked well for most types of silicon substrates except those that were heavily doped. This is evident in Fig. 1(d) for a very heavily doped sample, which resulted in short, disordered nanowires that were not properly separated from each other.

3. Formation of NW/Ag composite arrays

In order to investigate both hyperbolic and plasmonic properties of the NW arrays, we coated the Si NW arrays with 21 nm of Ag, using atomic layer deposition (ALD). The ALD process, due to its conformality and high aspect ratio coverage, was deemed ideal for achieving full coverage of the closely spaced NW arrays.

The growth of the Ag films was performed by remote plasma enhanced atomic layer deposition (PEALD), using $Ag(fod)(PEt_3)$ (fod = 2,2-dimethyl-6,6,7,7,8,8,8-

#187087 - $15.00 USD Received 15 Mar 2013; revised 15 May 2013; accepted 16 May 2013; published 17 Jun 2013
(C) 2013 OSA

heptafluorooctade-3,5-dionato) and hydrogen plasma as the precursors [45, 51]. The Ag films were deposited at 125°C onto the Si nanowire arrays, as well as on random Si nanowires.

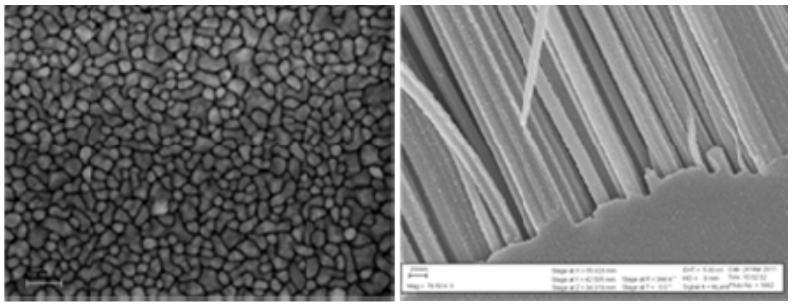

Fig. 2. a) SEM image of 21 nm thick Ag thin film deposited on Si using plasma enhanced atomic layer deposition (PEALD); b) SEM image of Si NW arrays coated with ALD Ag near the substrate.

The thicknesses of the deposited Ag films were 7 nm, 17 nm, 21 nm and 38 nm, as measured by ellipsometry and XTEM.

The PEALD film consisted of polycrystalline fcc flat Ag islands (Fig. 2(a)), separated by very small air gaps. No detectable contaminants (from EDS) were noted and the thicker films had a resistivity in line with metallic Ag. In terms of coating the Si NW arrays, although the Si nanowires in the arrays were 30 microns long and relatively closely spaced (separated by only 150 - 200 nm), we see conformal coverage of the ALD Ag along the whole length, down to the substrate, as shown in Fig. 2(b).

In terms of the optical response, however, the ALD Ag does not resemble a standard Ag thin film, in that the ALD Ag exhibits plasmonic behavior, as reported earlier [45]. This plasmonic behavior is also evident from Fig. 3(a), which shows an experimentally determined reflection spectrum for the PEALD Ag, along with an FDTD simulation of this Ag mosaic structure. The resonance near 600 nm is due to plasmonics, and it has been shown to blue shifts with decreasing film thickness [52]. This resonance is only present in ALD Ag and not in Ag films deposited by other means [52], which agrees well with the SERS enhancement only seen for ALD Ag [45]. Thus PEALD Ag is in fact a metamaterial due to its unique mosaic grain structure, modeled as a coaxial cylinder of Ag surrounded by an air gap [45]. Figure 3(b) shows a single coaxial cylinder used to model the Ag ALD film mosaic morphology in the FDTD simulation. The simulation was obtained by forming an array of these cylinders

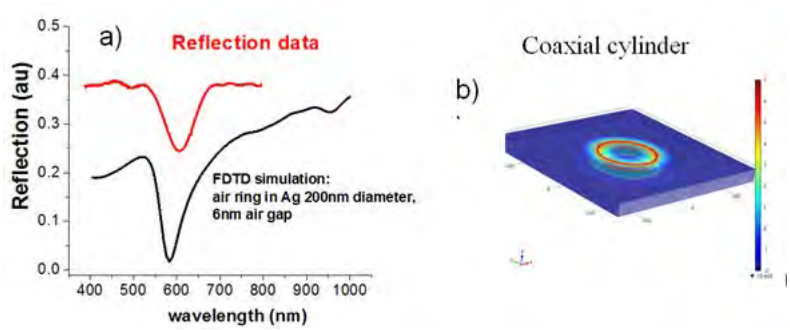

Fig. 3. a) Comparison of the measured reflection data of ALD Ag to a finite difference time domain simulation of a 200nm diameter air ring in a 40nm thick Ag film. Note that the data and simulation both have the same line shape and that the positions of the resonance agree well. b) Electric field simulation of a single element of the PEALD Ag microstructure (coaxial cylinder) used to obtain the simulation in a). Also shown are the resultant high electric fields in and above the air gap.

#187087 - $15.00 USD Received 15 Mar 2013; revised 15 May 2013; accepted 16 May 2013; published 17 Jun 2013
(C) 2013 OSA

in order to obtain the reflection data shown in Fig. 3(a) and the electric field enhancements shown in red in Fib 3(b). Note that these high electric fields form not only in the air gaps but also above the gaps, which leads to strong plasmonic behavior as measured by SERS [45].

4. Theoretical prediction of Hyperbolic Dispersion

To understand the topological properties of the waves propagating in our metamaterials, we used 2D finite-element-based solutions of Maxwell equations [53] to deduce the dependence of the z-component of wavevector on frequency and x-component of the wavevector. In these calculations we used a more general model of the structure than the one realized in experiments. Thus, the system was represented as a periodic array of infinitely long composite wires with shelled internal structure (one unit cell of such structure is shown in Fig. 4(a)). These calculations have revealed that, similar to previously studied nanowire-based metamaterials [38–42], Si-based nanowire arrays support two waves that differ by their polarization. The dispersion of these two waves was numerically calculated for the following set of parameters: free-space wavelength 900 nm, distance between centers of Si nanowires 250 nm, the diameter of nanowires: 150 nm, with thickness of ALD silver coatings ranging from 7 nm to 38 nm. In these calculations, we assumed that optical properties of components of metamaterials are significantly close to those of bulk media [54].

The calculations show that for small angles of incidence, the behavior of the metamaterial is consistent with what is expected of a uniaxial homogeneous medium. For smaller values of silver thickness, the material exhibits elliptical behavior, while for larger thickness of the silver shells, the behavior is hyperbolic-like. Least-square fitting of these numerically calculated dispersion curves to ellipses or hyperbolae yields the effective medium parameters for the structure [40]. These effective medium parameters are summarized in Fig. 4(b).

In the limit when the nanowire radius, shell thickness, and distance between the wires are much smaller than the wavelength, the dispersion of nanowire structures can be described by

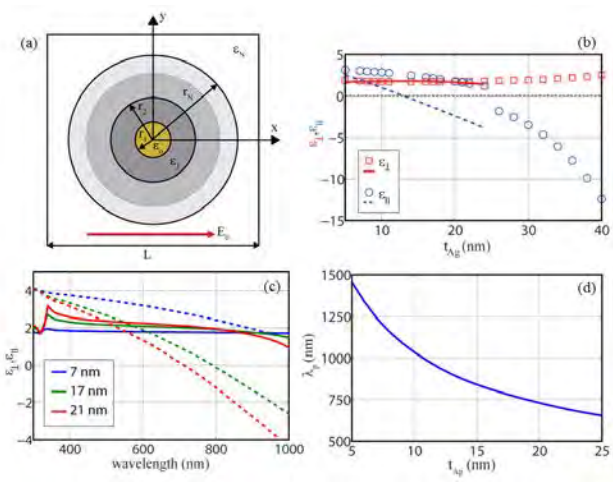

Fig. 4. (a) schematic geometry of the unit cell for a multi-shell nanowire composite, used in derivation of effective medium response; experimental configuration corresponds to a two shell system or N = 2; (b) effective medium parameters extracted from finite-element solutions of Maxwell equations (symbols) and from effective medium theory (lines); (c) spectral dependence of effective medium parameters for different thickness of Ag shell; (d) dependence of effective plasma wavelength of composite in (c) as a function of Ag shell thickness.

effective medium theory that can be calculated by straightforward generalization of Maxwell-Garnett approach to describe the composite containing N shell-type components. Explicitly, the component of the permittivity tensor along the wire, ε_{zz}, is calculated as the weighed average of the permittivities of the constituent components as

#187087 - $15.00 USD Received 15 Mar 2013; revised 15 May 2013; accepted 16 May 2013; published 17 Jun 2013
(C) 2013 OSA

$$\varepsilon_{\parallel} = \varepsilon_{zz} = \sum_i p_i \varepsilon_i, \tag{1}$$

with p_i being the (surface) concentration of the i-th component of the composite.

To calculate the component of permittivity tensor in the direction perpendicular to the wires, it is necessary to find field distribution along the nanowire system. Straightforward calculation yields:

$$\varepsilon_{\perp} = \varepsilon_{xx} = \varepsilon_{yy} = \sum_i \frac{p_i \varepsilon_i e_i}{p_i e_i} \tag{2}$$

with parameters e_i calculated using a simple iterative technique:

$$\begin{aligned} & e_{i-1} = T_i e_i \\ & T_i = \frac{2}{\frac{\varepsilon_{i-1}}{\varepsilon_i}\left(1 - \frac{S_{i-1}}{r_i^2}\right) + \left(1 + \frac{S_{i-1}}{r_i^2}\right)} \\ & S_i = r_i^2 \left[\left(1 + \frac{S_{i-1}}{r_i^2}\right) T_i - 1\right] \\ & S_0 = 0, e_N = 1 \end{aligned} \tag{3}$$

The agreement of the numerically-extracted effective medium parameters with prediction of generalized Maxwell-Garnett theory is illustrated in Fig. 4(b). It is seen that the iterative technique adequately describes the behavior of $\varepsilon_{\perp}$ in the regime when the concentration of inclusions is relatively small (the relative concentration of the host component of metamaterial p_N >70%). In contrast, the parallel component of the permittivity is only qualitatively described by the effective medium theory. This apparent disagreement has its origin in strong spatial dispersion that is expected in the vicinity of epsilon-near-zero behavior for composites with relatively large unit cells. Similar deviations have been previously observed in gold nanowire metamaterials [55]. The implications of this behavior for optical response of the nanowire composites and the analytical description of the properties of nanowire systems in ENZ regime will be detailed in our future works.

To explore the parameter space enabled by the Si/Ag nanowire arrays, effective medium theory was used to analyze the dependence of effective medium parameters as a function of wavelength for several fixed values of the Ag shell thickness. The results of these calculations are summarized in Fig. 4(c). It is seen that, similar to conventional plasmonic nanowire arrays, Si/Ag composites offer broadband hyperbolic response, with plasma-like behavior of $\varepsilon_{\parallel}$. As expected, the thickness of plasmonic shell plays a role of a convenient control parameter, that can be used to tune effective plasma frequency (the frequency at which $\varepsilon_{\parallel}$ crosses zero). Such tuning is shown in Fig. 4(d).

5. Experimental Studies of Reflection and Emission in Si/Ag arrays

5.1 Specular and Diffused Reflection of Si/Ag arrays

The four nanowire samples with the parameters described in Section 4 and thickness of ALD silver equal to 7 nm, 17 nm, 21 nm and 38 nm have been studied experimentally. According to the theoretical modeling presented in Section 4, all these samples have hyperbolic dispersion in the red and infrared ranges of the spectrum. All of them looked dark gray, likely due to a combination of roughness, which is inherent to nanomaterials fabricated by etching, and (as explained below) preferential scattering of light *inside* roughened hyperbolic metamaterials [35, 36]. Correspondingly, the specular reflection of the samples was very low, under 0.5%. We have attempted to obtain the values of dielectric permittivities extracted from

#187087 - $15.00 USD Received 15 Mar 2013; revised 15 May 2013; accepted 16 May 2013; published 17 Jun 2013
(C) 2013 OSA

the angular reflectance data (following [42]). However, due to the very weak specular reflection and strong diffused scattering, it is not clear if meaningful results can be obtained by this method.

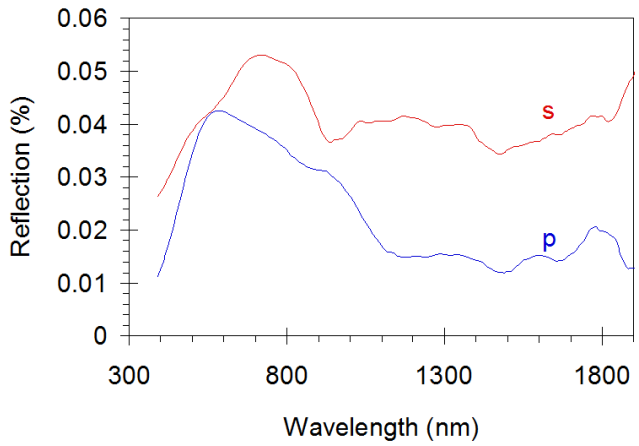

Fig. 5. Reflection spectra of Si/ALD silver sample with 21 nm ALD silver coating, measured in p and s polarizations in an integrating sphere setup at ~10° incidence angle.

At the same time, the reflection measured in an integrated sphere setup (which captured both specularly reflected light and diffusely reflected light) was significantly larger; see for example Fig. 5, depicting the reflection spectrum of the sample with 21 nm ALD silver coating. One can see that the reflectivity in p polarization is significantly smaller than that in s polarization, in particularly in the near-infrared part of the spectrum. This is expected from rough surfaces of metamaterials with hyperbolic dispersion [35,36], in which enhanced scattering of p polarized light *inside* the hyperbolic medium (where the density of photonic states is high) causes substantial reduction of reflection. No substantial reduction of reflectance is predicted for s polarized light [36]. Correspondingly, the experimental result depicted in Fig. 5 is consistent with the theoretical prediction of hyperbolic dispersion in the sample.

5.2 Kinetics and intensity of dye emission on top of Si/Ag nanowire array

In this particular experiment, we studied the array of Si/Ag nanowires coated with 21 nm ALD silver layer. A film of polymethyl methacrylate (PMMA) doped with IR140 laser dye (in concentration 0.013 M) was deposited on top of the nanowire array sample and onto the control substrates, which were glass and silver film deposited on glass. The film thickness in control samples was ~80 nm. The Si/Ag nanowire sample had approximately the same concentration of dye molecules per unit area of the sample. However, dye penetrated in the voids between nanowires, and the effective thickness could not be determined.

In order to measure the emission kinetics, the IR140:PMMA films were pumped using a 100 fs Ti:sapphire laser at λ = 792 nm. The emission was detected using a near-infrared Hamamatsu streak camera equipped with appropriate long-pass filters (λ >850 nm). All emission kinetics, averaged over multiple measurements, along with the kinetics of the pumping pulse scattered by a pure glass substrate (which shows the time resolution of the apparatus determined by jitter of the laser and wide open slit of the streak camera) are depicted in Fig. 6. One can see that the emission of dye on top of the metamaterial sample is strongly quenched in first ~100 ps, and its decay kinetics is significantly shortened (more than twofold in comparison to the control samples) at longer times.

#187087 - $15.00 USD Received 15 Mar 2013; revised 15 May 2013; accepted 16 May 2013; published 17 Jun 2013
(C) 2013 OSA

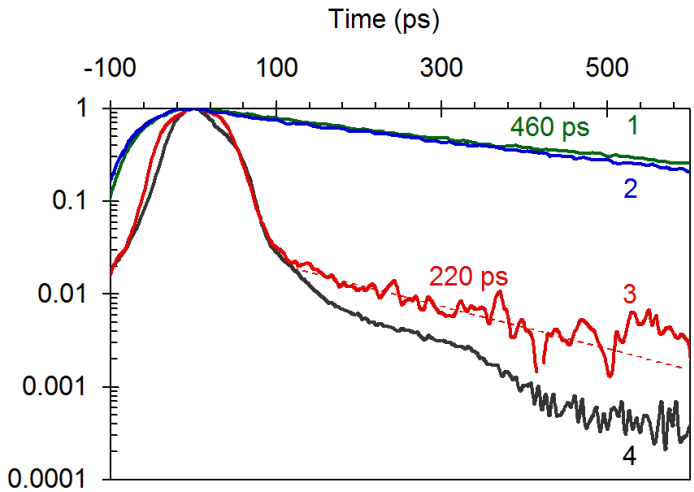

Fig. 6. (a) Spontaneous emission kinetics of the IR140:PMMA film deposited on the top of glass (1), 200 nm thick silver film (2), and the Si/ALD Ag metamaterial sample (3). Trace 4 shows the time resolution of the apparatus.

We have also studied the emission spectra of IR140:PMMA films deposited on top of the metamaterial sample and the glass substrate. In this particular experiment, the samples were pumped at 784 nm. The emission signal was detected with a photomultiplier tube (PMT) connected to the exit slit of a monochromator. The emission spectra are shown in Fig. 7. It can be seen that the emission of IR140:PMMA deposited on top of the metamaterial, is almost one order of magnitude smaller compared to the same dye-doped film deposited on glass. (The difference can be even larger considering the large error bar.)

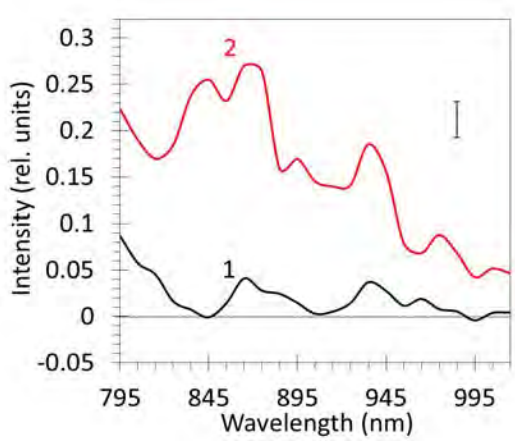

Fig. 7. Spontaneous emission spectra of the IR140:PMMA film deposited on top of the Si/Ag metamaterial sample with 21 nm ALD silver coating (1) and glass (2), pumped at λ = 784 nm into the absorption band of IR140.

The experimentally observed reduction of the dye emission intensity and shortening of the emission kinetics are consistent with the theoretical predictions for hyperbolic metamaterials [26]. In fact, high density of photonic states on the surface (and inside) of a metamaterial with hyperbolic dispersion causes enhancement of spontaneous emission directed *inside* the material. This determines the emission kinetics shortening and reduction of the emission

#187087 - $15.00 USD Received 15 Mar 2013; revised 15 May 2013; accepted 16 May 2013; published 17 Jun 2013
(C) 2013 OSA

intensity. Similar emission quenching and shortening of the emission decay time have been observed in a dye-doped film deposited on top of array of silver nanowires grown in alumina membrane [27].

5.3 Angular distribution of dye emission in Si/Ag nanowire array

Hyperbolic metamaterials have been predicted to produce cone-shaped or beam-like patterns of spontaneous emission inside the medium [26]. The angular distribution of emission outside the sample is much less researched. In the experimental study of this phenomenon, we deposited PMMA film doped with HITC laser dye (in concentration 0.04 M) onto array of Si/Ag nanowires with 38 nm silver coating as well as onto ALD silver film and thermal vapor deposited silver film. The thickness of the dye-doped PMMA films on top of silver films was ~80 nm. In the Si/Ag nanowire sample, dye (which had approximately the same concentration of dye molecules per unit area) penetrated between the wires.

Dye molecules were excited with ~5 nm pulses of the optical parametric oscillator (OPO) at λ = 750 nm and 45° incidence angle. The emission intensity was measured, in the spectral band centered at 815 nm, at a variety of detection angles ranging from 0° (normal to the sample surface) to ~90° (parallel to the surface). A long-pass filter in front of the detector blocked laser pumping and transmitted dye emission.

Angular distributions of emission in three samples studied are depicted in Fig. 8. One can see that the emission patterns from the Si/Ag nanowire array and ALD silver film are very close to Lambertian (~cos(θ)). This behavior could probably be expected, since surfaces of both samples are rough (the roughness of Si/Ag NW array much larger than that of ALD silver.) At the same time, the emission of dye on top of a much smoother (>5nm) thermal vapor deposited silver is slightly broader. The comparison of the experiment with the theory will be published elsewhere.

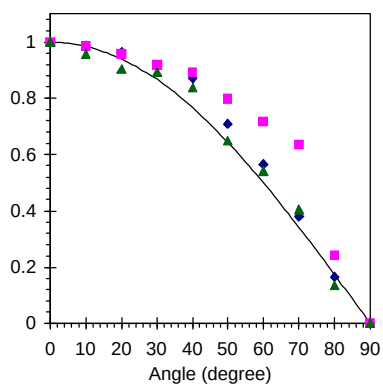

Fig. 8. Angular distributions of emission of HITC dye molecules on top of Si/Ag NW array (diamonds), ALD silver film (triangles) and silver film deposited via thermal vapor deposition (squares). Solid line: cos(θ).

6. Plasmonic Properties of Nanowire Arrays

Raman scattering is a technique, which can measure interatomic vibrations that are unique to each material, thus providing a chemical "fingerprint" for any material. Unfortunately, the scattering efficiencies are very low, roughly 10^{-8} of the incident laser light. However, the signal can be greatly enhanced by the use of metal nanoparticles, which enhance the local electric fields [56]. This process is referred to as Surface Enhanced Raman Scattering (SERS). One type of SERS nanostructures resulting in strong SERS signal are dielectric core/metal sheath nanowires [57,58], which have been shown to create electric field hotspots

#187087 - $15.00 USD Received 15 Mar 2013; revised 15 May 2013; accepted 16 May 2013; published 17 Jun 2013
(C) 2013 OSA

at their crossings due to plasmonic coupling. It has also been shown that two closely spaced parallel dielectric core/metal sheath nanowires result in a greater enhancement than those crossed at 90° [58].

A self-assembled monolayer of benzenethiol (BZT) was deposited on the NW arrays by soaking them in 10^{-4} M BZT/toluene solution overnight and rinsing with methanol, which removed excess BZT not bonded to the Ag surface. The SERS spectra were obtained using a DeltaNu Reporter 785 micro-Raman system, operating at 785 nm and the spectra were collected with a laser power of less than 3 mW. In addition, COMSOL electric field calculations were performed in order to interpret the experimental SERS results. The SERS results for the Si/Ag NW arrays are shown in Fig. 9(a). The major Raman peaks can be assigned to symmetric ring breathing, in plane C–H bending and in plane C–C stretching of the phenyl ring from the active molecules, benzenethiol (BT), which are in good agreement with those reported previously [59, 60]. As can be seen, very strong lines associated with the BZT molecule are seen, and the uniformity of the SERS signal intensity is quite uniform

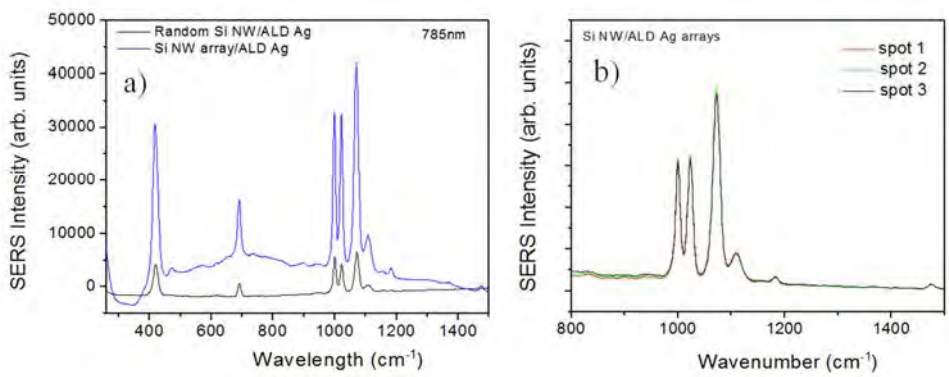

Fig. 9. (a) SERS spectrum for benzenethiol (BZT) for Si/Ag NW arrays compared to horizontal random Si/Ag NWs, and (b) SERS spectrum for three random locations on the Si NW array.

when taken from different regions of the sample (Fig. 9(b)). More importantly, the SERS signal of the closely spaced Si/Ag NW arrays is a factor of 7 stronger compared to a similar density of random Si/Ag nanowires placed on a flat Si substrate, Fig. 9(a). To arrive at this number, the SERS intensity of the arrays was normalized to the total number of NWs in a 2 micron diameter area (laser spot size). Similarly, the SERS intensity of the random horizontal nanowires was normalized to the total number of random NWs in the 2 micron area.

To explain the enhancement in the SERS intensity for the closely spaced NW arrays, we refer to Kotmann and Martin [61], who have shown that 2 parallel NWs with a small separation distances can result in the formation of hot spots corresponding to very intense electric field, leading to a significantly enhanced coupled plasmon resonance.

In order to understand the enhancement in the case of our closely spaced aligned high density nanowire arrays, we have performed COMSOL electric field calculations, shown in Fig. 10, which show the electric fields induced between the NW arrays upon irradiation by light. As can be seen in Fig. 10(a), for a 4x4 array, parallel and closely packed NWs induced high electric fields along the whole lengths of the nanowires, which may account for the very large enhancement of the observed SERS signals. Figure 10(b) is a side view of the parallel NW arrays and the electric fields generated, clearly demonstrating the strong plasmonic coupling between the NWs in the array. Due to the difficulty of computing electric fields for long NWs, only 300 nm long wires were modeled. However, these results are also applicable to longer NWs. Furthermore, COMSOL simulations also show that

#187087 - $15.00 USD Received 15 Mar 2013; revised 15 May 2013; accepted 16 May 2013; published 17 Jun 2013
(C) 2013 OSA

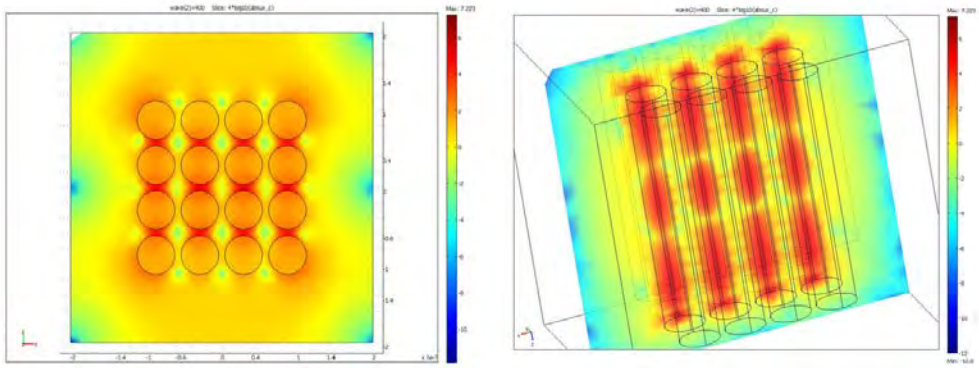

Fig. 10. COMSOL simulation of the electric field enhancement of closely spaced Ag nanowire arrays a) looking from top and b) along the NWs. In the simulations, the NWs were 100 nm in diameter and 300 nm in length.

on average, the strong plasmonic coupling is not dramatically influenced by small variations in the nanowire diameters. Since the nanowires in the arrays are aligned but randomly spaced from each other, if one assumes that some fraction of the nanowires are significantly closer than the average distance of 150-200 nm, strong plasmon coupling and thus a high SERS intensity would be expected, as discussed by Kotmann et al. [61]. The fact that these nanowires form regions where they are much more closely spaced is clearly seen in Fig. 1(b), 1(c).

Conclusions

In summary, we have synthesized arrays of silver coated silicon nanowires and studied their properties theoretically and experimentally. The arrays, which had a thicker Ag coating, have been predicted to have a hyperbolic dispersion in the visible and infrared ranges of the spectrum, modeled by finite-element-based solutions of Maxwell's equations. In terms of experimental results, we have noted a significant reduction of the samples' reflectance at p polarization (in comparison to s polarization), which is expected from rough surfaces of a hyperbolic metamaterial. Furthermore, the emission behavior of dye molecules deposited on top of the nanowire arrays has been obtained, and the results show strong dye emission quenching, by nearly an order of magnitude, and shortening of the emission kinetics. These two observations are consistent with the theoretical predictions for hyperbolic metamaterials.

The measured SERS signals for the Si/Ag array composites were enhanced by almost an order of magnitude for closely packed and aligned nanowires, compared to random nanowire composites deposited on a flat surface. COMSOL electric field simulations suggest that this enhancement is due to plasmon coupling in closely spaced nanowires, which are present in the arrays investigated.

Acknowledgments

The authors would like to thank Eric Epstein, Hua Qi, Alice King and Erin Cleveland for experimental assistance. The authors also thank Evgenii Narimanov for useful discussions. The authors thank the Office of Naval Research for financial support. J.E.L., T.U.T, J.K.K, G.Z, and M.A.N. acknowledge the supported by the NSF PREM grant DMR-1205457, NSF IGERT grant DGE-0966188, and AFOSR grant FA9550-09-1-0456, V.P. acknowledges support from NSF MWN grant DMR-1209761 and ARO grant W911NF-12-1-0533.

Hyperbolic metamaterials: new physics behind a classical problem

Vladimir P. Drachev,[1,*] Viktor A. Podolskiy,[2] and Alexander V. Kildishev[3]

[1]*Department of Physics and Center for Advanced Research & Technology, University of North Texas, Denton, TX 76203, USA*
[2]*Department of Physics and Applied Physics, University of Massachusetts Lowell, Lowell, MA 01854, USA*
[3]*Birck Nanotechnology Center and School of Electrical and Computer Engineering, Purdue University, West Lafayette, IN 47906, USA*
[*]*vladimir.drachev@unt.edu*

Abstract: *Hyperbolic* materials enable numerous surprising applications that include far-field subwavelength imaging, nanolithography, and emission engineering. The wavevector of a plane wave in these media follows the surface of a hyperboloid in contrast to an ellipsoid for conventional anisotropic dielectric. The consequences of *hyperbolic dispersion* were first studied in the 50's pertaining to the problems of electromagnetic wave propagation in the Earth's ionosphere and in the stratified artificial materials of transmission lines. Recent years have brought explosive growth in optics and photonics of hyperbolic media based on metamaterials across the optical spectrum. Here we summarize earlier theories in the Clemmow's prescription for transformation of the electromagnetic field in hyperbolic media and provide a review of recent developments in this active research area.

©2013 Optical Society of America

OCIS codes: (160.3918) Metamaterials; (160.1190) Anisotropic optical materials; (260.2110) Electromagnetic optics.

References and links

1. K. G. Budden, *Radio Waves in the Ionosphere*(Cambridge University, 1961).
2. P. Clemmow, "The theory of electromagnetic waves in a simple anisotropic medium," Proc. IEEE **110**(1), 101–106 (1963).
3. L. B. Felsen and N. Marcuvitz, *Radiation and Scattering of Waves* (Wiley-IEEE, 1973).
4. R. H. Ritchie, "Plasma losses by fast electrons in thin films," Phys. Rev. **106**(5), 874–881 (1957).
5. S. M. Rytov, "Electromagnetic properties of a finely stratified medium," Sov. Phys. JETP **2**, 10 (1956).
6. D. R. Smith and D. Schurig, "Electromagnetic wave propagation in media with indefinite permittivity and permeability tensors," Phys. Rev. Lett. **90**(7), 077405 (2003).
7. V. Bunkin, "On radiation in anisotropic media," Sov. Phys. JETP **5**(2), 277–283 (1957).
8. H. Kogelnik, "On electromagnetic radiation in magneto-ionic media," J. Res. Nat. Bur. Stand. D. **64D**, 515 (1960).
9. M. Born and E. Wolf, *Principles of Optics*(Cambridge University, 1999).
10. A. S. Potemkin, A. N. Poddubny, P. A. Belov, and Y. S. Kivshar, "Green function for hyperbolic media," Phys. Rev. A **86**(2), 023848 (2012).
11. H. H. Kuehl, "Electromagnetic radiation from an electric dipole in a cold anisotropic plasma," Plasma Phys. Fluids **5**(9), 1095 (1962).
12. K. G. Balmain, A. A. E. Luttgen, and P. C. Kremer, "Resonance cone formation, reflection, refraction, and focusing in a planar anisotropic metamaterial," IEEE Antennas Wirel. Propag. Lett. **1**(1), 146–149 (2002).
13. Z. Jacob, L. V. Alekseyev, and E. Narimanov, "Optical hyperlens: far-field imaging beyond the diffraction limit," Opt. Express **14**(18), 8247–8256 (2006).
14. A. Salandrino and N. Engheta, "Far-field subdiffraction optical microscopy using metamaterial crystals: theory and simulations," Phys. Rev. B **74**(7), 075103 (2006).
15. Z. Liu, H. Lee, Y. Xiong, C. Sun, and X. Zhang, "Far-field optical hyperlens magnifying sub-diffraction-limited objects," Science **315**(5819), 1686 (2007).
16. I. I. Smolyaninov, Y. J. Hung, and C. C. Davis, "Magnifying superlens in the visible frequency range," Science **315**(5819), 1699–1701 (2007).

#190862 - $15.00 USD Received 23 May 2013; revised 10 Jun 2013; accepted 10 Jun 2013; published 17 Jun 2013

17. W. Wang, H. Xing, L. Fang, Y. Liu, J. Ma, L. Lin, C. Wang, and X. Luo, "Far-field imaging device: planar hyperlens with magnification using multi-layer metamaterial," Opt. Express **16**(25), 21142–21148 (2008).
18. Y. Xiong, Z. Liu, and X. Zhang, "A simple design of flat hyperlens for lithography and imaging with half-pitch resolution down to 20 nm," Appl. Phys. Lett. **94**(20), 203108 (2009).
19. S. Thongrattanasiri and V. A. Podolskiy, "Hypergratings: nanophotonics in planar anisotropic metamaterials," Opt. Lett. **34**(7), 890–892 (2009).
20. L. Verslegers, P. B. Catrysse, Z. Yu, and S. Fan, "Deep-subwavelength focusing and steering of light in an aperiodic metallic waveguide array," Phys. Rev. Lett. **103**(3), 033902 (2009).
21. G. Ren, Z. Lai, C. Wang, Q. Feng, L. Liu, K. Liu, and X. Luo, "Subwavelength focusing of light in the planar anisotropic metamaterials with zone plates," Opt. Express **18**(17), 18151–18157 (2010).
22. C. Ma and Z. Liu, "A super resolution metalens with phase compensation mechanism," Appl. Phys. Lett. **96**(18), 183103 (2010).
23. G. Li, J. Li, and K. W. Cheah, "Subwavelength focusing using a hyperbolic medium with a single slit," Appl. Opt. **50**(31), G27–G30 (2011).
24. S. Ishii, A. V. Kildishev, E. Narimanov, V. Shalaev, and V. P. Drachev, "Sub-wavelength interference pattern from volume plasmon polaritons in a hyperbolic medium," Laser Photonics Rev. **7**(2), 265–271 (2013).
25. J. Kim, V. P. Drachev, Z. Jacob, G. V. Naik, A. Boltasseva, E. E. Narimanov, and V. M. Shalaev, "Improving the radiative decay rate for dye molecules with hyperbolic metamaterials," Opt. Express **20**(7), 8100–8116 (2012).
26. G. V. Naik, J. Liu, A. V. Kildishev, V. M. Shalaev, and A. Boltasseva, "Demonstration of Al:ZnO as a plasmonic component for near-infrared metamaterials," Proc. Natl. Acad. Sci. U.S.A. **109**(23), 8834–8838 (2012), doi:10.1073/pnas.1121517109.
27. A. J. Hoffman, L. Alekseyev, S. S. Howard, K. J. Franz, D. Wasserman, V. A. Podolskiy, E. E. Narimanov, D. L. Sivco, and C. Gmachl, "Negative refraction in semiconductor metamaterials," Nat. Mater. **6**(12), 946–950 (2007).
28. M. A. Noginov, H. Li, Y. A. Barnakov, D. Dryden, G. Nataraj, G. Zhu, C. E. Bonner, M. Mayy, Z. Jacob, and E. E. Narimanov, "Controlling spontaneous emission with metamaterials," Opt. Lett. **35**(11), 1863–1865 (2010).
29. R. J. Pollard, A. Murphy, W. R. Hendren, P. R. Evans, R. Atkinson, G. A. Wurtz, A. V. Zayats, and V. A. Podolskiy, "Optical nonlocalities and additional waves in epsilon-near-zero metamaterials," Phys. Rev. Lett. **102**(12), 127405 (2009).
30. J. Yao, Z. Liu, Y. Liu, Y. Wang, C. Sun, G. Bartal, A. M. Stacy, and X. Zhang, "Optical negative refraction in bulk metamaterials of nanowires," Science **321**(5891), 930 (2008).
31. J. Sun, J. Zhou, B. Li, and F. Kang, "Indefinite permittivity and negative refraction in natural material: graphite," Appl. Phys. Lett. **98**(10), 101901 (2011).
32. L. V. Alekseyev, V. A. Podolskiy, and E. E. Narimanov, "Homogeneous Hyperbolic Systems for Terahertz and Far-Infrared Frequencies," Adv. Optoelectron. **2012**, 267564 (2012).
33. E. Gerlach, P. Grosse, M. Rautenberg, and W. Senske, "Dynamical conductivity and plasmon excitation in Bi," Phys. Status Solidi B **75**(2), 553–558 (1976).
34. Y. Zhang, B. Fluegel, and A. Mascarenhas, "Total negative refraction in real crystals for ballistic electrons and light," Phys. Rev. Lett. **91**(15), 157404 (2003).
35. P. Belov, "Backward waves and negative refraction in uniaxial dielectrics with negative dielectric permittivity along the anisotropy axis," Microw. Opt. Technol. Lett. **37**(4), 259–263 (2003).
36. V. Veselago, "The electrodynamics of substances with simultaneously negative values of epsilon and mu," Sov. Phys. Usp. **10**(4), 509–514 (1968).
37. V. Podolskiy and E. Narimanov, "Strongly anisotropic waveguide as a nonmagnetic left-handed system," Phys. Rev. B **71**(20), 201101(R) (2005).
38. L. V. Alekseyev and E. Narimanov, "Slow light and 3D imaging with non-magnetic negative index systems," Opt. Express **14**(23), 11184–11193 (2006).
39. Y. Xiong, Z. Liu, and X. Zhang, "Projecting deep-subwavelength patterns from diffraction-limited masks using metal-dielectric multilayers," Appl. Phys. Lett. **93**(11), 111116 (2008).
40. J. B. Pendry, "Negative refraction makes a perfect lens," Phys. Rev. Lett. **85**(18), 3966–3969 (2000).
41. J. B. Pendry, "Perfect cylindrical lenses," Opt. Express **11**(7), 755–760 (2003).
42. S. A. Ramakrishna and J. B. Pendry, "Removal of absorption and increase in resolution in a near-field lens via optical gain," Phys. Rev. B **67**(20), 201101 (2003).
43. N. A. Nicorovici, R. C. McPhedran, and G. W. Milton, "Optical and dielectric properties of partially resonant composites," Phys. Rev. B Condens. Matter **49**(12), 8479–8482 (1994).
44. I. I. Smolyaninov, J. Elliott, A. V. Zayats, and C. C. Davis, "Far-field optical microscopy with a nanometer-scale resolution based on the in-plane image magnification by surface plasmon polaritons," Phys. Rev. Lett. **94**(5), 057401 (2005).
45. R. K. Fisher and R. W. Gould, "Resonance cones in the field patterns of a short antenna in anisotropic plasma," Phys. Rev. Lett. **22**(21), 1093–1095 (1969).
46. S. Feng and J. M. Elson, "Diffraction-suppressed high-resolution imaging through metallodielectric nanofilms," Opt. Express **14**(1), 216–221 (2006).

#190862 - $15.00 USD Received 23 May 2013; revised 10 Jun 2013; accepted 10 Jun 2013; published 17 Jun 2013
(C) 2013 OSA

47. P. A. Belov and Y. Hao, “Subwavelength imaging at optical frequencies using a transmission device formed by a periodic layered metal-dielectric structure operating in the canalization regime,” Phys. Rev. B **73**(11), 113110 (2006).
48. D. Schurig and D. R. Smith, “Sub-diffraction imaging with compensating bilayers,” New J. Phys. **7**, 162 (2005).
49. E. M. Purcell, “Spontaneous emission probabilities at radio frequencies,” Phys. Rev. **69**, 681 (1946).
50. L. Novotny and B. Hecht, *Principles of Nano-Optics* (Cambridge University, 2006).
51. Z. Jacob, I. Smolyaninov, and E. Narimanov, “Broadband Purcell effect: radiative decay engineering with metamaterials”, arXiv:0910.3981 [physics.optics].
52. I. I. Smolyaninov and E. E. Narimanov, “Metric Signature Transitions in Optical Metamaterials,” Phys. Rev. Lett. **105**(6), 067402 (2010).
53. L. V. Alekseyev and E. Narimanov, Radiative decay engineering in metamaterials,” in *Tutorials in Metamaterials*, ed. M.A. Noginov and V.A .Podolskiy (Taylor & Francis Group, 2012) pp. 209–223.
54. O. Kidwai, S. V. Zhukovsky, and J. E. Sipe, “Dipole radiation near hyperbolic metamaterials: applicability of effective-medium approximation,” Opt. Lett. **36**(13), 2530–2532 (2011).
55. A. N. Poddubny, P. A. Belov, and Y. S. Kivshar, “Spontaneous radiation of a finite-size dipole emitter in hyperbolic media,” Phys. Rev. A **84**(2), 023807 (2011).
56. B. Wood, J. Pendry, and D. Tsai, “Directed subwavelength imaging using a layered metal-dielectric system,” Phys. Rev. B **74**(11), 115116 (2006).
57. A. N. Poddubny, P. A. Belov, P. Ginzburg, A. V. Zayats, and Y. S. Kivshar, “Microscopic model of Purcell enhancement in hyperbolic metamaterials,” Phys. Rev. B **86**(3), 035148 (2012).
58. C. L. Cortes, W. Newman, S. Molesky, and Z. Jacob, “Quantum nanophotonics using hyperbolic metamaterials,” J. Opt. **14**(6), 063001 (2012).
59. S. I. Maslovski and M. G. Silveirinha, “Mimicking Boyer’s Casimir repulsion with a nanowire material,” Phys. Rev. A **83**(2), 022508 (2011).
60. O. Kidwai, S. V. Zhukovsky, and J. E. Sipe, “Effective-medium approach to planar multilayer hyperbolic metamaterials: Strengths and limitations,” Phys. Rev. A **85**(5), 053842 (2012).
61. H. N. Krishnamoorthy, Z. Jacob, E. Narimanov, I. Kretzschmar, and V. M. Menon, “Topological Transitions in Metamaterials,” Science **336**(6078), 205–209 (2012).
62. R. M. Bakker, V. P. Drachev, Z. Liu, H. K. Yuan, R. H. Pedersen, A. Boltasseva, J. Chen, J. Irudayaraj, A. V. Kildishev, and V. M. Shalaev, “Nanoantenna array-induced fluorescence enhancement and reduced lifetimes,” New J. Phys. **10**(12), 125022 (2008).
63. K. Drexhage, “Influence of a dielectric interface on fluorescence decay time,” J. Lumin. **1**, 693–701 (1970).
64. W. Barnes, “Fluorescence near interfaces: the role of photonic mode density,” J. Mod. Opt. **45**(4), 661–699 (1998).
65. G. Ford and W. Weber, “Electromagnetic interactions of molecules with metal surfaces,” Phys. Rep. **113**(4), 195–287 (1984).
66. J. J. Burke, G. I. Stegeman, and T. Tamir, “Surface-polariton-like waves guided by thin, lossy metal films,” Phys. Rev. B Condens. Matter **33**(8), 5186–5201 (1986).
67. E. H. Hellen and D. Axelrod, “Fluorescence emission at dielectric and metal-film interfaces,” J. Opt. Soc. Am. B **4**(3), 337–350 (1987).
68. G. Winter and W. L. Barnes, “Emission of light through thin silver films via near-field coupling to surface plasmon polaritons,” Appl. Phys. Lett. **88**(5), 051109 (2006).
69. J. B. Khurgin, G. Sun, and R. A. Soref, “Enhancement of luminescence efficiency using surface plasmon polaritons: figures of merit,” J. Opt. Soc. Am. B **24**(8), 1968–1980 (2007).
70. A. Govyadinov and V. Podolskiy, “Metamaterial photonic funnels for subdiffraction light compression and propagation,” Phys. Rev. B **73**(15), 155108 (2006).
71. M. Silveirinha and N. Engheta, “Tunneling of electromagnetic energy through subwavelength channels and bends using ε-near-zero materials,” Phys. Rev. Lett. **97**(15), 157403 (2006).
72. J. B. Pendry, D. Schurig, and D. R. Smith, “Controlling electromagnetic fields,” Science **312**(5781), 1780–1782 (2006).
73. W. Cai, U. Chettiar, A. Kildishev, and V. Shalaev, “Optical cloaking with metamaterials,” Nat. Photonics **1**(4), 224–227 (2007).
74. P. Yeh, A. Yariv, and C. Hong, “Electromagnetic propagation in periodic stratified media.I. General theory,” J. Opt. Soc. Am. **67**(4), 423 (1977).
75. A. P. Vinogradov, A. I. Ignatov, A. M. Merzlikin, S. A. Tretyakov, and C. R. Simovski, “Additional effective medium parameters for composite materials (excess surface currents),” Opt. Express **19**(7), 6699–6704 (2011).
76. V. Agranovich and V. Kravtsov, “Notes on crystal optics of superlattices,” Solid State Commun. **55**(1), 85–90 (1985).
77. S. I. Pekar, “The theory of electromagnetic waves in crystal in which excitons are produced,” Sov. Phys. JETP **6**, 785–796 (1958).
78. G. A. Wurtz, R. Pollard, W. Hendren, G. P. Wiederrecht, D. J. Gosztola, V. A. Podolskiy, and A. V. Zayats, “Designed ultrafast optical nonlinearity in a plasmonic nanorod metamaterial enhanced by nonlocality,” Nat. Nanotechnol. **6**(2), 107–111 (2011).

#190862 - $15.00 USD Received 23 May 2013; revised 10 Jun 2013; accepted 10 Jun 2013; published 17 Jun 2013
(C) 2013 OSA

79. P. A. Belov, R. Marqués, S. I. Maslovski, I. S. Nefedov, M. Silverinha, M. Simovski, and S. A. Tretyakov, "Strong spatial dispersion in wire media in the very large wavelength limit," Phys. Rev. B **67**(11), 113103 (2003).
80. A. Chebykin, A. Orlov, A. Vozianova, S. Maslovski, Y. Kivshar, and P. Belov, "Nonlocal effective medium model for multilayered metal-dielectric metamaterials," Phys. Rev. B **84**(11), 115438 (2011).
81. M. J. Thompson, M. J. DeVries, T. E. Tiwald, and J. A. Woollam, "Determination of optical anisotropy in calcite from ultraviolet to mid-infrared by generalized ellipsometry," Thin Solid Films **313–314**, 341–346 (1998).
82. L. J. Prokopeva, D. P. Brown, X. Ni, V. P. Drachev, A. Urbas, and A. Kildishev, "Pulse shaping using optical metamaterials with naturally anisotropic structural elements," in *CLEO: QELS-Fundamental Science, OSA Technical Digest (Optical Society of America)*, 2012.

1. Hyperbolic media in retrospect

Recent advances in nanofabrication, characterization, and high-performance computing, along with developments in the theory of light-matter interaction, have brought to life a new class of multi-scale composite systems, known as metamaterials. In metamaterials, it is material geometry that determines the interaction of these complex systems with electromagnetic fields. Metamaterials offer new avenues for manipulation of light, opening the door for such unusual applications as high-resolution imaging, lithography, and lifetime engineering. This review is focused on a subclass of metamaterials called hyperbolic that provide a flexible platform for manipulation of optical landscape.

Hyperbolic metamaterials (HMM), uniaxial structures that due to their extreme anisotropy combine the properties of transparent dielectrics and reflective metals, first attracted the attention of researchers in the middle of last century. These efforts were stimulated by the problem of propagation of radio waves in the Earth's ionosphere [1–4], and, more generally, by the behavior of the electromagnetic waves in a plasma of electrons and ions upon the applied permanent magnetic field. Along with the anisotropic plasmas, stratified man-made hyperbolic materials were studied for radiofrequency applications of transmission lines [5]. Today, hyperbolic metamaterials provide one of the most practical metamaterial platforms. Hyperbolic composites (also known as media with indefinite permittivity and permeability tensors [6]) and some homogeneous materials with hyperbolic dispersion were experimentally realized across the optical spectrum, from UV to visible, and from near-IR to mid-IR frequencies. Sub-wavelength imaging, focusing, lifetime engineering, and new approaches to enhance nonlinear response of optical structures, have all been demonstrated in hyperbolic structures. The hyperbolic media continue to be of great interest to the research community with possible applications emerging in heat transport and acoustics. The purpose of this review is to provide an outlook of this rapidly developing research area.

The review begins with a historical digest of the hyperbolic material's properties. Then, we systematically present the recent theoretical and experimental studies of optical hyperbolic metamaterials. While our main goal is to critically revise the existing experimental evidences of the potential applications of hyperbolic media for sub-diffraction imaging and spontaneous emission engineering, we also highlight the vital discrepancies with existing theoretical fundamentals.

2. Fundamentals of hyperbolic media

The vectors of electric displacement $\mathbf{D}$ and field $\mathbf{E}$ are not always parallel in electrically anisotropic media. They are connected by the constitutive equation $\mathbf{D} = \varepsilon_0[\varepsilon]\mathbf{E}$, where $[\varepsilon]$ is a symmetric *dielectric tensor* and ε_0 is the permittivity of vacuum. The unit coordinate vectors $\hat{\mathbf{x}}$, $\hat{\mathbf{y}}$, and $\hat{\mathbf{z}}$ represent the three Cartesian directions - *the principal axes* – for which $[\varepsilon] = \mathrm{diag}(\varepsilon_x, \varepsilon_y, \varepsilon_z)$, with ε_x, ε_y, and ε_z being *the principal dielectric constants*. In general, the three principal dielectric constants are distinct $\varepsilon_x \neq \varepsilon_y \neq \varepsilon_z$, referred to as optically *biaxial*, and may be wavelength dependent, i.e. exhibit dispersion of the optical axes. In

#190862 - $15.00 USD Received 23 May 2013; revised 10 Jun 2013; accepted 10 Jun 2013; published 17 Jun 2013
(C) 2013 OSA

optically *uniaxial* media, where $\varepsilon_x = \varepsilon_y = \varepsilon$, and $\varepsilon \neq \varepsilon_z$, the principal direction $\hat{\mathbf{z}}$ must coincide with the optic axis, which typically defines the three-fold, four-fold or six-fold axial symmetry of a given crystal, so that $[\varepsilon] = \mathrm{diag}(\varepsilon, \varepsilon, \varepsilon_z)$.

While in crystal optics a uniaxial medium corresponds to a wide class of crystalline structures with mainly elliptic dispersion, for magneto-ionic media it specifies the medium with an infinitely strong magnetostatic field bias [2], which, similar to hyperbolic metamaterials, can also have different signs of the principal dielectric constants, e.g. $\varepsilon > 0$, $\varepsilon_z < 0$ .Here, we restrict ourselves to uniaxial hyperbolic media, as the main known theoretical analyses have been done for the hyperbolic uniaxial plasmas in [3, 7, 8].

2.1 Clemmow's prescriptions

Anisotropy of material constants results in a transformation of the electromagnetic field distribution in space under diffraction or point source radiation. Because of the foreseeable complexity of the general analysis presented in [3, 7, 8] we review the Clemmow approach [2] and isolate the simple cases of TM and TE waves in hyperbolic plasma, which are then applied to the refraction and diffraction of light in novel artificial hyperbolic media. The analysis in [2] is restricted to a media of unit permeability, and starts with known E- and H-fields in free space (denoted respectfully as $\mathbf{E}^0(\mathbf{r}^0)$ and $\mathbf{H}^0(\mathbf{r}^0)$), with $\mathbf{r}^0 = \hat{\mathbf{x}}x^0 + \hat{\mathbf{y}}y^0 + \hat{\mathbf{z}}z^0$ defining an observation point. Then, the scaling procedure $\mathbf{E(r) = [e]E^0([n]r)}$ and $\mathbf{H(r) = [h]H^0([n]r)}$ is derived to find the corresponding fields, $\mathbf{E}(\mathbf{r})$ and $\mathbf{H}(\mathbf{r})$ in a given uniaxial media, where $\mathbf{[e]}, \mathbf{[n]}$, and $\mathbf{[h]}$ are linear transforms. The above procedure is impossible unless one of the *z*-components of either $\mathbf{H}^0$ or $\mathbf{E}^0$ is dropped, leading to solutions valid solely for either transverse magnetic (TM, $\hat{\mathbf{z}} \cdot \mathbf{H}^0 = 0$) or transverse electric (TE, $\hat{\mathbf{z}} \cdot \mathbf{E}^0 = 0$) waves.

From the symmetry considerations for TM-waves it follows that the metric and the *E*-field scaling transforms repeat the structure of the dielectric tensor, $[\varepsilon] = \mathrm{diag}(\varepsilon, \varepsilon, \varepsilon_z)$, so that $[\mathrm{e}] = \mathrm{diag}(e, e, e_z)$, and, while the transverse components of *H*-field are scaled uniformly, i.e. $[\mathbf{h}] = h[\mathbf{i}]$, where $[\mathbf{i}]$ is the identity matrix. From the Maxwell curl equations for the TM waves, it then follows that $nn_z[\mathbf{n}]^{-1}[\mathbf{s}]^{-1} = h^{-1}[\varepsilon]$ and $nn_z[\mathbf{n}]^{-1}[\mathbf{s}] = h[\varepsilon]$, or $ee_z[\mathbf{n}][\mathbf{e}]^{-1} = h[\varepsilon]$. Multiplying the above equations we first arrive at $n^2 = e^2 = \varepsilon_z$, $n_z^2 = e_z^2 = \varepsilon$, and $h^2 = \varepsilon\varepsilon_z$, and then, at the remarkably simple Clemmow's *TM-prescription*

$$\mathbf{E}(\mathbf{r}) = [\mathbf{n}]\mathbf{E}^0([\mathbf{n}]\mathbf{r}), \mathbf{H}(\mathbf{r}) = \sqrt{\varepsilon\varepsilon_z}\mathbf{H}^0([\mathbf{n}]\mathbf{r}), \tag{1}$$

where $[\mathbf{n}] = \mathrm{diag}\left(\sqrt{\varepsilon_z}, \sqrt{\varepsilon_z}, \sqrt{\varepsilon}\right)$.

In contrast, for TE-waves it can be expected that since $\hat{\mathbf{z}} \cdot \mathbf{E}^0 = 0$, then ε_z should not appear in the Maxwell equations for the uniaxial medium, as if that medium were isotropic with dielectric constant ε_z. Indeed, the final Clemmow's *TE-prescription* is, $\left(n = \sqrt{\varepsilon}\right)$

$$\mathbf{E}(\mathbf{r}) = \mathbf{E}^0(n\mathbf{r}), \mathbf{H}(\mathbf{r}) = n\mathbf{H}^0(n\mathbf{r}). \tag{2}$$

2.2 Dispersion relations in a uniaxial hyperbolic medium

Consider the behavior of monochromatic plane waves in uniaxial hyperbolic media before addressing the complex fields generated there by elementary sources. Following the general

#190862 - $15.00 USD Received 23 May 2013; revised 10 Jun 2013; accepted 10 Jun 2013; published 17 Jun 2013
(C) 2013 OSA

Clemmow approach, the space-time dependence $f(\mathbf{r};t)=\exp\left[\imath\left(\frac{\omega}{c}\mathbf{k}\cdot\mathbf{r}-\omega t\right)\right]$ is taken here for a plane wave defined for a given angular frequency ω and the free-space speed of light c using the material wavevector $\mathbf{k}=[\mathbf{n}]\mathbf{k}^0$ with the freespace wave-vector $\mathbf{k}^0$ $\left(\left|\mathbf{k}^0\right|=1\right)$. Then, the *phase velocity* of the plane wave is $v_{\mathrm{p}}=c/|\mathbf{k}|$. A plane wave [9] in a uniaxial media splits into two linearly polarized characteristic waves: *ordinary waves* for which the **E**-vector is normal to the principal plane, which contains both the wave vector and the optic axis, $\mathbf{z}$, and *extraordinary waves* with **E**-vector parallel to the principal plane. For ordinary waves, **E** is aligned with **D**, and the phase velocity is independent of propagation direction. As any free-space electromagnetic field can be represented as a superposition of coplanar TM- and TE-waves, there is always a matching superposition of coplanar TM- and TE-waves in the uniaxial medium obtained from the scaling transformations (1) and (2). These transformations are also reversible, since a representation of any uniaxial-medium field as a superposition of coplanar TM- and TE-waves is always possible. For example, the independent characteristic extraordinary (TM) and ordinary (TE) plane waves in the anisotropic medium are obtained from the corresponding free-space plane waves in [2].

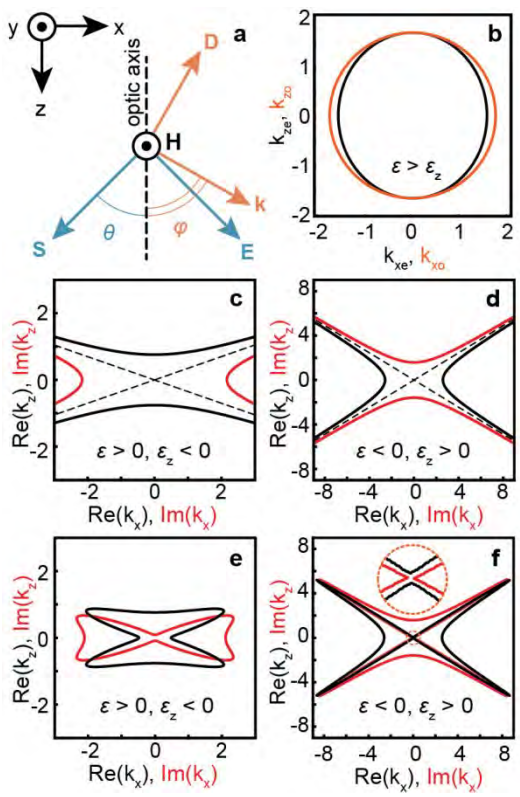

Fig. 1. Typical vector diagram and dispersion relations in uniaxial media. (a) Plane-wave vectors. (b), Isofrequency cross-sections for a negative elliptic media, $\varepsilon<\varepsilon_z$. c, d Isofrequency curves for different types of ideal, lossless hyperbolic media: dielectric, $\varepsilon_z<0, \varepsilon>0$ (c), metallic, $\varepsilon_z>0, \varepsilon<0$, (d). (e), (f) Isofrequency curves for different types of non-ideal, absorbing hyperbolic media: dielectric type, with $\varepsilon_{x,y}=0.57+\imath 0.13$, $\varepsilon_z=-4.22+\imath 2.03$ (e); metallic type, with $\varepsilon_{x,y}=-2.78+\imath 0.13$, $\varepsilon_z=6.31+i0.09$ (f).

#190862 - $15.00 USD Received 23 May 2013; revised 10 Jun 2013; accepted 10 Jun 2013; published 17 Jun 2013
(C) 2013 OSA

For a plane wave defined by $f(\mathbf{r};t)$, the Maxwell equations give,

$$\mathbf{k}\cdot\mathbf{D}=0,\mu_0\mathbf{k}\cdot\mathbf{H}=0,\mathbf{k}\times\mathbf{E}=\mu_0 c\mathbf{H},\mathbf{k}\times\mathbf{E}=\mu_0 c\mathbf{H},\text{and}\,\mathbf{k}\times\mathbf{H}=-c\mathbf{D} \tag{3}$$

While in general the Poynting vector $\mathbf{S}=\frac{1}{2}\mathrm{Re}\left(\mathbf{E}\times\mathbf{H}^*\right)$ is not parallel to $\mathbf{k}$, the vectors within the triads($\mathbf{k},\mathbf{H}$ and $\mathbf{D}$) and ($\mathbf{S},\mathbf{E}$ and $\mathbf{H}$) are mutually orthogonal and vector $\mathbf{H}$ is normal to coplanar vectors $\mathbf{k},\mathbf{D},\mathbf{E}$ and $\mathbf{S}$, as shown in Fig. 1(a).

The eigenvalue problem $\mathbf{k}\times(\mathbf{k}\times\mathbf{E})+[\varepsilon]\mathbf{E}=0$, obtained from the last two equations of (3), gives two distinct characteristic equations respectively for ordinary and extraordinary waves:

$$\frac{k_x^2+k_y^2+k_z^2}{\varepsilon}=1,\ \text{and}\ \frac{k_x^2+k_y^2}{\varepsilon_z}+\frac{k_z^2}{\varepsilon}=1. \tag{4}$$

Note that any "nonideality" of the hyperbolic medium results in a closed form of the iso-frequency curves instead of hyperboloid as shown in Figs. 1(e) and 1(f) for absorbing hyperbolic media.

2.3 Volume plasmon polaritons in hyperbolic media

Since the permittivity tensor has metallic properties for one of the principal components and dielectric for another, there should be a peculiarity in the angular dependence of wave propagation, namely the permittivity for extraordinary wave satisfies the condition $\mathrm{Re}\,\varepsilon(\varphi_c)=\varepsilon'(\varphi_c)=0$ at the critical angle. This condition determines an angular boundary between "metal" and "dielectric" types of propagation. Thus a coupling between plasmon and polariton can occur at this virtual boundary similar to the surface plasmon polariton at a metal-dielectric interface. In this case the hyperbolic media support *plasmon-polariton waves* propagating across the interfaces of real metal and dielectric structures, which are called here *volume plasmon polaritons,*. Consider a slab of hyperbolic uniaxial medium with optical axis in the $\mathbf{z}$ direction. Let displacement vector $\mathbf{D}$ lie in the principal plane containing both optic axis and wave vector $\mathbf{k}$.

Component of electric field directed along $\mathbf{D}$ is given by $E_D=\mathbf{E}\cdot\mathbf{D}/D=D/\varepsilon(\varphi)$, where

$$\frac{1}{\varepsilon(\varphi)}=\frac{\sin^2(\varphi)}{\varepsilon_e}+\frac{\cos^2(\varphi)}{\varepsilon_o}, \tag{5}$$

$\varepsilon_o=\varepsilon_x=\varepsilon_y$, $\varepsilon_e=\varepsilon_z$, and φ is the angle between the wave vector and optical axis. The wave vector refraction at the crystal-isotropic medium interface formally obeys the Snell's law. Once we know the wave vector direction, then the angle θ between the ray and optical axis is defined as follows

$$\tan\theta=\frac{\varepsilon_o}{\varepsilon_e}\tan\varphi. \tag{6}$$

In a hyperbolic media the angular dependence of the permittivity has a resonance behavior as shown in Fig. 2(a), where we have chosen exemplary values for multilayer structures $\varepsilon_o=-2.78+\imath 0.22$, and $\varepsilon_e=6.31+\imath 0.15$. It can be shown that for the critical angle, the angles between $\mathbf{D}$ and $\mathbf{E}$ as well as between $\mathbf{k}$ and are both about 90°, which is clear also from Figs. 2(a) and 2(b). Interestingly the resonance behavior results in a field confinement in the critical direction due to high values of $\mathrm{Im}(\varepsilon)$ as shown in Fig. 2(c).

#190862 - $15.00 USD Received 23 May 2013; revised 10 Jun 2013; accepted 10 Jun 2013; published 17 Jun 2013
(C) 2013 OSA

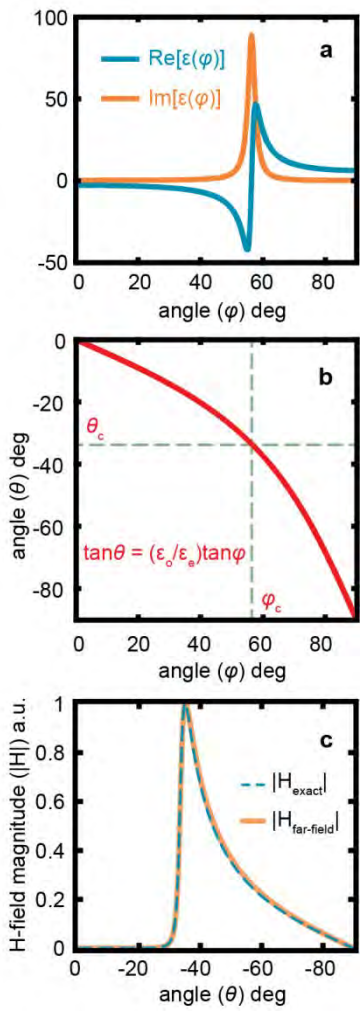

Fig. 2. Volume plasmon-polariton. a) Angular dependence of the permittivity for extraordinary wave, imaginary (brown) and real (blue) parts. Critical angle between wave vector and optic axis $\varphi_c = 57°$; b) Angle between Poynting vector and optic axis $\theta(\varphi), \theta_c = 33°$; c) magnetic field angular dependence localized at the critical angle (calculated at 650 nm from the source) [24]. Figures reproduced with permission from ©2013 Wiley-VCH

2.4 Radiation patterns from elementary sources

Clemmow's prescriptions (Eqs. (1), (2)) converts the field distribution of any localized elementary source in vacuum into the corresponding distribution inside a uniaxial material [2,10]. A gallery of the field distributions generated by various point sources upon different orientations and polarizations in 3D has been recently reviewed in [10] following the earlier works [2,3,7,8,11,12]. Here, our examples show the pseudo-color maps of the *H*-field $\mathbf{H} = \hat{\mathbf{y}}H$ generated by a line of dipolar sources $(\mathbf{p} = \hat{\mathbf{x}}p)$ continuously distributed along *y*-axis in a 2D space (xz-plane), as depicted in Fig. 3(a). The TM *H*-field in vacuum is given by $H^0(x,z) = -\frac{1}{4} p\omega H_1^{(1)}(\rho) z\rho^{-1}$, with $H_1^{(1)}(\rho)$ being the first order Hankel function of the first kind, and $\rho = \omega c^{-1}\sqrt{x^2 + y^2}$ [3]. Then the singular shadow region is aligned with the *xy*-

plane (Fig. 3(a)). By using Eqs. (1)-(2) into $H(x,z)$ and arrive at, $H(x,z) = n_z n H^0(nx, n_z z)$, where $n = \sqrt{\varepsilon_z}, n_z = \sqrt{\varepsilon}$.

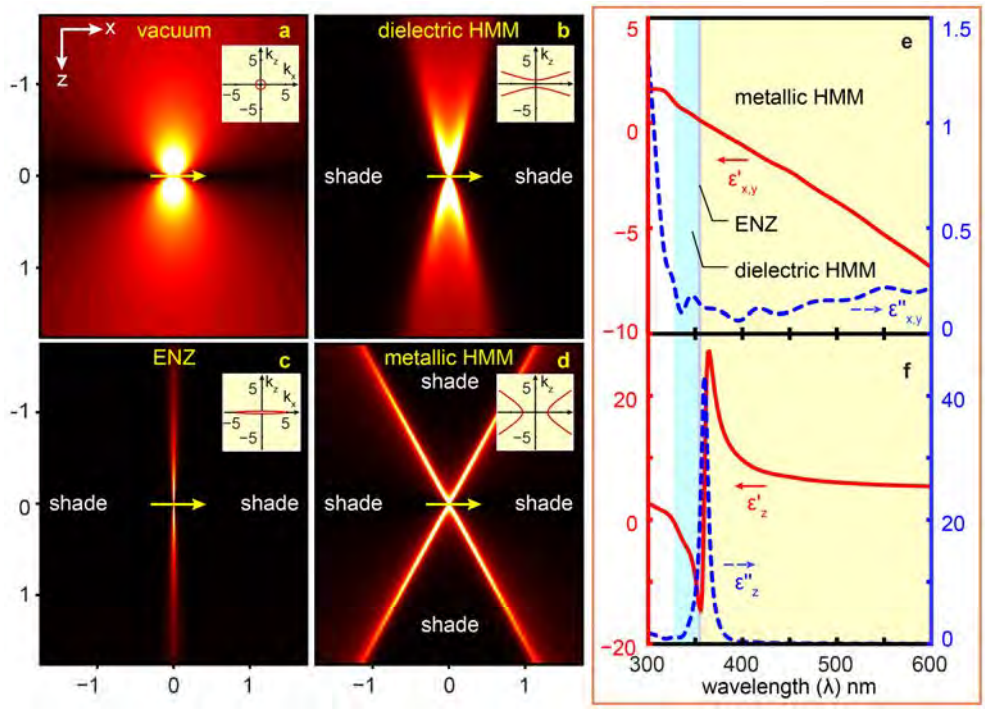

Fig. 3. Radiation from elementary 2D sources and permittivity spectra. a-d, Radiation from a 2D electric dipole in (a) vacuum; (b) lossy dielectric HMMat 340 nm with $\varepsilon_{x,y} = 0.57 + \imath 0.13$, $\varepsilon_z = -4.22 + \imath 2.03$,(the dispersion curve of Fig. 1(e)); (c) ENZ materialat 359.4 nm with $\varepsilon_{x,y} = 0.005 + \imath 0.123$, $\varepsilon_z = 2.82 + \imath 43.3$; and (d) lossy metallic HMMat 465 nm with $\varepsilon_{x,y} = -2.78 + \imath 0.13$, $\varepsilon_z = 6.31 + i 0.09$,(the dispersion curve of Fig. 1(f)); (e) spectra of the xy and (f) z components of the permittivity [24]. Figures reproduced with permission from ©2013 Wiley-VCH

The *H*-field pattern in vacuum, $\mathbf{H}^0(x, z)$, and the corresponding exact *H*-field patterns $\mathbf{H}(x, z)$, for all of the HMM regimes (epsilon near-zero (ENZ), dielectric, and metallic) are shown in Fig. 3(b), 3(c), and 3(d), where the optic axis is aligned with $\hat{z}$. The ENZ regime gives low divergence due to the highly anisotropic elliptical dispersion (see Fig. 3(c)), while the dielectric type of HMM dispersion may result in a similar directional propagation along the optic axis, as shown in Fig. 3(b). This case has been utilized in the new type of optical imaging device, often called hyperlens. The concept of the hyperlens, suggesting a far-field imaging beyond the diffraction limit, was first introduced in [13,14] and experimentally realized in [15,16]. In the hyperlenses light propagates along the optical axis of the hyperbolic anisotropic structure due to very small critical angle. In the metallic type of HMM the volume plasmon polaritons propagate along the resonance cone (Fig. 3(d)). Thus, in contrast to the imaging devices built on ENZ materials and dielectric HMMs [13,14,17,18], optical devices exploiting cone diffraction in metallic hyperbolic media may offer beneficial applications for photo-lithography and light response probing. Several numerical studies [19–23] and a recent experiment [24] have shown that it is possible to obtain an interference peak much smaller

#190862 - $15.00 USD Received 23 May 2013; revised 10 Jun 2013; accepted 10 Jun 2013; published 17 Jun 2013
(C) 2013 OSA

than the free-space wavelength using both diffracted rays as will be discussed in the next section.

Note that all the discussed types of hyperbolic metamaterials can be realized with the same structure by varying the wavelength of the incident light. Figures 3(e) and 3(f) show permittivity spectra for two components of multilayer structure with optic axis denoted by z. For the multilayer dispersion calculations, the Rytov effective medium theory with nonlocal corrections is employed [5]. According to [25], all structures containing one or more metal-dielectric interfaces can be qualitatively considered as a hyperbolic layer.

Depending on composition and component dimensions, multilayer systems provide hyperbolic dispersion at the UV (Ag/Al_2O_3) [13], near-IR(Al/ZnO) [26], and mid-IR (InGaAs/AlInAs) [27] frequency ranges. Hyperbolic dispersion has been also demonstrated in nanowire systems [28–30], and homogeneous materials [31–33].

3. Refraction in hyperbolic media

As described above, in hyperbolic media propagation of the energy, given by the Poynting vector, is not collinear to the propagation of the phase fronts, described by the wavevector, which has profound implications for refraction of the waves to and from the hyperbolic structures. Consider first a single plane wave that is incident at an HMM boundary. Electromagnetic field can be described as a linear combination of incident, reflected, and refracted electromagnetic waves. Existence of the continuous planar interface requires conservation of the component of the wavevector parallel to this interface [9], which fixes the directions of the reflected and refracted waves. Application of the boundary conditions results in the amplitudes of these waves.

Consider now the situation when the interface is illuminated not by a single plane wave, but by a rather wide, but finite-sized monochromatic beam. The electromagnetic field of the beam can be represented as a linear combination of the plane waves, and refraction/reflection of each component of the beam can be calculated using the single-wave formalism described above. When the beam is substantially wide, its plane wave decomposition will contain a relatively narrow spectrum of the wavevector components. Consequently, the Poynting vectors of all the refracted components of the beam will be aligned with each other. This common direction of the Poynting flux describes the direction of the propagation of the refracted beam.

Light refraction at the interface with anisotropic crystals is often non-trivial. Even with naturally-occurring materials it is possible to achieve negative refraction for a limited range of angles [34]. When the light is incident from isotropic material onto hyperbolic media, the beam can be refracted in the negative direction [35]. Negative refraction of the beam has been experimentally validated in layered metamaterials at mid-IR [27] and near-IR frequencies [26], in nanowire-based metamaterials at visible frequencies [30], and in homogeneous media at UV frequencies [31].

Negative refraction has been historically considered the hallmark of metamaterials, where it enables planar lenses that are not limited by spherical aberrations [36]. A classic Veselago lens should have an angle- and polarization-independent index of refraction, and thus requires use of an isotropic magnetic media. Nevertheless, hyperbolic materials can mimic the performance of a Veselago lens in waveguide geometry [37]. Practical applications of 3D lenses based on hyperbolic materials are affected by the dependence of their refractive index on the angle [38], which re-introduces image distortion similar to spherical aberration. Such distortions, however, can be limited in ENZ and in canalization imaging [13,14,39].

4. Diffraction in hyperbolic media: sub-wavelength imaging and nanolithography

Any inhomogeneity inside the material or any inhomogeneity along the boundary between two media necessarily leads to diffraction. Qualitatively, the profile of the diffracted beam can be calculated from the Huygens-Fresnel principle. Note that in contrast to conventional

#190862 - $15.00 USD Received 23 May 2013; revised 10 Jun 2013; accepted 10 Jun 2013; published 17 Jun 2013
(C) 2013 OSA

isotropic materials, emission of waves in hyperbolic systems is highly directional (Figs. 1 and 2). The unique dispersion allows hyperbolic systems to preserve high-wavevector components of the wave-packets that carry information about the subwavelength features of the source. Therefore, hyperbolic structures are capable of focusing radiation to subwavelength spots, a phenomenon that has been proposed in [19, 39] and recently realized in [24]. In this experiment, a double-slit interference of resonant cones produced by slits in Cr film results in a sub-diffraction pattern [19], which is highly beneficial for nanolithography applications [24]. The experiment scheme is shown in (Figs. 4(b) and 4(c)) where the flat Ag/SiO_2 hyperbolic structure forms a line of 90 nm width on the photoresist layer, which was simply brought in contact with the hyperbolic layer and detected then with an Atomic Force Microscope (AFM) [24].

Further, the hyperbolic structures can be used to magnify the subwavelength objects and thus enable far-field super-resolution imaging. Super-imaging is a challenging problem that is typically addressed by near-field optical microscopy. A super-lens made of metamaterial with both negative permittivity and permeability [40] provides a way to translate the information about subwavelength objects. This approach was further developed to incorporate alternating layers with optical gain [41] and to enlarge the objects in acylindrical geometry [42,43].An approach to magnify subwavelength objects in 2D plasmon-polariton systems was proposed in [44].

Curved hyperbolic metamaterials enable far-field magnification of 3D objects when subwavelength information, encoded in resonant cones [11,45] (see Sec. 2) is gradually translated into propagating information similar to the magnification by anisotropic structure [46–48]. Magnifying lens based on hyperbolic metamaterials was proposed in [13,14]; it was then realized in [15] for UV imaging in Ag/Al_2O_3 curved multilayer metamaterial (Fig. 4(a)).

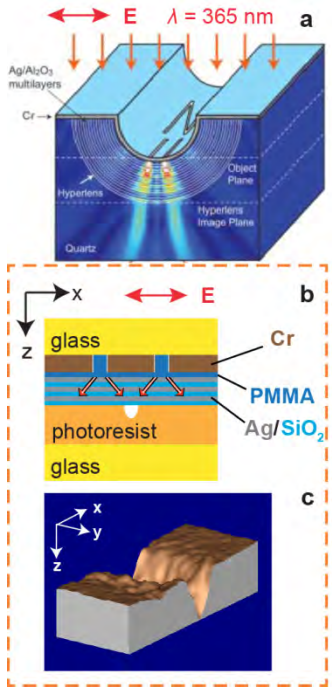

Fig. 4. Imaging (a) [15] and nanolithography (b), (c) [24] with hyperbolic metamaterials. Figures reproduced with permissions: (a) Ref [15] from ©2007 AAAS and (b),(c) Ref [24]. from ©2013 Wiley-VCH.

#190862 - $15.00 USD Received 23 May 2013; revised 10 Jun 2013; accepted 10 Jun 2013; published 17 Jun 2013
(C) 2013 OSA

5. Photonic density of states and radiative rate engineering

Fermi's golden rule with Purcell's effect links the radiative decay rate of spontaneous emission and photonic density of states, which can be modified due to environment in which fluorescent molecules are embedded [49,50]. The most attractive property of the hyperbolic metamaterials pointed in [51] is the broadband and strongly enhanced radiative decay rate for the fluorophore spontaneous emission near or inside a medium relative to free space (Purcell factor). The photonic density of states (PDS) in the metamaterial is related to the volume in k-space enclosed by the corresponding iso-frequency surface [50,51] and may have singularities [51–53]. As we discussed above, the iso-frequencies have closed trajectories (see Fig. 1) which eliminate singularities of the PDS. The value of the enhancement is theoretically limited only by losses [53] or finite period-to-wavelength ratio [53,54]. The finite size of the emitter distribution can limit the HMM density of states even at zero losses [55] and the Purcell factor in hyperbolic metamaterials stays finite due to the discreteness of the actual structure and specific geometry [56–60].

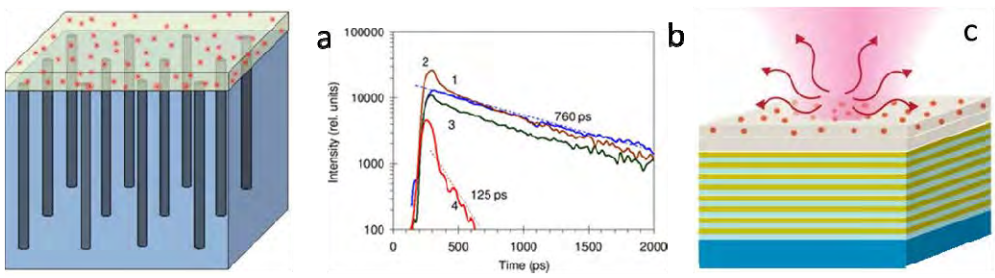

Fig. 5. Wire (a), (b) [28] and layered (c) [25] HMM samples for life time engineering. Figures reproduced with permissions: (a),(b) Ref [28]. from ©2010 OSA and (c) Ref [25]. from ©2012 OSA.

Table 1. Radiative, nonradiative decay rates, apparent quantum yield, and fluorescence and absorption enhancements in layered HMM are shown in the table for four samples, each at 89 and 21 nm dielectric spacer [25]. Table reproduced with permission from ©2012 OSA.

	$\Gamma_r\left(s^{-1}\right)10^{-8}$		$\kappa_{nr}\left(s^{-1}\right)10^{-8}$		Γ_r/κ_{nr}		Q		Fluorescence		Absorption	
nm	89	21	89	21	89	21	89	21	89	21	89	21
HMM	1.4	0.54	4.6	5.66	0.3	0.09	0.23	0.09	9.3	1.6	5.4	2.5
Thick Au	0.9	0.18	4.6	4.6	0.2	0.04	0.17	0.04	9.4	0.9	7.9	3.4
Thin Au	0.7	0.15	5.5	6.8	0.13	0.02	0.12	0.02	6.4	0.55	7.7	3.5
Glass, ref	0.62	0.63	3.9	3.96	0.16	0.16	0.14	0.14	1	1	1	3

Experimental studies mainly focus on life time measurements [28,61];this approach does not provide conclusions on the radiative decay and Purcell factor. In a general case, study of both life time and quantum yield is required [25]. Two types of hyperbolic metamaterials, alumina membrane embedded with silver nanowires [28] and multilayer metal-dielectric [25,29],are typically used in optical experiments to prove the theoretically predicted anomalously high photonic density of states in hyperbolic metamaterials. The material in [28] has exhibited a hyperbolic dispersion with the effective values of permittivity ($\varepsilon_\Pi = 5 + i0.22$, $\varepsilon_\perp = -0.15 + i1.1$).In the film deposited onto the silver-filled membrane, the emission life time of dye was as short as: 125 ps (Fig. 5). The shortening of the emission life time is claimed to be due to a large number of available radiative channels, although this was not proved by the measurements. The quantum yield and the lifetime were measured for the multilayer HMM samples in [25] which consisted of 16 stacked layers Au(19nm)/Al_2O_3(19nm) on a glass substrate, as shown in Fig. 5(c). The quantum yield and life time are related as follows:

#190862 - $15.00 USD Received 23 May 2013; revised 10 Jun 2013; accepted 10 Jun 2013; published 17 Jun 2013
(C) 2013 OSA

$$Q = \Gamma_r \tau,\ \tau = \left(\Gamma_r + \kappa_{nr}\right)^{-1} = \Gamma^{-1}. \quad (7)$$

Here, Γ_r is the radiative decay rate, κ_{nr} is the non-radiative decay rate, τ is the excited state lifetime, and Γ is the total decay rate. For Ag nanoantennae [62], direct measurements of both the lifetime and the quantum yield changes are necessary for conclusive results of the radiative decay rate and Purcell factor. The quantum yield is simply the ratio of the emitted to the absorbed photons and can be determined by measuring the absorption, emission, reflection, and lifetime of the dye molecules relative to a reference dye film. Then the results are compared with the radiative decay rate of control samples that are similar to those used in classic experiments, namely thin and thick gold films. By using the reference method, the quantum yield can be experimentally obtained through absorption and fluorescence measurements for the samples under study relative to the corresponding dye/epoxy reference sample [25]. Purcell factors are shown in Table 1. Our maximum changes in the radiative decay rates relative to Rh800 in methanol are about 1.2 for dye molecules on glass, 1.35 for thin gold films, 1.73 for thick gold, and 2.7 for multilayer HMM samples.

The photonic density of states (PDS) in emitters can be modified due to the interference of emitted and reflected waves near metal films [63,64], which have led to the development of PDS engineering that uses metal-dielectric interfaces [64,65], metal-film interfaces [66–68]. Non-radiative decay can be modified due to dipole-image interaction and excitation of the surface-plasmon polaritons or wave-guiding modes. Indeed, similar to SPP, the limiting factor of the radiative decay is in the out-coupling of the HMM modes to the low PDS of free space [69]. Thus the ratio between leaky and bound modes [66] should be a critical parameter in theory, which would allow to determine effect of HMM on both, the radiative and nonradiative rates. This is the main limitation of the existing theories.

6. Beyond the effective medium theory: nonlocality corrections and additional waves

Hyperbolic metamaterials provide unprecedented opportunities for controlling the flow of optical information. However, the majority of exciting applications of hyperbolic systems can be traced to extreme (either vanishingly small, or infinitely big) values of the components of the effective permittivity tensor or to extreme values of effective refractive index $n_{eff} = k_z c/\omega$. To name a few, traditional implementations of hyperlens and canalization imaging systems rely on $\varepsilon_e \gg \varepsilon_o$. Modulation of photonic density of states, as well as numerous designs leading to subwavelength focusing [19,70] rely on the existence of propagating modes at $n_{eff} \gg 1$. In fact, “extreme” photonics is deeply interweaved with the novel applications of metamaterials, and this relationship extends far beyond the area of hyperbolic systems to cloaking and light transmission through subwavelength channels [71–73] and other applications.

#190862 - $15.00 USD Received 23 May 2013; revised 10 Jun 2013; accepted 10 Jun 2013; published 17 Jun 2013
(C) 2013 OSA

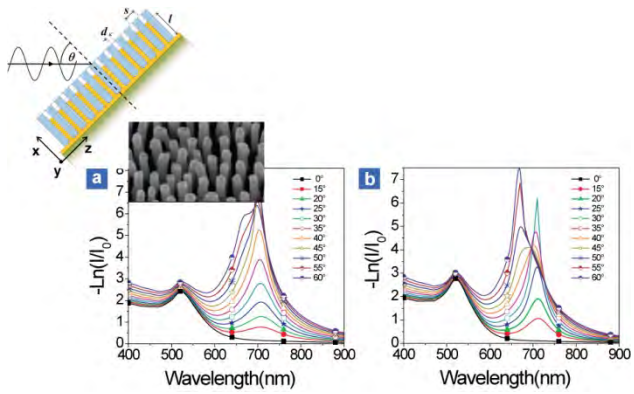

Fig. 6. Effect of nonlocality on extinction in nanowire medium: at high absorption (a) metamaterial exhibits the extinction spectrum consistent with predictions of effective medium theory, at smaller losses (b), interference of two TM-polarized beams becomes evident in transmission [29]. Figures reproduced with permission from ©2009 APS.

However, the very composites that bring to life the extreme behaviors usually provide tight limitations on what can be realized in realistic systems. The optics of nanolayered composites can be understood analytically, with the help of transfer matrix formalism [5,74].

The effective parameters for a multilayer, periodic structure with a period $d = b + a$ and containing both a metal (with permittivity ε_{m} and permeability μ_{m}) and a dielectric $(\varepsilon_{\mathrm{d}}, \mu_{\mathrm{d}})$ are given by [5]:

$$\varepsilon_{\mathrm{o}} = \bar{\varepsilon}_{\mathrm{o}}\left(1 - \frac{\imath kab}{4d}\frac{\mu_{\mathrm{d}}\varepsilon_{\mathrm{m}} - \mu_{\mathrm{m}}\varepsilon_{\mathrm{d}}}{\sqrt{\bar{\varepsilon}_{\mathrm{o}}\bar{\mu}_{\mathrm{o}}}}\right),\ \bar{\varepsilon}_{\mathrm{o}} = \left(\frac{b\varepsilon_{\mathrm{m}} + a\varepsilon_{\mathrm{d}}}{a+b}\right), \tag{8}$$

$$\mu_{\mathrm{o}} = \bar{\mu}_{\mathrm{o}}\left(1 + \frac{\imath kab}{4d}\frac{\mu_{\mathrm{d}}\varepsilon_{\mathrm{m}} - \mu_{\mathrm{m}}\varepsilon_{\mathrm{d}}}{\sqrt{\bar{\varepsilon}_{\mathrm{o}}\bar{\mu}_{\mathrm{o}}}}\right),\ \bar{\mu}_{\mathrm{o}} = \left(\frac{b\mu_{\mathrm{m}} + a\mu_{\mathrm{d}}}{a+b}\right), \tag{9}$$

$$\varepsilon_{\mathrm{e}} = \tilde{\varepsilon}_{\mathrm{e}}, \tilde{\varepsilon}_{\mathrm{e}}^{-1} = \frac{a/\varepsilon_{\mathrm{d}} + b/\varepsilon_{\mathrm{m}}}{a+b}. \tag{10}$$

It was shown in [54,56] that increasing the number of layers at the same thickness brings the results for the multilayer structure closer and closer to those of a homogeneous sample. Note that Eqs. (8)-(10) were obtained in [5] for infinite periodic system with elementary cell made of two layers. For bounded layered systems the key moment of the problems is the boundary conditions. Modification of the boundary conditions by introduction of additional surface currents suggested in [75] returns the conventional permittivity and permeability of metamaterials their usual physical properties. The modified retrieval procedure based on reflection/transmission yields bulk values of effective impedance and refractive index, which are independent of system size and boundary realization, whereas the conductivities of the excess surface currents depend on the property of the interface [75].

Note that the corrections to ideal effective medium theory (EMT) response can be described in terms of a permittivity tensor with wavevector-dependent components. Since wavevector dependence of permittivity can be related to long-range correlation in polarization [76,77], materials that exhibit such dependence are known as nonlocal media. The true response of any composite structure is nonlocal. The significance of nonlocal corrections, however, depends on the particular application and on geometry under consideration.

Optics of nanowire metamaterials offer unique opportunity to realize regimes where nonlocality not corrects, but rather dominates the response of the system. Nanowire materials

#190862 - $15.00 USD Received 23 May 2013; revised 10 Jun 2013; accepted 10 Jun 2013; published 17 Jun 2013
(C) 2013 OSA

are known to provide a flexible platform that can realize elliptic, hyperbolic, and ε-near-zero (ENZ) regimes in the same material. In the ENZ regime, the optical properties of the [meta]material can be approximated as $\varepsilon_{\mathrm{e}}\left(\omega,\mathbf{k}\right)=\imath\varepsilon''+\delta(\mathbf{k})$, with ε'' representing material absorption at ENZ frequency and $\delta(\mathbf{k})$ describing nonlocal correction to the EMT response [77].Therefore, when the losses in material are substantially small, the nonlocal "correction" dominates the polarization inside the system.

Direct solutions of Maxwell equations demonstrate that in this case, [meta-]material supports not two, but at least three different waves, at least two of which have identical (TM) polarization. The existence of additional waves fundamentally changes optical response of the system.

Thus, the spectrum of extinction in nonlocal ENZ metamaterials is dominated not by absorption-related angle-dependent maximum, but rather by collection of angle- and wavelength-dependent maxima corresponding to the points of destructive interference of two TM-polarized beams (Fig. 6). Such changes in optical response of nonlocal metamaterials were first observed in [29].

Any phenomenon that relies on optical response to change of material parameters can potentially be greatly enhanced. In particular, the interference-based transmission has already provided a new way to enhance nonlinear optical response employing nonlocal metamaterials. A clear manifestation of such an enhancement was reported in [78], where optical nonlocality provides a four-fold enhancement to optical nonlinearity in TM-polarized response in comparison to local TE-polarized response of the same metamaterial.

Strong optical nonlocality and existence of additional waves in ENZ regime in layered structures was reported in [79,80], and many other designs of ENZ metamaterials are likely to follow this trend. Optical nonlocality remains an active research area with multiple groups working on better understanding of the collective excitations that underline ENZ response of macroscopic materials

7. Natural hyperbolic materials

The vital aspects in designing an optical element with hyperbolic dispersion is either developing a metamaterial or selecting a natural dispersive material with strong anisotropy. This alternative approach to hyperbolic media has been recently demonstrated as a simulated example of negative refraction in graphite (see Fig. 7(a)) [31]. For far-infrared and THz domains naturally occurring hyperbolic materials have been discussed for a waveguide application at about 20 μm, 58 μm, and 255 μm using, respectively, sapphire, bismuth, or triglycine sulfate [32].

#190862 - $15.00 USD Received 23 May 2013; revised 10 Jun 2013; accepted 10 Jun 2013; published 17 Jun 2013
(C) 2013 OSA

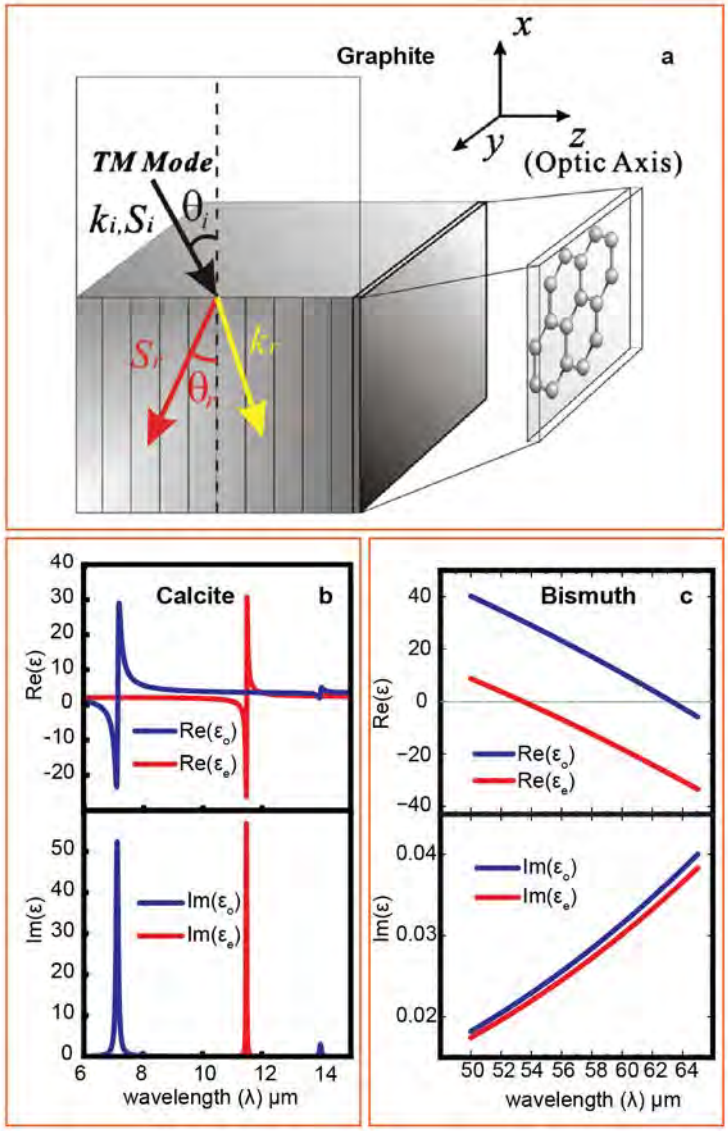

Fig. 7. Natural hyperbolic media. a, Negative refraction in graphite [31]; b, c, Components of the principal dielectric tensor of calcite (b) [81] and monocrystalline Bismuth (c) [32]. Figure 7(a) reproduced with permission from Appl. Phys. Lett. **98**, 101901 (2011) Copyright 2011 American Institute of Physics.

A similar example has been demonstrated [81] with one of the most common mineral, calcite ($CaCO_3$), which, on top of its text-book famous birefringence, exhibits two very distinct non-overlapping ordinary and extraordinary absorption bands in the mid-infrared spectral range as a result of the internal vibration modes of its planar carbonate ions. Two sets of optical dispersion parameters, ordinary and extraordinary, using just a few terms of the Lorentz oscillator model, have been fit to the experimental data using generalized ellipsometry [82].

Dispersion spectra of ε_o and ε_e depicted in Fig. 7(b), indicate that the best figure of merit $FOM_j = -\mathrm{Re}(\varepsilon_j)/\mathrm{Im}(\varepsilon_j), (j = \{o, e\})$ is around 4.7 at 6.75 μm, and around 6.3 at 11.33 μm for the ordinary and extraordinary components respectively

$\varepsilon_{\mathrm{o}}(\lambda = 6.75\,\mu m) = -2.59 + \imath 0.55, \varepsilon_{\mathrm{e}}(\lambda = 11.33\,\mu m) = -1.90 + \imath 0.30$. The major absorption peaks for the ordinary and extraordinary rays are correspondingly located at $\lambda = 7.13\,\mu m$ and $11.48\,\mu m$. Strong hyperbolic anisotropy is not limited to resonance phonon excitations that occur for example in calcite. For example in Bi, a Group V semimetal with rhombohedral lattice and trigonal symmetry, such anisotropy is induced by a substantial difference in its electron effective masses along different directions in the crystal. Hence, the most interesting feature of the Bi dispersion - transition from $\mathrm{Re}(\varepsilon_j) > 0$ to $\mathrm{Re}(\varepsilon_j) < 0,\ j = \{\mathrm{o,e}\}$, _ is determined by the strong anisotropy of its plasma frequency within a band between $\lambda = 53.7\,\mu m$ and $63.2\,\mu m$ as shown in Fig. 7(c). The existence of that 10-μm band has been confirmed experimentally in [33].

In conclusion, while important fundamentals of understanding of optics of hyperbolic media have been laid in the middle of previous century, this unique research area continued explosive growth during the past decade, allowing to advancements beyond the traditional material and functional choices for all components of the optical part of electromagnetic spectrum. These materials lay the foundations for numerous applications with unparalleled performance in lithography, imaging, sensing, and quantum photonics. Effects and devices based on hyperbolic dispersion provide numerous exciting opportunities for future research at the convergence of material science, physics, engineering, and numerical modeling.

Acknowledgments

VPD and AVK acknowledge the support from AFRL Materials and Manufacturing Directorate - Applied Metamaterials Program. VP acknowledges the support from NSF (grant ## ECCS-1102183, DMR-1209761) and ARO (grant # W911NF-12-1-0533)

NONLOCAL OPTICAL RESPONSE OF PLASMONIC NANOWIRE METAMATERIALS

BY

BRIAN MICHAEL WELLS
B.A. (PHYSICS), CLARK UNIVERSITY, WORCESTER, MASSACHUSETTS

SUBMITTED IN PARTIAL FULFILLMENT OF THE REQUIREMENTS
FOR THE DEGREE OF MASTER OF SCIENCE
DEPARTMENT OF PHYSICS AND APPLIED PHYSICS
UNIVERSITY OF MASSACHUSETTS, LOWELL

Signature of Author

Signature of Thesis Supervisor:

Dr. Viktor A. Podolskiy

Signatures of Thesis Committee Members:

Dr. James J. Egan

Dr. Wei Guo

Abstract of Thesis:

Nanowire metamaterials are a class of composite photonic media formed by an array of aligned plasmonic nanowires embedded in a dielectric matrix. Depending on exact composition, geometry, and excitation wavelength, nanowire structures are known to exhibit elliptical, hyperbolic, or epsilon-near-zero (ENZ) responses. In the ENZ regime, optical response of the composite becomes strongly nonlocal. Excitation of an additional wave, caused by nonlocality, has been experimentally demonstrated in nanowire-based metamaterials. In this thesis, a computational study of the nonlocal optical response in plasmonic nanowire arrays has been conducted to better understand such materials. The results of this computational study were used to develop an analytical technique that provides an adequate description of the optical response of wire based metamaterials. This formalism combines the local and nonlocal effective-medium theories often used to describe the optics of nanowire composites. It provides insight into the origin of the additional wave and allows implementation of additional boundary conditions. This approach can be straightforwardly extended to describe the optics for numerious plasmonic structures.

EMISSION MODULATION AND OTHER APPLICATIONS OF NONLOCAL PLASMONIC NANOWIRE METAMATERIALS

BY

BRIAN MICHAEL WELLS
B.A. (PHYSICS), CLARK UNIVERSITY, WORCESTER, MASSACHUSETTS (2004)
M.S. (PHYSICS), UNIVERSITY OF MASSACUSETTS LOWELL, LOWELL, MASSACHUSETTS (2014)

SUBMITTED IN PARTIAL FULFILLMENT OF THE REQUIREMENTS
FOR THE DEGREE OF DOCTOR OF PHILOSOPHY
DEPARTMENT OF PHYSICS AND APPLIED PHYSICS
UNIVERSITY OF MASSACHUSETTS, LOWELL

Signature of
Author: _____ Date:_____

Signature of Dissertation Chair:_____
Dr. Viktor A. Podolskiy

Signatures of Dissertation Committee Members:

_____
Dr. Timothy Cook

_____
Dr. Christopher Baird

EMISSION MODULATION AND OTHER APPLICATIONS OF NONLOCAL PLASMONIC NANOWIRE METAMATERIALS

BY

BRIAN MICHAEL WELLS

ABSTRACT OF A DISSERTATION SUBMITTED TO THE FACULTY OF THE
DEPARTMANET OF PHYSICS AND APPLIED PHYSICS
IN PARTIAL FULFILLMENT OF THE REQUIREMENTS

FOR THE DEGREE OF
DOCTOR OF PHILOSOPHY
PHYSICS
UNIVERSITY OF MASSACHUSETTS LOWELL
2015

Dissertation Supervisor: Viktor A. Podolskiy, Ph.D.
Associate Professor, Assistant Chair, Department of Physics

ABSTRACT

Nanowire metamaterials are a class of composite photonic media formed by arrays of aligned plasmonic nanowires incorporated in dielectric substrates. Numerous applications in modern optics can be realized through the study and understanding of light's interaction with nanowire metamaterials. Depending on exact composition, geometry, and excitation wavelength, nanowire structures are known to exhibit elliptical, hyperbolic, or epsilon-near-zero (ENZ) responses. It was shown, however that the optical properties of these composites deviate from the predictions of effective-medium theories (EMTs). The reason for this deviation is a longitudinal electromagnetic wave that only exists in nonlocal systems. It has been previously shown that this wave originates from the coupling of cylindrical surface plasmon modes propagating along the nanowires. An analytical technique has been developed that provides an adequate description of the optical response of wire-based metamaterials. In this dissertation a simplified analytical approach is developed that can be used to approximate the dispersion of the longitudinal wave in the wire-based metamaterials, avoiding numerical solutions to an eigenvalue problem. Using this developed formalism, it is demonstrated that the incorporation of nonlocal nanowire metamaterials into Salisbury screens allows for a substantial reduction of the dependence of incident angle on the absorption maximum. It is also illustrated that the enhancement of electric field in a non-magnetic, anisotropic, transition metamaterial with a hyperbolic transition layer is largely

overestimated by local effective medium calculations. Nonlocal effects must be taken into account to appropriately descibe the enhancement. Finally, light emission in plasmonic nanowire metamaterials is analyzed analytically and computationally. The emission lifetime is demonstrated to be a complex function of geometrical and material parameters of the system that can not be reduced to the 'trivial' hyperbolic or elliptic dispersion topology. In particular, the presented work suggests that the Purcell factor can often be maximized when the metamaterial operates in the elliptic regime, which is in contrast to the accepted 'hyperbolicity related' enhancement.

Important Notice to Authors

Attached is a PDF proof of your forthcoming article in PRB. Your article has 8 pages and the Accession Code is **BD12966**.

Please note that as part of the production process, APS converts all articles, regardless of their original source, into standardized XML that in turn is used to create the PDF and online versions of the article as well as to populate third-party systems such as Portico, CrossRef, and Web of Science. We share our authors' high expectations for the fidelity of the conversion into XML and for the accuracy and appearance of the final, formatted PDF. This process works exceptionally well for the vast majority of articles; however, please check carefully all key elements of your PDF proof, particularly any equations or tables.

Figures submitted electronically as separate PostScript files containing color appear in color in the online journal. However, all figures will appear as grayscale images in the print journal unless the color figure charges have been paid in advance, in accordance with our policy for color in print (http://journals.aps.org/authors/color-figures-print). For figures that will be color online but grayscale in print, please ensure that the text and captions clearly describe the figures to readers who view the article only in grayscale.

No further publication processing will occur until we receive your response to this proof.

Specific Questions and Comments to Address for This Paper

1 Please provide department or lab for affiliations 2 and 6.
2 Please check equation numbering throughout. Although equations may be numbered by section, the preference is for equations to start with 1 and be numbered continuously throughout. Also, since this is Sec. III, equations numbered by section would have had to start with "3" in this section, so a change was required regardless.
3 Which author is meant by P.S.O.? There is no author with these initials in the list.
4 Is A.P.S. or A.S.S. meant here?
5 Please verify Ref. [12].
6 Please update Ref. [21] with a published article if possible.
7 Please provide page/citation number for Ref. [30].
8 Please check page no. in Ref. [34].
9 Please provide publisher's location for Ref. [36].
10 Please provide page/citation number for Ref. [39].
FQ: This funding provider could not be uniquely identified during our search of the FundRef registry. Please check information and amend if incomplete or incorrect.
Q: This reference could not be uniquely identified due to incomplete information or improper format. Please check all information and amend if applicable.

Titles in References: The editors now encourage insertion of article titles in references to journal articles and e-prints. This format is optional, but if chosen, authors should provide titles for *all* eligible references. If article titles remain missing from eligible references, the production team will remove the existing titles at final proof stage.

FundRef: Information about an article's funding sources is now submitted to CrossRef to help you comply with current or future funding agency mandates. Please ensure that your acknowledgments include all sources of funding for your article following any requirements of your funding sources. CrossRef's FundRef registry (http://www.crossref.org/fundref/) is the definitive registry of funding agencies. Please carefully check the following funder information we have already extracted from your article and ensure its accuracy and completeness:

EPSRC (United Kingdom)
ERC iPLASMM, 321268
U.S. Army Research Office (USA), W911NF-12-1-0533
Australian Research Council (Australia)
SPIE Scholarship
Australian Research Council (Australia)
CONACYT (Mexico)
EC FP7, 304179
Royal Society
Wolfson Foundation (United Kingdom)
Russian Federation, 074-U01
Russian Fund for Basic Research, N13-02-00623
Russian Federation, MK-5220.2015.2
Russian Foundation for Basic Research, 14-02-31783

Other Items to Check

- Please note that the original manuscript has been converted to XML prior to the creation of the PDF proof, as described above. Please carefully check all key elements of the paper, particularly the equations and tabular data.
- Please check PACS numbers. More information on PACS numbers is available online at http://journals.aps.org/PACS/.
- Title: Please check; be mindful that the title may have been changed during the peer review process.
- Author list: Please make sure all authors are presented, in the appropriate order, and that all names are spelled correctly.
- Please make sure you have inserted a byline footnote containing the email address for the corresponding author, if desired. Please note that this is not inserted automatically by this journal.
- Affiliations: Please check to be sure the institution names are spelled correctly and attributed to the appropriate author(s).
- Receipt date: Please confirm accuracy.
- Acknowledgments: Please be sure to appropriately acknowledge all funding sources.
- Hyphenation: Please note hyphens may have been inserted in word pairs that function as adjectives when they occur before a noun, as in "x-ray diffraction," "4-mm-long gas cell," and "*R*-matrix theory." However, hyphens are deleted from word pairs when they are not used as adjectives before nouns, as in "emission by x rays," "was 4 mm in length," and "the *R* matrix is tested."

  Note also that Physical Review follows U.S. English guidelines in that hyphens are not used after prefixes or before suffixes: superresolution, quasiequilibrium, nanoprecipitates, resonancelike, clockwise.
- Please check that your figures are accurate and sized properly. Make sure all labeling is sufficiently legible. Figure quality in this proof is representative of the quality to be used in the online journal. To achieve manageable file size for online delivery, some compression and downsampling of figures may have occurred. Fine details may have become somewhat fuzzy, especially in color figures. The print journal uses files of higher resolution and therefore details may be sharper in print. Figures to be published in color online will appear in color on these proofs if viewed on a color monitor or printed on a color printer.
- Please check to ensure that titles are given as appropriate.
- ***Overall, please proofread the entire article very carefully.***

Ways to Respond

- ***Web:*** If you accessed this proof online, follow the instructions on the web page to submit corrections.
- ***Email:*** Send corrections to prbproofs@aptaracorp.com
  Subject: **BD12966** proof corrections
- ***Fax:*** Return this proof with corrections to +1.703.791.1217. Write **Attention:** PRB Project Manager and the Article ID, **BD12966**, on the proof copy unless it is already printed on your proof printout.
- ***Mail:*** Return this proof with corrections to **Attention:** PRB Project Manager, Physical Review B, c/o Aptara, 3110 Fairview Park Drive, Suite #900, Falls Church, VA 22042-4534, USA.

PHYSICAL REVIEW B **00**, 005100 (2015)

Purcell effect in hyperbolic metamaterial resonators

Alexey P. Slobozhanyuk,[1,2,*] Pavel Ginzburg,[3,4,†] David A. Powell,[1] Ivan Iorsh,[2] Alexander S. Shalin,[2,5,6] Paulina Segovia,[3] Alexey V. Krasavin,[3] Gregory A. Wurtz,[3] Viktor A. Podolskiy,[7] Pavel A. Belov,[2] and Anatoly V. Zayats[3]

[1]*Nonlinear Physics Center, Research School of Physics and Engineering, Australian National University, Canberra, ACT 0200, Australia*

[2]*ITMO University, St. Petersburg 197101, Russia*

[3]*Department of Physics, King's College London, Strand, London WC2R 2LS, United Kingdom*

[4]*Department of Physical Electronics, Fleischman Faculty of Engineering, Tel Aviv University, Tel Aviv 69978, Israel*

[5]*Kotel'nikov Institute of Radio Engineering and Electronics, RAS (Ulyanovsk branch), Ulyanovsk 432011, Russia*

[6]*Ulyanovsk State University, Ulyanovsk 432017, Russia*

[7]*Department of Physics and Applied Physics, University of Massachusetts Lowell, One University Avenue, Lowell, Massachusetts 01854, USA*

(Received 22 April 2015; revised manuscript received 12 August 2015; published xxxxxx)

The radiation dynamics of optical emitters can be manipulated by properly designed material structures providing high local density of photonic states, a phenomenon often referred to as the Purcell effect. Plasmonic nanorod metamaterials with hyperbolic dispersion of electromagnetic modes are believed to deliver a significant Purcell enhancement with both a broadband and a nonresonant nature. Here, we have investigated finite-size resonators formed by nanorod metamaterials and shown that the main mechanism of the Purcell effect in such resonators originates from the supported hyperbolic modes, which stem from the interacting cylindrical surface plasmon modes of the finite number of nanorods forming the resonator. The Purcell factors delivered by these resonator modes reach several hundreds, which is up to 5 times larger than those in the ε-near-zero regime. It is shown that while the Purcell factor delivered by the Fabry-Pérot modes depends on the resonator size, the decay rate in the ε-near-zero regime is almost insensitive to geometry. The presented analysis shows a possibility to engineer emission properties in structured metamaterials, taking into account their internal composition.

DOI: 10.1103/PhysRevB.00.005100 PACS number(s): 81.05.Xj, 73.20.Mf, 78.67.Pt

I. INTRODUCTION

The local density of optical states (LDOS) related to various photonic modes can strongly affect quantum dynamics of light-matter interactions [1]. Free-space electromagnetic modes can be modified in the vicinity of material structures, and as a result, either a local enhancement or reduction of the interaction strength can be achieved. The rate of spontaneous emission in a weak light-matter coupling regime, calculated on the basis of the Fermi golden rule, is proportional to the LDOS, and its change relative to free space is referred to as a Purcell factor [2]. Furthermore, the formalism of the Purcell effect can be generalized to higher-order effects, such as spontaneous two-photon emission [3,4]. The Purcell enhancement in dielectric cavities is typically related to the ratio of the quality factor of the resonance to the volume occupied by the resonant mode. Various types of photonic cavities can deliver quality Q factors as high as 10^{10} and satisfy the conditions to reach the strong-coupling regime [5] where the Purcell factor description of decay dynamics breaks down [6]. Noble metal (plasmonic) nanostructures provide relatively low quality factors but yield subwavelength optical confinement [7] and, as a result, also efficiently influence spontaneous emission [8,9]. This nanoplasmonic approach is extremely beneficial for certain quantum optical applications, where improved and designed scattering cross sections are required to develop functionalities at the nanoscale and single-photon levels [10]. The Purcell enhancement in plasmonic nanostructures depends significantly on the relative position of the emitters with respect to a metal nanostructure, posing serious challenges and limitations for large-scale practical implementations [11]. Furthermore, the enhancement, based on local plasmonic resonances approach, still has a limited bandwidth, even though it is much broader than for high-Q optical cavities.

A qualitatively different approach to decay rate engineering relies on designing the hyperbolic dispersion of modes supported by anisotropic metamaterials, which ensures high nonresonant Purcell factors in a broad wavelength range [12]. These metamaterials with extreme anisotropy of dielectric permittivity, also known as hyperbolic metamaterials, have recently attracted significant attention due to their unusual electromagnetic properties. Homogenized hyperbolic metamaterials were theoretically shown to provide infinitely large LDOS and, as a result, are expected to deliver extremely high Purcell enhancements [13]. This diverging LDOS originates from the hyperbolic dispersion of modes in uniaxial crystals, having opposite sign of the permittivity components in the ordinary and extraordinary directions, perpendicular and parallel to the optical axis, respectively. The fundamental limitations for this type of enhancement result from a particular metamaterial realization as composites of finite-length scale components, commonly referred to as "meta-atoms" [14], as well as the metamaterials' nonlocal response [15,16]. The most widely used realizations of hyperbolic metamaterials are based on layered metal-dielectric structures [17] or vertically aligned nanorod arrays [18]. Hyperbolic metamaterials also served as building blocks for optical components with enhanced capabilities, such as hyperbolic cavities [19] and waveguides [20], as well as for delivering nonreciprocal effects [21], for Hamiltonian optics-based cavities [22], and for many others.

*Corresponding author: a.slobozhanyuk@phoi.ifmo.ru
†Corresponding author: pginzburg@post.tau.ac.il

 ©2015 American Physical Society

In this work, we analyze emission properties of a radiating dipole embedded inside or in close proximity to a finite-size three-dimensional resonator formed by a nanorod-based hyperbolic metamaterial. Taking into account the details of the hyperbolic metamaterial realization as a finite number of plasmonic nanorods, we show that the Purcell enhancement originates from Fabry-Pérot modes of the resonator formed by a hyperbolic metamaterial. The role of the modes of the metamaterial resonators on the Purcell factor was investigated for different resonator sizes, and the importance of the emitter's position within the resonator has been considered. We also demonstrate the fast convergence of the Purcell enhancement with the increase of the number of nanorods in the array, with a 16×16 nanorod array having properties of the infinite metamaterial slab (infinite number of finite-length rods). This enables comparison of the Purcell enhancement provided by both finite-sized and infinite structures and separating the impact of the modal structure of finite-size resonators.

II. EFFECTIVE MEDIUM THEORY AND NUMERICAL MODELING

We consider a metamaterial consisting of a square array of plasmonic (Au) nanorods (Fig. 1). This basic configuration enables addressing all the relevant effects, with substrate material and embedding dielectric material straightforwardly included in numerical modeling. In the first approximation, neglecting nonlocal effects [23], the optical response of such a structure can be obtained from a homogenization procedure of the nanorod composite [24], representing it as an effective uniaxial medium with permittivity tensor $\varepsilon = \mathrm{diag}(\varepsilon_{xx}, \varepsilon_{xx}, \varepsilon_{zz})$, where $\varepsilon_{xx} = \varepsilon_{yy}$ and ε_{zz} are the permittivities for the light polarization perpendicular to and along the nanorod axes, respectively [Figs. 1(a) and 1(b)]. In the frequency range where ε_{xx} and ε_{zz} have opposite signs [Fig. 1(c)], extraordinary electromagnetic modes, propagating in such an anisotropic medium, have hyperbolic dispersion. For the considered system, this crossing from the conventional elliptic to hyperbolic dispersion regime occurs at around 520-nm wavelength, where the real part of the effective permittivity ε_{zz} becomes vanishingly small [Fig. 1(c)]. The frequency range around $\mathrm{Re}(\varepsilon_{zz}) = 0$ is called the ε-near-zero (ENZ) regime. This ability to support the quasistatic behavior of electromagnetic waves (freeze phase) has various intriguing consequences on wave propagation in bended structures [25] and in tailoring radiation properties [26]. It should be noted that the ENZ regime is usually connected to the strong spatial dispersion effects since the vanishing leading term in the permittivity coefficient makes the next term of significant importance [27].

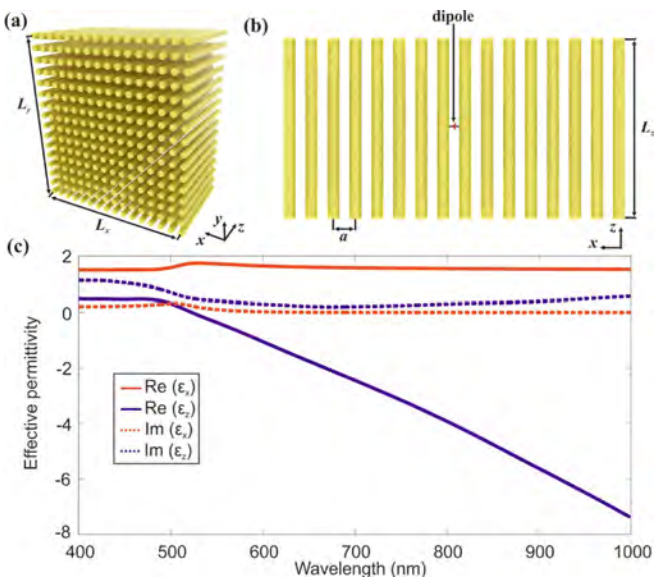

FIG. 1. (Color online) (a) Schematic view of the hyperbolic metamaterial resonator with the transverse dimensions L_x and L_y. (b) Schematics of the numerical setup. An emitting dipole is inserted in the center of the resonator. (c) The effective permittivity of the metamaterial calculated for an infinite array of nanorods with $L_z = 350\,\mathrm{nm}$, $a = 60\,\mathrm{nm}$, $r = 15\,\mathrm{nm}$ (Au permittivity was taken from [32]).

The nonlocal (spatial dispersion) behavior of the nanorod metamaterials cannot be described in the conventional effective medium theory and has an impact on both reflection and transmission of the metamaterial as well as emission and nonlinear effects [23]. Electromagnetic nonlocalities could be classified as structural, material, and collective [28]. While constitutive material components of the considered metamaterial may, in principle, exhibit collective hydrodynamic-type nonlocalities [29], their contribution is small for the geometrical sizes considered here. Structural nonlocality due to the retardation effects in the unit cell is much stronger in the case of nanorod metamaterial, requiring modifications in the homogenization approach and the use of modified effective medium models [30]. Numerical modeling which considers the internal, microscopic structure of metamaterial composites takes the structural nonlocality into consideration automatically without the need for any additional considerations.

The numerical simulations have been performed using the time-domain solver of the CST MICROWAVE STUDIO 2014 package [31]. We used a perfect matched layer (PML) boundary, and additional space was added between the structure and the PMLs in order to prevent evanescent waves from interacting with the boundaries. Optical constants for gold were taken from Ref. [32]. The subwavelength dipolar emitter was modeled here as a perfect electric conductor (PEC) nanorod with a length of 28 nm and a radius of 1 nm [Fig. 1(b)]. The Purcell factor was calculated through an input impedance of a point dipole source. As was previously shown [33,34], this method is completely equivalent to the Green's function approach, which is widely used in photonics [35].The overall number of mesh cells was around 3×10^6, with mesh density locally adjusted in order to accurately represent the source. In order to reach reliable results and to prevent the oscillation of the output time signal after the excitation has been turned off, the duration of the simulation is usually increased above the interval needed to transmit the excitation pulse.

The numerical analysis based on the Green's function approach enables evaluation of both the decay rates, which are proportional to the imaginary part of the Green's function, and the energy shift, which is proportional to its real part [36]. A similar approach taking into account nonlocal response, Lamb shift, and linewidth modifications was recently used for layered hyperbolic metamaterials [37]. The analysis, reported

here, concentrates on Purcell factor evaluation. Since the rate enhancement has not shown extremely high values, wavelength shift was neglected for emitters.

III. RESULTS

A. Hyperbolic metamaterial resonators

We begin with an analytical description of the modal structure of finite-size resonators made of a homogenized hyperbolic metamaterial based on the nanorod assembly. The Purcell factor is proportional to the imaginary part of the Green's function in a medium [1]:

$$R(\omega) = \mathrm{Im}G(\mathbf{r},\mathbf{r},\omega) \approx \mathrm{Im}\sum_{n,l,m,\sigma}\frac{\left|E_x^{n,l,m,\sigma}(\mathbf{r})\right|^2}{\omega^2-\omega_{n,l,m,\sigma}^2}, \quad (1)$$

where n, l, m are integers denoting the eigenmode number of the resonator made of the metamaterial and $\sigma = \{\mathrm{TE},\mathrm{TM}\}$ is the mode's polarization, where TE corresponds to the modes with the electric field lying in the xy plane and TM corresponds to the modes with the magnetic field in the xy plane. The imaginary part of electromagnetic Green's functions describes the LDOS and does not diverge due to losses in the system if the emitter is placed in lossless dielectric between the nanorods. On the other hand, material losses in the nanorods themselves and radiation from the resonator into the far field remove divergence of Eq. (1) in the vicinity of the poles.

The rigorous eigenmode analysis of the anisotropic and lossy rectangular resonator requires sophisticated numerical techniques. However, approximate expressions for the eigenfrequencies and field distributions in the resonator can be derived within an approximate analytical formalism [38]. Within this formalism, perfect electric conductor (PEC) boundary conditions are imposed at the sidewalls of the resonator at $x = \pm L_x/2$, $y = \pm L_y/2$ in order to obtain the resonator mode numbers, corresponding to quantized $k_{x,(m)}$ and $k_{y,(l)}$ wave vectors in x and y directions, respectively:

$$\begin{aligned} k_{x,(m)} &= \frac{\pi m}{L_x}, \quad m = 1,3,5\ldots, \\ k_{y,(l)} &= \frac{\pi l}{L_y}, \quad l = 1,3,5\ldots. \end{aligned} \quad (2)$$

If the radiating dipole is situated on the $(0,0,z)$ axis, only the modes with symmetric E_x and E_y field distributions with respect to inversions $x \to -x, y \to -y$ can be excited by the dipole and will contribute to the Purcell effect.

In order to obtain the mode structure in the remaining z direction, a slab waveguide is then considered which may support TM and TE guided modes confined in the z direction. The propagation constant of these modes $k_{\perp,(m,l)}$ satisfies the condition

$$k_{\perp,(m,l)} = \sqrt{k_{x,(m)}^2 + k_{y,(l)}^2}. \quad (3)$$

This $k_{\perp,(m,l)}$ propagation constant can be evaluated by finding the modes of a hyperbolic-metamaterial-slab waveguide in the effective medium approximation [39]. As has been shown in the analysis of the metamaterial waveguides [39] and can also be seen from the numerical modeling below, this approximation holds for lower-order highly confined modes of sufficiently large resonators.

First, we will consider quasi-TE modes of the resonator. By substituting Eq. (2) into the dispersion equation (3) for a slab waveguide which is symmetric with the respect to the $z \to -z$ inversion, we find two classes of modes with the tangential electric field either symmetric ($n = 0, 2, 4, \ldots$) or antisymmetric ($n = 1, 3, 5\ldots$) along the z axis (the index here corresponds to the number of zero crossings for a leading field component: electric field for TE and magnetic field for TM modes):

$$\frac{\sqrt{k_{\perp,(m,l)}^2 - \left(\frac{\omega_{m,l,n,\mathrm{TE}}}{c}\right)^2}}{\sqrt{\varepsilon_{xx}\left(\frac{\omega_{m,l,n,\mathrm{TE}}}{c}\right)^2 - k_{\perp,(m,l)}^2}} = \tan\left\{\frac{\sqrt{\varepsilon_{xx}\left(\frac{\omega_{m,l,n,\mathrm{TE}}}{c}\right)^2 - k_{\perp,(m,l)}^2}\,L_z}{2} + \frac{\pi}{4}[1-(-1)^n]\right\}. \quad (4)$$

If the dipole is placed at $z = 0$, the antisymmetric modes will have the node of the electric field at the dipole position and thus cannot be excited and will not contribute to the Purcell effect [Eq. (1)]. When the dipole is shifted from $z = 0$, both symmetric and antisymmetric modes will contribute to the Purcell factor. Similarly, using the waveguide dispersion for TM polarized modes, we obtain

$$\frac{\sqrt{\varepsilon_{xx}}\sqrt{k_{x,(m)}^2 + k_{y,(l)}^2 - \left(\frac{\omega_{m,l,n,\mathrm{TM}}}{c}\right)^2}}{\sqrt{\left(\frac{\omega_{m,l,n,\mathrm{TM}}}{c}\right)^2 - \frac{k_{\perp,(m,l)}^2}{\varepsilon_{zz}}}} = \tan\left\{\frac{\sqrt{\varepsilon_{xx}}\sqrt{\left(\frac{\omega_{m,l,n,\mathrm{TM}}}{c}\right)^2 - \frac{k_{\perp,(m,l)}^2}{\varepsilon_{zz}}}\,L_z}{2} + \frac{\pi}{4}[1-(-1)^n]\right\}, \quad (5)$$

In this case, however, the modes are symmetric ($n = 0, 2, 4, \ldots$) or antisymmetric ($n = 1, 3, 5\ldots$) with respect to the tangential component of the magnetic field, with the electric field having opposite symmetry.

In order to distinguish the mode contributions to the Purcell effect, the spectrum of the eigenmodes will first be analyzed assuming vanishing Ohmic losses in the metamaterial. In this approximation, following Eq. (4), the TE mode eigenfrequencies are limited by

$$\frac{\pi}{L_x}\sqrt{(m)^2+(l)^2} < \frac{\omega_{m,l,n,\mathrm{TE}}}{c} < \frac{\pi}{L_x}\sqrt{\varepsilon_{xx}}\sqrt{(m)^2+(l)^2}, \quad (6)$$

satisfying the requirement that the left-hand side of Eqs. (2) and (4) should be real valued. Therefore, for any finite-frequency range, only a finite number of pairs (m,l) exists that satisfy Eq. (6). For each (m,l) pair, a finite set of mode numbers n can be found from the solution of Eq. (3). Thus, in a finite-frequency range, only a finite number of eigenmodes (m,l,n) of the metamaterial resonator exists.

Specifically, for the metamaterial resonator of the square cross section with $L_x = L_y = 900$ nm and $L_z = 350$ nm and

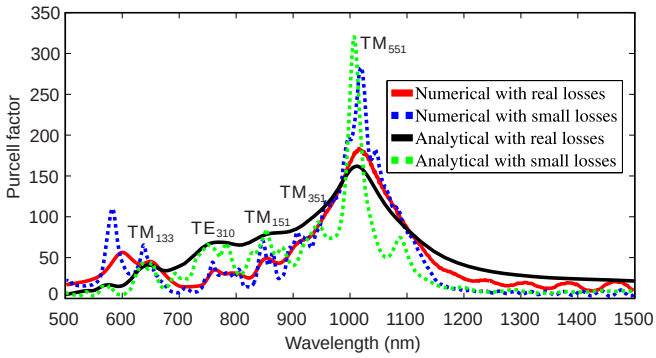

FIG. 2. (Color online) Comparison of the numerical (red and blue lines) and analytical (green and black lines) of the Purcell factor in the case of real losses (solid lines) and reduced losses $\mathrm{Im}(\varepsilon)/10$ (dashed lines). The metamaterial parameters are as in Fig. 1. The resonator size is 16×16 nanorods with $L_x = L_y = 900$ nm.

the effective permittivity as in Fig. 1(c), the following eigenmodes can be excited in the spectral range from 500 to 1500 nm: TE_{110} at $\lambda = 1450$ nm, TE_{130} and TE_{310} at $\lambda = 780$ nm, and TE_{330} at $\lambda = 570$ nm. It should be noted that while the predicted higher-order modes were observed in the rigorous numerical simulations of the nanorod composite, the fundamental mode in the vicinity of 1450 nm has not been observed and occurs at wavelengths larger than 1500 nm (Fig. 2). This is a known discrepancy [40] related to the fact that the simplified analysis used above works worse for the fundamental modes with lower confinement within a resonator, and thus, the actual frequency of the TE_{111} mode frequency can deviate substantially from the value predicted by the simplified analytical formalism.

Contrary to TE modes, the eigenfrequencies of TM modes decrease with the increase of m and l, as can be seen from Eq. (5). This property of the hyperbolic resonators has been observed both theoretically and experimentally [19] and can be understood from the requirement for the TM eigenfrequencies analogous to Eq. (6):

$$\frac{\pi^2}{L_x^2}[m^2 + l^2] > \frac{\omega_{m,l,n,\mathrm{TM}}^2}{c^2} > \frac{\pi^2}{L_x^2 \varepsilon_{zz}}[(m)^2 + l^2]. \qquad (7)$$

Since ε_{zz} is negative in the hyperbolic regime, the right-hand-side inequality holds for any frequency and m, l. Thus, there exist modes with arbitrary large m, l that satisfy the left-hand-side inequality. The number of the supported modes is, however, limited due to the metamaterial realization as a periodic nanorod array. Contrary to the case of the uniform hyperbolic metamaterial, the x and y wave vectors should be within the first Brillouin zone of the array, $k_{x,y} < \pi/a$, where a is the period of the array. Thus, for TM modes, m and l eigenvalues can be 1, 3, 5, and 7 in the case of the 16×16 nanorod array with the parameters as in Fig. 1. For simplicity, in these analytical calculations we do not consider possible coupling between TE and TM modes due to three-dimensional geometrical confinement (the numerical modeling includes all the effects).

For each value of m and l there is a number of eigenmodes corresponding to different n. This number is finite and increases with m, l. Despite the large number of the TM polarized eigenmodes supported by the resonator, many of them have a minor contribution to the overall Purcell factor since those modes are characterized either by small Q factors due to the large damping inside the resonator when the losses in metal are considered or by a small value of the x component of the electric field at the dipole's position due to the different symmetry properties of the eigenmodes. Namely, some of the eigenmodes would have a minimum of the x component of the electric field at the dipole position, and some would have maxima [41]. Moreover, in the vicinity of the ENZ frequency, the modes with large values of n are excited. However, these modes have large losses and thus give little contribution to the overall Purcell effect. It should be noted, however, that calculations of the Purcell enhancement for emitters placed in contact with lossy media face several challenges as the Green's functions diverge [30]. This problem is usually addressed by introducing a depolarization volume (a small lossless cavity) around the emitter [30]. The numerical modeling below does not, however, face the above issues, as the emitter is placed in the lossless space between actual rods, forming the metamaterial.

The dependences of the resonant wavelength on the resonator height L_z for modes TE_{130}, TM_{151}, and TM_{551} are shown in Fig. 3(a). The higher-order mode TM_{551} is lower in frequency than the lower-order mode TM_{151}, as is expected for the hyperbolic resonators. This can be intuitively understood considering PEC boundary conditions on the

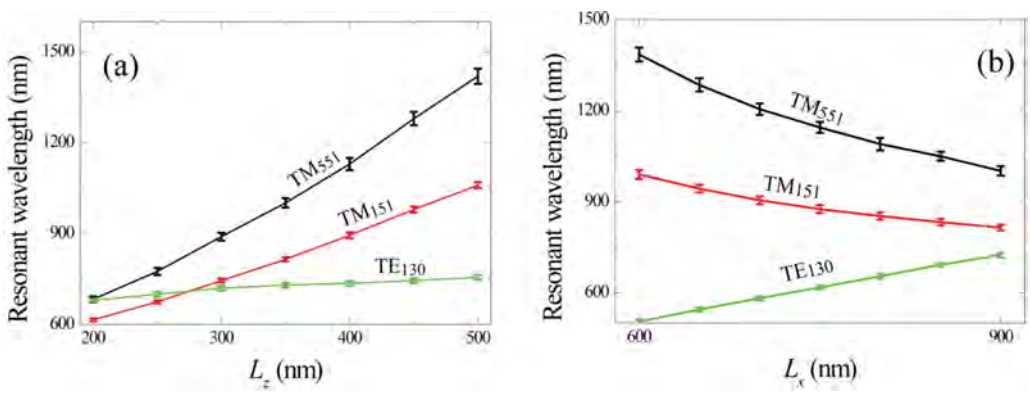

FIG. 3. (Color online) Dependence of the resonant wavelength of the eigenmodes on (a) L_z for the fixed $L_x = L_y = 900$ nm and (b) L_x for fixed $L_z = 350$ nm. Error bars indicate the width of the resonance.

interface perpendicular to the z axis. In this case, k_z is simplified to $k_z = \pi n L_z = \sqrt{\varepsilon_{xx}}\sqrt{\omega^2/c^2 - k_\perp^2/\varepsilon_{zz}}$, where n is an integer. It can be seen that for fixed n, the eigenfrequency decreases with increasing $k_\perp$. The dependence of the resonant wavelength on the resonator width L_x at the fixed resonator length $L_z = 350$ nm is shown in Fig. 3(b). As we can see, the resonant wavelengths of the TM modes decrease with the increase of the resonator lateral size. This behavior is evident from Eq. (3) since it can be seen that for the fixed value of k_z^{TM} the resonant frequency should increase with increasing L_x. In contrast, the wavelengths of the TE modes increase with the increase of the resonator width L_x, similar to the case of a conventional anisotropic dielectric resonator.

B. Purcell enhancement due to the hyperbolic resonator modes

The analytical analysis performed above does not account for either the microscopic structure of the metamaterial or the radiation from the resonator. We now compare the effective medium analytical description to the results of the numerical modeling in the case of an x-polarized dipole placed in the center of the 16×16 array of Au nanorods (period $a = 60$ nm and radius $r = 15$ nm) which corresponds to the resonator dimensions $L_y = L_x = 900$ nm and $L_z = 350$ nm. We have considered real losses in gold for comparison to the analytical model as well as artificial low losses (artificially reduced in 10 times) in order to articulate the mode position (Fig. 2). The analytical model provides a clear correspondence to the numerical results, and the individual eigenmodes can be identified. The highest Purcell factor corresponds to the excitation of the TM_{551} eigenmode in the vicinity of 1000 nm. The Purcell factor near the ENZ frequency range does not have extremely large values, as would be expected in the case of an infinitely large metamaterial [30].

C. Saturation of the Purcell enhancement in finite-size arrays

The Purcell factor for the electric dipole placed in the center of the metamaterial resonator was numerically calculated for different sizes of the resonator (Fig. 4). Both parallel and perpendicular to the nanorods, orientations of the emitting dipole were analyzed in square and rectangular resonators with up to 18 rods in one direction. The obtained dependence of the Purcell factor shows a fast convergence with an increasing number of rods in the array. In fact, in the arrays larger than 16×16 rods (900×900 nm), the Purcell factor approaches the values for the infinite (in the x and y directions) planar metamaterial slab, so that the Purcell factors for 16×16 and 18×18 arrays are essentially the same without the signatures of the resonant modes of the resonator due to the reduced quality factor of the modes [Fig. 4(a)]. This quality factor reduction in larger systems is the result of increased material losses due to the mode being spread over larger number of rods. Rectangular nanorod arrays show similarly fast convergence, enabling us to state that the behavior of 16×16 nanorod structures is extremely close to that of the infinite metamaterial [Fig. 4(a)]. In particular, the x-oriented dipole source which is located in the central part of the array can excite only even modes [Fig. 4(a)]. It can be seen that for the 2×2 array the highest Purcell factor (around 500)

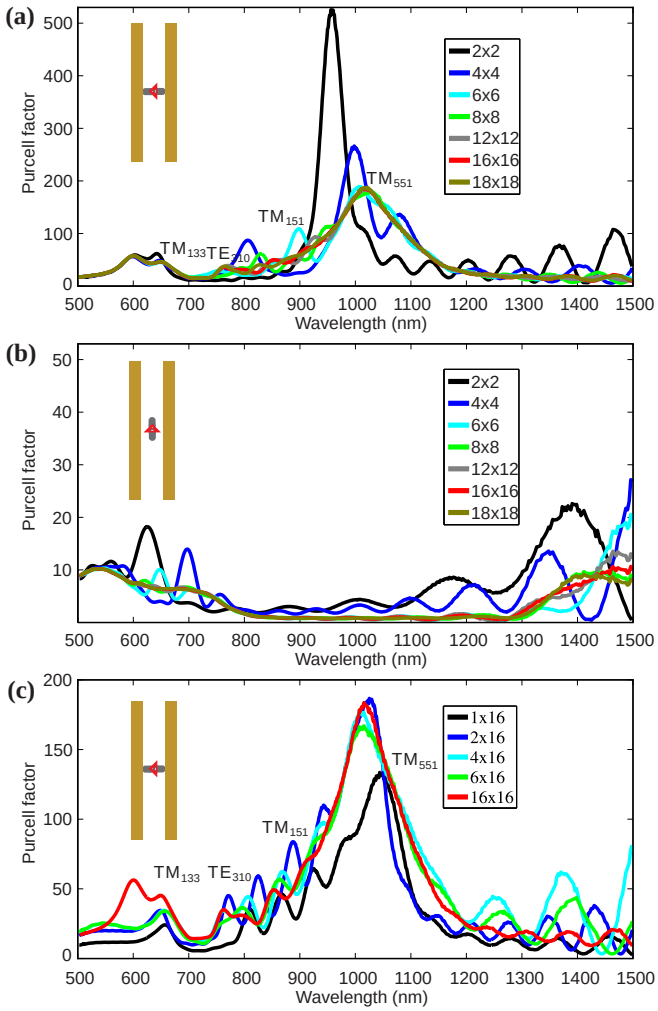

FIG. 4. (Color online) The Purcell factor dependence on the number of nanorods in (a) and (b) square and (c) rectangular lattices for an emitting dipole (a) and (c) perpendicular and (b) parallel to the nanorods. The dipole is located in the center of the array.

is reached at 950-nm wavelength (due to the small number of the rods forming the resonator, the identification of the mode structure of the resonator is not possible in the effective medium formalism as in Sec. III A). The highest Purcell factor obtained for the smallest array can be attributed to a small modal volume. For larger arrays this mode exhibits a slight shift to longer wavelengths, as expected from Eq. (4), and the Purcell factor decreases up to the value of 200. The Purcell factor for a z-oriented dipole is very low but also follows the mode structure of the resonator with the increase of number of rods [Fig. 4(b)]. The rectangular nanorod arrays provide a Purcell factor of around 200 already for two rows of nanorods [Fig. 4(c)]. The contribution of different transverse modes of the rectangular array in the Purcell factor is more pronounced for arrays with a smaller number of rows and becomes indistinguishable for arrays with six or more rows of rods [Fig. 4(c), green curve]. For all considered sizes of the resonators, a Purcell factor of less than 100 is observed in the ENZ regime, at around 520-nm wavelength [Fig. 1(c)]. As one can see from the consideration of rectangular metamaterial resonators, the optical response of the finite-size resonators

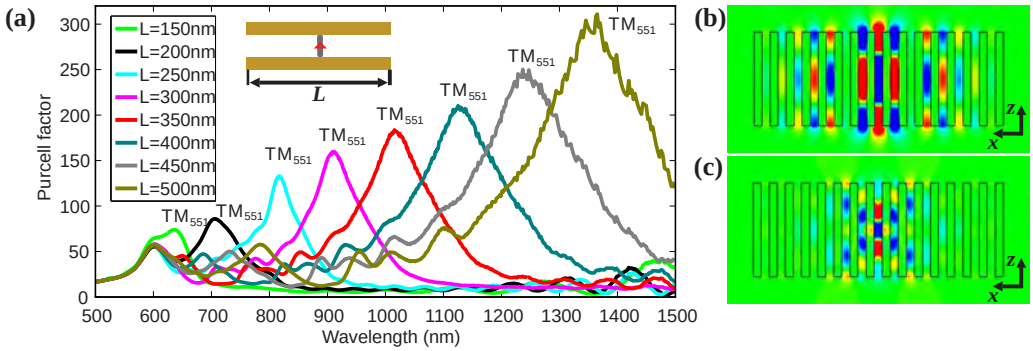

FIG. 5. (Color online) (a) The Purcell factor dependence on the height of the hyperbolic metamaterial resonator (16 × 16 nanorod array, $L_x = L_y = 900$ nm). The electric field E_x distributions excited by the dipole positioned at the center of the resonator with $L_z = 350$ nm at the wavelength of (b) 1000 nm and (c) 600 nm (nonresonant wavelength).

converges quickly to the response of the infinitely extended metamaterial slabs.

D. Purcell enhancement dependence on the rod length

We will now investigate the impact of the resonator height (rod length) on the Purcell factor (Fig. 5). In this section, resonators made of an array of 16 × 16 rods were considered. For all nanorod heights, there is a relatively small peak in the vicinity of the ENZ frequency related to the high modal density of bulk plasmon-polariton modes at this frequency [39,42]. The highest observed Purcell factor strongly depends on the rod length. Its maximum shifts to longer wavelengths with the increase in rod height, in accordance with the frequency shift of the resonator mode [Eq. (4)]. This (TM_{551}) mode has a characteristic field distribution inside the resonator [Fig. 5(b)] with three pronounced maxima of the electric field (two maxima of the magnetic field with one zero crossing), typical of the second Fabry-Pérot TM mode along the rods. Away from the modes of the resonator, the electric field has the characteristic cross-shaped form [Fig. 5(c)] typical for a radiating dipole field distribution in a hyperbolic dispersion regime [12].

E. Purcell enhancement in small hyperbolic resonators

If, starting from a single nanorod, the number of rods in the resonator is gradually increased, nontrivial behavior of the Purcell factor is observed (Fig. 6). The highest Purcell factor is obtained neither with a single rod nor in the limit of an infinite number of rods. The optimal structure provides a resonant mode with a high LDOS which enhances the decay rate. It can be seen that the dipole positioned near the center of a single nanorod excites the second-order mode $n = 2$ with three maxima of the electric field [Fig. 6(b)] at a wavelength of around 855 nm and the fourth mode $n = 4$ with five field maxima [Fig. 6(c)] at a wavelength of around 610 nm. Adding more nanorods to the resonator and thus changing its size and the modal structure lead to a shift of the resonant frequencies in the red spectral range, in accordance with Eq. (4). In particular, for the geometry with four nanorods, the second mode is excited at a wavelength of ∼940 nm [Fig. 6(d)], and the fourth mode is excited at a wavelength of ∼640 nm [Fig. 6(e)]. As mentioned above, the dipole located near the middle section of the nanorod layer can only couple to even modes.

F. Purcell enhancement dependence on the dipole position.

In order to understand the average Purcell factor for an ensemble of randomly distributed emitters, the position-dependent Purcell factor has been investigated. When the position of the emitter is changed along the nanorod length from just outside the metamaterial towards the center of the metamaterial layer, the Purcell factor has four maxima,

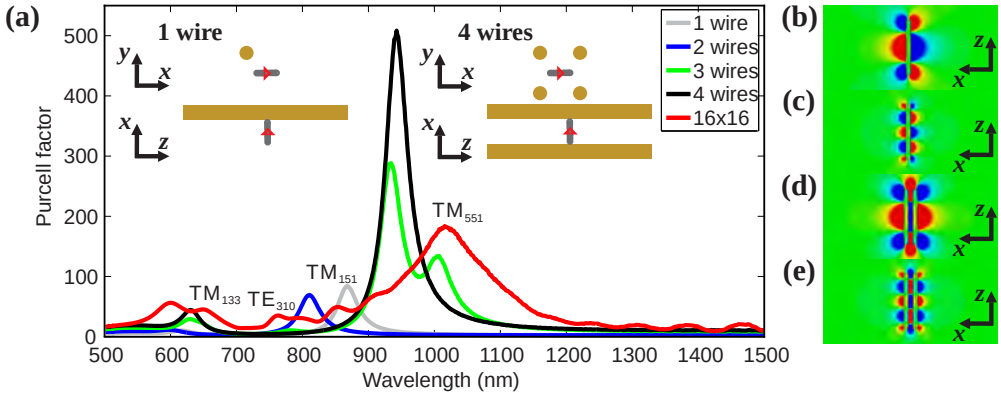

FIG. 6. (Color online) (a) Comparison of the Purcell factor for different numbers of plasmonic rods forming a resonator. Electric fields E_x of the dipole (b) and (c) near a single nanorod and (d) and (e) near a four-nanorod array at the wavelengths of (b) 856 nm, (c) 611 nm, (d) 937 nm. and (e) 637 nm.

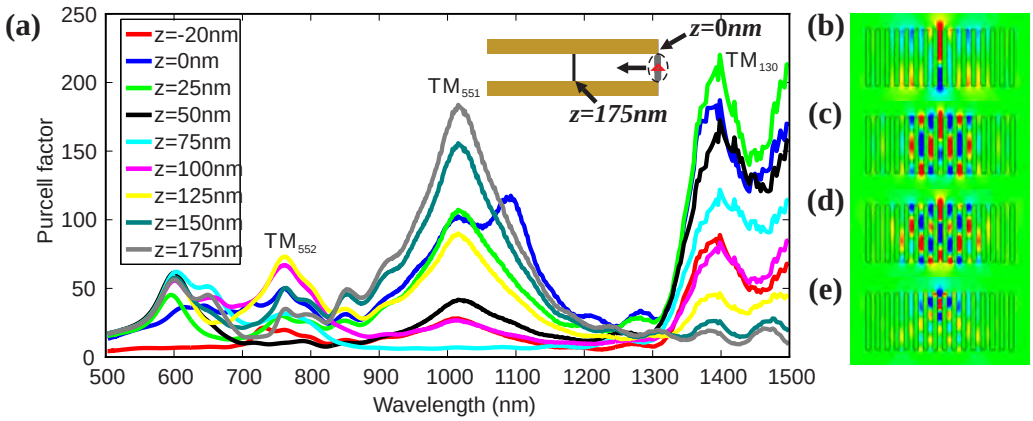

FIG. 7. (Color online) (a) The Purcell factor dependence on an emitter position inside the metamaterial resonator with $L_z = 350$ nm and $L_x = L_y = 900$ nm. The coordinate $z = 0$ corresponds to the edge of the hyperbolic medium. (b)–(e) The electric field E_x distributions excited by the dipole positioned at $z = 0$ for the wavelengths of (b) 1363 nm (TM_{130} mode, first Fabry-Pérot resonance $n = 0$, with two electric field maxima, one magnetic field maximum, no magnetic field zero crossing), (c) 1000 nm (TM_{551} mode, second Fabry-Pérot resonance $n = 1$ with three electric field maxima, two magnetic field maxima, one magnetic field zero crossing), (d) 750 nm (TM_{552} mode, third Fabry-Pérot resonance $n = 2$ with four electric field maxima, three magnetic field maxima, two magnetic field zero crossings), and (e) 600 nm (nonresonant wavelength). All other parameters are as in Fig. 3.

which correspond to the four lowest modes of the resonator (Fig. 7). The odd modes were not excited by the dipole situated at the central point of the array due to symmetry-induced selection rules. It can be seen from the LDOS spectrum [Fig. 7(a)] that the efficiency of the excitation of the resonator modes depends on the local field strength of a particular mode at the position of the radiating dipole. It can be seen that at different dipole positions, preferential excitation of the modes TM_{130} (two electric field maxima, one magnetic field maximum, no magnetic field zero crossing), TM_{551} (three electric field maxima, two magnetic field maxima, one magnetic field zero crossing), and TM_{552} (four electric field maxima, three magnetic field maxima, two magnetic field zero crossings) occurs at the wavelengths of 1363, 1000, and 750 nm, respectively. For the shorter wavelength of 600 nm, the electric field is shaped as an inverted V [Fig. 7(e)], typical of the nonresonant hyperbolic regime. The Purcell factor drops off very quickly with increasing distance between the dipole and the metamaterial surface: dipoles situated more than 20 nm away from the interface do not exhibit any significant Purcell enhancement (Fig. 7).

IV. CONCLUSION

A comprehensive numerical and analytical analysis of the Purcell enhancement in finite-size nanorod metamaterial resonators was performed. Using a nanorod metamaterial with hyperbolic dispersion of electromagnetic modes, the resonators with a complex hierarchy of modes can be realized. We have shown that the modes of the hyperbolic resonator are responsible for the enhancement of spontaneous emission rates of emitters placed inside the resonator. Thus, a controllable Purcell enhancement can be achieved in the desired wavelength range by choosing appropriate resonator sizes. A detailed analysis of various types of geometrical arrangements of the metamaterial and emitter was carried out. The results suggest that finite-size metamaterial resonators with properly designed modes outperform infinite metamaterials in terms of radiation efficiency enhancement. It was shown that the influence of only the 16×16 nanorod array on the dipole emission properties converges to that of an infinite metamaterial. Our work can provide guidelines for modeling and optimization of experimental samples. As for an outlook for possible future applications, it is worth mentioning nanostructured light-emitting devices with high-speed switching rates, cavities for surface plasmon amplification by stimulated emission of radiation (SPASERs), and sensing applications.

ACKNOWLEDGMENTS

This work has been supported, in part, by EPSRC (UK), the ERC iPLASMM project (321268), the U.S. Army Research Office (W911NF-12-1-0533), and the Australian Research Council. A.P.S. acknowledges support via the SPIE Scholarship. A.P.S. and D.A.P. acknowledge support from the Australian Research Council (Australia). P.S.O. is grateful for the support from CONACYT. G.A.W. acknowledges support from the EC FP7 project 304179 (Marie Curie Actions). A.V.Z. acknowledges support from the Royal Society and the Wolfson Foundation and rejects any involvement in the grants, listed below. The work of I.I., A.S.S., and P.A.B. was supported by the Ministry of Education and Science of the Russian Federation, by the government of the Russian Federation (Grant No. 074-U01), by the Russian Fund for Basic Research (N13-02-00623), and by the Dynasty Foundation (Russia). I.I. acknowledges a grant of the president of the Russian Federation (Grant No. MK-5220.2015.2). A.S. acknowledges the Russian Foundation for Basic Research (Project No. 14-02-31783).

[1] L. Novotny and B. Hecht, *Principles of Nano-optics* (Cambridge University Press, Cambridge, 2006).
Q [2] E. M. Purcell, Phys. Rev. **69**, 681 (1946).
[3] A. Hayat, P. Ginzburg, and M. Orenstein, Phys. Rev. Lett. **103**, 023601 (2009).
[4] A. N. Poddubny, P. Ginzburg, P. A. Belov, A. V. Zayats, and Y. S. Kivshar, Phys. Rev. A **86**, 033826 (2012).
[5] K. J. Vahala, Nature (London) **424**, 839 (2003).
[6] P. Ginzburg, A. V. Krasavin, D. Richards, and A. V. Zayats, Phys. Rev. A **90**, 043836 (2014).
[7] D. K. Gramotnev and S.I. Bozhevolnyi, Nat. Photonics **4**, 83 (2010).
[8] L. Novotny and N. van Hulst, Nat. Photonics **5**, 83 (2011).
[9] J.-J. Greffet, Science **308**, 1561 (2005).
[10] A. V. Akimov, A. Mukherjee, C. L. Yu, D. E. Chang, A. S. Zibrov, P. R. Hemmer, H. Park, and M. D. Lukin, Nature (London) **450**, 402 (2007).
[11] A. G. Curto, G. Volpe, T. H. Taminiau, M. P. Kreuzer, R. Quidant, and N. F. van Hulst, Science **329**, 930 (2010).
[12] P. Shekhar, J. Atkinson, and Z. Jacob, Nano Convergence **1**:14,
5 (2014).
[13] Z. Jacob, J. Kim, G. V. Naik, A. Boltasseva, E. E. Narimanov, and V. M. Shalaev, Appl. Phys. B **100**, 215 (2010).
[14] A. N. Poddubny, P. A. Belov, P. Ginzburg, A.V. Zayats, and Y. S. Kivshar, Phys. Rev. B **86**, 035148 (2012).
[15] W. Yan, M. Wubs, and N. A. Mortensen, Phys. Rev. B **86**, 205429 (2012).
[16] T. Tumkur, G. Zhu, P. Black, Yu. A. Barnakov, C. E. Bonner, and M. A. Noginov, Appl. Phys. Lett. **99**, 151115 (2011).
[17] H. N. S. Krishnamoorthy, Z. Jacob, E. Narimanov, I. Kretzschmar, and V. M. Menon, Science **336**, 205 (2012).
[18] P. Ginzburg, F. J. Rodríguez Fortuño, G. A. Wurtz, W. Dickson, A. Murphy, F. Morgan, R. J. Pollard, I. Iorsh, A. Atrashchenko, P. A. Belov, Y. S. Kivshar, A. Nevet, G. Ankonina, M. Orenstein, and A. V. Zayats, Opt. Express **21**, 14907 (2013).
[19] X. Yang, J. Yao, J. Rho, X. Yin, and X. Zhang, Nat. Photonics **6**, 450 (2012).
[20] Y. He, S. He, and X. Yang, Opt. Lett. **37**, 2907 (2012).
[21] A. Leviyev, B. Stein, T. Galfsky, H. Krishnamoorthy, I. L. Kuskovsky, V. Menon, and A. B. Khanikaev, arXiv:1505.05438. 6
[22] Z. Sun, Á. Gutiérrez-Rubio, D. N. Basov, and M. M. Fogler, Nano Lett. **15**, 4455 (2015).
[23] B. M. Wells, A. V. Zayats, and V. A. Podolskiy, Phys. Rev. B **89**, 035111 (2014).
[24] J. Elser, R. Wangberg, V. A. Podolskiy, and E. Narimanov, Appl. Phys. Lett. **89**, 261102 (2006).
[25] M. Silveirinha and N. Engheta, Phys. Rev. Lett. **97**, 157403 (2006).
[26] A. Alù, M. G. Silveirinha, A. Salandrino, and N. Engheta, Phys. Rev. B **75**, 155410 (2007).
[27] E. Forati and G. W. Hanson, New J. Phys. **15**, 123027 (2013).
[28] P. Ginzburg and A. V. Zayats, ACS Nano **7**, 4334 (2013).
[29] N. A. Mortensen, S. Raza, M. Wubs, T. Sondergaard, and S. I. Bozhevolnyi, Nat. Commun. **5**, 3809 (2014). Q
[30] V. Podolskiy, P. Ginzburg, B. Wells, and A. Zayats, Faraday Discuss. **178**, (2014). 7
[31] CST MICROWAVE STUDIO 2014, http://www.cst.com.
[32] P. B. Johnson and R. W. Christy, Phys. Rev. B **6**, 4370 (1972).
[33] A. P. Slobozhanyuk, A. N. Poddubny, A. E. Krasnok, and P. A. Belov, Appl. Phys. Lett. **104**, 161105 (2014).
[34] A. E. Krasnok, A. P. Slobozhanyuk, C. R. Simovski, S. A. Tretyakov, A. N. Poddubny, A. E. Miroshnichenko, Y. S. Kivshar, and P. A. Belov, Sci. Rep. **5**, 12956 (2015). 8
[35] M. Agioand and A. Alu, *Optical Antennas* (Cambridge University Press, Cambridge, 2013).
[36] W. Vogel and D.-G. Welsch, *Quantum Optics*, 3rd rev. ed. (Wiley-VCH, 2006). 9
[37] F. Intravaia and K. Busch, Phys. Rev. A **91**, 053836 (2015).
[38] A. K. Okaya and L. F. Barash, Proc. IRE **50**, 2081 (1962).
[39] N. Vasilantonakis, M. Nasir, W. Dickson, G. A. Wurtz, and A. V. Zayats, Laser Photics Rev. **9**, (2015). 10
[40] R. K. Moniga and A. Ittipiboon, IEEE Trans. Antennas Propag. **45**, 1348 (1997).
[41] F. Lemoult, M. Fink, and G. Lerosey, Nat. Commun. **3**, 889 (2012).
[42] S. V. Zhukovsky, O. Kidwai, and J. E. Sipe, Opt. Express **21**, 14982 (2013).

Second-harmonic generation from hyperbolic plasmonic nanorod metamaterial slab

Giuseppe Marino, Paulina Segovia, Alexey V. Krasavin, Pavel Ginzburg†, Nicolas Olivier, Gregory A. Wurtz, Anatoly V. Zayats.*

Department of Physics, King's College London, Strand, London, United Kingdom

ABSTRACT: Hyperbolic plasmonic metamaterials provide numerous opportunities for designing unusual linear and nonlinear optical properties. We show that the modal overlap of fundamental and second-harmonic light in an anisotropic plasmonic metamaterial slab results in the broadband enhancement of radiated second-harmonic intensity by up to 2 and 11 orders of magnitudes for TM- and TE-polarized fundamental light, respectively, compared to a smooth Au film under TM-polarised illumination. The results open up possibilities to design tuneable frequency-doubling metamaterial with the goal to overcome limitations associated with classical phase matching conditions in thick nonlinear crystals.

KEYWORDS: Hyperbolic metamaterials, plasmonics, second harmonic generation

Second-harmonic generation (SHG) is used frequently in modern laser technologies and applications[1]. The main advantage of this frequency doubling technique is the possibility of light generation at wavelengths rarely accessible via typical radiative decay channels of a gain medium and metrology of ultrashort pulses[2]. Approaches based on nonlinear optical crystals are constrained by phase matching conditions: fundamental and second-harmonic waves are required to propagate in phase to obtain optimum nonlinear energy conversion[1]. The operational bandwidth for ultrashort pulses is another limitation for frequency conversion in bulk nonlinear crystals[3].

To overcome these limitations and increase integrability, various nonlinear nanostructured media have been proposed based on nanoparticles, optical nanoantennas, and metamaterials[4-7]. These approaches use the light confinement and enhancement in plasmonic (metallic) nanostructures to locally increase the fundamental field strength upon which SHG depends quadratically[2]. In multi-resonant structures, SHG effect can be further enhanced with the additional resonant scattering provided by the nanostructure at the SH frequency[4]. Thus, conventional phase matching conditions can be replaced with a modal overlap at the fundamental and second-harmonic (SH) frequencies in the nanostructures[4-7]. In order to realise these conditions experimentally, various geometries have been used such as a broadband optical nanoantenna[6], a composite nanoparticle made of a rod and a V-shaped nanoantenna[4], and split-ring resonator based metamaterials[7].

In another approach to achieve broadband and alignment-free phase-matching, the so-called ε-near-zero (ENZ) metamaterials were proposed which by their nature achieve phase-matching conditions due to the electrostatic nature of the second-harmonic field inside the medium[8]. They however operate only at a finite frequency where the ENZ occurs. ENZ

metamaterials also typically possess broadband hyperbolic and anisotropic elliptic dispersions allowing a rich structure of the supported modes, including low and negative group velocity modes[9]. Such metamaterials can be realised on a macroscopic scale using arrays of aligned plasmonic nanorods so that the mode structure of the metamaterial can be efficiently tuned by changing the nanorod array geometrical parameters. In particular, Au nanorod based metamaterials provide tuneable ENZ behaviour throughout both the visible and near infrared spectral ranges via adjustment of structural parameters. While the centrosymmetric crystal lattice of gold, limits the source of the second-order nonlinearity to the surface nonlinear contributions, the nanostructured geometry of the Au nanorod metamaterial provides a large surface area needed for exploiting the intrinsic surface nonlinearity of gold. Due to the fact that this internal structure of the metamaterial and local fields inside the metamaterial are paramount for the description and understanding of SHG processes, the effective medium approximation for the metamaterial description is not applicable for modelling SHG processes and full vectorial, microscopic considerations should be employed.

In this paper, we study intrinsic second-harmonic generation processes in plasmonic nanorod metamaterial slabs and show its enhancement at multiple resonant wavelengths determined by the mode structure of the metamaterial at both fundamental and second-harmonic frequencies. The enhancement related to phase matching due to ENZ is shown to be negligible in the considered geometry of thin metamaterial slab, with TE mode providing higher SHG due to the orientation of the nanorods perpendicular to the metamaterial slab. SHG enhancement by several orders of magnitude, is observed when a modal overlap between the fundamental and second harmonic frequencies takes place, emulating the so-called double-resonant conditions[4,10,11]. To this end, the perturbative hydrodynamic approach for Au nonlinearity description in a broad

spectral range has been developed, and microscopic numerical simulations of the near-field and radiated SHG have been performed in both reflection and transmission. By designing such plasmonic nanorod metamaterials, the enhancement of frequency doubling efficiency can be achieved in a desired wavelength range, in the same way as third-order nonlinearity has been designed[12].

The metamaterial studied here is formed by an assembly of aligned metallic (Au) nanorods (12 nm radius, 300 nm length and 60 nm period of a square lattice) hosted in an alumina matrix (Fig. 1). The optical properties of this uniaxial metamaterial can be inferred from the effective medium theory[14] via the diagonal effective permittivity tensor of the form $\hat{\varepsilon}^{eff} = \left[\varepsilon_x^{eff}, \varepsilon_y^{eff} = \varepsilon_x^{eff}, \varepsilon_z^{eff}\right]$ (Fig. 1). A TE-polarized incident light with the electric field normal to the nanorod axis always experiences positive effective permittivity $\varepsilon_{x,y}^{eff}$. In contrast, a TM polarized incident light, having an electric field component along the nanorod axis will be governed by the effective permittivity components $\varepsilon_{x,y}^{eff}$ and ε_z^{eff}. In the former case, the metamaterial behaves as a dielectric over the entire spectral range investigated, while in the latter, the optical response of the metamaterial transitions from an anisotropic dielectric behaviour ($\varepsilon_{x,y}^{eff}$, $\varepsilon_z^{eff} > 0$, elliptic dispersion) to a hyperbolic behaviour ($\varepsilon_{x,y}^{eff} > 0$, $\varepsilon_z^{eff} < 0$, hyperbolic dispersion) passing through the ENZ wavelength range at around a wavelength of 710 nm at which $\mathcal{R}e\left(\varepsilon_z^{eff}\right) = 0$ determining the effective plasma frequency of metamaterial[9].

The anisotropic metamaterial slab placed on a glass substrate supports a set of TE and TM modes through the near-infrared, visible, and ultra-violet spectral range (Fig. 2 a,b). Above the light line in air, these modes are the cavity modes of the planar slab of the metamaterial. Below the light line, the modes are accessible only with the illumination through the substrate and are

leaky waveguided mode of the metamaterial slab[9]. Above the effective plasma frequency of the metamaterial, both TE and TM modes are typical modes of the anisotropic planar waveguide, while below it the metamaterial supports bulk plasmon polaritons[9], and the TM modes may have positive, vanishingly small or negative group velocity. TE modes always behave as modes of anisotropic dielectric.

The modal structure of the metamaterial slab has a crucial effect on both transmitted and reflected SHG enhancement (Fig. 2 c-f). Considering both linear reflectance and SH generation either for TE (Fig. 2a,c,e) or TM incident polarization (Fig. 2b,d,f), it becomes clear that the slab modes are responsible for the enhancement of the observed SHG. The fundamental light coupling to the modes results in the field enhancement which in turn influences SHG intensity. If the generated SHG light is also coupled to the slab mode, which is possible due to the rich dispersion of modes available in the metamaterial cavity, the efficiency of SHG is further increased. This far-field radiated SHG which is solely related to the electronic nonlinearity of Au nanorods forming the metamaterial is TM-polarised in both reflection and transmission irrespectively of the polarisation of the fundamental light. Both reflected and transmitted SHG have comparable intensities. Interestingly, the intensity of SHG excited by TE polarized fundamental light is almost 10 orders of magnitude higher than that excited by TM polarized light. This is a direct consequence of the internal structure of the nanorod metamaterial, providing both field enhancement[15] and large surface area (approximately 7 times larger than for a smooth Au film) and the vectorial nature of the SH process, which favours the electric field oscillating orthogonally to the surface of metal. Please note that under the excitation at normal incidence, low SHG intensities are observed for all polarisation configurations due to the symmetry breaking requirements for far-field SHG[16,17] (these requirements are not applicable in the near-field region[18]). In this geometry, nonlinear

sources derive from the nanorod extremities. For a smooth Au film under normal incidence illumination, the simulated SHG is vanishingly small, within numerical noise, as expected from symmetry considerations.

In order to benchmark the observed SHG intensities from the metamaterial, the reflected-SHG spectrum excited with TM-polarized fundamental light from a smooth Au surface has been calculated using the same model for Au nonlinearity (Fig. 3). The SHG has a featureless wavelength dependence with a sole resonance in the vicinity of the interband transitions in Au. Compared to the SH power reflected from the nanorod metamaterial slab, the SHG from a smooth film is much lower in the visible and near-IR spectral range (up to 2 orders of magnitude), while higher for short wavelengths in the UV (Fig 3 a). For a TE-polarized fundamental light, the SHG from the metamaterial is more than 11 orders of magnitude higher compared to a smooth Au under TM-polarised excitation (Fig. 3b). While for TM-polarized light, the resonant SHG from the metamaterial is up to 2 orders of magnitude higher than from the smooth Au film (Fig. 3c). For different angles of incidence, there is redistribution of the peak intensities in the SHG spectra according to the dispersion of the involved modes of the slab, but the maximum enhancement measured with respect to the smooth film remains within a similar intensity range. Interestingly, strong radiated SHG is also observed in transmission even for the excitation under total internal reflection (TIR) conditions as the dispersion of the metamaterial slab has the modes at the SH frequencies outside TIR range (Fig. 2e,f).

While for the far-field radiated SHG, the integration over the SHG propagation direction smears out the contribution of individual modes, the analyses of the near-field SHG intensities allows one to identify the role of TM and TE modes of the metamaterial slab (Fig. 4). The modes supported by the metamaterial slab were identified by comparing the dispersion to the analytically

calculated mode structure in the framework of the effective medium theory[9] (Fig. 4a,b). A good agreement between the simulated and analytical modes allows to label the observed modes corresponding to the minima in the reflection dispersion (See also Supplementary Information, Fig. S2). For TE polarisation, a set of modes of the anisotropic dielectric slab can be identified (denoted with TE_n, where n is the mode index). For TM polarisation, bulk plasmon polaritons are supported by the metamaterial slab (the modes denoted with $TM_{h,n}$) at the frequencies below the effective plasma frequency, while modes at higher frequencies correspond to the modes of a conventional elliptic-dispersion dielectric slab and are denoted as $TM_{e,n}$ (Fig. 4 a,b).

The analysis of the SHG spectra allows one to identify the SHG enhancement at the positions of the modes of the metamaterial slab at either fundamental or SH frequencies, considering that SH emission is always TM-polarized (Fig. 4). The strongest SHG enhancement corresponds however to an overlap of the modes at fundamental and second-harmonic frequencies (Fig. 4 c and d)). The spectral features of the far-field (Figs. 2 c,d) and near-field (Figs. 4 e,f) SH spectra are the same with maxima corresponding to the modes of the metamaterial slab. The far-field SHG is about 10 orders of magnitude higher for TE excitation compared to TM fundamental light, while the near-field SHG excited with TE fundamental light is only about 4 orders of magnitude higher. The metamaterial slab modes identified on the SHG spectral dependencies (red circles for either elliptic or hyperbolic modes at the fundamental frequency and green circles for hyperbolic SHG modes, due to the TM polarisation of the generated SH light), unambiguously show the correspondence of the mode position and the SHG enhancement in the single-resonant (when either the fundamental or SH light is coupled to the mode) and especially double-resonant (when both the fundamental and SH light is coupled to the slab modes) conditions. The double-resonant conditions for TE modes occur primarily for the

SHG in the UV spectral range, while can be achieved for TM modes in a broader spectral range (cf. Fig. 4e and 4f) due to the involvement of bulk plasmon-polaritons in the hyperbolic spectral range, e.g., the hyperbolic $TM_{h,1}$ mode at the fundamental frequency and the $TM_{e,1}$ mode at the SH frequency. Thus, strong SHG enhancement can be observed at multiple "double-resonant" wavelengths allowing for efficient SH generation at multiple wavelength with the same metamaterial slab.

The field confinement near the nanorods forming the metamaterial, associated with the excitation of different modes was simulated and can be seen from the plotted polarisation distributions: the stronger field enhancement the higher the induced SH polarization. For example, one can observe that the mode TE_3 at 2.3 eV (Fig. 5a) yields the highest field confinement, followed by TE_2 (Fig. S1a), TE_4, TE_5, and TE_1. In addition to the mode spectral position, an overlap integral between the microscopic nonlinear polarization at second-harmonic and fundamental frequencies is important to observe efficient SHG enhancement[7]. The orthogonal to the surface components of both the nonlinear polarization proportional to $E_{\perp}^{(\omega)}(\vec{r},\omega)E_{\perp}^{(\omega)}(\vec{r},\omega)$ and the SH field distributions $E_{\perp}^{(\omega)}(\vec{r},2\omega)$, together with the associated relative overlap $E_{\perp}^{(\omega)}(\vec{r},\omega)E_{\perp}^{(\omega)}(\vec{r},\omega)E_{\perp}^{(\omega)}(\vec{r},2\omega)$ are plotted for the selected modes and both fundamental light polarizations in Figs. 5 and S1, confirming this requirement. The corresponding values of the relative overlap integrals over the nanorod surface are equal to approximately 14 and 10 for TE and 0.04 and 0.01 for TM polarized excitations at 2.3 eV and 1.77 eV excitations, respectively (for comparison, for the off resonant excitation at 0.4 eV, the field overlap values are much smaller being $3 \cdot 10^{-5}$ for both TE and TM polarisations, respectively). The relative overlap integrals are of about 2 order of magnitude higher for TE compared to TM polarized excitation light. On the

other hand, considering only TE polarized excitation, the largest relative overlap integral is found for the TE_3 and $TM_{e,3}$ modes at the excitation of 2.3 eV (Fig. 5c), followed by the TE_2 and $TM_{e,2}$ modes at the excitation of 1.77 eV, with the latter being 30% lower (Fig. S1c). This microscopic picture highlights the importance of mode selection rules responsible for the SH enhancement in nanorod-based metamaterials. Firstly, a high field enhancement at the fundamental frequency favors the respective modes for achieving strong SH enhancement. Secondly, a strong field enhancement at the SH frequency, along with a multiresonant response, enhances SH even further. Last but not least, the symmetry of the two field distributions is crucial allowing for strongest overlap of the resonant fields.

In conclusion, we have numerically studied SHG from an anisotropic hyperbolic metamaterial in different polarisation configurations and for different angles of incidence. We have adopted a perturbative, nondepleted pump approximation of the SHG description with hydrodynamic nonlinearity of Au nanorod meta-atoms forming the metamaterial and also taken into account the internal structure of the metamaterial composite. The simulations show a strongly enhanced SHG when both fundamental and generated light is coupled to the modes of the metamaterial slab, which is facilitated by the modes' dispersion in the hyperbolic regime. Due to a rich spectrum of the modes supported by the hyperbolic anisotropic slab waveguide, the enhanced SHG can be observed in a broad spectral range. The SHG excited with TE polarized light is much more efficient due to the internal structure of the metamaterial and the surface nonlinearity of Au nanorods. The enhancement related to phase matching due to ENZ is shown to be negligible in the considered geometry of a thin metamaterial slab. By designing the plasmonic

nanorod metamaterials, the enhancement of frequency doubling efficiency can be achieved in a desired wavelength range by the design of the mode structure of the metamaterial slab.

Methods.

Model for second-order nonlinearity of Au. For modelling second-order nonlinear response of metamaterials, we characterized the interaction between the nonlinear sources and the metamaterial at the harmonic frequency (2ω), via the nonlinear wave equation in the frequency domain $\boldsymbol{\nabla} \wedge \boldsymbol{\nabla} \wedge \boldsymbol{E}^{(2\omega)}(\boldsymbol{r}) - {k_0}^2 \varepsilon^{(2\omega)}(\boldsymbol{r}) \boldsymbol{E}^{(2\omega)}(\boldsymbol{r}) = \mu_0 {k_0}^2 \boldsymbol{P}^{(2\omega)}(\boldsymbol{r})$, where $\boldsymbol{E}^{(2\omega)}$ is the field at the SH, k_0 is the wavevector of light in air, $\varepsilon^{(2\omega)}$ is the permittivity of the nonlinear material at the SH, and $\boldsymbol{P}^{(2\omega)}$ is the nonlinear polarizability generated within the nonlinear (nonmagnetic $\mu_0 = 1$) metallic rods of the metamaterial. Nonlinear polarization in conduction band of noble metals, such as gold and silver, is well described by the hydrodynamic model[19]. The latter holds only for the spectral range below the plasma frequency such that the real part of the permittivity is negative, but both away from interband transitions and Coulomb collisions, occurring respectively at high and low frequencies. Following[20,21], both conduction and bound electron losses can be included in the model, and a complex permittivity at both fundamental and SH frequencies, can be then considered. Let us consider the classical hydrodynamic equation for conduction electrons: $m^* \frac{d\boldsymbol{v}}{dt} + m^* \boldsymbol{v} \cdot \boldsymbol{\nabla} \boldsymbol{v} = -e\boldsymbol{E} - \gamma_0 m^* \boldsymbol{v} - e\mu_0 \boldsymbol{v} \wedge \boldsymbol{H}$, where $\boldsymbol{v}(\boldsymbol{r}, t) = \boldsymbol{j}_D(\boldsymbol{r}, t)/en(\boldsymbol{r}, t)$ is the electron velocity, $\boldsymbol{j}_D(\boldsymbol{r}, t)$ and $n(\boldsymbol{r}, t)$ being electron current density and electron density, respectively. The equation includes a convective term accounting for the acceleration of charges, a linear term in the charge density, a viscosity term containing the damping frequency γ_0 of conduction electrons and finally the Lorentz force term. Nevertheless, additional terms such us quantum pressure of electron gas are not taken into account in this model[21]. Given the continuity equation: $\dot{n}(\boldsymbol{r}, t) =$

$-1/e(\boldsymbol{\nabla}\cdot\boldsymbol{P})$, the hydrodynamic equation can be written in terms of the polarizability $\boldsymbol{P}$. Thus, adopting a perturbative approach in the undepleted pump approximation, one can move into the frequency domain and write the current density at the SH frequency as a function of the fundamental frequency field by collecting terms up to the second order: $\boldsymbol{P}_S^{(2\omega)} = 4\pi\varepsilon_0\Big[\beta\boldsymbol{E}^{(\omega)}\boldsymbol{\nabla}\cdot\chi_D^{(\omega)}\boldsymbol{E}^{(\omega)} + \gamma\boldsymbol{\nabla}\big(\boldsymbol{E}^{(\omega)}\cdot\boldsymbol{E}^{(\omega)}\big)\Big]$, where $\gamma = \frac{{\omega_p}^2}{\omega^2}\frac{\beta}{4}$ and $\beta = \frac{e}{8\pi m^*\omega^2}\left[\frac{\omega^2}{{\omega_p}^2}\right]\chi_D^{(\omega)}\left[\frac{(2\omega)^2}{{\omega_p}^2}\right]\chi_D^{(2\omega)}$. The first term accounting for a dot product between the electric field and its divergence is the quadrupole-like Coulomb term while the second term accounting for the gradient of the square of the electric field is produced by convective and Lorentz forces. These terms have a δ-function-like behaviour at the metal surface, thus we have neglected the bulk contribution to second-order response. It is interesting to note that in the limit of a free electron gas when $\beta = \frac{e}{8\pi m^*\omega^2}$, the above polarizability takes the form reported in Ref.[19] Finally, due to the continuity of the electric displacement across the metal surface, we can write the electric field as a function of the spatial varying complex permittivity ε_r, considering both intraband and interband transitions. We, then, obtain the following tangential and orthogonal terms for the current density at the surface

$$\begin{cases} \widehat{\boldsymbol{Z}}\cdot\boldsymbol{j}_S^{(2\omega)} = -2i\omega\varepsilon_0\alpha\chi_D^{(2\omega)}{\chi_D^{(\omega)}}^2\,(\varepsilon_r+3)/4\,\boldsymbol{E}_{s,\widehat{\boldsymbol{Z}}}^{(\omega)}\boldsymbol{E}_{s,\widehat{\boldsymbol{Z}}}^{(\omega)} \\ \widehat{\boldsymbol{X}}\cdot\boldsymbol{j}_S^{(2\omega)} = -2i\omega\varepsilon_0\alpha\chi_D^{(2\omega)}{\chi_D^{(\omega)}}^2\boldsymbol{E}_{s,\widehat{\boldsymbol{X}}}^{(\omega)}\boldsymbol{E}_{s,\widehat{\boldsymbol{Z}}}^{(\omega)} \end{cases} \quad (1)$$

where $\alpha = \frac{2e\omega^2}{m^*{\omega_p}^4}$. Here, it should be noted that the proportionality between the current density and the electric field, contains the susceptibility at the fundamental frequency taken twice and the susceptibility at the SH frequency, as expected for a three-wave interaction. While the tangential term is derived only from the quadrupole-like Coulomb term, the orthogonal term is derived by both surface current density terms, resulting in a tangential term being continuous at the surface in

the opposite trend to the orthogonal component. From this consideration and from an additional $(\varepsilon_r + 3)/4$ factor follows that the orthogonal term is dominant, which is in agreement with previously observed results[22,23]. Only the orthogonal term is considered thereafter.

Numerical modelling of linear response and SHG in a metamaterial slab. For the numerical implementation of the SHG emitted by the metamaterial we used a frequency-domain Finite Element solver (Comsol Multiphysics), in the framework of the undepleted pump approximation described above. The model uses Floquet boundary conditions for a metamaterial square unit cell to mimic a planar infinite slab. Rounded extremities have been considered for rods to avoid the computational complexity associated with unnecessary mesh. The model has also been tested on Au nanoparticles such as nanospheres and nanoprisms leading to a SH emission in agreement with Ref.[24].

FIGURES

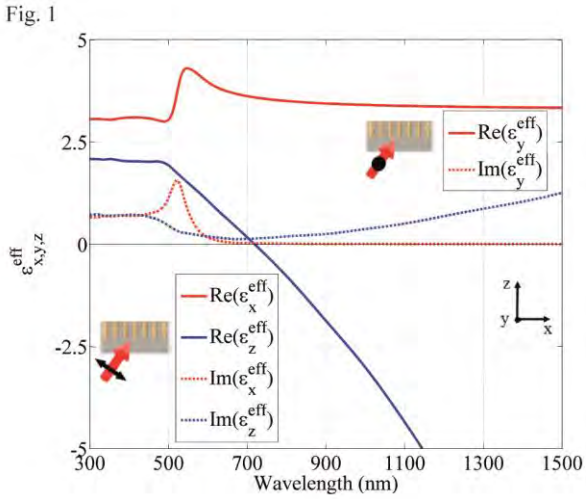

Figure 1. Effective permittivity for the anisotropic nanorod metamaterial based on a square array of Au nanorods (12 nm radius, 300 nm length and 60 nm period) embedded in alumina. Au permittivity has been taken from [13] and for alumina n=1.6.

Fig. 2

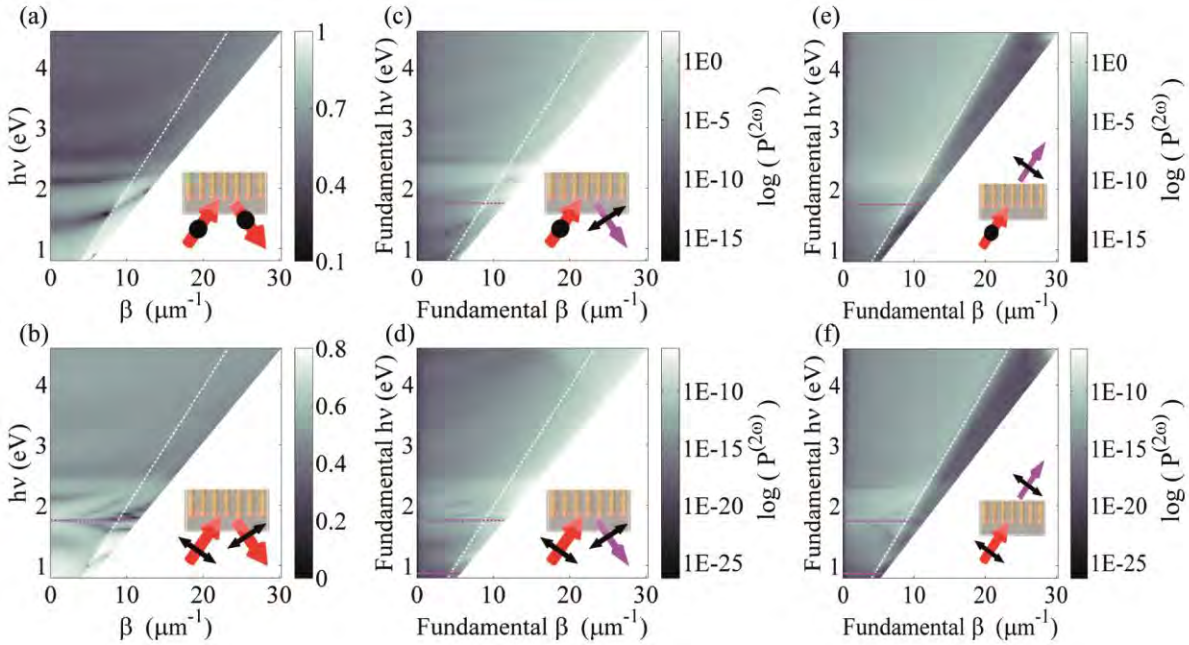

Figure 2. (a,b) Reflection dispersion of the metamaterial slab as in Fig. 1 for (a) TE and (b) TM polarisations. (c-f) The spectra of the radiated (far-field) SH intensity for different angles of incidence of the fundamental light: (c,d) reflected and (e,f) transmitted SHG signal for (c,e) TE-polarised and (d,f) TM-polarised fundamental light. SHG is always TM-polarised. The effective plasma frequency of the metamaterial at the fundamental and SH wavelengths is shown with the horizontal dashed and solid lines, respectively. The light line in air is shown with a white dashed line. Please note low SHG intensity near the normal incidence excitation, which is related due to the symmetry consideration of far-field SHG.

Fig. 3

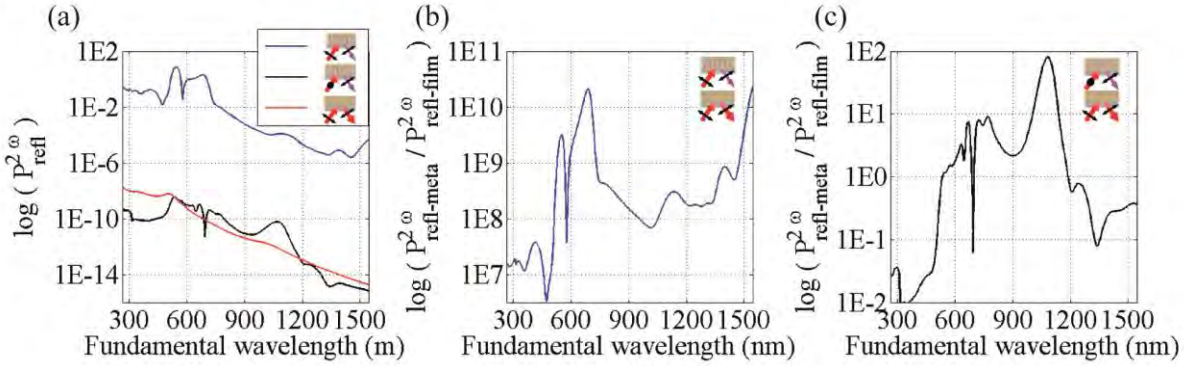

Figure 3. (a) Reflected SH spectra from a smooth Au surface (red line) and the nanorod metamaterial (extracted from Fig. 2c,d) for TE-polarised (blue line) and TM-polarised (black line) excitation, respectively. (b,c) The ratio of the SHG intensities reflected from the metamaterial for (b) TM- and (c) TE-polarised excitation and smooth Au surface for TM-polarised excitation. The angle of incidence is 48° in all cases.

Fig. 4

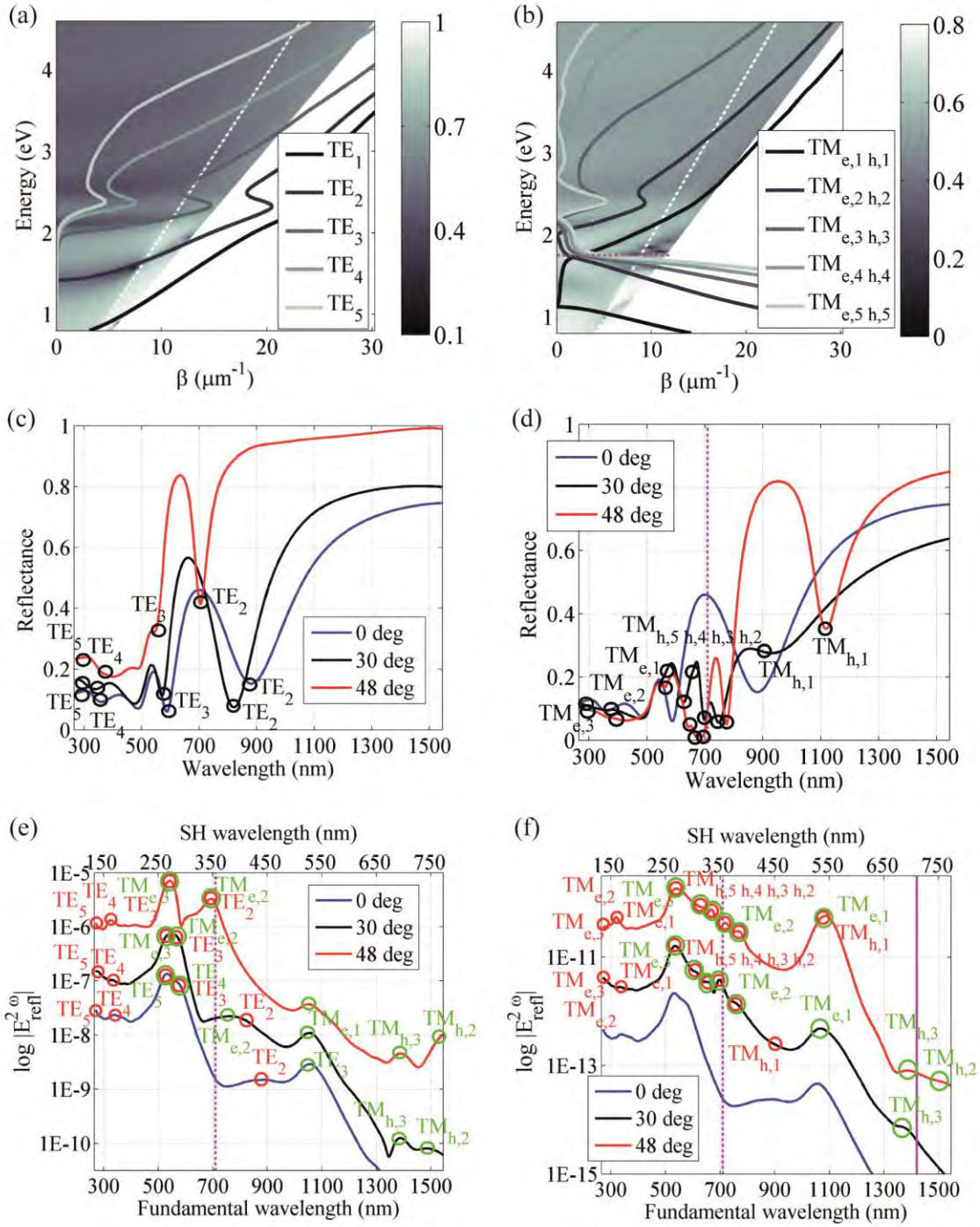

Figure 4. (a) TE and (b) TM reflectance dispersion of the metamaterial slab overlaid with the analytically simulated mode structure. The effective bulk plasma frequency of the metamaterial is shown with the horizontal line. (c) TE and (d) TM reflectance spectra for selected wavelengths with mode identification: TE_n modes refer to modes allowed for ordinary polarization, $TM_{e,n}$ and

$TM_{h,n}$ modes refer to modes allowed in the elliptical and hyperbolic regimes, respectively, for extraordinary polarization. (e,f) Spectra of the near-field SHG measured 5 nm below the metamaterial in glass substrate for (e) TE and (f) TM polarization of excitation. SH light has TM polarization irrespectively of the fundamental polarization. Red and green circles identify modes at the fundamental and second-harmonic frequencies, respectively. The effective plasma frequency of the metamaterial at the fundamental and SH wavelengths is shown with the horizontal dashed and solid lines, respectively.

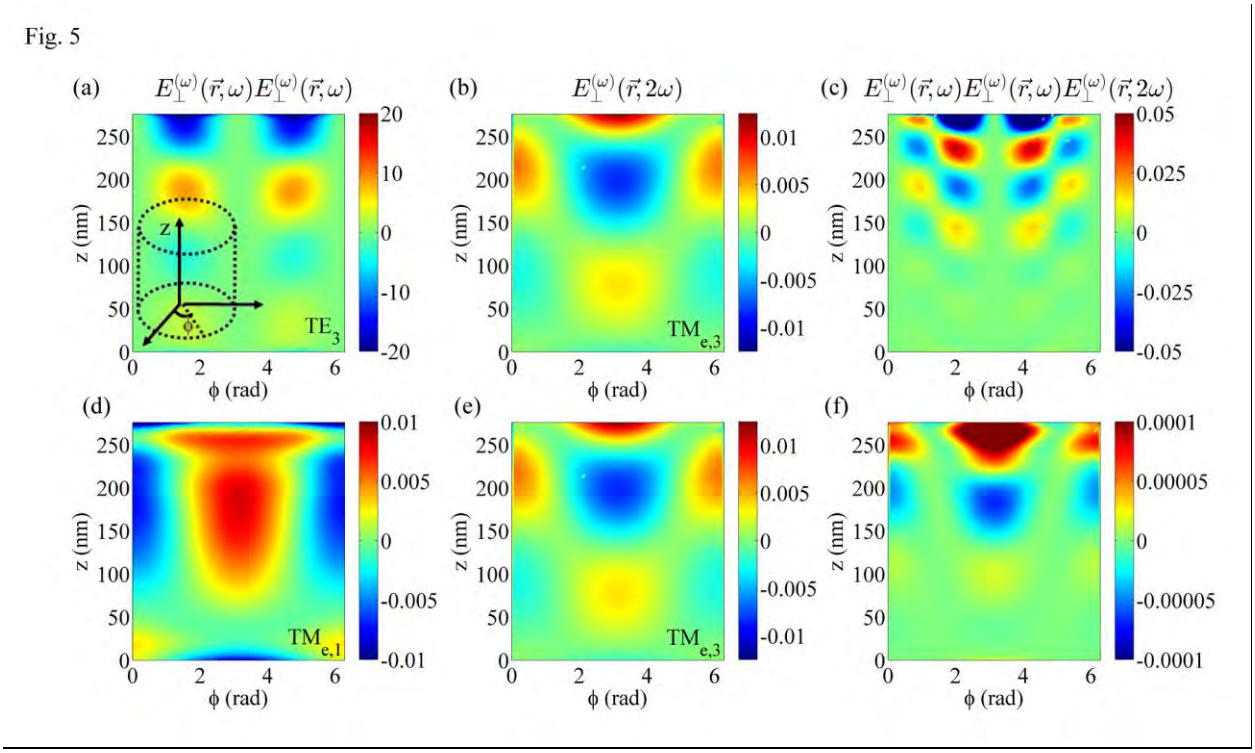

Figure 5. (a,d) Orthogonal to the nanorod surface (P_n) component of the nonlinear polarization in (a) TE_3 and (d) $TM_{e,1}$ modes induced by the TE and TM polarized fundamental light, respectively, at 2.3 eV. (b,e) The electric field distribution of the $TM_{e,3}$ mode at the SH frequency (4.6 eV). (c,f) Relative overlap integral between (c) TE_3 and $TM_{e,3}$ modes and (f) $TM_{e,1}$ and $TM_{e,3}$ modes. Fundamental light is incident from the top at the angle of incidence of 48°. The plots are presented around the nanorod circumference.

ASSOCIATED CONTENT

Supporting Information. **S1.** Field distribution analyses. **S2.** Analysis of the mode spectrum in the UV. This material is available free of charge via the Internet at http://pubs.acs.org.

AUTHOR INFORMATION

Corresponding Author

*Giuseppe Marino. giuseppe.marino@kcl.ac.uk.

Present Addresses

† Department of Electrical Engineering Physical Electronics, Tel Aviv University, Ramat Aviv 69978, Israel

Author Contributions

G.M., G.W and A.Z developed the idea. G.M. made numerical simulations. All authors analysed the results and wrote the manuscript.

Funding Sources

This work was supported, in part, by EPSRC (UK), the ERC iPLASMM project (321268), and US Army Research Office (W911NF-12-1-0533). A.Z. acknowledges support from the Royal Society and the Wolfson Foundation. G.W. acknowledges support from the EC FP7 project 304179 (Marie Curie Actions).

ACKNOWLEDGMENT

This work was supported, in part, by EPSRC (UK), the ERC iPLASMM project (321268), and US Army Research Office (W911NF-12-1-0533). A.Z. acknowledges support from the Royal Society and the Wolfson Foundation. G.W. acknowledges support from the EC FP7 project 304179 (Marie Curie Actions). The data access statement: all data supporting this research are provided in full in the results section in supplementary information.

REFERENCES

1. Boyd, R. W. *Nonlinear optics,* Ed 3; Academic press: New York, 2007.

2. Holzwarth, R.; Udem, T.; Hänsch, T. W.; Knight, J. C.; Wadsworth, W. J.; Russell, P. S. J. Optical frequency synthesizer for precision spectroscopy. *Phys. Rev. Lett.* **2000,** *85* (11), 2264.

3. Rullière, C. *Femtosecond laser pulses, Principles and Experiments,* Ed 2; Springer: New York, 2004

4. Ginzburg, P.; Krasavin, A.; Sonnefraud, Y.; Murphy, A.; Pollard, R. J.; Maier, S. A.; Zayats, A. V. Nonlinearly coupled localized plasmon resonances: Resonant second-harmonic generation. *Phys Rev. B: Condens. Matter Mater. Phys.* **2012,** *86* (8), 085422.

5. Celebrano, M.; Wu, X.; Baselli, M.; Großmann, S.; Biagioni, P.; Locatelli, A.; & Finazzi, M. Mode matching in multiresonant plasmonic nanoantennas for enhanced second harmonic generation. *Nature Nanotechnol.* **2015,** *10* (5), 412-417.

6. Aouani, H.; Navarro-Cia, M.; Rahmani, M.; Sidiropoulos, T. P.; Hong, M.; Oulton, R. F.; Maier S. A. Multiresonant broadband optical antennas as efficient tunable nanosources of second harmonic light. *Nano Lett.* **2012,** *12* (9), 4997-5002.

7. O'Brien, K.; Suchowski, H.; Rho, J.; Salandrino, A.; Kante, B.; Yin, X.; Zhang X. Predicting nonlinear properties of metamaterials from the linear response. *Nature Mater.* **2015,** *14* (4), 379-383.

8. Vincenti, M. A.; Campione, S.; de Ceglia, D.; Capolino, F.; & Scalora, M. Gain-assisted harmonic generation in near-zero permittivity metamaterials made of plasmonic nanoshells. *New J. Phys.* **2012,** *14* (10), 103016.

9. Vasilantonakis, N.; Nasir, M. E.; Dickson, W.; Wurtz, G. A.; Zayats, A. V. Bulk plasmon-polaritons in hyperbolic nanorod metamaterial waveguides. *Laser Photonics Rev.* **2015,** 9, 345-353

10. Hayat, A.; Orenstein, M. Standing-wave nonlinear optics in an integrated semiconductor microcavity. *Opt. Lett.* **2007,** *32* (19), 2864-2866.

11. de Ceglia, D.; Vincenti, M. A.; De Angelis, C.; Locatelli, A.; Haus, J. W.; Scalora, M. Role of antenna modes and field enhancement in second harmonic generation from dipole nanoantennas. *Opt. Express*, **2015,** *23* (2), 1715-1729.

12. Neira, A. D.; Olivier, N.; Nasir, M. E.; Dickson, W.; Wurtz, G. A.; Zayats, A. V. Eliminating material constraints for nonlinearity with plasmonic metamaterials. *Nat. Commun*. **2015**, *6*.

13. Johnson, P. B.; Christy, R. W. Optical constants of the noble metals. *Phys Rev. B: Condens. Matter Mater. Phys.* **1972,** *6* (12), 4370.

14. Elser, J.; Wangberg, R.; Podolskiy, V. A.; Narimanov, E. E. Nanowire metamaterials with extreme optical anisotropy. *Appl. Phys. Lett.* **2006,** *89* (26), 261102.

15. Tsai, K. T.; Wurtz, G. A.; Chu, J. Y.; Cheng, T. Y.; Wang, H. H.; Krasavin, A. V.; Zayats, A. V. Looking into meta-atoms of plasmonic nanowire metamaterial. *Nano letters*, **2014,** *14* (9), 4971-4976.

16. McMahon, M. D.; Lopez, R.; Haglund Jr, R. F.; Ray, E. A.; Bunton, P. H. Second-harmonic generation from arrays of symmetric gold nanoparticles. *Phys Rev. B: Condens. Matter Mater. Phys.* **2006,** *73* (4), 041401.

17. Hubert, C.; Billot, L.; Adam, P. M.; Bachelot, R.; Royer, P.; Grand, J.; Fort, A. Role of surface plasmon in second harmonic generation from gold nanorods. *Appl. Phys. Lett.* **2007,** *90* (18), 181105.

18. Smolyaninov, I. I.; Zayats, A. V.; Davis, C. C. Near-field second harmonic generation from a rough metal surface. *Physical Review B*, **1997,** *56* (15), 9290.

19. Bloembergen, N.; Chang, R. K.; Jha, S. S.; Lee, C. H. Optical second-harmonic generation in reflection from media with inversion symmetry. *Phys. Rev.* **1968,** *174* (3), 813.

20. Benedetti, A.; Centini, M.; Sibilia, C.; Bertolotti, M. Engineering the second harmonic generation pattern from coupled gold nanowires. *J. Opt. Soc. Am. B* **2010,** *27* (3), 408-416.

21. Scalora, M.; Vincenti, M. A.; De Ceglia, D.; Roppo, V.; Centini, M.; Akozbek, N.; Bloemer, M. J. Second-and third-harmonic generation in metal-based structures. *Phys. Rev. A: At., Mol., Opt. Phys.* **2010,** *82* (4), 043828.

22. Wang, F. X.; Rodríguez, F. J.; Albers, W. M.; Ahorinta, R.; Sipe, J. E.; Kauranen, M. Surface and bulk contributions to the second-order nonlinear optical response of a gold film. *Phys Rev. B: Condens. Matter Mater. Phys.* **2009,** *80* (23), 233402.

23. Berthelot, J.; Bachelier, G.; Song, M.; Rai, P.; Colas des Francs, G.; Dereux, A.; Bouhelier, A. Silencing and enhancement of second-harmonic generation in optical gap antennas. *Opt. Express* **2012,** *20* (10), 10498-10508.

24. Forestiere, C.; Iadarola, G.; Rubinacci, G.; Tamburrino, A.; Dal Negro, L.; Miano, G. Surface integral formulations for the design of plasmonic nanostructures. *J. Opt. Soc. Am. A* **2012,** *29* (11), 2314-2327.

25. Bohren, C. F.; Huffman, D. R. *Absorption and scattering of light by small particles*. Ed. 1, John Wiley & Sons: New York, 1983.

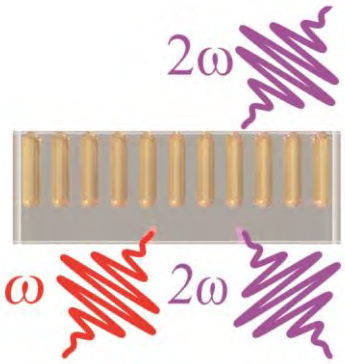

Table of Contents Graphic and Synopsis

SUPPLEMENTARY INFO

S1. Field distribution analysis.

Figure 5 shows the distributions of the selected fundamental and second-harmonic modes in order to illustrate the resonant conditions. The TE mode at fundamental frequency generates the respective TM mode at the second-harmonic frequency. At the fundamental frequency (Fig. 5a) the orthogonal to the surface component of the nonlinear polarization has a clear signature of TE_3 with the expected two valleys and a peak. However, at the rod extremities some lightning rods effects are also present. On the other hand, the field distribution at the second-harmonic frequency (Fig. 4b) has two valleys and two peaks, as expected for a $TM_{e,3}$ mode. Significant overlap is obvious. In analogy to Fig. 5a,b, the orthogonal component of both the nonlinear polarization at 1.77 eV and the electromagnetic field at 3.54 eV in Fig. S1a,b, should show the same number of peaks and valleys as the corresponding modes in Ref.[9] One can note that the field at 1.77 eV reports a clear signature of TE_2 with the expected one node one valley and one peak. Interestingly, TE_2 lies in a spectral range which is away from both interband and intraband transitions, thereby showing sharp modal characteristics. In contrast to this, the map in Figure S1b reports two valleys and a peak, typical of $TM_{e,2}$ mode. Similarly to the case of $TM_{e,3}$, the last valley is less pronounced due to interband transitions and to the arbitrary angle of incidence. Significant relative overlap is obvious in Fig.S1c, which results one order of magnitude lower at the substrate side in comparison with the overlap integral between the modes TE_3 and $TM_{e,3}$ (Fig. 5c).

Fig. SI 1

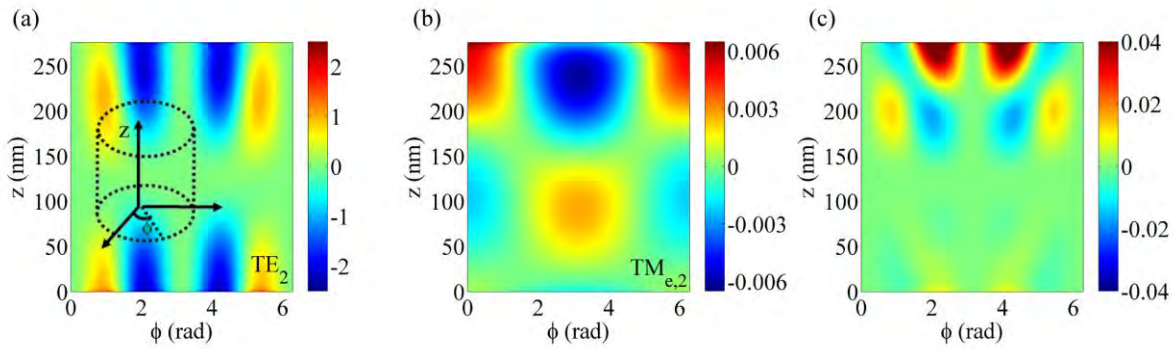

Figure S1. (a) Orthogonal to the nanorod surface (P_n) component of the nonlinear polarization in TE_2 mode induced by the TE polarized fundamental light at 1.77 eV. (b) The electric field distribution of the $TM_{e,2}$ mode at the SH frequency (3.54 eV). (c) Relative overlap integral between TE_2 and $TM_{e,2}$ modes. Fundamental light is incident from the top at the angle of incidence of 48°. The plots are presented around the nanorod circumference.

S2. Analysis of the mode spectrum in the UV

Due to the high losses in the UV spectral range, especially close to the interband transitions, the identification of the mode in the linear spectra is not straightforward as they become broader[25]. Moreover, superposition of several interband transitions occurring in the UV spectral range results in the characteristic "oscillating" wavelength dependence of the Au permittivity measured in Ref.[13]. In order to deconvolute these sporadic oscillations from the true broad resonances of the metamaterial slab, we simulated the reflectance spectra with a constant value of the complex permittivity typical of gold in the UV ($\varepsilon_r = -1.26 + 5.5i$ at a wavelength of 350 nm) and compared to the reflectance of the metamaterial with the factual permittivity dispersion[13] (Fig. S2). Since the Au permittivity in the UV does not fluctuate far from the value it assumes at 350 nm, we can, then, concentrate our investigation on the mode identification (black line in Fig. S2). Two minima occurring at

400 and 285 nm corresponds to the near field distributions typical of the modes $TM_{e,2}$ and $TM_{e,3}$, respectively. By comparing the field distributions at 400 nm (285 nm) with those at 350 (270 nm), within a FWHM of the respective modes, it is evident that the distributions are the same apart from a small dephasing. Therefore, the oscillations of the blue curve corresponds to the oscillations of the permittivity while the metamaterial slab mode is the same.

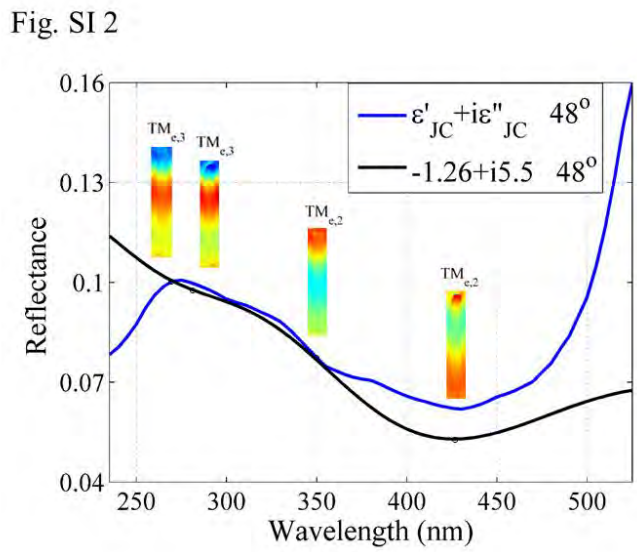

Figure S2. Reflectance spectra of the metamaterial for the TM polarized light at 48° angle of incidence simulated for the actual Au permittivity[13] (blue line) and for a fixed dispersionless permittivity (black line). The near-field distributions inside the elementary cell plotted for the dispersionless permittivity at wavelengths of 270 nm, 285 nm, 350 nm, and 400 nm (black circles).